

Adaptation of atomistic and continuum methods for multiscale simulation of quasi-brittle intergranular damage

Weiterentwicklung numerischer Methoden der Atomistik
und Kontinuumsmechanik zur Multiskalen-Simulation
quasi-spröder intergranularer Schädigung

DISSERTATION

zur Erlangung des akademischen Grades
Doktor-Ingenieur
an der Fakultät Bauingenieurwesen
der Bauhaus-Universität Weimar

vorgelegt von
Dipl.-Ing. Torsten Luther
geboren am 22. März 1979 in Quedlinburg

Weimar, Juni 2010

Gutachter:

1. Prof. Dr.-Ing. habil. Carsten Könke, Bauhaus-Universität Weimar
2. Prof. Dr. Anthony R. Ingraffea, Cornell-Universität Ithaca, NY
3. Prof. Dr. rer. nat. Klaus Hackl, Ruhr-Universität Bochum

Tag der Disputation: 02.09.2010

Für meine Familie

“All three principles - the conformability of nature to herself, the applicability of the criterion of simplicity, and the utility of certain parts of mathematics in describing physical reality - are thus consequences of the underlying law of the elementary particles and their interactions. Those three principles need not be assumed as separate metaphysical postulates. Instead, they are emergent properties of the fundamental laws of physics.”

Murray Gell-Mann. Nature Conformable to Herself.
Complexity 1(4), pp. 9-12., 1995/96.

“Die Möglichkeit einer mechanischen Erklärung der ganzen Natur ist nicht bewiesen, ja, dass wir dieses Ziel vollkommen erreichen werden, kaum denkbar.”

Ludwig Boltzmann. Zur Energetik, Vortrag 1895.
Annalen der Physik u. Chemie, N.F. Bd. 58, S. 595.

Vorwort

Die vorliegende Arbeit entstand während meiner Tätigkeit als wissenschaftlicher Mitarbeiter am Institut für Strukturmechanik. Der darin dokumentierte Forschungsbeitrag steht im engen Zusammenhang mit der Bearbeitung des DFG-geförderten Projektes “Simulation der Schädigungsevolution in polykristallinen Werkstoffen auf der Grundlage von Modellen der Meso- und Mikroskala”.

Während meiner Zeit am Institut für Strukturmechanik in Weimar erhielt ich vielfältige Unterstützung bei der Umsetzung meiner wissenschaftlichen Vorhaben. Mein besonderer Dank gilt Herrn Professor Carsten Könke für die bereits während meines Studiums erfolgte Einbindung in die Arbeit am Institut und die anschließend ermöglichte wissenschaftliche Tätigkeit als Mitarbeiter. Darüber hinaus danke ich Herrn Professor Könke als Mentor meiner Arbeit für die fachlichen Diskussionen und die Motivation zum stets befürworteten regen wissenschaftlichen Austausch auf internationalen Konferenzen.

Danken möchte ich Herrn Professor Klaus Hackl und Herrn Professor Anthony R. Ingraffea für die Bereitschaft zur Begutachtung meiner Dissertation und die wertvollen Hinweise zur Arbeit. Zum erfolgreichen Abschluß der Arbeit hat mein leider viel zu kurzer Aufenthalt an der Cornell-Universität in Ithaca entscheidend beigetragen, bei dem ich von der Cornell Fracture Group um Professor Ingraffea herzlich aufgenommen wurde.

Einen ebenfalls großen Beitrag zum Gelingen meiner Arbeit habe ich den vielen Kollegen des Instituts zu verdanken, die mir durch administrative und fachliche Unterstützung geholfen haben. Ein besonderer Dank gilt dabei Herrn Maik Brehm und Herrn Ingmar Stade, für ein stets offenes Ohr in fachlichen und außerfachlichen Debatten. Daneben danke ich meinen langjährigen Kollegen Dr. Stefan Eckardt, Dr. Thomas Most und Dr. Jörg F. Unger für die jederzeit abrufbare Hilfe bei Fragestellungen zu Implementationen in der Institutssoftware SLang. Nicht zu vergessen ist die mir erbrachte Unterstützung durch studentische Mitarbeiter, denen mein vollster Dank gilt.

Hervorheben möchte ich die freundschaftliche Atmosphäre am Institut, die das Arbeiten über all die Jahre äußerst angenehm gestaltet hat. Stellvertretend gilt dafür mein herzlicher Dank unserer Sekräterin Frau Terber, die mit ihre positiven Einstellung Probleme schnell verschwinden läßt. In besonderer Erinnerung wird mir auch das ISM-Volleyballteam in seiner vielfältigen Besetzung bleiben, mit dem wir außerhalb des Arbeitsalltags viel Spaß hatten und sogar unerwartete Erfolge feiern konnten.

Mein herzlicher Dank gilt meiner Frau Wiebke für die uneingeschränkte Unterstützung während meiner Promotion, in der Sie viel Zeit mit mir entbehren mußte. Ebenso herzlich danke ich meiner Tochter Finja für das bescherte Glück, mein Leben zu bereichern und mich auch an anstrengenden Tagen der Promotionszeit fröhlich gestimmt zu haben.

Danken möchte ich meinen Eltern, für meine behütete Kindheit und das Ermöglichen meines beruflichen Werdegangs. Daneben gilt mein besonderer Dank meiner Schwester Ivonne, die mich stets bei der Umsetzung meiner Interessen unterstützt und somit entscheidend zu meiner persönlichen Entwicklung beigetragen hat.

Abstract

The numerical simulation of damage using phenomenological models on the macroscale was state of the art for many decades. However, such models are not able to capture the complex nature of damage, which simultaneously proceeds on multiple length scales. Furthermore, these phenomenological models usually contain damage parameters, which are physically not interpretable. Consequently, a reasonable experimental determination of these parameters is often impossible.

In the last twenty years, the ongoing advance in computational capacities provided new opportunities for more and more detailed studies of the microstructural damage behavior. Today, multiphase models with several million degrees of freedom enable for the numerical simulation of micro-damage phenomena in naturally heterogeneous materials. Therewith, the application of multiscale concepts for the numerical investigation of the complex nature of damage can be realized.

The presented thesis contributes to a hierarchical multiscale strategy for the simulation of brittle intergranular damage in polycrystalline materials, for example aluminum. The numerical investigation of physical damage phenomena on an atomistic microscale and the integration of these physically based information into damage models on the continuum meso- and macroscale is intended. Therefore, numerical methods for the damage analysis on the micro- and mesoscale including the scale transfer are presented and the transition to the macroscale is discussed.

The investigation of brittle intergranular damage on the microscale is realized by the application of the nonlocal Quasicontinuum method, which fully describes the material behavior by atomistic potential functions, but reduces the number of atomic degrees of freedom by introducing kinematic couplings. Since this promising method is applied only by a limited group of researchers for special problems, necessary improvements have been realized in an own parallelized implementation of the 3D nonlocal Quasicontinuum method. The aim of this implementation was to develop and combine robust and efficient algorithms for a general use of the Quasicontinuum method, and therewith to allow for the atomistic damage analysis in arbitrary grain boundary configurations. The implementation is applied in analyses of brittle intergranular damage in ideal and nonideal grain boundary models of FCC aluminum, considering arbitrary misorientations.

From the microscale simulations traction separation laws are derived, which describe

grain boundary decohesion on the mesoscale. Traction separation laws are part of cohesive zone models to simulate the brittle interface decohesion in heterogeneous polycrystal structures. 2D and 3D mesoscale models are presented, which are able to reproduce crack initiation and propagation along cohesive interfaces in polycrystals. An improved Voronoi algorithm is developed in 2D to generate polycrystal material structures based on arbitrary distribution functions of grain size. The new model is more flexible in representing realistic grain size distributions. Further improvements of the 2D model are realized by the implementation and application of an orthotropic material model with Hill plasticity criterion to grains. The 2D and 3D polycrystal models are applied to analyze crack initiation and propagation in statically loaded samples of aluminum on the mesoscale without the necessity of initial damage definition.

Kurzfassung

Strukturmechanische Ermüdungs- und Lebensdaueranalysen basieren meist auf der Anwendung phänomenologischer Modelle der Schädigungs- und Bruchmechanik zur numerischen Simulationen des makroskopischen Schädigungsverhaltens. Ausgehend von einer definierten Anfangsschädigung sind diese Modelle nicht in der Lage, die tatsächlichen Vorgänge der Rissinitiierung und unterschiedlichen Rissausbreitung zu erfassen. Eine physikalische Interpretation der phänomenologisch eingeführten Schädigungsparameter ist oftmals nicht möglich und deren experimentelle Bestimmung schwierig.

Die Berücksichtigung des mikrostrukturellen Aufbaus von Materialien in numerischen Modellen der Schädigungs- und Bruchmechanik bietet neue Möglichkeiten, die für die Rissinitiierung und Rissausbreitung ursächlichen physikalischen Phänomene abzubilden. Zunehmende Erkenntnisse über gleichzeitig auftretende Mikro- und Makroschädigungsvorgänge resultieren in verbesserten numerischen Modellen, mit denen aufwändige und kostenintensive Experimente in der Materialentwicklung zum Teil ersetzt werden können.

In Kenntnis einer Vielfalt von unterschiedlichen Schädigungsphänomenen in technischen Materialien fokussiert die vorliegende Dissertation auf die Entwicklung und Verbesserung numerischer Methoden der Atomistik und der Kontinuumsmechanik zur Mehrskalenuntersuchung spröder Korngrenzenschädigung in polykristallinen Werkstoffen, z.B. Aluminium. Die kombinierte Anwendung dieser Methoden ist Teil eines hierarchischen Mehrskalenansatzes zur Integration des physikalisch beschriebenen Materialverhaltens der Atomistik in ein ingenieurmäßiges Kontinuumschädigungsmodell.

Ziel der Dissertation ist die Entwicklung einer Methodik, die es erlaubt, den Verlust atomarer Bindungen als physikalische Ursache spröder Schädigung zu simulieren und Ergebnisse aus diesen atomistischen Mikroskalen-Simulationen zur Parametrisierung von kohäsiven Materialmodellen der Kontinuumsmechanik zu nutzen. Diese beschreiben den intergranularen Spröbruch in heterogenen Polykristallmodellen der Mesoskala. Der Einfluss der Heterogenität wird in nichtlinearen Finite-Elemente-Simulationen durch explizite Abbildung der Kornstruktur im mesoskopischen Polykristallmodell berücksichtigt. Durch den Einsatz des kohäsiven Interface-Gesetzes erlaubt das auf der Mesoskala angewandte Kontinuumsmodell die Simulation spröder Korngrenzenschädigung in statisch belasteten 2D und 3D Modellen ohne die Notwendigkeit der Definition einer Anfangsschädigung, wie dies in klassischen Modellen der linear-elastischen Bruchmechanik notwendig ist.

Zur effizienten Realisierung der atomistischen Mikroskalen-Simulationen wird eine Implementation der nichtlokalen 3D Quasikontinuuumsmethode angewandt. Diese Methode basiert auf einem atomistischen Ansatz und beschreibt das Materialverhalten auf Grundlage atomarer Bindungskräfte. In Modellgebieten mit gleichmäßigem Verformungsfeld werden kinematische Kopplungen atomarer Freiheitsgrade eingeführt, sodass sich die Zahl unabhängiger Freiheitsgrade stark reduziert. Deren effizienter Einsatz erlaubt Simulationen an größeren Modellen ohne Kopplung mit kontinuumsmechanischen Methoden. Eine verbesserte Vernetzung, ein robuster Optimierungsalgorithmus und die vorgenommene Parallelisierung machen die implementierte nichtlokale 3D Quasikontinuuumsmethode zu einem effizienten Werkzeug für die robuste Simulation von physikalischen Schädigungsphänomenen in beliebigen atomistischen Konfigurationen. In quasistatischen Simulationen wird eine deutliche Beschleunigung gegenüber der Methode der Gitterstatik bei vergleichbarer Qualität der Ergebnisse erreicht.

Contents

Nomenclature	xix
1 Introduction	1
1.1 Motivation	1
1.2 Intention of the presented thesis	3
1.3 Innovations of the presented thesis	5
1.4 Outline	6
2 Numerical methods in material modeling	8
2.1 Continuum mechanics	8
2.1.1 Fundamentals	8
2.1.2 Finite element method	14
2.2 Atomistic methods	17
2.2.1 Potential functions	17
2.2.2 Lattice statics	21
2.2.3 Molecular dynamics	22
2.2.4 Reduced units	24
2.3 Mixed atomistic-continuum methods	26
3 Geometrical characterization of grain boundaries	30
3.1 Definition of individual crystallite orientation	30
3.1.1 Orientation by Miller indices	30
3.1.2 Orientation by Eulerian angles	31
3.1.3 Transformation from Eulerian angles into Miller indices	33
3.2 Definition of grain boundary misorientation	34
3.2.1 CSL misorientation scheme	34
3.2.2 Interface-plane scheme (IPS)	35
3.2.3 Transformation from IPS and CSL misorientation scheme into grain boundary definition by Miller indices and vice versa	35
3.2.4 Relation between CSL misorientation scheme and IPS description	37
3.3 Experimental measurements of grain boundary misorientation	38

4	The Quasicontinuum method: Theory and implementation	40
4.1	Theory	41
4.1.1	Fundamentals of the Quasicontinuum theory at zero temperature	41
4.1.2	Local Quasicontinuum formulation at zero temperature	43
4.1.3	Nonlocal Quasicontinuum formulation at zero temperature	46
4.1.4	Coupling of the local and nonlocal Quasicontinuum formulations	50
4.1.5	Adaption of discretization in Quasicontinuum models	52
4.1.6	Approaches of Quasicontinuum formulations with dynamics of atoms and at finite temperature	53
4.2	Implementation of a robust and parallelized 3D nonlocal Quasicontinuum method	56
4.2.1	Motivation and requirements for the implementation	56
4.2.2	Definition of representative atoms and generation of the FE mesh	58
4.2.3	Computation of neighborlists	60
4.2.4	Weighting factor calculation	62
4.2.5	Energy and force calculation from EAM potentials	65
4.2.6	Optimization method	69
4.2.7	Parallelization	72
4.2.8	Calculation of stress at the atomic level	75
4.2.9	Determination of the geometry of defects	76
4.3	Examples	78
4.3.1	Nanoindentation in FCC aluminum	78
4.3.2	Generation of samples with low energy grain boundaries	81
5	Scale transition by atomistic-based cohesive zone representations	87
5.1	A review on cohesive zone representations	87
5.1.1	On the history of cohesive zone models	87
5.1.2	Atomistic-based cohesive zone representations	87
5.2	Calculation of cohesive parameters from atomistics	89
5.2.1	Modeling of general grain boundaries without periodicity	89
5.2.2	Cohesive parameters from tensile simulations	91
5.2.3	Cohesive parameters from shear simulations	95
5.2.4	Combining properties from normal and shear loading in a coupled CZM	99
5.3	Influence of atomic level defects on grain boundary characteristics	103
5.3.1	Measurement of nanoporosity near interfaces	103
5.3.2	Effect of introduced point vacancies near interfaces	105

6	Polycrystal modeling on the mesoscale	108
6.1	A review on polycrystal modeling and damage mechanics	108
6.2	Geometrical features	109
6.2.1	Classical 2D and 3D Voronoi diagrams	109
6.2.2	Modified 2D Voronoi diagram	110
6.2.3	Modified 3D Voronoi diagram	114
6.3	Constitutive Models	115
6.3.1	Orthotropic grains	116
6.3.2	Cohesive grain boundaries	125
6.4	Examples	127
6.4.1	Polycrystal models with orthotropic linear elastic grains	127
6.4.2	2D Polycrystal models with orthotropic elastoplastic grains	133
6.5	Application of atomistic-based cohesive zone representations in continuum polycrystal models	136
7	Conclusions	145
7.1	Application of the 3D nonlocal Quasicontinuum method on the microscale	145
7.2	Derivation of traction separation laws from atomistic simulations	147
7.3	Damage simulations by continuum polycrystal models on the mesoscale . .	149
8	Outlook	150
8.1	Atomistic-based cohesive zone representations	150
8.2	Polycrystal modeling on the mesoscale and transition to the macroscale . .	151
	Appendices	154
	A Summary of the implemented 3D nonlocal QC formulation	154
	B SLang commands for atomistic-based microscale simulations	156
	C Input file with EAM potential functions	170
	Bibliography	171

List of Figures

1.1	The proposed hierarchical multiscale concept for the damage analysis in polycrystalline materials consists of numerical models on three different length scales.	4
2.1	Reference or initial configuration respectively, and deformed configuration.	9
2.2	Right and left polar decomposition of deformation gradient \mathbf{F}	10
2.3	Stress \mathbf{t} at the surface s	11
2.4	Interatomic potential function and interatomic force function with repulsion at short spacing and attraction at large spacing.	18
2.5	Potential functions for aluminum provided by F. Ercolessi [Ercolessi 2009] (continuous lines) and the group of Mishin [Mishin 2009] (dotted lines) in the framework of the EAM. Left: Electron density contribution $\rho_{ij}(r_{ij})$. Middle: Embedding energy $U_i(\rho_i)$. Right: Pair potential $\phi_{ij}(r_{ij})$	20
2.6	Left: Scheme of the FEAt model of a crack tip [Kohlhoff et al. 1991]. Small circles in the central model region around the crack tip denote atomic sites while squares in the outer model region show finite elements. Overlapping transition zones are between the atomistic and the FE region. Right: Scheme of the MAAD and CLS model respectively surrounding a crack (from [Broughton et al. 1999]). TB stands for the quantum Tight-Binding region.	27
2.7	Quasicontinuum model for the fracture analysis in aluminum (from [Buehler et al. 2005]).	28
3.1	Examples of Miller indices. Left: (112)-plane. Right: [110]- and [011]-direction.	31
3.2	Global orientation of two FCC crystallites building a $\Sigma 5$ STGB (symmetric tilt grain boundary). In both crystallites the [210]-direction is parallel to global X. The $[\bar{1}20]$ -direction in the lower crystallite and the $[\bar{1}20]$ -direction in the upper crystallite are parallel to global Y.	31
3.3	From left to right: $Z'X'Z'$ -rotation of coordinate system $(X'Y'Z')$ by Eulerian angles $\{\varphi_1\phi\varphi_2\}$ starting with $(X'Y'Z')$ lies parallel to global coordinate system (XYZ)	32

3.4	HRTEM images of a $\Sigma 11$ grain boundary (left) from [Schmidt 2003] and a $\Sigma 7$ grain boundary (right) from [Hu et al. 2000], both in aluminum. White dots are interpretable as atomic positions.	38
4.1	Reference configuration: Definition of lattice positions of atomic nuclei by the Bravais lattice vectors \mathbf{A}_n and the position vector \mathbf{X}_0 of a reference atom.	41
4.2	FE mesh (dark lines) linked to the atomic lattice by nodes at sites of representative atoms (red).	42
4.3	Deformation of a unit cell according to the deformation gradient \mathbf{F} . Left: Reference configuration with undistorted Bravais lattice vectors \mathbf{A}_n . Right: Deformed configuration with distorted Bravais lattice vectors \mathbf{a}_n	44
4.4	Left: The amount of shadowed domains build the cell assigned to representative atom α_1 . Right: Triangular elements are subdivided by medians into equal parts per node. The partitioning can be adopted straightforward to tetrahedral elements.	45
4.5	Explicit energy calculation of nonlocal representative atoms by interactions within a cutoff distance r_c . Surface and interface effects are directly involved.	46
4.6	Nonlocal QC formulation of [Knap et al. 2001]: Cluster of atoms (dark yellow) are used to calculate forces and energies assigned to representative atoms (red) by an averaging procedure. Remaining atoms (light grey) do not explicitly contribute to calculated forces and energies.	47
4.7	Partitioning of energy from cluster atom k to the representative atoms of the associated element.	48
4.8	Surface energies for samples of the same size. Left: In the limit of full atomistic resolution only the surface region itself is influenced by the surface energy. Right: A coarse mesh at the surface causes unphysical surface energies deep in the solid.	49
4.9	“Ghost forces” arise near the interface between local (circles) and nonlocal (dots) representative atoms due to various force calculation rules. The dotted circle includes all atoms within the cutoff distance r_c around atom α_2 . While the interaction between atoms α_1 and α_2 explicitly contributes to the force of nonlocal atom α_2 , local atom α_1 is affected only by the deformation gradient in its associated elements (grey).	51

4.10	Definition of representative atoms (red) from the atomic lattice of a GB model and subsequent mesh generation. Dashed lines surround the adjacent crystallites with different orientation. (a) Vertices of the convex hull of each crystallite define sites of representative atoms. (b) Additional representative atoms are defined by the aimed resolution. (c) Delaunay triangulation with the total set of representative atoms as generation points. Distorted elements (light blue) at non-convex geometrical boundaries can be removed. (d) Final non-convex mesh.	59
4.11	Neighbor calculation by domain partitioning: The search of relevant neighbors of cluster atom k is reduced to atoms of its own sub-domain Ω_6 and the adjacent sub-domains $\Omega_2, \Omega_3, \Omega_7$, which partially overlay with the relevant neighbor region (defined by radius R) of atom k	61
4.12	The nonlocal QC formulation of [Knap et al. 2001] with force-based cluster scheme implies for cluster atoms (yellow) the calculation of interaction forces also based on the electron density at sites of 1st order neighbors (black). To calculate electron densities at sites of 1st order neighbors, the 2nd order neighbors (grey) have to be considered additionally in the force calculation.	68
4.13	(a) Speed-up of parallelized subroutines in the present QC implementation. The computations of the system matrix, atomic forces, electron densities, and atomic energies as well as the interpolation of atomic positions in the deformed configuration and the PARDISO equation solver are evaluated. (b) Speed-up of one complete iteration step using Newton's method with line-search and backtracking, and the FIRE algorithm. The speed-up is measured for the nanoindentation problem of Section 4.3.1.	74
4.14	Determination of fracture surfaces by the energy method (left) and the centrosymmetry technique (right). Observed is a cracked surface part of an aluminum sample under tension. Atoms on the left sample boundary indicate the free surface.	76
4.15	Determination of dislocation loops by the energy method (left), and the centrosymmetry technique (right). Observed is a part of an aluminum sample in a nanoindentation simulation. Blue atoms on the top indicate the free surface.	77
4.16	(a) Model dimensions and crystal orientation for the simulation of nanoindentation in a FCC aluminum cube of approximately one million atoms. (b) Cut at middle z-dimension through the atomic lattice of the QC model with representative atoms (red).	78
4.17	Force-depth curves of nanoindentation simulation with lattice statics and the QC implementation.	79

4.18	Three different views on dislocation loops under the indenter visualized by the centrosymmetry technique. The graphics refer to the lattice statics simulation at indenter depth 7.5 Å.	81
4.19	Three different views on dislocation loops in the QC simulation with $r_{cl}=\sqrt{2}a_0$ at indenter depth 7.5 Å.	81
4.20	Three different views on dislocation loops in the QC simulation with $r_{cl}=\sqrt{\frac{1}{2}}a_0$ at indenter depth 7.5 Å.	81
4.21	Search for the low energy configuration of a $\Sigma_{33} \langle 110 \rangle (2\bar{2}5)$ STGB. (a) Initial configuration of two separate crystallites with a distance of about 1 Å between them. The z-dimension is also 100 Å. Red atoms are representative atoms of the QC model with free surfaces. (b) Cut through the final configuration with atomic energies in the GB region. The GB energy is calculated from an analysis of the atoms within the centered box of size 60 Å x 40 Å x 60 Å (black lines).	82
4.22	Calculated GB energies of $\Sigma_{33} \langle 110 \rangle (2\bar{2}5)$ STGB configurations with various vertical shifts of the atomic lattice of the upper crystallite. The minimum GB energy is calculated with a shift of 4 Å.	83
4.23	GB energies of $\langle 110 \rangle$ STGBs calculated by [Sansoz et al. 2005], [Chandra et al. 1999], and in the present study, in comparison with experimental values of [Otsuki et al. 1986].	85
4.24	$\Sigma_{11} \langle 110 \rangle (2\bar{2}5)/(4\bar{4}1)$ ATGB. (a) Initial atomic configuration of the QC model with free surfaces. Representative atoms are red colored. The z-dimension is 100 Å. (b) Cut through the final configuration with atomic energies in the GB region and with the energy evaluation box (black lines).	86
5.1	3D QC model with boundary layers of 14 Å thickness at all six boundary faces of the model. Constraints are applied to the atoms in the boundary layers to realize rolled boundary conditions. Additionally, displacements are applied to some of these atoms to force tensile (illustrated) or shear stress.	90
5.2	Interface separation curves from tensile simulations on aluminum models with $\Sigma_{33} \langle 110 \rangle (2\bar{2}5)$ STGB and $\Sigma_{11} \langle 110 \rangle (2\bar{2}5)/(4\bar{4}1)$ ATGB, respectively.	92
5.3	Simulated fracture process of $\Sigma_{11} \langle 110 \rangle (2\bar{2}5)/(4\bar{4}1)$ ATGB under tension. Atoms within a central part of the model are visualized by the energy method. Strain ϵ_{yy}^{gl} means the effective sample strain perpendicular to the interface.	93
5.4	Interface separation curves from tensile simulations on aluminum $\Sigma_{33} \langle 110 \rangle (2\bar{2}5)$ STGB models of different sample height.	94

5.5	Interface separation curves from tensile simulations on aluminum $\Sigma 33 \langle 110 \rangle (2\bar{2}5)$ STGB models of different sample size.	94
5.6	Interface separation curves from shear simulations on aluminum models with $\Sigma 33 \langle 110 \rangle (2\bar{2}5)$ STGB and $\Sigma 11 \langle 110 \rangle (2\bar{2}5)/(4\bar{4}1)$ ATGB, respectively. Boundary displacements are applied parallel to the global x-axis in positive (left diagram) and negative (right diagram) direction.	96
5.7	Simulated fracture process of $\Sigma 11 \langle 110 \rangle (2\bar{2}5)/(4\bar{4}1)$ ATGB under shear in negative x-direction. Atoms within a central part of the model are visualized by their potential energy values. Displacement u_x^b refers to the relative x-displacement of the upper boundary layer compared to the lower boundary layer.	97
5.8	Interface separation curves from shear simulations on aluminum models with $\Sigma 33 \langle 110 \rangle (2\bar{2}5)$ STGB and $\Sigma 11 \langle 110 \rangle (2\bar{2}5)/(4\bar{4}1)$ ATGB, respectively. Boundary displacements are applied parallel to the global z-axis.	97
5.9	Simulated fracture process of $\Sigma 11 \langle 110 \rangle (2\bar{2}5)/(4\bar{4}1)$ ATGB under shear in z-direction. Atoms within a central part of the model are visualized by their potential energy values. Displacement u_z^b refers to the relative z-displacement of the upper boundary layer compared to the lower boundary layer.	98
5.10	TSL of the coupled CZM which is assigned to interfaces in continuum polycrystal models.	100
5.11	Atomistic-based traction separation laws of the coupled CZM for an aluminum $\Sigma 33 \langle 110 \rangle (2\bar{2}5)$ STGB and an aluminum $\Sigma 11 \langle 110 \rangle (2\bar{2}5)/(4\bar{4}1)$ ATGB, respectively.	103
5.12	Evolution of interface energy and nanoporosity in tensile (left) and shear (right) simulations on the $\Sigma 11 \langle 110 \rangle (2\bar{2}5)/(4\bar{4}1)$ ATGB.	104
5.13	Evolution of nanoporosity compared to the stress state of the $\Sigma 11 \langle 110 \rangle (2\bar{2}5)/(4\bar{4}1)$ ATGB in tensile (left) and shear (right) simulations.	105
5.14	Average stress-opening response curves of an aluminum $\Sigma 33 \langle 110 \rangle (2\bar{2}5)$ STGB with different levels of initial damage D_c	106
5.15	Tensile and shear strength vs initial cumulative damage of an aluminum $\Sigma 11 \langle 110 \rangle (2\bar{2}5)/(4\bar{4}1)$ ATGB (left) and an aluminum $\Sigma 33 \langle 110 \rangle (2\bar{2}5)$ STGB (right).	106
6.1	Classical 2D and 3D Voronoi diagrams.	109
6.2	Light microscopy photograph of an Al-Si-Ge grain structure (from [Kirchner 2001]).	110
6.3	Cumulative grain size distribution.	111
6.4	Circles are placed into a box (outer boundary) larger than the aimed sample (inner boundary).	111

6.5	Construction of modified Voronoi points after Delaunay triangulation. . . .	112
6.6	Cell structure around the circles within the sample.	112
6.7	Sample with modified Voronoi diagram.	113
6.8	Comparison of predefined cumulative lognormal distribution function and resulting grain size distribution of generated cell structure.	114
6.9	Geometrical 3D polycrystal structure generated by a former <i>mBuilder</i> ver- sion provided by [Rollett et al. 2010]. The grains are build by clusters of Voronoi cells.	115
6.10	2D crystallite with local CS (X'Y') defined by the orthotropic material axes. The crystal orientation is obtained by a counterclockwise rotation from global CS (XY) by angle φ	120
6.11	Description of misorientation in 3D by angles β_i (left), and in 2D by angle β (right).	126
6.12	Boundary and loading conditions of tensile test.	128
6.13	Example of a 2D FE mesh (sample size/median grain size = 5.3).	129
6.14	Mean values and standard deviation σ of tensile strength calculated on numerical samples of aluminum on the mesoscale.	129
6.15	Representative 2D examples of simulated crack propagation showing the deformed state at 1.0% global strain. Deformation is enlarged by factor 10. Left: Modified Voronoi structure, Right: Classical Voronoi structure. .	130
6.16	Von Mises stress states with values in (MPa) in a 2D modified Voronoi structure while the crack propagates at about 0.875% global strain. Deform- ation is enlarged by factor 10.	130
6.17	Von Mises stress states with values in (MPa) in a 3D classical Voronoi struc- ture while the crack propagates at about 0.9% global strain. Deformation is enlarged by factor 10.	132
6.18	Response curves of tensile test simulations using samples with the same underlying geometry and the same elastic material parameters.	133
6.19	Simulated crack propagation in the elastic model (a), the plastic model with yield stress values of set 1 (b), and set 2 (c), respectively. Equivalent plastic strain in grains is visualized, where grey color indicates the highest value. White color indicates interface opening. Deformation is enlarged by factor 10.	134
6.20	Equivalent plastic strain states at (a) 0.9% global strain, and (b) 1.2% global strain, simulated with yield stress values of set 1. Deformation is enlarged by factor 10.	135
6.21	Equivalent plastic strain states at (a) 0.9% global strain, and (b) 1.2% global strain, simulated with yield stress values of set 2. Deformation is enlarged by factor 10.	135

6.22	Response curves of tensile test simulations using samples with the same underlying geometry. Mean values of elastic and plastic material properties (set 2) are the same, but individual values vary due to different stochastic realizations.	135
6.23	Left: Grain structure with orientation of material axes. Right: FE mesh. .	136
6.24	Definition of GB orientations $\delta_{i,j}$ and grain orientations φ_i . Thick continuous lines indicate GBs. Dashed rectangles contain orientation data of crystallites for the GB models on microscale.	138
6.25	GB energies of $\langle 110 \rangle$ ATGBs with various misorientation.	142
6.26	GB strength of $\langle 110 \rangle$ ATGBs with various misorientation.	142
6.27	Response curve of the tensile simulation on mesoscale.	143
6.28	Progress of interface decohesion during tensile simulation on mesoscale. The contour plots visualize the von Mises stress in grains.	143
8.1	$\{100\}$ pole figure from [DoITPoMS 2010]. Black dots indicate $\{100\}$ poles of the crystallites. RD and TD denote the rolling and transverse directions, respectively.	152

List of Tables

4.1	Distribution of CPU time to several parallelized QC subroutines for the application of Newton’s method, and for the application of the gradient-based FIRE algorithm. The CPU time is measured for the nanoindentation problem of Section 4.3.1.	73
4.2	Normalized centrosymmetry parameters for various types of defects. Therein, a_0 is the lattice parameter. The last column contains ranges for the distinction of defects. The table is taken from [Buehler 2008].	78
4.3	Summary of simulating nanoindentation into the (010) plane of aluminum.	80
4.4	Calculated GB energies of thirteen $\langle 110 \rangle$ symmetric tilt GBs (STGB) and one $\langle 110 \rangle$ asymmetric tilt GB (ATGB). Comparison with computational results of [Sansoz et al. 2005] and [Chandra et al. 1999].	84
5.1	Elastic constants of FCC aluminum, from [Ercolessi et al. 1994].	91
5.2	Cohesive parameters of five aluminum $\Sigma 33 \langle 110 \rangle (2\bar{2}5)$ STGB models and one aluminum $\Sigma 11 \langle 110 \rangle (2\bar{2}5)/(4\bar{4}1)$ ATGB model, extracted from tensile simulations.	95
5.3	Cohesive parameters extracted from shear simulations on five aluminum $\Sigma 33 \langle 110 \rangle (2\bar{2}5)$ STGB models and one aluminum $\Sigma 11 \langle 110 \rangle (2\bar{2}5)/(4\bar{4}1)$ ATGB model.	99
5.4	Atomistic-based constitutive parameters of a coupled CZM, exemplary derived for two different aluminum GBs.	102
5.5	Measured values of nanoporosity for initial and broken configurations of two different GBs.	104
6.1	Material parameters of the 2D polycrystal model with linear elastic grains.	128
6.2	Additional material parameters of the 3D polycrystal model with linear elastic grains.	131
6.3	Mean values of tensile strength for the smallest sample size.	132
6.4	Mean values of yield stress and standard deviation σ_d	133
6.5	Orientation of orthotropic grain material axes by angle φ and stochastically distributed orthotropic material parameters of grains.	137
6.6	Geometrical data of grain boundaries.	140

6.7 Atomistic-based constitutive parameters of the coupled CZMs. 141

Nomenclature

Abbreviations

AtC	Atomistic to Continuum
ATGB	Asymmetric Tilt Grain Boundary
BSM	Bridging Scale Method
CADD	Coupled Atomistic and Discrete Dislocation
CGMD	Coarse-Grained Molecular Dynamics
CLS	Coupling of Length Scales
CS	Coordinate System
CSL	Coincident-Site Lattice
CZM	Cohesive Zone Model
DFT	Density Functional Theory
DOF	Degree Of Freedom
EAM	Embedded Atom Method
ESCM	Embedded Statistical Coupling Method
FCC	Face Cubic Centered
FE	Finite Element
FEAt	Finite-Element-Atom
FIRE	Fast Inertial Relaxation Engine
GB	Grain Boundary
HRTEM	High Resolution Transmission Electron Microscopy
IPS	Interface-Plane Scheme
MAAD	Macro Atomistic Ab initio Dynamics
MD	Molecular Dynamics
NVE	Micro canonical ensemble (constant particle Number, Volume, Energy)
NVT	Canonical ensemble (constant particle Number, Volume, Temperature)
QC	Quasicontinuum
SEM	Scanning Electron Microscopy
SI	Système International d'unités - International system of units
STEM	Scanning Transmission Electron Microscopy
STGB	Symmetric Tilt Grain Boundary
TEM	Transmission Electron Microscopy
TSL	Traction Separation Law

General notations

(XYZ)	global coordinate system
$(X'Y'Z')$	local coordinate system
$(\cdot)'$	first derivative of \cdot
$(\cdot)''$	second derivative of \cdot
$\delta(\cdot)$	variation of \cdot
$\ \cdot\ $	euclidian vector norm of \cdot , also defined as $\ \cdot\ _2$
$ \cdot $	absolute value of a scalar expression \cdot
$\mathcal{O}(\cdot)$	mathematical term depending on \cdot
$\det(\cdot)$	determinant of \cdot
$e^{(\cdot)}$	exponential function of \cdot
$\text{grad}(\cdot)$	gradient of \cdot
$\text{lin}(\cdot)$	linearization of \cdot
$\ln(\cdot)$	natural logarithm of \cdot
$\text{sgn}(\cdot)$	signum function of \cdot
\otimes	tensor product
ϵ	strain tensor
σ	stress tensor
ν	Poisson's ratio
\mathbf{E}	elastic constitutive matrix
\mathbf{I}	identity matrix
\mathbf{N}	elastic compliance matrix
E	Young's modulus
G	shear modulus
h	Planck's constant
k_B	Boltzmann constant
m	atomic mass
T	temperature
t	time
u	atomic mass unit

Numerical methods in material modeling

ϵ^e	elastic strain tensor
ϵ^p	plastic strain tensor
χ	temperature correction factor
ϵ	energy parameter within the context of reduced units
ϵ^{LJ}	material dependent energy parameter in the Lennard-Jones potential

Φ	transformation from \mathbf{X} to \mathbf{x}
ϕ_{ij}	pairwise isotropic interatomic potential between atoms i and j
ρ_{ij}	electron density contribution of atom j at site of atom i
ρ_i	local electron density at site of atom i
σ	length parameter within the context of reduced units
σ^{LJ}	material dependent length parameter in the Lennard-Jones potential
τ	time parameter within the context of reduced units
Ω	average density of the material
Π	potential of the atomic system
Π^{ext}	external applied potential
Π_{ij}	pair potential between atoms i and j
\mathbb{C}	second elasticity tensor
Δt	time step
$\ddot{\mathbf{x}}_i$	acceleration vector of atom i (equals \mathbf{a}_i)
\mathbf{a}_i	acceleration vector of atom i (equals $\ddot{\mathbf{x}}_i$)
\mathbf{B}_e	element-wise strain displacement matrix
\mathbf{C}	right Cauchy-Green tensor
$\mathbf{D}_e, \mathbf{D}_k$	differential operators
\mathbf{e}_i	basis vectors of the Cartesian coordinate system
\mathbf{F}	deformation gradient
\mathbf{f}_a	nodal force vector acting on site of atom a
\mathbf{f}_i	atomic force vector acting on atom i
\mathbf{f}_i^{ext}	external force vector acting on atom i
\mathbf{f}_t	force vector at time t
\mathbf{G}	Green-Lagrangian strain tensor
\mathbf{K}_α	matrix of hardening parameters
\mathbf{k}_e	local element stiffness matrix
\mathbf{k}_{gl}	global stiffness matrix
\mathbf{n}	normal vector
\mathbf{N}_e	element-wise matrix of shape functions
\mathbf{P}	first Piola-Kirchhoff stress tensor
\mathbf{p}	external force vector
\mathbf{q}_e	local element load vector
\mathbf{q}_{gl}	global load vector
\mathbf{R}	rotation tensor
\mathbf{r}_{ij}	vector between atoms i and j
\mathbf{S}	second Piola-Kirchhoff stress tensor
\mathbf{T}	Cauchy stress tensor
\mathbf{t}	stress vector affecting a surface
\mathbf{T}_e	element-wise transformation matrix
\mathbf{U}	material right stretch tensor
\mathbf{u}	displacement vector

\mathbf{V}	spatial left stretch tensor
\mathbf{v}_i	velocity vector of atom i
\mathbf{X}	position vector in the reference configuration
\mathbf{x}	position vector in the deformed configuration
\mathbf{x}_i	position vector of atom i in the deformed configuration
$\tilde{\mathbf{u}}_e$	vector of element-wise nodal degrees of freedom
$\tilde{\mathbf{u}}_{gl}$	vector of global nodal degrees of freedom
B	continuous material body
B_0, B_t	continuous material body at time $t = 0$ and $t = t$
C	cohesive contribution to the total atomic energy
E_{kin}	internal kinetic energy of the atomic system
E_k	energy of atom k
E_{pot}	internal potential energy of the atomic system
E_{tot}	total internal energy of the atomic system
f	yield function
m_a	mass parameter within the context of reduced units
m_i	mass of particle i or atom i , respectively
N	number of atoms in the system
N_f	number of degrees of freedom in the system
r_{ij}	spacing between atoms i and j
S	surface of a continuous material body
S^t	Neumann boundary surface
S^u	Dirichlet boundary surface
t_0	initial time
T_{ref}	reference temperature
U_i	embedding energy of atom i
W	mechanical work
dS	infinitesimal surface element in the reference configuration
ds	infinitesimal surface element in the deformed configuration
$\left(\frac{\tilde{m}}{\tilde{s}^2}\right)$	unit of acceleration on the atomistic scale
$\left(\frac{\tilde{m}}{\tilde{s}}\right)$	unit of velocity on the atomistic scale
(\AA)	unit of length on the atomistic scale: Angstrom
$(\tilde{\text{kg}})$	unit of mass on the atomistic scale
$(\tilde{\text{K}})$	unit of temperature on the atomistic scale
$(\tilde{\text{N}})$	unit of force on the atomistic scale
$(\tilde{\text{s}})$	unit of time on the atomistic scale
(eV)	unit of energy on the atomistic scale: electron volt

Geometrical characterization of grain boundaries

$(XYZ)^{GB}$	grain boundary CS (global CS on the microscale)
(h, k, l)	lattice plane
$[h, k, l]$	lattice direction
$\langle h, k, l \rangle$	lattice directions, that are equivalent to $[h, k, l]$ by crystal symmetry
$\{h, k, l\}$	lattice planes, that are equivalent to (h, k, l) by crystal symmetry
η	twist angle of a grain boundary, equals the rotation angle in the IPS
ϕ	Eulerian angle of rotation about crystallites X'-axis
Ψ	tilt angle of a grain boundary
ψ	Eulerian angle of rotation about crystallites Y'-axis
$\Sigma \cdot$	\cdot is the ratio of lattice sites of the crystal to those of the CSL
Θ	rotation angle in the CSL misorientation scheme
$\varphi, \varphi_1, \varphi_2$	Eulerian angles of rotation about crystallites Z'-axis
$\hat{\mathbf{n}}_1, \hat{\mathbf{n}}_2$	grain boundary normal directions in the CSL misorientation scheme
$\hat{\mathbf{n}}_R$	rotation axis in the CSL misorientation scheme
$\hat{\mathbf{n}}_{T,1}, \hat{\mathbf{n}}_{T,2}$	tilt axes in the principal coordinate system of crystallite 1 and 2
$\mathbf{a}_1, \mathbf{a}_2, \mathbf{a}_3$	lattice vectors
\mathbf{g}^{act}	active rotation matrix
\mathbf{g}^{pas}	passive rotation matrix
$\mathbf{g}_\phi^{X'}$	matrix of rotation about X'-axis through Eulerian angle ϕ
$\mathbf{g}_\psi^{Y'}$	matrix of rotation about Y'-axis through Eulerian angle ψ
$\mathbf{g}_\varphi^{Z'}$	matrix of rotation about Z'-axis through Eulerian angle φ
\mathbf{T}	translation vector in grain boundary characterizations
$\mathbf{x}_{GB}, \mathbf{y}_{GB}, \mathbf{z}_{GB}$	vectors in the global CS that define the grain boundary CS
h, k, l	Miller indices

The Quasicontinuum method

σ_i^{BDT}	atomic-level stress according to Basinski, Duesberry, and Taylor (BDT)
λ_k	k th eigenvalue of the right stretch tensor
\mathcal{E}	strain energy density
Ω_0	volume of a unit cell
Ω_e	volume of element e
Ω_e^α	partial volume of element e that is assigned to representative atom α
Ω_i	volume assigned to a single atom i
$\Phi(\alpha, \alpha)$	self force constant tensor of atom α
Θ	grain boundary misorientation
θ	step function
Π^{QC}	energetic potential of the QC system

$\bar{\mathbf{f}}_\alpha^{ext}$	vector of averaged external forces acting on atom α
\mathbf{A}_n	Bravais lattice vectors in the reference configuration
\mathbf{a}_n	Bravais lattice vectors in the deformed configuration
\mathbf{c}^{ind}	position vector of the indenter center
\mathbf{F}	deformation gradient
\mathbf{f}_α^G	dead load vector for the ghost-force correction of atom α
$\mathbf{f}_\mathbf{a}$	nodal force vector
\mathbf{f}_k^{ext}	vector of external forces acting on atom k
$\mathbf{k}_{\mathbf{ab}}$	system matrix
\mathbf{p}_α	momentum vector of atom α
\mathbf{U}	right stretch tensor
\mathbf{u}	array of displacement vectors of all atoms in the deformed configuration
\mathbf{u}_α	displacement vector of atom α in the deformed configuration
\mathbf{v}_α	velocity vector of atom α
\mathbf{X}_0	position vector of the reference atom in the reference configuration
\mathbf{X}_α	position vector of atom α in the reference configuration
\mathbf{x}_α	position vector of atom α in the deformed configuration
A	strength of repulsive force in the potential definition of a nanoindenter
a_0	lattice parameter
A_i	Helmholtz free energy of atom i
C	number of cluster atoms in the system
C_α	number of cluster atoms assigned to representative atom α
c_i	centrosymmetry parameter of atom i
E_0	internal energy of a deformed unit cell
E_i	internal energy of the i th atom
E_{tot}	total internal energy of the system
G	Gibbs free energy of the atomistic system
G^{QC}	Gibbs free energy of the QC system
H	Hamiltonian of the atomistic system
H^{QC}	Hamiltonian of the QC system
N	number of atoms in the system
N_α	interpolation function of the node at site of representative atom α
n_α	weighting factor of the representative atom α
n_α^c	weighting divisor of atom cluster c associated to representative atom α
$N_{\mathbf{a}}, N_{\mathbf{b}}$	interpolation functions of nodes \mathbf{a} and \mathbf{b} , respectively
N_{elem}	number of elements in the system
n_e	number of atoms assigned to element e
R	number of representative atoms in the system
R^{ind}	indenter radius
r_{cl}	cluster radius
r_c	cutoff radius
w_α	weighting factor of atom cluster associated to representative atom α

Scale transition

α	constant to control the ratio of normal and tangential crack opening
λ	relative crack opening
λ_0	maximal relative crack opening of the linear elastic path of the TSL
Φ	potential of TSL
\mathbb{Z}_i	first-order coordination number of atom i
\mathbb{Z}_{ref}	reference first-order coordination number
\mathbb{Z}_{th}	threshold first-order coordination number
\hat{N}	number of atoms within a statistical volume minus the number of naturally damaged atoms at initially free boundary surfaces
C_{11}, C_{22}, C_{44}	independent elastic parameters in the crystal unit cell CS
$C_{22}^{gl}, C_{44}^{gl}, C_{66}^{gl}$	elastic parameters in the global CS of the model
D_c	cumulative damage parameter
D_i	point-wise damage parameter of atom i
G_f	localized fracture energy
h^e	effective elastic height of the GB model on microscale
k_n	initial normal stiffness
l_i, m_i, n_i	direction cosines
t	traction
T_n	normal traction
t_p	peak strength
T_t	tangential traction
u_n	normal crack opening
u_t	relative tangential slip of crack surfaces

Polycrystal modeling on the mesoscale

β	angle of misorientation
\mathbf{E}_n	algorithmic moduli in load step n
$\delta_{i,j}$	orientation angle of GB between grains i and j
σ_d	standard deviation
σ_{yld}	yield stress
τ_{yld}	yield shear stress
$\Delta\gamma_n$	consistency parameter in load step n
φ_i	orientation angle of material axes of grain i
\mathbf{D}_n	elastoplastic tangent moduli in load step n
\mathbf{R}	Reuter's matrix
\mathbf{R}_n	residual vector in load step n

\mathbf{T}, \mathbf{A}	transformation matrices
a, b	parameters of Weibull distribution function
d	grain size, equals the diameter of a circle with equivalent area
d_{50}	median value
F	cumulative distribution function
F, G, H, L, M, N	material dependent parameters of the orthotropic Hill criterion
f_{LN}	lognormal distribution function
F_W	cumulative Weibull distribution function
f_W	Weibull distribution function
h	plane thickness
I_1	first invariant of Cauchy stress tensor
p	hydrostatic stress

Chapter 1

Introduction

The presented thesis contributes to the wide field of damage mechanics and uses the powerful approach of hierarchical multiscale strategies to capture the brittle intergranular damage phenomena in polycrystalline materials. Since the physical process of damage simultaneously proceeds on multiple length scales the intergranular damage is subsequently investigated on the atomistic as well as on the continuum scale. Various numerical methods are improved for this purpose. In this way, the integration of atomistic knowledge into continuum damage models is aimed. In the following sections the motivation for this thesis as well as the use of a multiscale strategy are presented and the intention of the research in numerical methods for the simulation of brittle intergranular damage is emphasized.

1.1 Motivation

In the course of technical progress a more effective use of materials is aimed. Up to the first decades of the last century the design of new engineering structures was mainly based on experience and feasible experiments. Designs at the limit of material capacity frequently showed structural failure, when unknown damage phenomena arose due to novel methods of manufacturing. Combined with a prompt demand of new products rapid developments sometimes led to catastrophic collapses due to missing experience in new technologies and less time for experimental tests. The best known example of such a collapse by material failure is the brittle fracture failure in numerous liberty ships, which were constructed during second world war. Many times this fracture was associated with breaking the ships in two parts. Finally, from 2708 constructed liberty ships more than thousand were damaged by brittle fracture within the first five years after construction and more than 200 ships sank or failed without repairability [Kobayashi 2009]. The abrupt break in two was caused by the formation and fast propagation of brittle cracks in a continuously welded joint in the middle of the ships. The lack of fracture toughness of the welded joints caused the brittle fracture with catastrophic effects. These and other similar accidents raised the

awareness of damage and fracture phenomena in technical materials. Consequently, since the mid of the 20th century damage and fracture mechanics became an important field of research in material science, and simulation as well as experimental methods for the prediction of durability were developed.

At present, durability and life cycle analyses of civil as well as mechanical engineering structures are often based on numerical simulations of damage behavior on the macroscale using phenomenological damage and fracture models. Based on the definition of an initial damage situation these models can not capture the true mechanisms of crack initiation and various crack propagation. Moreover, it is difficult to find a physically reasonable interpretation of phenomenologically introduced damage parameters and therewith to determine necessary material input parameters by experiments. Taking into account the microstructure of materials offers new options to integrate physical phenomena, which are driving crack initiation as well as crack propagation. Moreover, micro- and mesoscale analysis are promising disciplines to cover the various fracture phenomena in engineering structures. Above all, the understanding of damage phenomena on multiple length scales results in improved numerical models. An advanced computational support in the design of high strength materials is provided and expensive material tests can be partially substituted by computational simulations.

In polycrystalline metal materials different damage phenomena can lead to the initiation of microcracks. Ductile metals usually fail by nucleation, growth, and the coalescence of microscopic voids. Beside this, ductile damage behavior of polycrystalline materials is also caused by dislocations and the formation of shear bands within grains that can lead to shear cracks. Apart from that, corrosion can cause intergranular failure due to oxygen embrittlement [Iesulauro et al. 2002]. Another grain boundary damage phenomena that can be observed for polycrystalline metals (e.g. copper), at elevated temperatures, is the intergranular creep failure under monotonic loading caused by grain boundary cavitation [van der Giessen et al. 1996]. An introduction to situations that can lead to cracking along grain boundaries is given by [Anderson 2005] including an exemplary microscopic photo of intergranular fracture in a steel tank. Being aware of the variety of damage phenomena in polycrystalline metals the presented dissertation focuses on numerical methods to reproduce the brittle intergranular fracture process in this type of materials.

Since the break in atomic bonds is the initial source of brittle fracture, atomistic analyses provide new insights in related damage phenomena. The basic question, how materials fail, can be answered in-depth by a profound understanding of the atomic debonding process in the materials microstructure. While for many decades the use of atomistic simulation methods, like lattice statics or molecular dynamics, was limited due to the high number of atomic DOF for relatively small sample sizes, the enormous progress in computational technologies in the last 20 years allows for comprehensive applications of these methods, at present. Therewith, the source of brittle damage can be investigated

taking into account basic physical phenomena induced by atomic interactions. While the investigation of atomic debonding processes provides an improved understanding of driving effects for several fracture phenomena, engineers are interested in applicable constitutive formulations for simulating damage behavior of materials on the macroscale. For this reason there is a need for strategies combining both, atomistic insights and engineering abstractions, in one model. A promising concept for the integration of physical phenomena investigated by atomistics into engineering damage models is provided by hierarchical multiscale strategies and a successive transfer of damage information from the finer to the coarser scales. Based on this concept the presented dissertation includes adaptations and improvements of numerical methods for the investigation of brittle intergranular damage on different length scales.

1.2 Intention of the presented thesis

The presented dissertation contributes to a hierarchical multiscale concept for the damage analysis in polycrystalline materials, especially metals like aluminum. In polycrystalline materials it has been observed that the grain boundary decohesion is one important mechanism that leads to microcrack initiation. Based on this observation the thesis focuses on the adaptation and development of numerical methods for the simulation of brittle intergranular damage.

The main emphasis of the presented research is to substitute pure phenomenological damage models by models that are derived from the underlying physical phenomena of damage. Following the intention of finally integrating knowledge on basic physical phenomena of intergranular fracture into a continuum damage model the hierarchical multiscale concept starts on the microscale ($10^{-10}\text{m} - 10^{-6}\text{m}$), where grain boundaries are explicitly modeled by the underlying atomic lattice. On the microscale the contributed research aims for the computation of cohesive parameters from simulations of grain boundary fracture by atomic debonding. A traction separation law shall be derived, considering the dependency between mechanical properties and geometrical characteristics of grain boundaries. The traction separation law describes the constitutive behavior of cohesive interface elements to simulate the interface decohesion process within a finite element continuum model on the mesoscale ($10^{-6}\text{m} - 10^{-3}\text{m}$). The heterogeneous polycrystal model on the mesoscale consists of grains (crystallites) and cohesive grain boundaries. Since the presented dissertation focuses on the investigation of brittle intergranular damage, the fracture process is restricted to interface elements only and damage within the grains is not modeled.

With the integration of simulation results from the atomistical informed microscale into the continuum polycrystal model the main intention of the presented thesis is accomplished. Additionally, as discussed in the outlook, the formulation of a continuum damage model on the engineering scale or macroscale ($10^{-3} - 10^0\text{m}$), respectively, is aimed. The effective parameters of an anisotropic damage tensor could be derived by suitable homo-

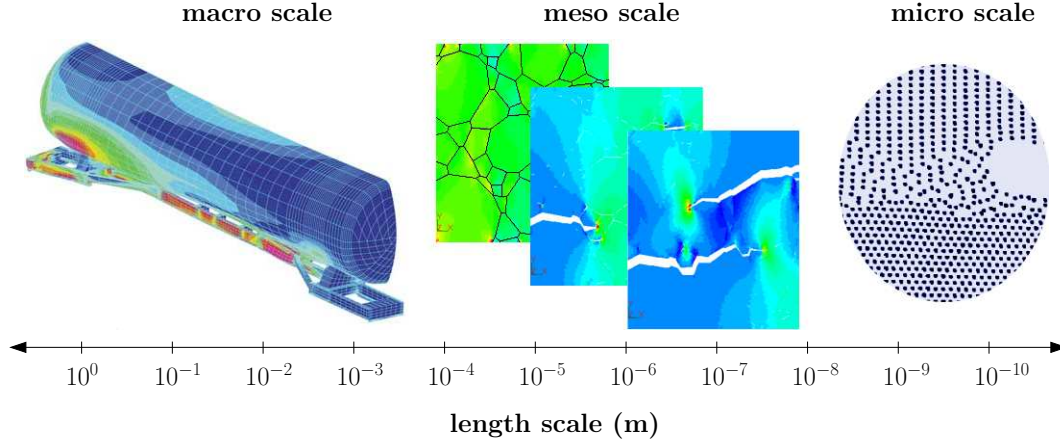


Figure 1.1: The proposed hierarchical multiscale concept for the damage analysis in polycrystalline materials consists of numerical models on three different length scales.

genization methods from the polycrystal damage model on mesoscale. The definition of length scales within the proposed hierarchical multiscale concept is illustrated in Figure 1.1.

Since the atomistic structure of crystalline materials has a strong 3D character, it is consequently aimed to perform 3D simulations on the microscale. This rapidly increases the number of DOF in pure atomistic models. Exemplary, an aluminum cube of $(1 \mu\text{m})^3$ has approximately $6 \cdot 10^{10}$ atoms what is in the limit of the largest atomistic systems which are computable on the best super computers at present. Accordingly, the aim on the microscale is to reduce the atomic DOF which are explicitly treated in the simulations. Mixed atomistic-continuum methods provide a more efficient use of DOF due to a full atomistic resolution in zones of damage localization and a coarsen resolution in regions of uniform deformation. Such a method, namely the Quasicontinuum (QC) method, is applied in the presented thesis.

A further speed-up in computational time is intended by the implementation of a parallelized QC formulation. While pure atomistic methods are well suited for parallelization based on domain decomposition, new strategies have to be developed for the parallelized computation especially of forces and energies of the QC model, where the DOF are not uniformly distributed in the domain.

Summarizing, the intention on the microscale is to efficiently simulate the intergranular damage behavior based on the physical phenomena of atomic debonding. To represent the physics, interatomic potential functions are applied, which describe the many-body interactions between the atoms. For efficiency, the model is coarsen in undamaged regions and the numerical algorithms are implemented for parallelized computation.

On the mesoscale the interface decohesion as one important mechanism of microcrack initiation in polycrystals shall be explicitly reproduced in finite element simulations. Therefore, a polycrystal model is developed in 2D as well as in 3D. To simulate the brittle intergranular fracture the material structure is described by a cell diagram, wherein each

cell is assigned to a single grain. In the finite element model orthotropic linear elastic or elastoplastic material laws are applied to the grains considering the dependency of material properties on grain orientation. A cohesive zone model (CZM) with the traction separation law (TSL) derived from microscale computations is assigned to the grain boundaries for simulating intergranular crack propagation.

At the beginning, the geometry of the polycrystal model was generated using a classical Voronoi tessellation. Since the grain size distribution in classical Voronoi diagrams is limited to a short range, a modified 2D Voronoi diagram was developed that better fits the measured grain size distribution in real polycrystalline materials. The modification allows for the generation of cell structures with size distributions following a lognormal or Weibull distribution function. Simulations of tensile tests using 2D samples with modified Voronoi geometry have shown a significant higher mean value of the effective tensile strength compared to samples with a classical Voronoi geometry. Since the modification algorithm is not transferable to 3D, other approaches are discussed to flexibly generate 3D polycrystal geometries with realistic grain size distribution.

Finally, the mesoscale models are able to investigate the intergranular crack initiation and propagation in statically loaded samples of polycrystals without the necessity of initial damage definition. Therewith, these models provide a basis for further extensions, for example to ductile behavior by crystal plasticity, and provide the conceptionally motivated derivation of the engineering damage model on macroscale.

1.3 Innovations of the presented thesis

The presented thesis provides a methodology for atomistic-based cohesive zone representations which is applicable for the simulation of brittle intergranular damage phenomena. The transition from the atomistical informed microscale to the continuum mesoscale is realized by a hierarchical multiscale concept. On the microscale a generalized QC model is applied to efficiently calculate cohesive parameters of various grain boundaries.

Existing 2D QC models have shown less robustness in case of interface models with arbitrary oriented crystallites and existing 3D QC models are developed only for special investigations on crystallites with convenient orientation [Knap et al. 2001] [Eidel et al. 2009]. In the framework of the presented dissertation a novel QC implementation was realized to robustly and efficiently perform quasistatic 3D simulations on grain boundary configurations with arbitrarily oriented crystallites. This generalized 3D nonlocal QC implementation applies improved meshing algorithms, consistent energy and force formulations, and a robust optimization method to ensure numerical stability. Moreover, high efficiency is gained due to parallelization of the generalized nonlocal QC implementation.

While former atomistic studies of grain boundary characteristics, for example by [Coffman et al. 2008a] and [Sansoz et al. 2005], are restricted to periodic 2D or quasiplanar samples, the modeling strategy of the presented thesis enables 3D investigations on all

possible grain boundary configurations. New 3D QC models are applied to find low energy grain boundary situations by a proceeding, which minimizes the number of necessarily investigated initial grain boundary configurations. The calculated interface energies are closer to experimental results than comparable values from other numerical studies of [Chandra et al. 1999] and [Sansoz et al. 2005].

In the presented dissertation atomistic-based cohesive parameters of grain boundaries are derived from both, tensile and shear simulations. Therewith traction separation laws of coupled CZMs can be parameterized and applied in continuum models to simulate the interface decohesion caused by tensile stresses as well as by shear stresses. Improvements in the atomistic-based cohesive zone representations are realized by the generation of atomic level defects (point vacancies) along grain boundaries.

A novel algorithm is applied on the mesoscale to generate polycrystal geometries with realistic grain size distribution. Simulation results from improved polycrystal models are compared to results from state of the art models and differences are documented. The polycrystal models are applied to analyze the brittle intergranular fracture behavior of aluminum samples on the mesoscale.

On-the-fly simulations of atomistic-based cohesive zone representations are performed to parameterize the traction separation laws assigned to grain boundaries in the mesoscale model. This finalizes the intended methodology of substituting phenomenological interface laws on the mesoscale by atomistic-based cohesive zone representations.

1.4 Outline

The organization of the presented dissertation follows the hierarchical concept from the atomistics to the continuum scales. An overview on several numerical approximation schemes of atomistics and continuum mechanics is preceded in Chapter 2 including basics related to the adapted methodologies.

Various options are presented in Chapter 3 to characterize the geometry of grain boundaries, especially the misorientation of adjacent crystallites. Furthermore, transformations between the applied characterization schemes are formulated.

Chapter 4 discusses theoretical formulations of the QC method, that is a mixed atomistic-continuum method applied on the microscale. Additionally, this chapter describes in detail relevant issues concerning the implementation of a 3D nonlocal QC method, that was realized in the framework of the documented dissertation.

The application of the QC method for simulations of brittle intergranular damage on the microscale is documented in Chapter 5. Moreover, this chapter addresses the transfer of insights about the brittle grain boundary damage process from the atomistic microscale into a coupled cohesive zone model, which describes grain boundary decohesion in a polycrystal model by continuum mechanics. Also the influence of atomic level defects on cohesive parameters of grain boundaries is studied.

The continuum polycrystal model on the mesoscale and the applied numerical methods for brittle intergranular damage analysis are treated in Chapter 6. An advanced algorithm for the generation of realistic polycrystal geometries is developed and the associated improvement in damage analysis compared to the use of standard polycrystal geometries is discussed in this chapter. The applied constitutive models of grains and grain boundaries are addressed and computational studies on effective parameters of mesoscale samples are documented. Finally, one example demonstrates on-the-fly simulations of cohesive grain boundary parameters from microscale simulations to substitute the previously used phenomenological interface separation laws by atomistic-based cohesive zone representations.

Chapter 7 concludes the presented dissertation by summarizing the new insights concerning brittle intergranular damage in polycrystals from simulations on the micro- and mesoscale, and the scale transition. Thereby, the capabilities as well as the limits of the adapted and refined numerical methods are evaluated.

After all, Chapter 8 gives an outlook to reasonable extensions of the implemented micro- and mesoscale models, especially in directions of imperfect materials, and concluding comments of related research are considered. Finally, the completion of the hierarchical multiscale realization by a subsequent scale transition to the macroscale is discussed.

Chapter 2

Numerical methods in material modeling

This chapter gives a compact overview on numerical methods of continuum mechanics as well as particle mechanics and dynamics on the atomistic scale. Furthermore, several types of mixed atomistic-continuum methods are introduced. A basic knowledge on these methods is necessary for the understanding of the following chapters. The geometrical definitions generally refer to a Cartesian coordinate system.

2.1 Continuum mechanics

2.1.1 Fundamentals

Comprehensive overviews on continuum mechanics and constitutive modeling can be read exemplary in [Jog 2007] and [Ottosen et al. 2005]. The continuum is assumed to be a continuous set of material points. At each point in time all material points are uniquely defined (Figure 2.1), either by their position vector in the reference configuration

$$\mathbf{X} = X_i \mathbf{e}_i, \quad (2.1)$$

or by their position vector in the deformed configuration

$$\mathbf{x} = x_i \mathbf{e}_i. \quad (2.2)$$

For each material point the three components of the displacement vector are introduced as kinematic variables

$$\mathbf{u} = \mathbf{x} - \mathbf{X}. \quad (2.3)$$

In the Lagrangian description the motion of bodies is described as a function of the reference coordinates of the material points

$$\mathbf{x} = \Phi(\mathbf{X}, t) = \Phi(\mathbf{X}). \quad (2.4)$$

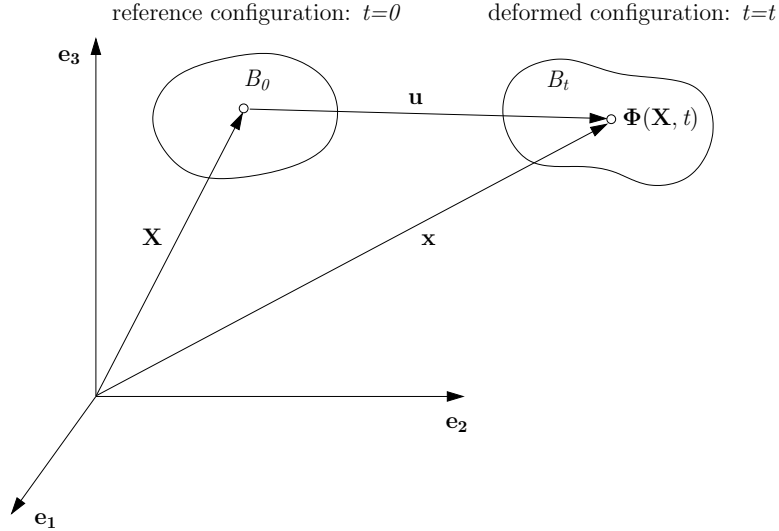


Figure 2.1: Reference or initial configuration respectively, and deformed configuration.

In comparison the Eulerian description defines the motion of bodies based on the current coordinates \mathbf{x} of spatial points in the deformed configuration. The Eulerian description is mainly applied in fluid mechanics to analyze the properties of the material in a spatial point over the course of time. In the following, the Lagrangian description as usually used in solid mechanics is applied.

The deformation of a differential line element

$$d\mathbf{x} = \mathbf{F} d\mathbf{X} \quad (2.5)$$

is described by the deformation gradient

$$\mathbf{F} = \frac{\partial \mathbf{x}}{\partial \mathbf{X}} = \text{grad } \mathbf{x}. \quad (2.6)$$

The deformation gradient \mathbf{F} is an asymmetric second order tensor and can be decomposed by a right polar decomposition

$$\mathbf{F} = \mathbf{R} \mathbf{U} \quad (2.7)$$

into the orthogonal rotation tensor \mathbf{R} ($\det \mathbf{R} = 1$) and the symmetric material right stretch tensor \mathbf{U} . Alternatively, a left polar decomposition

$$\mathbf{F} = \mathbf{V} \mathbf{R} \quad (2.8)$$

decomposes \mathbf{F} into the symmetric spatial left stretch tensor \mathbf{V} and the orthogonal rotation tensor \mathbf{R} (Figure 2.2).

The deformation gradient \mathbf{F} describes the rigid body motions (translation and rotation) as well as the deformation of the domain. The deformation can be expressed by the Green-Lagrangian strain tensor \mathbf{G} as

$$\mathbf{G} = \frac{1}{2} (\mathbf{F}^T \mathbf{F} - \mathbf{I}) = \frac{1}{2} (\mathbf{C} - \mathbf{I}), \quad (2.9)$$

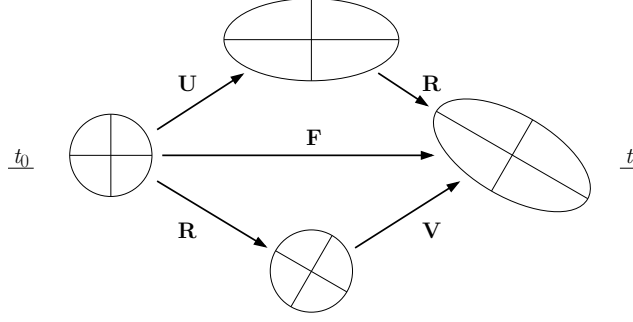


Figure 2.2: Right and left polar decomposition of deformation gradient \mathbf{F} .

with \mathbf{C} is the right Cauchy-Green tensor

$$\mathbf{C} = \mathbf{F}^T \mathbf{F}. \quad (2.10)$$

The absolute elongation of a differential line element can be calculated with

$$ds^2 = d\mathbf{x}^T d\mathbf{x} = d\mathbf{X}^T \mathbf{F}^T \mathbf{F} d\mathbf{X} \quad (2.11)$$

and

$$dS^2 = d\mathbf{X}^T d\mathbf{X} \quad (2.12)$$

as follows

$$\begin{aligned} ds^2 - dS^2 &= d\mathbf{X}^T \mathbf{F}^T \mathbf{F} d\mathbf{X} - d\mathbf{X}^T d\mathbf{X} \\ &= d\mathbf{X}^T (\mathbf{F}^T \mathbf{F} - \mathbf{I}) d\mathbf{X} \\ &= d\mathbf{X}^T 2\mathbf{G} d\mathbf{X}. \end{aligned} \quad (2.13)$$

As next the first Piola-Kirchhoff stress tensor shall be introduced based on the Cauchy stress formula. Therein, the resulting force \mathbf{f}_t on a surface s is calculated in the deformed configuration by an integral of the stress \mathbf{t} (Figure 2.3)

$$\begin{aligned} \mathbf{f}_t &= \int_s \mathbf{t}(\mathbf{x}, t, \mathbf{n}) ds \\ &= \int_s \mathbf{T} \mathbf{n} ds \\ &= \int_s \mathbf{T} ds \end{aligned} \quad (2.14)$$

with

$$\mathbf{t}(\mathbf{x}, t, \mathbf{n}) = \mathbf{T} \mathbf{n}, \quad (2.15)$$

where \mathbf{T} is the symmetric Cauchy stress tensor and \mathbf{n} is the normal to the surface s_t . Introducing the transformation rule for the infinitesimal surface element

$$ds = \det(\mathbf{F}) (\mathbf{F}^T)^{-1} dS \quad (2.16)$$

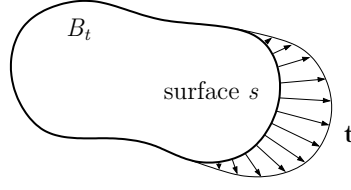


Figure 2.3: Stress \mathbf{t} at the surface s .

into Equation (2.14) leads to

$$\mathbf{f}_t = \int_S \det(\mathbf{F}) \mathbf{T} (\mathbf{F}^T)^{-1} dS. \quad (2.17)$$

The first Piola-Kirchhoff stress tensor is defined as

$$\mathbf{P} = \det(\mathbf{F}) \mathbf{T} (\mathbf{F}^T)^{-1} \quad (2.18)$$

also named as technical stress. Because of the asymmetric character of \mathbf{P} the second Piola-Kirchhoff stress tensor is introduced as

$$\mathbf{S} = \mathbf{F}^{-1} \mathbf{P}. \quad (2.19)$$

The relation between the Green-Lagrangian strain tensor \mathbf{G} and its energy conjugate stress tensor \mathbf{S} is defined by Hooke's law for linear elastic materials

$$\mathbf{S} = \mathbb{C} \mathbf{G}, \quad (2.20)$$

where \mathbb{C} is the (second) elasticity tensor, which is of fourth order in the general formulation. Assuming small strain the linearized strain tensor $\boldsymbol{\epsilon}$ results from the linearization of the Green-Lagrangian strain tensor

$$\begin{aligned} \boldsymbol{\epsilon} &= \text{lin } \mathbf{G} \\ \epsilon_{ij} &= \frac{1}{2} \left(\frac{\partial u_i}{\partial X_j} + \frac{\partial u_j}{\partial X_i} \right) \end{aligned} \quad (2.21)$$

and the linearized stress tensor $\boldsymbol{\sigma}$ is obtained from the linearized stress-strain relation

$$\boldsymbol{\sigma} = \mathbf{E} \boldsymbol{\epsilon}, \quad (2.22)$$

with \mathbf{E} is the elastic constitutive matrix. Equation (2.22) defines the constitutive law for elastic materials and can be written in terms of stress and strain components in the form

$$\begin{bmatrix} \sigma_{xx} \\ \sigma_{yy} \\ \sigma_{zz} \\ \tau_{xy} \\ \tau_{xz} \\ \tau_{yz} \end{bmatrix} = \mathbf{E} \begin{bmatrix} \epsilon_{xx} \\ \epsilon_{yy} \\ \epsilon_{zz} \\ \gamma_{xy} \\ \gamma_{xz} \\ \gamma_{yz} \end{bmatrix}. \quad (2.23)$$

In the simplest case of isotropic material the constitutive matrix \mathbf{E} reads with the Young's modulus E and the Poisson's ratio ν

$$\mathbf{E}^{iso} = \frac{E}{(1+\nu)(1-2\nu)} \begin{bmatrix} 1-\nu & \nu & \nu & 0 & 0 & 0 \\ \nu & 1-\nu & \nu & 0 & 0 & 0 \\ \nu & \nu & 1-\nu & 0 & 0 & 0 \\ 0 & 0 & 0 & \frac{1-2\nu}{2} & 0 & 0 \\ 0 & 0 & 0 & 0 & \frac{1-2\nu}{2} & 0 \\ 0 & 0 & 0 & 0 & 0 & \frac{1-2\nu}{2} \end{bmatrix}. \quad (2.24)$$

The corresponding compliance matrix

$$\mathbf{N} = \mathbf{E}^{-1} \quad (2.25)$$

is given by

$$\mathbf{N}^{iso} = \frac{1}{E} \begin{bmatrix} 1 & -\nu & -\nu & 0 & 0 & 0 \\ -\nu & 1 & -\nu & 0 & 0 & 0 \\ -\nu & -\nu & 1 & 0 & 0 & 0 \\ 0 & 0 & 0 & 2(1+\nu) & 0 & 0 \\ 0 & 0 & 0 & 0 & 2(1+\nu) & 0 \\ 0 & 0 & 0 & 0 & 0 & 2(1+\nu) \end{bmatrix}. \quad (2.26)$$

and links the linearized strain to the stress

$$\boldsymbol{\epsilon} = \mathbf{N} \boldsymbol{\sigma}. \quad (2.27)$$

In case of orthotropic material behavior, as it is assumed in polycrystal models on the mesoscale (Chapter 6), the compliance matrix \mathbf{N} reads

$$\mathbf{N}^{ort} = \begin{bmatrix} \frac{1}{E_1} & -\nu_{21} & -\nu_{31} & 0 & 0 & 0 \\ \frac{1}{E_1} & \frac{1}{E_2} & \frac{1}{E_3} & 0 & 0 & 0 \\ -\nu_{12} & \frac{1}{E_2} & -\nu_{32} & 0 & 0 & 0 \\ \frac{1}{E_1} & -\nu_{23} & \frac{1}{E_3} & 0 & 0 & 0 \\ -\nu_{13} & \frac{1}{E_2} & \frac{1}{E_3} & 0 & 0 & 0 \\ 0 & 0 & 0 & \frac{1}{G_{12}} & 0 & 0 \\ 0 & 0 & 0 & 0 & \frac{1}{G_{13}} & 0 \\ 0 & 0 & 0 & 0 & 0 & \frac{1}{G_{23}} \end{bmatrix}, \quad (2.28)$$

where G is the shear modulus and

$$\nu_{21} = \frac{E_2}{E_1} \nu_{12} \quad (2.29)$$

$$\nu_{31} = \frac{E_3}{E_1} \nu_{13} \quad (2.30)$$

$$\nu_{32} = \frac{E_3}{E_2} \nu_{23} \quad (2.31)$$

$$G_{12} = \frac{E_1}{2(1 + \nu_{12})} \quad (2.32)$$

$$G_{13} = \frac{E_3}{2(1 + \nu_{13})} \quad (2.33)$$

$$G_{23} = \frac{E_2}{2(1 + \nu_{23})}. \quad (2.34)$$

The associated material parameters are related to the normal directions of the three orthogonal planes, which are defined by the symmetries of orthotropic material. Correspondingly, the orthotropic compliance matrix links the strain and stress expressed in the material coordinate system that is spanned by the normal directions of the orthogonal planes

$$\begin{bmatrix} \epsilon_{11} \\ \epsilon_{22} \\ \epsilon_{33} \\ \gamma_{12} \\ \gamma_{13} \\ \gamma_{23} \end{bmatrix} = \mathbf{N}^{ort} \begin{bmatrix} \sigma_{11} \\ \sigma_{22} \\ \sigma_{33} \\ \tau_{12} \\ \tau_{13} \\ \tau_{23} \end{bmatrix}. \quad (2.35)$$

The frequently useful transformation of strain and stress components from the material coordinate system into a global coordinate system and vice versa is explained in Chapter 6.

The extension of the elasticity theory by a general plasticity theory involves the introduction of plastic strains $\boldsymbol{\epsilon}^p$ additionally to elastic strains $\boldsymbol{\epsilon}^e$. Therewith, the total strains can be decomposed

$$\boldsymbol{\epsilon} = \boldsymbol{\epsilon}^e + \boldsymbol{\epsilon}^p. \quad (2.36)$$

Based on Equation (2.22) the stresses are linked to the elastic strains now by

$$\boldsymbol{\sigma} = \mathbf{E} (\boldsymbol{\epsilon} - \boldsymbol{\epsilon}^p). \quad (2.37)$$

The development of plastic strains starts when an assumed yield function

$$f(\boldsymbol{\sigma}, \mathbf{K}_\alpha) = 0 \quad (2.38)$$

is fulfilled. The term $f(\boldsymbol{\sigma}, \mathbf{K}_\alpha)$ defines the yield surface and \mathbf{K}_α denotes the hardening parameters. By convention, the sign of the yield function is defined so that the elastic

behavior is described by

$$f(\boldsymbol{\sigma}, \mathbf{K}_\alpha) < 0. \quad (2.39)$$

In case of no hardening ($\mathbf{K}_\alpha = \mathbf{0}$) the former equations reduce to a flow rule that depends on the initial yield surface

$$f(\boldsymbol{\sigma}) \leq 0. \quad (2.40)$$

In Chapter 6 the von Mises yield criterion and the Hill's orthotropic yield criterion are introduced.

2.1.2 Finite element method

The structural behavior of a mechanical system can be described by the following set of fundamental equations for a linear elastic continuum $B \in R^3$ with boundary surface S :

- The equilibrium equation, that connects internal and external forces by the differential operator \mathbf{D}_e in B

$$\mathbf{D}_e \boldsymbol{\sigma} + \mathbf{p} = \mathbf{0}. \quad (2.41)$$

- The kinematic equation, that connects internal and external displacements by the differential operator \mathbf{D}_k in B

$$\boldsymbol{\epsilon} = \mathbf{D}_k \mathbf{u}. \quad (2.42)$$

- The constitutive law, that connects internal forces and internal displacements by the constitutive matrix \mathbf{E} in B

$$\boldsymbol{\sigma} = \mathbf{E} \boldsymbol{\epsilon}. \quad (2.43)$$

- The essential or kinematic boundary conditions that define prescribed displacements \mathbf{u}_S on the Dirichlet boundary surface S^u

$$\mathbf{u} = \mathbf{u}_S. \quad (2.44)$$

- The natural or static boundary conditions that define prescribed traction \mathbf{t}_S on the Neumann boundary surface S^t

$$\mathbf{t} = \mathbf{t}_S. \quad (2.45)$$

Therein, the boundary surface has to satisfy the conditions

$$S = S^u \cup S^t \quad \text{and} \quad S^u \cap S^t = \emptyset. \quad (2.46)$$

The finite element method is a numerical approximation procedure to solve the above system of differential equations and boundary conditions by an element-wise discretization of the model domain and an associated interpolation of the independent variables. Comprehensive publications on finite element procedures and applications to engineering problems, not only in structural mechanics, are written exemplarily by Bathe [Bathe 1996] and Hughes [Hughes 2000].

The energy law of mechanics

$$W = \int_B \mathbf{u}^T \mathbf{p} \, dB + \int_{S^t} \mathbf{u}^T \mathbf{t}_S \, dS^t - \int_B \boldsymbol{\epsilon}^T \boldsymbol{\sigma} \, dB = 0 \quad (2.47)$$

describes the equilibrium of external, boundary surface, and internal energy parts. Varying the displacements

$$\mathbf{u} = \bar{\mathbf{u}} + \delta \mathbf{u} \quad (2.48)$$

$$\boldsymbol{\epsilon} = \mathbf{D}_k (\bar{\mathbf{u}} + \delta \mathbf{u}) = \bar{\boldsymbol{\epsilon}} + \delta \boldsymbol{\epsilon} \quad (2.49)$$

leads to the weak form of the equilibrium averaged over B and S_t

$$\delta W = \int_B \delta \mathbf{u}^T \mathbf{p} \, dB + \int_{S^t} \delta \mathbf{u}^T \mathbf{t}_S \, dS^t - \int_B \delta \boldsymbol{\epsilon}^T \boldsymbol{\sigma} \, dB = 0. \quad (2.50)$$

In this weak form, also known as the principle of virtual displacements, the external displacements are the independent variables that have to be interpolated. Therefore, a matrix of shape functions \mathbf{N}_e is introduced locally to interpolate the displacements \mathbf{u}_e in an element e from the nodal degrees of freedom $\tilde{\mathbf{u}}_e$

$$\mathbf{u}_e = \mathbf{N}_e \tilde{\mathbf{u}}_e. \quad (2.51)$$

Every shape function in \mathbf{N}_e stands for the element deformation state caused by a unit nodal displacement. Shape functions have the value 1 at the point where the associated nodal degree of freedom is defined and at all other nodes the function value is zero. By introducing Equation (2.51) into Equation (2.42) the strain within an element is obtained as

$$\boldsymbol{\epsilon}_e = \mathbf{D}_k \mathbf{N}_e \tilde{\mathbf{u}}_e = \mathbf{B}_e \tilde{\mathbf{u}}_e, \quad (2.52)$$

where the strain-displacement matrix \mathbf{B}_e constitutes the shape functions of strain. Applying the variation of displacements to Equations (2.51) and (2.52) yields

$$\delta \mathbf{u}_e = \mathbf{N}_e \delta \tilde{\mathbf{u}}_e, \quad (2.53)$$

$$\delta \boldsymbol{\epsilon}_e = \mathbf{B}_e \delta \tilde{\mathbf{u}}_e. \quad (2.54)$$

Combined with the constitutive law (Equation (2.43)) the discrete formulation of the principle of virtual displacements (Equation (2.50)) reads for a single element

$$- \int_{B_e} \delta \tilde{\mathbf{u}}_e^T \mathbf{B}_e^T \mathbf{E} \mathbf{B}_e \tilde{\mathbf{u}}_e \, dB_e + \int_{B_e} \delta \tilde{\mathbf{u}}_e^T \mathbf{N}_e^T \mathbf{p} \, dB_e + \int_{S_e^t} \delta \tilde{\mathbf{u}}_e^T \mathbf{N}_e^T \mathbf{t}_S \, dS_e^t = 0. \quad (2.55)$$

The nodal displacements that are independent on element coordinates are not affected by the integrals

$$\delta \tilde{\mathbf{u}}_e^T \left(- \int_{B_e} \mathbf{B}_e^T \mathbf{E} \mathbf{B}_e dB_e \cdot \tilde{\mathbf{u}}_e + \int_{B_e} \mathbf{N}_e^T \mathbf{p} dB_e + \int_{S_e^t} \mathbf{N}_e^T \mathbf{t}_S dS_e^t \right) = 0. \quad (2.56)$$

The remaining integral of the internal energy part results in the local element stiffness matrix \mathbf{k}_e

$$\mathbf{k}_e = \int_{B_e} \mathbf{B}_e^T \mathbf{E} \mathbf{B}_e dB_e \quad (2.57)$$

and the remaining integrals of the external energy parts result in the local element load vector \mathbf{q}_e

$$\mathbf{q}_e = \int_{B_e} \mathbf{N}_e^T \mathbf{p} dB_e + \int_{S_e^t} \mathbf{N}_e^T \mathbf{t}_S dS_e^t. \quad (2.58)$$

Finally, Equation (2.55) reads

$$\delta \tilde{\mathbf{u}}_e^T (-\mathbf{k}_e \tilde{\mathbf{u}}_e + \mathbf{q}_e) = 0. \quad (2.59)$$

This discrete equilibrium formulation has to be valid for every variation $\delta \tilde{\mathbf{u}}_e^T \neq \mathbf{0}$. The formulation simplifies to the element-stiffness relation

$$\mathbf{k}_e \tilde{\mathbf{u}}_e = \mathbf{q}_e. \quad (2.60)$$

To connect the local element-wise stiffness relation to a global stiffness relation for the total structure, the locally defined degrees of freedom $\tilde{\mathbf{u}}_e$ have to be transformed element-wise to a common global coordinate system

$$\tilde{\mathbf{u}}_e = \mathbf{T}_e \tilde{\mathbf{u}}_{gl}, \quad (2.61)$$

with \mathbf{T}_e is the transformation matrix of element e and $\tilde{\mathbf{u}}_{gl}$ is the vector of the global degrees of freedom. Insertion of this transformation in Equation (2.59) and summarizing over all elements leads to

$$\delta \tilde{\mathbf{u}}_{gl}^T \sum_e [\mathbf{T}_e^T (-\mathbf{k}_e \mathbf{T}_e \tilde{\mathbf{u}}_{gl} + \mathbf{q}_e)] = 0. \quad (2.62)$$

With

$$\mathbf{k}_{gl} = \sum_e \mathbf{T}_e^T \mathbf{k}_e \mathbf{T}_e \quad (2.63)$$

and

$$\mathbf{q}_{gl} = \sum_e \mathbf{T}_e \mathbf{q}_e \quad (2.64)$$

the global stiffness relation reads in the simplified form

$$\mathbf{k}_{gl} \tilde{\mathbf{u}}_{gl} = \mathbf{q}_{gl}. \quad (2.65)$$

Equation (2.65) can be solved for the unknown global displacement vector $\tilde{\mathbf{u}}_{gl}$.

2.2 Atomistic methods

The structure and the properties of materials depend strongly on the interatomic binding forces. Thus, atomistic simulations provide a useful tool in the computational study of material properties as well as in the numerical investigation of physical phenomena which are leading to material failure. Since all atomic DOF are explicitly treated in atomistic simulations the model size in 3D is actually limited to less than $(1\ \mu\text{m})^3$. But with the ongoing increase in computational power researchers are more and more able to apply atomistic methods for the investigation of complex failure mechanism on the atomistic scale. Beside Monte Carlo methods, which are often applied in statistical mechanics to compute macroscopic properties from atomistic samples with stochastic character [Binder et al. 1992] [Raabe 1998] [Frenkel et al. 2002], the methods of lattice statics and molecular dynamics are established on the atomistic scale to calculate the mechanical response of atomistic models. These methods directly incorporate the interatomic binding forces, which are defined in terms of potential functions.

2.2.1 Potential functions

Depending on the mode of action the interatomic bonds are distinguished into four types: van der Waals, ionic, covalent and metallic bond. As exemplary pointed out by [Raabe 1998] the van der Waals forces between atoms or molecules are very weak and are often negligible compared to the other bond types. The ionic bond is characterized by electron transfer from one ion to another. On the other hand, the binding forces in case of covalent and metallic bond are based on electron delocalization into itinerant states forming large molecular orbitals.

Binding forces between atoms can be derived from quantum mechanics theory. Therefore, the Schrödinger equation has to be solved for a many-body problem taking into account the interactions between all nuclei and electrons in the system as explained in detail in [Raabe 1998]. According to [Sholl et al. 2009] the exact solution of the Schrödinger equation results for a nanocluster with 100 Pd atoms in a problem with more than 23,000 dimensions. A significant reduction of problem dimensions can be achieved by the introduction of the first Hohenberg-Kohn theorem, which is that the ground-state energy from the Schrödinger equation is a unique functional of the electron density. By approximating the ground-state energy as a functional of the electron density the above mentioned nanocluster problem can be reduced to only three dimensions [Sholl et al. 2009]. In combination with the Kohn-Sham equations the Hohenberg-Kohn theorems constitute the basis of the density functional theory (DFT). The aim of the DFT is to find numerical solutions of the Schrödinger equation. With these numerical solutions the energies calculated with the DFT are not the exact ground-state energies of the Schrödinger equation. But for many physical problems the DFT provides a powerful

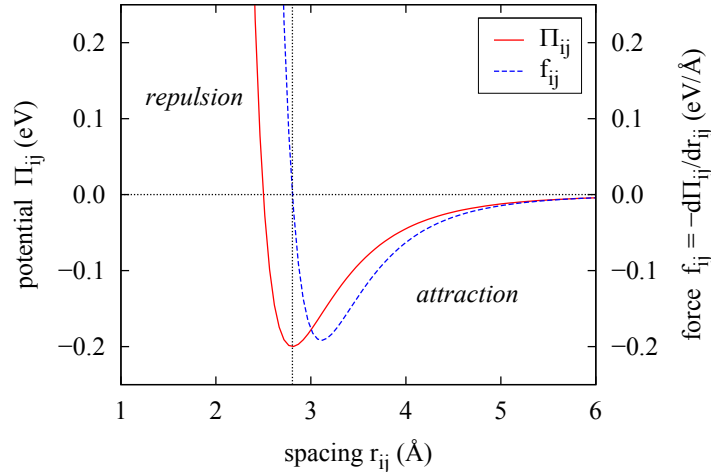


Figure 2.4: Interatomic potential function and interatomic force function with repulsion at short spacing and attraction at large spacing.

tool for solutions with acceptable accuracy. An introduction to the DFT is given in [Sholl et al. 2009].

Because a full quantum mechanical treatment of the binding forces involves huge numerical effort, quantum mechanical models are limited to a few hundreds of atoms. For this reason it is necessary to apply numerically simpler potential functions to atomistic simulations with millions of atoms. Empirical potential functions were developed which describe the atomic interactions phenomenologically. These kind of interatomic potentials allow for meaningful simulations up to 10^{10} atoms on present high performance computers. Additionally, semi-empirical potential functions (e.g. the tight-binding potentials) are formulated, that partially consist of quantum mechanical approaches as well as phenomenological descriptions [Sutton et al. 1996] [Voter 1996].

Usually, empirical potential functions are of exponential or higher order polynomial form and are fitted to simulate material properties from experiments or to reproduce material parameters, for example the lattice parameter or the cohesive energy. The functional values of these potentials decrease fast with an increasing distance between atoms. Consequently, the interactions of an atom with its nearest neighbors are of main importance and interactions with atoms in larger distance are negligible. A cutoff radius r_c is introduced to reduce the considered interactions of an atom only to the nearest neighbors, which are positioned within the cutoff distance.

Instead of many-body potentials most atomistic simulations make use of empirical pair potentials to describe the forces and energies of atomic interactions. In the concept of pair potentials the energy and force of an atom are calculated by the sum of pairwise interactions between the atom and its neighbors. According to [Buehler 2008] pair potentials must capture the repulsion at short distances which is caused by the increasing overlap of electrons in the same orbitals. At large distances the potentials must capture the effect that atoms attract each other to form a bond. Figure 2.4 shows a potential

function and the corresponding atomic force function which is derived from the gradient of the potential. The repulsive forces at short distances are characterized by positive sign while the attractive forces at large distances have negative sign. The action of these interatomic forces rules the chemical characteristics of materials as well as the structural response of materials on the microscale.

An overview on different types of potential functions, which are applicable in atomistic simulations is given in [Raabe 1998]. According to this reference pair potentials can be distinguished in two general types, the isotropic weak pseudo potentials and the classical pair potentials. Isotropic weak pseudo potentials describe energy changes of the system associated with structural changes and consists of an additional cohesive term beside the pairwise interaction term. Based on an isotropic weak pseudopotential the calculation of the total energy of a system with N atoms follows the principal formula

$$E_{tot} = \frac{1}{2} \sum_{i=1}^N \sum_{\substack{j=1 \\ j \neq i}}^N \Pi_{ij}(r_{ij}) + C(\Omega) . \quad (2.66)$$

Π_{ij} is the pair potential between two atoms i and j with a spacing $r_{ij} = \|\mathbf{r}_{ij}\|$. C is the cohesive contribution to the total energy depending on the average density of the material Ω . Classical pair potentials calculate the total energy of the system without further cohesive terms and can be written

$$E_{tot} = \frac{1}{2} \sum_{i=1}^N \sum_{\substack{j=1 \\ j \neq i}}^N \Pi_{ij}(r_{ij}) . \quad (2.67)$$

An established and simple classical pair potential is the Lennard-Jones potential that consists of a repulsive and an attractive component. The attractive term reproduces a van der Waals bond especially at large distances and the repulsive term mimics the Coloumb interaction of nuclei and the electron influence at short distances. The Lennard-Jones potential has the general form

$$\Pi_{ij}^{LJ} = 4\epsilon^{LJ} \left[\left(\frac{\sigma^{LJ}}{r_{ij}} \right)^{12} - \left(\frac{\sigma^{LJ}}{r_{ij}} \right)^6 \right] , \quad (2.68)$$

where σ^{LJ} is a material dependent length parameter and ϵ^{LJ} is a material dependent energy parameter.

A special class of empirical or semi-empirical pair potentials is defined by pair-functional methods. These methods determine the cohesion energy of an atom depending on the electron density at the appropriate atomic position as

$$E_{tot} = \sum_{i=1}^N U_i(\rho_i) + \frac{1}{2} \sum_{i=1}^N \sum_{\substack{j=1 \\ j \neq i}}^N \phi_{ij}(r_{ij}) . \quad (2.69)$$

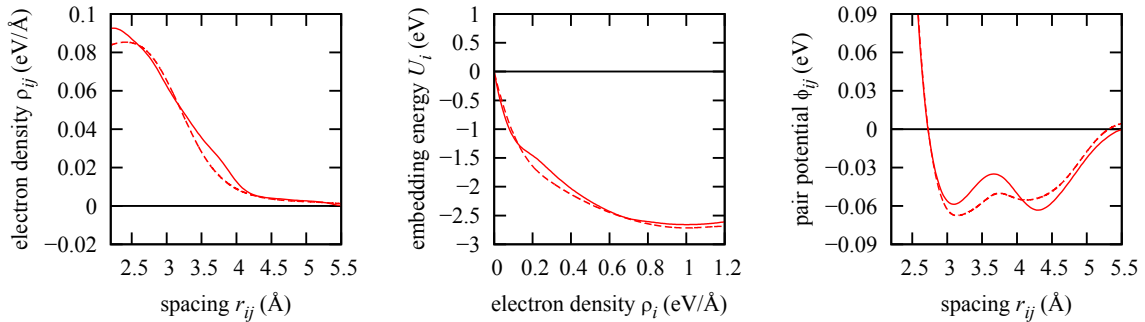


Figure 2.5: Potential functions for aluminum provided by F. Ercolessi [Ercolessi 2009] (continuous lines) and the group of Mishin [Mishin 2009] (dotted lines) in the framework of the EAM. Left: Electron density contribution $\rho_{ij}(r_{ij})$. Middle: Embedding energy $U_i(\rho_i)$. Right: Pair potential $\phi_{ij}(r_{ij})$.

Therein, the embedding part $U_i(\rho_i)$ describes the attractive interaction depending on the local electron density ρ_i into which atom i is placed. In the attractive term the local electron density is calculated by contributions caused by the neighboring atoms as

$$\rho_i = \sum_{\substack{j=1 \\ j \neq i}}^N \rho_{ij}(r_{ij}) . \quad (2.70)$$

The pair potential $\phi_{ij}(r_{ij})$ in the repulsive term of Equation (2.69) is an isotropic interatomic potential function. Usually, the three functions $U_i(\rho_i)$, $\rho_{ij}(r_{ij})$ and $\phi_{ij}(r_{ij})$ are fitted to experimental data or to data obtained in ab-initio calculations [Pfeiler 2007].

An advantage of pair-functional potentials is the incorporation of an approximate variation of the bond strength with the atomic coordination [Raabe 1998]. An established version of pair-functional methods is the embedded atom method (EAM), which is well suited for the reproduction of metallic bond [Daw et al. 1983] [Daw et al. 1984] [Foiles et al. 1986]. For this reason, EAM potentials are applied in the appropriate examples of the following chapters. The EAM calculates the local electron density at atomic sites based on the assumption of a homogeneous free-electron gas.

Different ways are proposed in the literature to choose a suitable database for fitting the EAM potential functions and to parameterize and optimize these functions. [Ercolessi et al. 1994] present the force-matching method to develop EAM potentials by fitting both, experimental data and ab-initio atomic forces. Later, [Mishin et al. 1999] published a fitting procedure using a database that consists of experimental data and ab-initio energies instead of forces. Both kinds of EAM potentials can be used for fracture simulation. The three potential functions of Equations (2.69) and (2.70) which describe the interatomic bond in aluminum according to the EAM are illustrated in Figure 2.5. Therein, the functions provided by Furio Ercolessi [Ercolessi 2009] are compared to the functions of Mishin's group [Mishin 2009].

The forces acting on atoms are calculated by the gradient of the atomic energies. By application of the EAM the forces acting on atom i due to the interactions with all other

atoms are according to [Sunyk et al. 2006]

$$\begin{aligned}
\mathbf{f}_i &= -\frac{\partial E_{tot}}{\partial \mathbf{u}_i} = \sum_{\substack{j=1 \\ j \neq i}}^N \mathbf{f}_{ij} = [E'_i(r_{ij}) + E'_j(r_{ji})] \frac{\mathbf{r}_{ij}}{r_{ij}} \\
&= -\sum_{\substack{j=1 \\ j \neq i}}^N \left\{ [(U'_i(\rho_i) + U'_j(\rho_j)) \rho'_{ij}(r_{ij}) + \phi'_{ij}(r_{ij})] \cdot \frac{\mathbf{r}_{ij}}{r_{ij}} \right\},
\end{aligned} \tag{2.71}$$

where $\cdot'()$ denotes the first derivative of a function with respect to the variable in brackets. External forces can be defined by the application of additional potential functions to certain atoms.

2.2.2 Lattice statics

Often, the numerical investigation of material properties of crystalline materials can be sufficiently realized by the method of lattice statics, that only considers static states of equilibrium. Kinetic as well as thermal energies are neglected. Therewith, this quasistatic method assumes that external actions on the system proceed on a significant lower time scale than the atomic relaxation and that thermal energies are much lower than defect-based atomic energies. Based on these assumptions the lattice statics theory includes only the potential energy of the atomic system calculated as the sum over the energies of all single atoms i in the system [Stukowski 2006]

$$E_{tot} = \sum_{i=1}^N E_i. \tag{2.72}$$

The energies of single atoms are calculated according to interatomic potentials (see Section 2.2.1). In addition to the total internal energy the energy from external loads \mathbf{f}_i^{ext} acting on atoms i is calculated as follows to obtain the potential of the system

$$\Pi = E_{tot} - \sum_{i=1}^N \mathbf{f}_i^{ext} \mathbf{u}_i, \tag{2.73}$$

with \mathbf{u}_i is the vector of displacements of atom i .

The equilibrium state of the system has to be found by minimizing the potential Π depending on the atomic positions \mathbf{x}_i

$$\min_{\mathbf{x}_i} \Pi(\mathbf{x}_i). \tag{2.74}$$

To solve the optimization problem, the atomic forces \mathbf{f}_i need to be calculated from external forces and from the gradient of the internal atomic energies with respect to the atomic displacements \mathbf{u}_i

$$\mathbf{f}_i = -\frac{\partial E_{tot}}{\partial \mathbf{u}_i} + \mathbf{f}_i^{ext}. \tag{2.75}$$

Initially, the theory of lattice statics was introduced by [Matsubara 1952] to investigate the lattice distortion about point defects. Subsequent publications, for example [Kanzaki 1957], [Hardy 1968], [Flocken et al. 1968], [Boyer et al. 1971], [Dash et al. 1983], and [Pfeiler 2007], have documented the developments in this method with treating the crystal either wholly or partially as an elastic continuum.

2.2.3 Molecular dynamics

Molecular dynamics (MD) methods are simulation techniques that predict the motion in a system of interacting particles, especially atoms. Detailed introductions to MD algorithms are published exemplarily by [Pfeiler 2007], [Li 2005], [Frenkel et al. 2002], and [Raabe 1998]. The basic idea of MD is the numerical integration of the equations of motion (Newton's equations) for a particle or especially an atomic system, which is described by the differential equation

$$m_i \ddot{\mathbf{x}}_i = \mathbf{f}_i(\mathbf{x}_i) , \quad (2.76)$$

where $\mathbf{f}_i(\mathbf{x}_i)$ denotes the force vector acting on atom i , \mathbf{x}_i and $\ddot{\mathbf{x}}_i$ are the location and the acceleration vector of the atom and m_i is its atomic mass.

The time integration of the set of Equations (2.76) for all atoms in a system yields the trajectory $\mathbf{x}_i(t)$ for all these atoms at every time t . To include the oscillating motions (lattice vibrations) of the atoms the time step Δt for the integration must be chosen significantly smaller than the lattice vibrational period, which is typically between 0.1 ps and 1 ps. An usual time step is in the order of femtoseconds. This limits MD systems to a maximum simulation time of microseconds. To overcome the limitation in time an accelerated MD method is introduced, for example, by [Uberuaga 2005].

For the numerical integration of the equations of motion different integration schemes are applicable, which differ in the numerical effort and accuracy. Usual schemes applied in MD are Verlet, Velocity Verlet, leap-frog, predictor corrector, and symplectic integrators. Comprehensive overviews on these algorithms are given by [Li 2005] and [Frenkel et al. 2002]. From all of them, Velocity Verlet integration is very popular since atomic positions and velocities are obtained simultaneously in one time step. Based on the values at an initial time t_0 the atomic positions \mathbf{x}_i at a new time $t_0 + \Delta t$ are calculated by a Taylor expansion as follows [Li 2005]

$$\mathbf{x}_i(t_0 + \Delta t) = \mathbf{x}_i(t_0) + \mathbf{v}_i(t_0) \Delta t + \frac{1}{2} \left(\frac{\mathbf{f}_i(t_0)}{m_i} \right) (\Delta t)^2 + \mathcal{O}((\Delta t)^3) , \quad (2.77)$$

and with the forces $\mathbf{f}_i(t_0 + \Delta t)$, which are evaluated from interatomic potentials, the velocities are obtained as

$$\mathbf{v}_i(t_0 + \Delta t) = \mathbf{v}_i(t_0) + \frac{1}{2} \left(\frac{\mathbf{f}_i(t_0)}{m_i} + \frac{\mathbf{f}_i(t_0 + \Delta t)}{m_i} \right) \Delta t + \mathcal{O}((\Delta t)^3) . \quad (2.78)$$

This basic MD algorithm describes a micro canonical ensemble with constant number of particles, volume, and energy (NVE), but with variable temperature.

To simulate a system at constant temperature (canonical ensemble - NVT) instead of constant energy a thermal equilibrium must be defined and controlled during the simulation. The thermal equilibrium is derived from the kinetic energy of the atomic system

$$E_{kin} = \frac{1}{2} k_B T(t) N_f = \frac{1}{2} \sum_{i=1}^N m_i \|\mathbf{v}_i(t)\|^2, \quad (2.79)$$

where k_B is the Boltzmann constant, $T(t)$ is the average temperature of the system at time t , N_f denotes the number of DOF and N the number of atoms. From Equation (2.79) the instantaneous temperature can be calculated as follows [Frenkel et al. 2002]

$$T(t) = \frac{1}{k_B N_f} \sum_{i=1}^N m_i \|\mathbf{v}_i(t)\|^2. \quad (2.80)$$

To control the temperature in a MD system the correction factor χ is introduced depending on the instantaneous temperature and the reference temperature $T_{ref}(t)$ as

$$\chi(t) = \sqrt{\frac{T_{ref}(t)}{T(t)}}. \quad (2.81)$$

During the simulation $\chi(t)$ scales the velocity to heat or cool the system so that the system keeps the reference temperature (Equation (2.83)).

Finally, the basic MD procedure with temperature control, energy calculation using the potential functions of the EAM (Section 2.2.1), and Velocity Verlet integretors is given for one time step Δt by the following algorithm assuming that for a certain time t the factor $\chi(t)$ is calculated according to Equations (2.81) and (2.80):

$$\mathbf{x}_i(t + \Delta t) = \mathbf{x}_i(t) + \mathbf{v}_i(t) \Delta t + \frac{1}{2} \mathbf{a}_i(t) (\Delta t)^2 \quad (2.82)$$

$$\mathbf{v}_i\left(t + \frac{1}{2}\Delta t\right) = \chi(t) \mathbf{v}_i(t) + \frac{1}{2} \mathbf{a}_i(t) \Delta t \quad (2.83)$$

$$\mathbf{f}_i(t + \Delta t) = - \sum_{\substack{j=1 \\ j \neq i}}^N \left[\left((U'_i(\rho_i) + U'_j(\rho_j)) \rho'_{ij}(r_{ij}) + \phi'_{ij}(r_{ij}) \right) \cdot \frac{\mathbf{r}_{ij}}{r_{ij}} \right] + \mathbf{f}_i^{ext}(t + \Delta t) \quad (2.84)$$

$$\text{with: } \mathbf{r}_{ij} = \mathbf{x}_i(t + \Delta t) - \mathbf{x}_j(t + \Delta t) \quad (2.85)$$

$$\mathbf{a}_i(t + \Delta t) = \frac{\mathbf{f}_i(t + \Delta t)}{m_i} \quad (2.86)$$

$$\mathbf{v}_i(t + \Delta t) = \mathbf{v}_i\left(t + \frac{1}{2}\Delta t\right) + \frac{1}{2} \mathbf{a}_i(t + \Delta t) \Delta t \quad (2.87)$$

$$E_{kin} = \frac{1}{2} \sum_{i=1}^N m_i \|\mathbf{v}_i(t + \Delta t)\|^2 \quad (2.88)$$

$$E_{pot} = \sum_{i=1}^N \left[U_i(\rho_i) + \frac{1}{2} \sum_{\substack{j=1 \\ j \neq i}}^N \phi_{ij}(r_{ij}) + \Pi_i^{ext} \right] \quad (2.89)$$

Therein, \mathbf{a}_i is the acceleration vector of atom i , \mathbf{f}_i^{ext} is the vector of external forces acting on atom i , Π_i^{ext} is its external applied potential and E_{pot} denotes the potential energy of the MD system. The split calculation of $\mathbf{v}_i(t + \Delta t)$ in a first part based on $\mathbf{a}_i(t)$ and in a second part based on $\mathbf{a}_i(t + \Delta t)$ aims at the temperature correction and at the error reduction in the numerical integration (according to Equation (2.78)).

At the beginning of the simulation a suitable set of initial values $\mathbf{x}_i(t_0)$, $\mathbf{v}_i(t_0)$, and $\mathbf{a}_i(t_0)$ has to be chosen. Usually, the initial atomic locations $\mathbf{x}_i(t_0)$ are defined by ideal lattice positions combined with random imperfections and the initial atomic velocities $\mathbf{v}_i(t_0)$ are defined by stochastic fields considering the condition that the system naturally is not moving,

$$\sum_{i=1}^N \|\mathbf{v}_i(t_0)\| = 0. \quad (2.90)$$

The initial atomic accelerations $\mathbf{a}_i(t_0)$ can be defined as zero. It is recommended to compute a suitable number of time steps in the unloaded state to relax the system for predefined temperature before starting the real simulation.

Beside the basic algorithm, advanced MD techniques were published in the last decades, exemplary the famous Car-Parinello method [Car et al. 1985].

2.2.4 Reduced units

On the atomistic scale the application of values in the international system of units (SI units) is unusual because in this case the typical atomistic values of length, mass, and time are extremely small. For instance, the lattice parameter of aluminum is about $4.032 \cdot 10^{-10}$ m, the atomic mass of aluminum is about $4.479 \cdot 10^{-26}$ kg and a typical lattice vibrational period is lower than 10^{-12} s. Consequently, precision errors will occur since these values expressed in SI units are very close to the numerical limit of computational machines. To avoid such problems, reduced units are introduced on the atomistic scale [Li 2005]. Exemplary, the length unit (\AA) is introduced and substitutes the SI unit (m) based on the relation

$$(\text{\AA}) = \sigma (\text{m}), \quad (2.91)$$

with the length parameter $\sigma = 10^{-10}$. With respect to the invariant algebraic expressions of fundamental physical laws other units must also be altered if one unit is substituted

and a completely new unit system must be defined on the atomistic scale. The atomic energies are expressed in the unit (eV) that is related to the SI unit (J) by the energy parameter ϵ as

$$(\text{eV}) = \epsilon (\text{J}), \quad (2.92)$$

where $\epsilon = 1.602176 \cdot 10^{-19}$ (related to the elementary charge). In our definition the reduced unit of mass is ($\tilde{\text{kg}}$) and depends on the atomic mass m_a of a reference material including the atomic mass unit (u) = $1.660539 \cdot 10^{-27}(\text{kg})$ in the form

$$(\tilde{\text{kg}}) = m_a (\text{kg}), \quad (2.93)$$

which results for aluminum in $m_a^{\text{Al}} = 26.9815 \cdot 1.660539 \cdot 10^{-27}$. The reduced time unit ($\tilde{\text{s}}$) is related to the SI unit (s) by the time parameter τ

$$(\tilde{\text{s}}) = \tau (\text{s}). \quad (2.94)$$

Based on the mentioned requirement of invariant physical laws the time parameter τ can be derived from the energy unit as follows

$$\epsilon = \frac{m_a \sigma^2}{\tau^2} \implies \tau = \sqrt{\frac{m_a \sigma^2}{\epsilon}}, \quad (2.95)$$

which yields for aluminum $\tau^{\text{Al}} = 5.28742 \cdot 10^{-14}$. The reduced force unit ($\tilde{\text{N}}$) is related to the appropriate SI unit (N) by the energy and length parameter as

$$(\tilde{\text{N}}) = \frac{\epsilon}{\sigma} (\text{N}). \quad (2.96)$$

Equivalently, the relations for the atomic velocity and acceleration can be written as

$$\left(\frac{\tilde{\text{m}}}{\tilde{\text{s}}}\right) = \frac{\sigma}{\tau} \left(\frac{\text{m}}{\text{s}}\right) \quad (2.97)$$

and

$$\left(\frac{\tilde{\text{m}}}{\tilde{\text{s}}^2}\right) = \frac{\sigma}{\tau^2} \left(\frac{\text{m}}{\text{s}^2}\right). \quad (2.98)$$

A further suitable modification concerning the temperature is frequently applied in atomistic simulations. Therefore, the temperature in the SI unit (K) is multiplied with the Boltzmann constant $k_B = 8.617343 \cdot 10^5 \text{eV/K}$

$$(\tilde{\text{K}}) = k_B (\text{K}). \quad (2.99)$$

This modification results in an energy equivalent temperature expression which is a term of many temperature dependent energy formulations on the atomistic scale.

2.3 Mixed atomistic-continuum methods

Mixed atomistic-continuum models are developed intensively since the early 1990s. These hybrid multiscale models couple regions of atomistic discretization with that of applied continuum mechanics. The atomistic-continuum models are aimed at a more effective application of computational power to numerically investigate larger model domains including atomistic features. In mixed atomistic-continuum models atomistic calculations are performed only in regions in which important physical processes proceed in the atomic lattice. In all other regions of the model domain continuum mechanics approaches are applied. Hence, unnecessary atomic degrees of freedom are removed and simulations are feasible on larger model domains without losing atomistic resolution in zones of local damage or plasticity.

It is known that the mechanical and thermodynamical coupling within hybrid models of different length and time scales causes problems concerning the spurious wave reflections at the boundary between model domains of different spatial resolution. That is, high-frequency waves can not pass the boundary and exemplarily the fracture energy is not completely transferred to higher scales. The introduction of artificial 'silent' boundaries with nonlinear viscous behavior can avoid the spurious wave reflections by damping high-frequency waves. Different approaches of coupling atomistics to continuum mechanics are developed in the last two decades. An overview on these mixed atomistic-continuum models is given in the following paragraphs.

A pioneering work was done especially by [Mullins et al. 1982] who combined atomistic and finite element models to study crack propagation in crystals. The same idea is applied in the Finite-Element-Atom (FEAt) model of [Kohlhoff et al. 1991] and [Gumbsch 1995] that was firstly developed for the analysis of defects in crystals, for example dislocations. Later the FEAt model was extended for fracture mechanical simulations on the atomistic scale. The FEAt model consists of an inner atomistic domain that is coupled to an outer FE region by two transition zones in which the atomistic and the FE regions overlap. While the atoms in the outer transition zone rigidly move with the FE nodes, the FE nodes in the inner transition zone rigidly move with the atoms. Thereby, a one-to-one correspondence of atoms and FE nodes is required. The coupling is realized by application of the nonlocal elasticity theory of [Kröner 1963]. A scheme of the FEAt model is illustrated in Figure 2.6.

The Macro Atomistic Ab initio Dynamics (MAAD) model of [Abraham et al. 1998] combines three different numerical methods for the multiscale simulation of fracture phenomena. Approaches from quantum mechanics at the crack tip are coupled with molecular dynamics (MD) around the crack and finite elements away from the crack (Figure 2.6). In the coupling zone between finite elements and molecular dynamics the FE mesh spacing is scaled to atomistic resolution and the nodal displacements are updated by the atomic displacements. Thus, the displacements of the FE nodes are dynamical variables

that follow in lockstep with the atomic displacements in the MD region. To minimize the above mentioned problems at boundaries between different numerical approaches and spatial resolutions the coupling zone must be far away from the fracture zone center. The approach of the MAAD method is also known as the Coupling of Length Scales (CLS) [Broughton et al. 1999]. As advancement to the MAAD and CLS method respectively, [Rudd et al. 2000] presented a Coarse-Grained Molecular Dynamics (CGMD) with a higher quality coupling of atomistics to continuum. The coupling is based on a derivation of the physical scaling properties of the system. Therewith, the FE/MD interface can be defined closer to the center of the fracture zone.

Another approach to overcome the problems at the atomistic-continuum transition is used in the Bridging Scale Method (BSM) [Wagner et al. 2003] [Park et al. 2004]. In the BSM the MD solution is projected onto the coarse scale shape functions. This projection defines the solution part that is obtainable by both solution methods. Spurious wave reflections are avoided by these method and the time step on the coarse scale can be chosen separately from the time step of the fine scale. The approach of the BSM is applied successfully also by [Xiao et al. 2004] in the framework of a bridging domain method. Furthermore, [Weinan et al. 2002] proposed new boundary conditions for the atomistic-continuum transition to minimize the reflection of phonons at the interface. [Fish et al. 2007] published a concurrent atomistic to continuum (AtC) coupling method based on a blending of the continuum stress and the atomistic force in the equilibrium equation. The blended atomistic-continuum description is applied to an overlap sub-domain between the atomistic and the continuum sub-domain.

While the above mentioned models imply a continuum region without defects, the Coupled Atomistic and Discrete Dislocation (CADD) model is able to simulate the move-

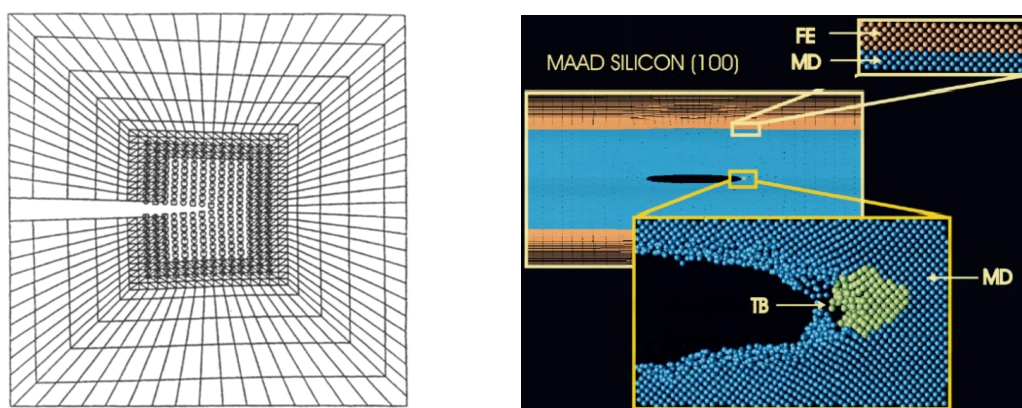


Figure 2.6: Left: Scheme of the FEAt model of a crack tip [Kohlhoff et al. 1991]. Small circles in the central model region around the crack tip denote atomic sites while squares in the outer model region show finite elements. Overlapping transition zones are between the atomistic and the FE region. Right: Scheme of the MAAD and CLS model respectively surrounding a crack (from [Broughton et al. 1999]). TB stands for the quantum Tight-Binding region.

ment of dislocations across the atomistic-continuum interface [Shilkrot et al. 2002b] [Shilkrot et al. 2004]. In the continuum domain dislocations are reproduced by the application of finite elements with elastoplastic material behavior. Due to the larger possible size of the CADD model compared to pure atomistic models, the interaction of multiple dislocations can be investigated. The coupling scheme of the CADD method follows closely that of the FEAt model of [Kohlhoff et al. 1991]. Another method with the same intention but different from the CADD model is proposed by [Shilkrot et al. 2002a]. This method couples the below described Quasicontinuum model with continuum defect models to allow movements of dislocations from the atomistic to the continuum description.

A new concept of a coupled atomistic-continuum model is published in [Saether et al. 2009]. Therein, the Embedded Statistical Coupling Method (ESCM) is explained, that connects a MD domain with the FE representation via statistical mechanics at the MD/FE interface. Following the idea that the continuum representation of a material is a statistical representation of its atomic structure, the method uses statistical averaging over both, time and volume, of atomistic sub-domains at the MD/FE interface to provide nodal displacement boundary conditions to the continuum domain. In the continuum domain the FE method generates reaction forces at the interface that are uniformly distributed over the interface atoms as constant traction boundary conditions to the MD domain [Yamakov et al. 2008]. By the introduction of statistical averages of atomistic quantities at the atomistic-continuum interface the ESCM concept avoids discretization of the continuum model to atomistic resolution. This advantage has to be considered as a main improvement compared to the most former coupling methods.

The above introduced models consist of predefined atomistic and continuum regions that are often not adaptable during the simulation. However, the Quasicontinuum (QC) method proposed by [Tadmor et al. 1996a] integrates mesh adaption procedures to follow

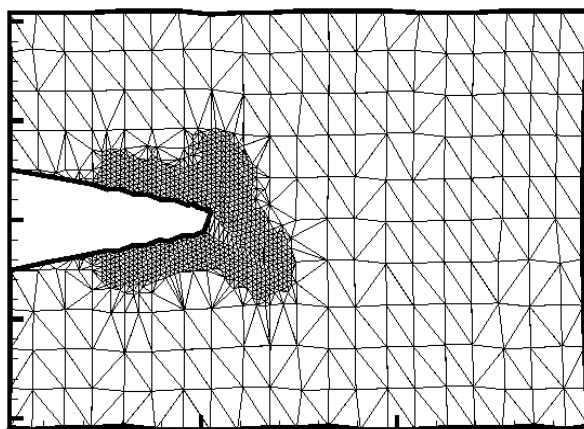


Figure 2.7: Quasicontinuum model for the fracture analysis in aluminum (from [Buehler et al. 2005]).

propagating defects with suitable discretization (Figure 2.7). The QC method couples an underlying atomic lattice to finite elements by kinematic couplings between nodal DOF and atomic DOF at sites of so called representative atoms. Special finite elements are applied which describe the material behavior by interatomic potentials. Since the Quasicontinuum method is originally limited to quasistatic calculations at zero temperature [Knap et al. 2001] [Miller et al. 2002] [Tadmor et al. 2005], some proposals are published to extend the method either to finite temperature [Shenoy et al. 1999a] or to include the dynamics of atoms [Dupuy et al. 2005]. A detailed description of the QC method follows in Chapter 4.

Chapter 3

Geometrical characterization of grain boundaries

The damage simulation on microscale needs a well defined geometrical description of the atomic sites in the underlying crystal lattice. The orientation of individual crystallites related to global coordinates can be defined by Eulerian angles or by Miller indices [Bunge 1993] [Randle et al. 2000]. Furthermore, the characterization of crystallites misorientation along grain boundaries is usually done by either the coincident-site lattice (CSL) description or the interface-plane scheme (IPS) [Wolf et al. 1989] [Wolf 1992]. Another way to describe the geometry of grain boundaries was also proposed by [Bishop et al. 1968] within the concept of structural units. In the following the usually used CSL and IPS descriptions are explained.

3.1 Definition of individual crystallite orientation

3.1.1 Orientation by Miller indices

In crystallography Miller indices are frequently used to clearly identify planes and directions in crystal (Bravais) lattices by a triple of integer values [Bunge 1993]. The definition of Miller indices is based on atomic sites in the Bravais lattice, which axes are defined by the three lattice vectors \mathbf{a}_1 , \mathbf{a}_2 and \mathbf{a}_3 that span the unit cell of the crystal.

Integer triples that define a lattice plane in a crystal are written in round brackets. Exemplary, (hkl) denotes a plane that intercepts the axes of the unit cell in the points \mathbf{a}_1/h , \mathbf{a}_2/k and \mathbf{a}_3/l , and all parallel planes. The notation $\{hkl\}$ denotes all planes that are equivalent to (hkl) by the symmetry of the crystal. The definition of lattice directions is characterized by square brackets. The integer triple $[hkl]$ defines the vector $h\mathbf{a}_1 + k\mathbf{a}_2 + l\mathbf{a}_3$ and the notation $\langle hkl \rangle$ denotes all directions that are equivalent to $[hkl]$ by the symmetry of the crystal. By convention, negative integers are written with a bar, as in $\bar{3}$ for -3 . The integers are usually written in lowest terms, this means that their greatest common divisor should be 1 (Figure 3.1).

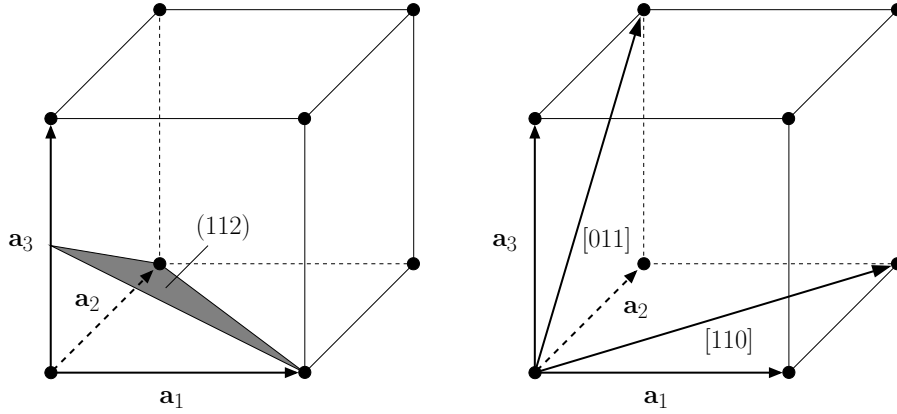


Figure 3.1: Examples of Miller indices. Left: (112)-plane. Right: [110]- and [011]-direction.

Based on Miller indices, the orientation of individual crystallites in a global Cartesian coordinate system can be defined by the crystallites lattice directions that are parallel to the global coordinate axes. Therewith, the generation of general grain boundaries depending on the global orientation of neighboring crystallites is practicable (Figure 3.2).

3.1.2 Orientation by Eulerian angles

Another way of defining the orientation of a crystallite is given by a sequence of rotations about the local axes of the crystallite through Eulerian angles [Bunge 1993]. Three sequential rotations with respect to the global coordinate system are sufficient to clearly characterize any spatial orientation. The usual algorithm starts with an orientation of the crystallite coordinate system ($X'Y'Z'$) in which the axes are parallel to those of the global coordinate system (XYZ). The first rotation is applied about the Z' -axis through the angle φ_1 , followed by a rotation about the new orientation of the X' -axis through the

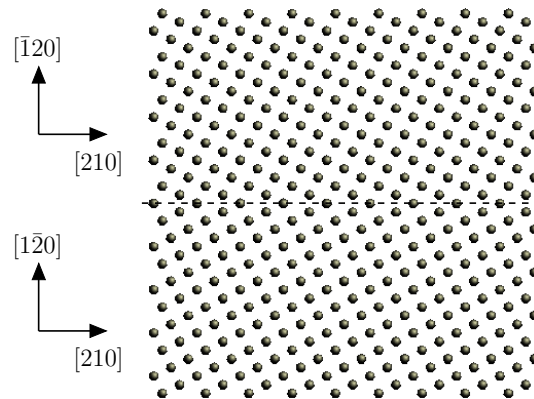


Figure 3.2: Global orientation of two FCC crystallites building a $\Sigma 5$ STGB (symmetric tilt grain boundary). In both crystallites the [210]-direction is parallel to global X. The [1̄20]-direction in the lower crystallite and the [1̄20]-direction in the upper crystallite are parallel to global Y.

angle ϕ . Finally, the crystallite coordinate system is rotated again about the Z' -axis (in its new orientation) through the angle φ_2 . The $Z'X'Z'$ -rotation is expressed by the three Eulerian angles $\varphi_1\phi\varphi_2$ (Figure 3.3). Alternatively, the second rotation about the X' -axis is substituted by a rotation about the Y' -axis through the angle ψ . The three possible rotations about local axes are expressed in matrix notation [Randle et al. 2000] as

$$\mathbf{g}_\phi^{X'} = \begin{bmatrix} 1 & 0 & 0 \\ 0 & \cos \phi & -\sin \phi \\ 0 & \sin \phi & \cos \phi \end{bmatrix} \quad \dots \text{ rotation about local } X'\text{-axis}, \quad (3.1)$$

$$\mathbf{g}_\psi^{Y'} = \begin{bmatrix} \cos \psi & 0 & \sin \psi \\ 0 & 1 & 0 \\ -\sin \psi & 0 & \cos \psi \end{bmatrix} \quad \dots \text{ rotation about local } Y'\text{-axis}, \quad (3.2)$$

$$\mathbf{g}_\varphi^{Z'} = \begin{bmatrix} \cos \varphi & -\sin \varphi & 0 \\ \sin \varphi & \cos \varphi & 0 \\ 0 & 0 & 1 \end{bmatrix} \quad \dots \text{ rotation about local } Z'\text{-axis}. \quad (3.3)$$

Positive rotation angles effect a rotation about local X' -axis from Y' towards Z' , about local Y' -axis from Z' towards X' , and about local Z' -axis from X' towards Y' . The complete sequence of rotation can be described by one rotation matrix \mathbf{g} that follows from the product notation. Exemplary, the $Z'X'Z'$ -rotation is expressed by

$$\mathbf{g}^{act} = \mathbf{g}_{\varphi_2}^{Z'} \cdot \mathbf{g}_\phi^{X'} \cdot \mathbf{g}_{\varphi_1}^{Z'}. \quad (3.4)$$

The rotation matrix \mathbf{g}^{act} describes an active rotation. That is a rotation of a vector about local coordinate axes. By contrast a passive rotation describes the rotation of the coordinate system. The coordinates of the vector in the rotated coordinate system are calculated by the multiplication with the inverse rotation matrices. For rotations in orthogonal right-hand-systems it is essential that the inverse rotation matrices equal the transposed rotation matrices. The passive $Z'X'Z'$ -rotation in 3D space can be described by the following rotation matrix \mathbf{g}^{pas} ,

$$\mathbf{g}^{pas} = \left(\mathbf{g}_{\varphi_2}^{Z'}\right)^T \cdot \left(\mathbf{g}_\phi^{X'}\right)^T \cdot \left(\mathbf{g}_{\varphi_1}^{Z'}\right)^T = \left(\mathbf{g}_{\varphi_1}^{Z'} \cdot \mathbf{g}_\phi^{X'} \cdot \mathbf{g}_{\varphi_2}^{Z'}\right)^T. \quad (3.5)$$

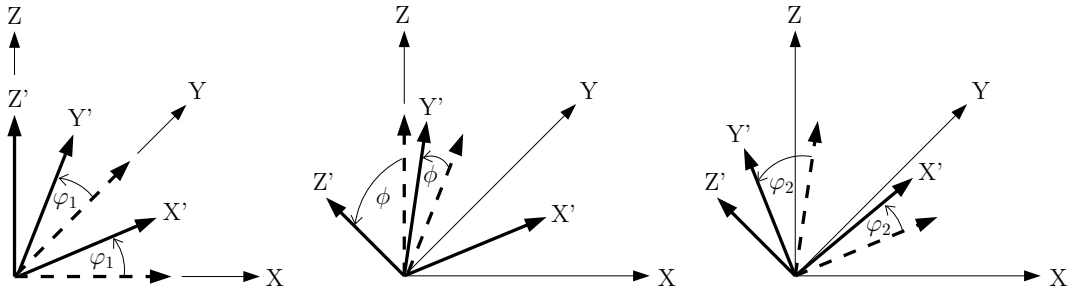


Figure 3.3: From left to right: $Z'X'Z'$ -rotation of coordinate system $(X'Y'Z')$ by Eulerian angles $\{\varphi_1\phi\varphi_2\}$ starting with $(X'Y'Z')$ lies parallel to global coordinate system (XYZ) .

3.1.3 Transformation from Eulerian angles into Miller indices

In the current thesis the orientation of crystallites in the mesoscale model is described by Eulerian angles because continuum mechanics are applied on the mesoscale and the crystal lattice is not explicitly defined. By contrast, in the microscale model the crystallites along a grain boundary are oriented by Miller indices and the underlying crystal lattice is the basis of the applied numerical method. In the course of scale coupling a transformation from Eulerian angles into Miller indices is necessary. Exemplary, this transformation is shown in the following for FCC crystallites.

Let assume a grain boundary with a normal vector \mathbf{z}_{GB} defined in the global coordinate system (XYZ) on the mesoscale. This normal vector characterizes the Z-axis of the grain boundary coordinate system $(XYZ)^{GB}$, which is the basis of the grain boundary model on the microscale. The X- and Y-axis are defined by two vectors \mathbf{x}_{GB} and \mathbf{y}_{GB} that span the grain boundary plane and define an orthogonal right-hand-system with \mathbf{z}_{GB}

$$\mathbf{x}_{GB} = \begin{bmatrix} 1 \\ 1 \\ 1 \end{bmatrix} \quad \mathbf{y}_{GB} = \begin{bmatrix} -1 \\ 1 \\ 0 \end{bmatrix} \quad \mathbf{z}_{GB} = \begin{bmatrix} 1 \\ 1 \\ -2 \end{bmatrix}. \quad (3.6)$$

The orientation of the two crystallites building the common grain boundary is expressed by the Eulerian angles of a Z'X'Z'-rotation in the mesoscale coordinate system as

$$\{\varphi_1\phi\varphi_2\}^1 = \{213.4^\circ, 63.0^\circ, 177.8^\circ\}, \quad (3.7)$$

$$\{\varphi_1\phi\varphi_2\}^2 = \{59.5^\circ, 109.5^\circ, -25.7^\circ\}. \quad (3.8)$$

These rotations result in two crystallite coordinate systems $(X'Y'Z')^{1,2}$, with the X'-axis is equal to the particular [100] lattice direction, the Y'-axis is equal to the particular [010] lattice direction, and the Z'-axis is equal to the particular [001] lattice direction.

Now, the lattice directions of the crystallites which are parallel to the grain boundary coordinate system $(XYZ)^{GB}$ have to be calculated to generate the crystal lattices in the grain boundary model on the microscale. The global coordinate system (XYZ) has to be rotated by the Eulerian angles into the crystallites coordinate systems $(X'Y'Z')^1$ and $(X'Y'Z')^2$, respectively and these passive rotations have to be applied to the vectors \mathbf{x}_{GB} , \mathbf{y}_{GB} and \mathbf{z}_{GB} , that define the $(XYZ)^{GB}$ coordinate system. For the two crystallites, Equations (3.1), (3.3) and (3.5) result with the Eulerian angles of Equations (3.7) and (3.8) in the following passive rotation matrices

$$\mathbf{g}^{pas,1} = \begin{bmatrix} 0.844 & 0.536 & 0.034 \\ -0.218 & 0.400 & -0.890 \\ -0.490 & 0.744 & 0.454 \end{bmatrix}, \quad (3.9)$$

$$\mathbf{g}^{pas,2} = \begin{bmatrix} 0.333 & 0.850 & -0.409 \\ 0.479 & 0.221 & 0.849 \\ 0.812 & -0.478 & -0.334 \end{bmatrix}. \quad (3.10)$$

The application of the passive rotation matrices to the vectors \mathbf{x}_{GB} , \mathbf{y}_{GB} and \mathbf{z}_{GB} results in the lattice directions, which are parallel to the axes of the grain boundary coordinate system.

$$\{\mathbf{x}', \mathbf{y}', \mathbf{z}'\}_1 = \mathbf{g}^{pas,1} \cdot \{\mathbf{x}, \mathbf{y}, \mathbf{z}\}_{GB} \quad (3.11)$$

$$\mathbf{x}'_1 = \begin{bmatrix} 1.414 \\ -0.708 \\ 0.707 \end{bmatrix} \quad \mathbf{y}'_1 = \begin{bmatrix} -0.308 \\ 0.618 \\ 1.234 \end{bmatrix} \quad \mathbf{z}'_1 = \begin{bmatrix} 1.311 \\ 1.963 \\ -0.655 \end{bmatrix}$$

$$\{\mathbf{x}', \mathbf{y}', \mathbf{z}'\}_2 = \mathbf{g}^{pas,2} \cdot \{\mathbf{x}, \mathbf{y}, \mathbf{z}\}_{GB} \quad (3.12)$$

$$\mathbf{x}'_2 = \begin{bmatrix} 0.774 \\ 1.550 \\ 0.000 \end{bmatrix} \quad \mathbf{y}'_2 = \begin{bmatrix} 0.517 \\ -0.258 \\ -1.291 \end{bmatrix} \quad \mathbf{z}'_2 = \begin{bmatrix} 2.000 \\ -0.999 \\ 1.001 \end{bmatrix}$$

Finally the lowest integer triples are chosen, which have similar relations to each other compared to the components of the orientation vectors calculated by Equations (3.11) and (3.12). For each crystallite, these integer triples define the lattice directions which are parallel to the axes of the grain boundary coordinate system. For the given example the orientation of crystallite 1 in the grain boundary coordinate system is defined by the lattice directions

$$(X, Y, Z)^{GB,1} \equiv \{[2\bar{1}1], [\bar{1}24], [23\bar{1}]\}, \quad (3.13)$$

and the appropriate definition for crystallite 2 is

$$(X, Y, Z)^{GB,2} \equiv \{[120], [2\bar{1}\bar{5}], [2\bar{1}1]\}. \quad (3.14)$$

3.2 Definition of grain boundary misorientation

3.2.1 CSL misorientation scheme

The interface between two different crystallites is fully characterized by eight geometrical parameters, that are five macroscopic and three microscopic. The three microscopic parameters are the two parallel and one perpendicular relative displacements between the crystallites and they are summarized in the translation vector \mathbf{T} . The five macroscopic parameters can be defined by different ways. One possible definition follows the coincident-site-lattice (CSL) misorientation scheme [Wolf et al. 1989].

In the concept of CSL, at certain crystallographic misorientations, a three-dimensional lattice could be constructed with lattice points common to both adjacent crystallites. The CSL is considered as the smallest common sublattice of the adjoining grains. The volume

ratio of the unit cell of the CSL to that of the crystal is described by the parameter Σ , which can also be considered as the reciprocal density of coincident sites.

In the CSL scheme the misorientation along a grain boundary is defined by the relative rotation of the crystallites about a rotation axes $\hat{\mathbf{n}}_R$ through the angle Θ and by the grain boundary normal direction $\hat{\mathbf{n}}_1$, which is defined in the principal coordinate system of the first crystallite. The two direction vectors $\hat{\mathbf{n}}_R$ and $\hat{\mathbf{n}}_1$ are characterized each with two DOF (two polar coordinates [Bunge 1993]) and together with the rotation angle Θ they define the five macroscopic parameters. Exemplary, in the CSL misorientation scheme a grain boundary which is described in terms of Miller indices as follows

$$\hat{\mathbf{n}}_R, \Theta, \hat{\mathbf{n}}_1, \mathbf{T} = [110], 70.53^\circ, [111], \mathbf{T} \quad (3.15)$$

represents with $\mathbf{T} = \frac{1}{2} [110]$ the (111) twin grain boundary [Wolf et al. 1989].

3.2.2 Interface-plane scheme (IPS)

An alternative way of defining the five macroscopic parameters of a grain boundary is given by the interface-plane scheme (IPS) [Wolf et al. 1989], which allows an explicit differentiation between the tilt and the twist component of an interface plane. In the IPS, two normal vectors $\hat{\mathbf{n}}_1$ and $\hat{\mathbf{n}}_2$ represent the grain boundary plane in the principal coordinate systems of crystallite 1 and 2, respectively. Therewith, the tilt component of the grain boundary is defined by only these two relative orientations and the tilt angle Ψ is determined by

$$\sin \Psi = \left\| \frac{\hat{\mathbf{n}}_1}{\|\hat{\mathbf{n}}_1\|} \times \frac{\hat{\mathbf{n}}_2}{\|\hat{\mathbf{n}}_2\|} \right\|. \quad (3.16)$$

The angle η controls the relative rotation of the two crystallites about the plane normal. Thus, the twist component of the grain boundary is clearly characterized by $\hat{\mathbf{n}}_1$ and η . For instance, in the interface-plane scheme the twin boundary of section 3.2.1 is described by

$$\hat{\mathbf{n}}_1, \hat{\mathbf{n}}_2, \eta, \mathbf{T} = [111], [111], 60^\circ, \mathbf{T} \quad (3.17)$$

as a 60° (111) twist boundary [Wolf et al. 1989].

3.2.3 Transformation from IPS and CSL misorientation scheme into grain boundary definition by Miller indices and vice versa

Since the orientation of crystallites in the microscale model is defined by Miller indices, the transformation from the usual interface characterization by IPS or CSL scheme into the definition by Miller indices and vice versa shall be explained.

Let assume a grain boundary that is characterized by the following five macroscopic parameters in the IPS and CSL scheme, respectively:

$$\text{IPS:} \quad \hat{\mathbf{n}}_1, \hat{\mathbf{n}}_2, \eta = [110], [543], 26.52^\circ \quad (3.18)$$

$$\text{CSL: } \hat{\mathbf{n}}_{\mathbf{R}}, \Theta, \hat{\mathbf{n}}_1 = [100], 36.87^\circ, [110] . \quad (3.19)$$

The transformation from the IPS description into the CSL scheme and vice versa is explained in detail in [Wolf et al. 1989] and in Section 3.2.4. The interface normals $\hat{\mathbf{n}}_1$ and $\hat{\mathbf{n}}_2$ are perpendicular to the Z-axis of the grain boundary coordinate system $(X, Y, Z)^{GB}$, which is the global coordinate system of the microscale model. The Miller indices of the Z-orientation of the two crystallites are equal to $\hat{\mathbf{n}}_1$ and $\hat{\mathbf{n}}_2$, respectively. The tilt axis $\hat{\mathbf{n}}_{\mathbf{T},1}$ in the principal coordinate system of crystallite 1 is perpendicular to the interface normals $\hat{\mathbf{n}}_1$ and $\hat{\mathbf{n}}_2$. Hence, $\hat{\mathbf{n}}_{\mathbf{T},1}$ is given by

$$\hat{\mathbf{n}}_{\mathbf{T},1} = \hat{\mathbf{n}}_1 \times \hat{\mathbf{n}}_2 = \begin{bmatrix} 1 \\ 1 \\ 0 \end{bmatrix} \times \begin{bmatrix} 5 \\ 4 \\ 3 \end{bmatrix} = \begin{bmatrix} 3 \\ -3 \\ -1 \end{bmatrix}, \quad (3.20)$$

and can be defined as the global X-orientation of crystallite 1. According to Equation (3.28) the rotation matrix $\mathbf{R}(\hat{\mathbf{n}}_{\mathbf{R}}, \Theta)$ is obtainable for the example as

$$\mathbf{R}(\hat{\mathbf{n}}_{\mathbf{R}}, \Theta) = \begin{bmatrix} 1 & 0 & 0 \\ 0 & 0.8 & -0.6 \\ 0 & 0.6 & 0.8 \end{bmatrix}. \quad (3.21)$$

Now, $\hat{\mathbf{n}}_{\mathbf{T},2}$ can be determined by application of the rotation matrix $\mathbf{R}(\hat{\mathbf{n}}_{\mathbf{R}}, \Theta)$ to $\hat{\mathbf{n}}_{\mathbf{T},1}$ similar to Equation (3.29)

$$\hat{\mathbf{n}}_{\mathbf{T},2} = \mathbf{R}(\hat{\mathbf{n}}_{\mathbf{R}}, \Theta) \cdot \hat{\mathbf{n}}_{\mathbf{T},1} = \begin{bmatrix} 1 & 0 & 0 \\ 0 & 0.8 & -0.6 \\ 0 & 0.6 & 0.8 \end{bmatrix} \begin{bmatrix} 3 \\ -3 \\ -1 \end{bmatrix} = \begin{bmatrix} 3 \\ -1.8 \\ -2.6 \end{bmatrix} \equiv \begin{bmatrix} 15 \\ -9 \\ -13 \end{bmatrix}, \quad (3.22)$$

and can be defined as the global X-orientation of crystallite 2. Because the local coordinate systems of the crystallites are orthogonal right-hand-systems, the global Y-orientation of each crystallite can be calculated by

$$\{\mathbf{y} = \mathbf{z} \times \mathbf{x} = \hat{\mathbf{n}} \times \hat{\mathbf{n}}_{\mathbf{T}}\}_{1,2}. \quad (3.23)$$

After all, the crystal directions that are parallel to global coordinate axes can be summarized for the two crystallites, which build the grain boundary of the example.

$$\begin{array}{lll} \text{crystallite 1 : } & \text{X : } & \hat{\mathbf{n}}_{\mathbf{T},1} = [3\bar{3}\bar{1}] \\ & \text{Y : } & \hat{\mathbf{n}}_1 \times \hat{\mathbf{n}}_{\mathbf{T},1} = [\bar{1}1\bar{6}] \\ & \text{Z : } & \hat{\mathbf{n}}_1 = [110] \\ \text{crystallite 2 : } & \text{X : } & \hat{\mathbf{n}}_{\mathbf{T},2} = [15, \bar{9}, \bar{13}] \\ & \text{Y : } & \hat{\mathbf{n}}_2 \times \hat{\mathbf{n}}_{\mathbf{T},2} = [\bar{5}, 22, \bar{21}] \\ & \text{Z : } & \hat{\mathbf{n}}_2 = [543] \end{array} \quad (3.24)$$

In the course of inverse transformation from Miller indices into IPS and CSL misorientation scheme the twist angle η is determined from the tilt axes defined in the principal

coordinate systems of the two crystallites. These tilt axes are the crystallites directions parallel to the global X-orientation (Equation (3.24))

$$\sin \eta = \left\| \frac{\hat{\mathbf{n}}_{T,1}}{\|\hat{\mathbf{n}}_{T,1}\|} \times \frac{\hat{\mathbf{n}}_{T,2}}{\|\hat{\mathbf{n}}_{T,2}\|} \right\|. \quad (3.25)$$

The current example yields the twist angle

$$\eta = 26.52^\circ. \quad (3.26)$$

As shown in Equation (3.18) the exemplary grain boundary is defined in the IPS description by the direction vectors $\hat{\mathbf{n}}_1$ and $\hat{\mathbf{n}}_2$, which are the crystallites directions parallel to the global Z-orientation (Equation (3.24)), and the angle η . The further transformation into the CSL misorientation scheme is explained in the following section.

3.2.4 Relation between CSL misorientation scheme and IPS description

According to [Wolf et al. 1989] the transformation of a grain boundary characterization from the CSL misorientation scheme into the IPS description is done as follows.

The five macroscopic parameters, which describe the grain boundary misorientation in the CSL scheme are $\hat{\mathbf{n}}_R, \Theta, \hat{\mathbf{n}}_1$. As first, the direction vectors $\hat{\mathbf{n}}_R$ and $\hat{\mathbf{n}}_1$ are scaled by its norm to obtain unit vectors. Based on the rotation axes

$$\hat{\mathbf{n}}_R = \begin{bmatrix} \hat{n}_{R,1} \\ \hat{n}_{R,2} \\ \hat{n}_{R,3} \end{bmatrix}, \quad (3.27)$$

with $|\hat{\mathbf{n}}_R| = 1$ and the rotation angle Θ the rotation matrix is calculated

$$\mathbf{R}(\hat{\mathbf{n}}_R, \Theta) = \quad (3.28)$$

$$(1 - \cos\Theta) \begin{bmatrix} (\hat{n}_{R,1})^2 & \hat{n}_{R,1} \cdot \hat{n}_{R,2} & \hat{n}_{R,1} \cdot \hat{n}_{R,3} \\ \hat{n}_{R,1} \cdot \hat{n}_{R,2} & (\hat{n}_{R,2})^2 & \hat{n}_{R,2} \cdot \hat{n}_{R,3} \\ \hat{n}_{R,1} \cdot \hat{n}_{R,3} & \hat{n}_{R,2} \cdot \hat{n}_{R,3} & (\hat{n}_{R,3})^2 \end{bmatrix} + \begin{bmatrix} \cos\Theta & -\hat{n}_{R,3} \cdot \sin\Theta & \hat{n}_{R,2} \cdot \sin\Theta \\ \hat{n}_{R,3} \cdot \sin\Theta & \cos\Theta & -\hat{n}_{R,1} \cdot \sin\Theta \\ -\hat{n}_{R,2} \cdot \sin\Theta & \hat{n}_{R,1} \cdot \sin\Theta & \cos\Theta \end{bmatrix}.$$

The grain boundary normal $\hat{\mathbf{n}}_2$ is determined by the transformation

$$\hat{\mathbf{n}}_2 = \mathbf{R}(\hat{\mathbf{n}}_R, \Theta) \cdot \hat{\mathbf{n}}_1, \quad (3.29)$$

with $|\hat{\mathbf{n}}_1| = 1$. The tilt axis $\hat{\mathbf{n}}_T$ and the tilt angle Ψ are obtained by

$$\hat{\mathbf{n}}_T = \frac{\hat{\mathbf{n}}_1 \times \hat{\mathbf{n}}_2}{|\hat{\mathbf{n}}_1 \times \hat{\mathbf{n}}_2|}, \quad (3.30)$$

$$\sin \Psi = |\hat{\mathbf{n}}_1 \times \hat{\mathbf{n}}_2|, \quad (3.31)$$

and the twist angle η is calculated from the relation

$$1 + \cos \eta = 2 \cdot \frac{1 + \cos \Theta}{1 + \cos \Psi}. \quad (3.32)$$

Thus, the macroscopic IPS parameters $\hat{\mathbf{n}}_1, \hat{\mathbf{n}}_2, \eta$ are readily calculated.

The inverse transformation starts from the IPS description of a grain boundary with the parameters $\hat{\mathbf{n}}_1, \hat{\mathbf{n}}_2, \eta$. Again, the direction vectors have to be scaled by their norm. With $|\hat{\mathbf{n}}_1| = |\hat{\mathbf{n}}_2| = 1$ and Equations (3.30) and (3.31) the tilt axis $\hat{\mathbf{n}}_T$ and the tilt angle Ψ are determined. The rotation axes $\hat{\mathbf{n}}_R$ is obtained by the following equation

$$\hat{\mathbf{n}}_R = \frac{\sqrt{(1 + \cos \eta)(1 - \cos \Psi)} \hat{\mathbf{n}}_T + \sqrt{(1 - \cos \eta)(1 + \cos \Psi)} \hat{\mathbf{n}}_1 + \sqrt{(1 - \cos \eta)(1 - \cos \Psi)} [\hat{\mathbf{n}}_T \times \hat{\mathbf{n}}_1]}{\sqrt{3 - \cos \eta - \cos \Psi + \cos \eta \cos \Psi}} \quad (3.33)$$

With the given twist angle η and the calculated tilt angle Ψ the rotation angle Θ can be determined by relation (3.32). Now, the grain boundary is totally described in the CSL misorientation scheme by $\hat{\mathbf{n}}_R, \Theta, \hat{\mathbf{n}}_1$.

3.3 Experimental measurements of grain boundary misorientation

In nanotechnology powerful electron microscopes offer the possibility of experimental studies of interfaces at the atomic level. Modern electron microscopes have resolution up to 0.05 nm. Therewith, the misorientation of grain boundaries can be experimentally measured. Moreover, the characterization schemes for grain boundary misorientation can be verified by experimental studies.

Electron microscopy includes scanning electron microscopy (SEM), transmission electron microscopy (TEM), and scanning transmission electron microscopy (STEM). SEM constructs an image from signals generated sequential as a finely focused beam of electrons

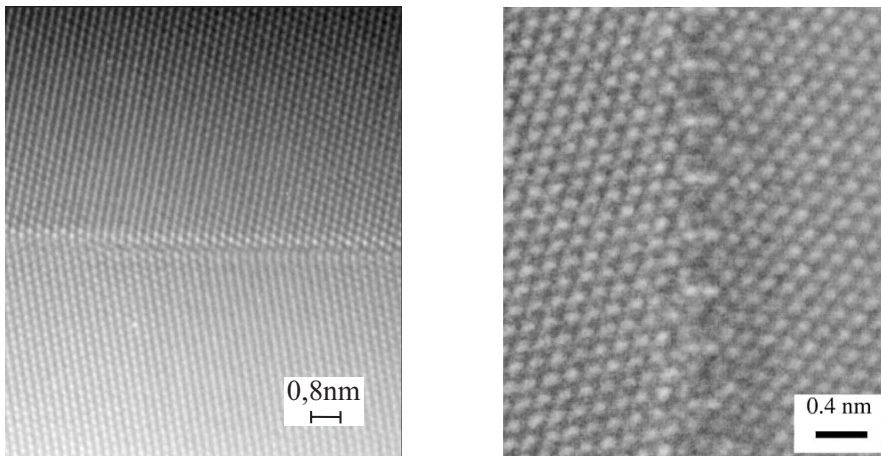


Figure 3.4: HRTEM images of a $\Sigma 11$ grain boundary (left) from [Schmidt 2003] and a $\Sigma 7$ grain boundary (right) from [Hu et al. 2000], both in aluminum. White dots are interpretable as atomic positions.

scans the surface of a bulk sample. Thus, SEM resolution is limited by the scattering of beam electrons within the sample. TEM and STEM use signals generated by beam electrons as they transit a very thin sample (typically less than 100 nm). TEM focuses the transmitted electrons themselves into a real image on a fluorescent screen or electronic detector array. STEM, similar to SEM, scans a focused beam over the thin sample, mapping transmitted electron intensity or some other signal into a virtual image. Exemplary, two high resolution TEM (HRTEM) images of aluminum grain boundaries are shown in Figure 3.4.

Chapter 4

The Quasicontinuum method: Theory and implementation

In general, the Quasicontinuum (QC) method belongs to the class of concurrent multi-scale methods that couples atomistics with continuum mechanics. The QC approach was originally developed at Brown University in the mid 1990s by Tadmor, Miller, Shenoy, and coworkers under the guidance of Ortiz and Phillips [Tadmor 1996] [Tadmor et al. 1996a] [Tadmor et al. 1996b] [Miller 1997] [Shenoy 1998]. Following the idea of saving atomic DOF in regions with smooth deformation fields, kinematic constraints are introduced in appropriate parts of the model to couple numerous atomic DOF to those of few representative atoms. In this way, the large number of DOF in atomistic simulations is mainly reduced to the DOF of atoms with significant different behavior compared to their neighborhood. Effective QC models include on one side full atomistic resolution in regions of defects and interfaces that cause significant variations in the deformation field and have on the other side coarse resolution with many kinematic couplings in regions of a smooth deformation field. Section 4.1 gives an overview on the theories of the quasistatic local and nonlocal QC method and discusses approaches to additionally consider dynamics and finite temperature in the QC formulation.

In the framework of the presented research a fully 3D nonlocal QC model was implemented for quasistatic simulations of brittle intergranular fracture of various grain boundaries (GB) in polycrystals. Based on QC simulations effective cohesive GB parameters, for example strength and fracture energy, are determined to model the intergranular fracture in continuum polycrystal models by cohesive zone approaches. In addition to the theory several issues are addressed in Section 4.2 concerning the implementation of main features of the nonlocal QC method. Especially the geometrical generation of low energy grain boundaries, the calculation of atomic forces and the robust energy minimization procedure, as well as the parallelization of time-consuming parts of the simulation are outlined.

While the following sections describe general formulations of the QC method, which

is implemented for 3D simulations using tetrahedral elements, some of the associated illustrations show 2D structures with triangular elements. The visualization of theoretical details in 2D is more suitable for explanations and the understanding of the QC method.

4.1 Theory

4.1.1 Fundamentals of the Quasicontinuum theory at zero temperature

As pointed out in the QC overviews of [Shenoy et al. 1999b], [Knap et al. 2001], [Miller et al. 2002], and [Tadmor et al. 2005], the QC method is based on a conventional atomistic approach, that is the computation of the system energy as a function of atomic positions. A reference configuration is assumed, which describes the positions of N atomic nuclei in the system by a lattice (Figure 4.1). The reference position \mathbf{X}_i of atom i is defined by an integer combination of lattice vectors added to the position vector \mathbf{X}_0 of a reference atom

$$\mathbf{X}_i = \mathbf{X}_0 + \sum_{n=1}^d l_i^n \mathbf{A}_n. \quad (4.1)$$

\mathbf{A}_n are the Bravais lattice vectors in d dimensions multiplied with the integers l_i^n of the i th atomic position. An atomic position \mathbf{x}_i in the deformed configuration is defined by the associated reference position and the unique displacement vector \mathbf{u}_i of the i th atom

$$\mathbf{x}_i = \mathbf{X}_i + \mathbf{u}_i. \quad (4.2)$$

The atomic displacements of all N atoms in the system are summarized in the displacement array \mathbf{u}

$$\mathbf{u} = \{\mathbf{u}_1, \mathbf{u}_2, \dots, \mathbf{u}_i, \dots, \mathbf{u}_N\}. \quad (4.3)$$

For the use of semi-empirical potentials the exact total internal energy calculation at zero temperature equals Equation (2.72) from lattice statics (Section 2.2.2) and is based on

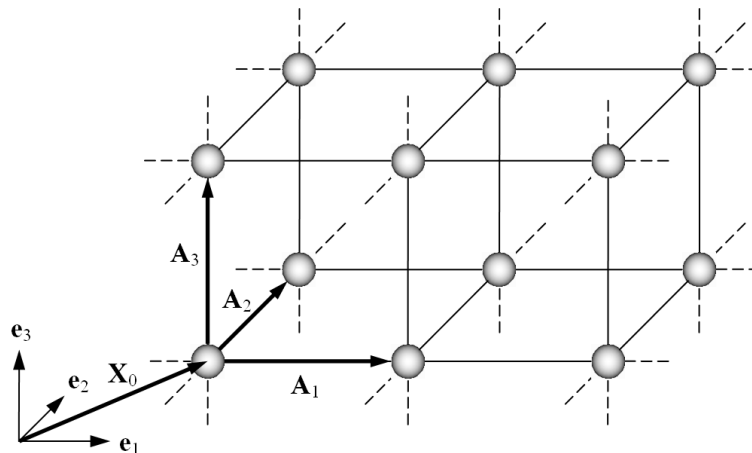


Figure 4.1: Reference configuration: Definition of lattice positions of atomic nuclei by the Bravais lattice vectors \mathbf{A}_n and the position vector \mathbf{X}_0 of a reference atom.

the sum over all individual atomic energies depending on the atomic displacements \mathbf{u}

$$E_{tot} = \sum_{i=1}^N E_i(\mathbf{u}). \quad (4.4)$$

Following the idea of reducing degrees of freedom by introducing representative atoms, only the displacements of representative atoms are treated explicitly and the displacements of remaining atoms are interpolated. For the interpolation, a mesh of finite elements with nodes at sites of representative atoms is overlaid with the atomic lattice (Figure 4.2). Usually, linear interpolation functions associated with the representative atoms are introduced by finite elements to approximate a uniform displacement field within the elements. The interpolation of displacements \mathbf{u}_i^h of the i th atom is done in the form

$$\mathbf{u}_i^h = \sum_{\alpha=1}^R N_{\alpha}(\mathbf{X}_i) \mathbf{u}_{\alpha}, \quad (4.5)$$

where α runs over the set of R representative atoms in the system. \mathbf{u}_{α} is the displacement vector of the representative atom α and N_{α} is the interpolation function associated with representative atom α and evaluated at the reference coordinates of atom i . The array of approximated atomic displacements \mathbf{u}^h can be defined as

$$\mathbf{u}^h = \{\mathbf{u}_1^h, \mathbf{u}_2^h, \dots, \mathbf{u}_N^h\}. \quad (4.6)$$

The interpolation of atomic positions in the deformed configuration corresponds to the displacement interpolation and reads

$$\mathbf{x}_i^h = \sum_{\alpha=1}^R N_{\alpha}(\mathbf{X}_i) \mathbf{x}_{\alpha}. \quad (4.7)$$

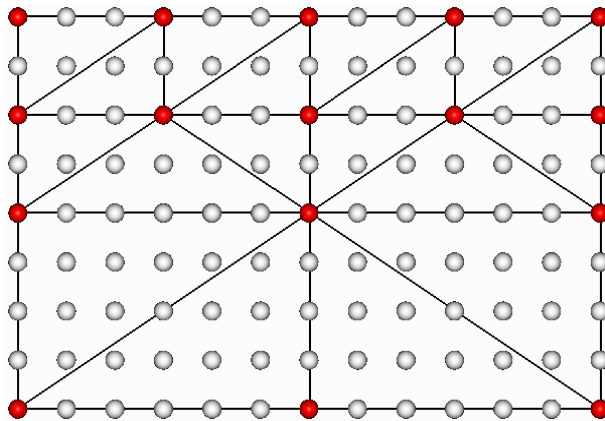


Figure 4.2: FE mesh (dark lines) linked to the atomic lattice by nodes at sites of representative atoms (red).

Through the element-wise interpolation of atomic displacements the total internal energy of the system E_{tot} is replaced by the approximated energy E_{tot}^h

$$E_{tot}^h = \sum_{i=1}^N E_i(\mathbf{u}^h). \quad (4.8)$$

In a next approximation step, the calculation of atomic energies is reduced to the set of representative atoms α and the energies of these atoms are weighted by factors n_α . The total internal energy is approximated by the QC method as follows

$$E_{tot}^h \approx E_{tot}^{QC} = \sum_{\alpha=1}^R n_\alpha E_\alpha(\mathbf{u}^h). \quad (4.9)$$

The weighting factors n_α must be chosen in such a way, that in case of full atomistic resolution, where all atoms are representative atoms, all n_α have the value 1. This condition also includes the requirement that the sum over all weighting factors must equal the number of atoms in the system

$$\sum_{\alpha=1}^R n_\alpha = N. \quad (4.10)$$

The calculation of weighting factors n_α can follow different approaches as explained in [Shenoy et al. 1999b]. Two suitable ways of defining n_α are suggested in Sections 4.1.2 and 4.1.3. In principle, the two ways are independent of each other and both could be applied to the local formulation as well as to the nonlocal formulation of the QC method.

Finally, according to the lattice statics formulation of Equation (2.73), the potential of the QC system Π^{QC} including the external energy reads

$$\Pi^{QC}(\mathbf{u}^h) = \sum_{\alpha=1}^R n_\alpha E_\alpha(\mathbf{u}^h) - \sum_{\alpha=1}^R n_\alpha \bar{\mathbf{f}}_\alpha^{ext} \mathbf{u}_\alpha, \quad (4.11)$$

with $\bar{\mathbf{f}}_\alpha^{ext}$ is the average external force assigned to representative atom α . The equilibrium state of the system has to be found by minimizing the potential Π^{QC} depending on the positions \mathbf{x}_α of representative atoms corresponding to Equation (2.74)

$$\min_{\mathbf{x}_\alpha} \Pi^{QC}(\mathbf{x}_\alpha). \quad (4.12)$$

4.1.2 Local Quasicontinuum formulation at zero temperature

The local QC formulation makes use of the discretization of the QC domain with finite elements. The introduction of linear shape functions for the interpolation of atomic displacements within a finite element results in a uniform deformation gradient \mathbf{F} within each element. According to [Miller et al. 2002] the application of the Cauchy-Born rule assumes that a uniform deformation gradient at the macroscale can be mapped directly to the same uniform deformation on the microscale. Following this rule, every atom of

a simple crystallographic lattice is energetically equivalent, when the lattice underlies a uniform deformation gradient. Consequently, the energy E_e within a finite element in the deformed state equals the energy E_i^e of one atom of the element multiplied with the number of atoms n_e assigned to this element. The total internal energy of the local QC domain can be computed as a sum over all element energies by

$$E_{tot}^{QC\,loc} = \sum_{e=1}^{N_{elem}} n_e E_i^e. \quad (4.13)$$

The computational effort of the energy calculation reduces to the summation of element energies and the explicit calculation of only one atomic energy per element. Alternatively, the Cauchy-Born energy can be calculated depending on the deformation gradient \mathbf{F} from a unit cell with periodic boundary conditions. Therefore, the lattice vectors of the unit cell are distorted according to a given deformation gradient (Figure 4.3)

$$\mathbf{a}_n = \mathbf{F} \mathbf{A}_n \quad (4.14)$$

and the energy E_0 of the deformed unit cell with lattice vectors \mathbf{a}_n can be computed. The strain energy density \mathcal{E} in the element can be calculated by

$$\mathcal{E}(\mathbf{F}) = \frac{E_0(\mathbf{F})}{\Omega_0}, \quad (4.15)$$

with Ω_0 is the unit cell volume. Based on the strain energy density in the elements the total internal energy of Equation (4.13) is alternatively obtained by the equation

$$E_{tot}^{QC\,loc} = \sum_{e=1}^{N_{elem}} \Omega_e \mathcal{E}(\mathbf{F}_e), \quad (4.16)$$

as the sum over all elements for which the strain energy density is multiplied with the volume Ω_e of the appropriate e th element. To follow the concept of representative atoms, the element energy can be distributed to the representative atoms at sites of element

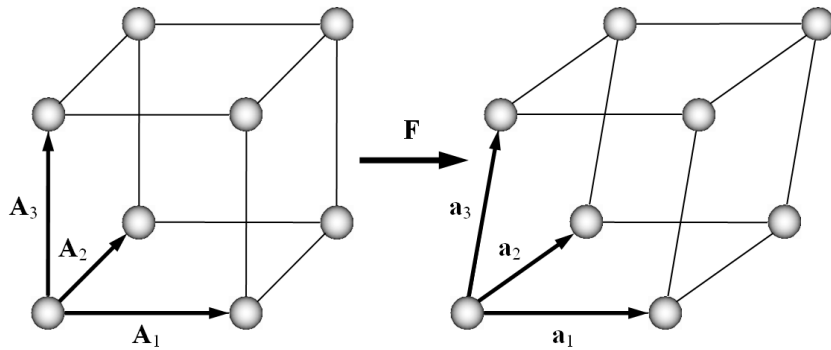


Figure 4.3: Deformation of a unit cell according to the deformation gradient \mathbf{F} . Left: Reference configuration with undistorted Bravais lattice vectors \mathbf{A}_n . Right: Deformed configuration with distorted Bravais lattice vectors \mathbf{a}_n .

nodes. For this reason the model is divided by a tessellation into cells in such a way, that each cell surrounds a representative atom. This can be realized by a Voronoi tessellation or a simpler partitioning of the elements in equal parts per node as illustrated in Figure 4.4. The amount M of partial element volumes Ω_e^α which are adjacent to the representative atom α defines the local QC region that is represented by this atom. The element-wise multiplication of the strain energy density with the partial element volumes results in element-wise contributions to the weighted energy of representative atoms

$$n_\alpha E_\alpha = \sum_{e=1}^M \Omega_e^\alpha \mathcal{E}(\mathbf{F}_e), \quad (4.17)$$

that is needed for the summation according to Equation (4.9). The weighting factor n_α can be expressed as the ratio of the sum of partial element volumes Ω_e^α and the volume of one single atom Ω_i

$$n_\alpha = \frac{1}{\Omega_i} \sum_{e=1}^M \Omega_e^\alpha. \quad (4.18)$$

The atomic volume Ω_i is approximated by the Wigner-Seitz cell depending on the lattice parameter a_0 , that is for instance in case of FCC crystals [Tadmor 1996]

$$\Omega_i = \frac{a_0^3}{4}. \quad (4.19)$$

Inserting Equation (4.17) into Equation (4.11) results in the potential of the local QC formulation

$$\Pi^{QC\,loc}(\mathbf{u}^h) = \sum_{\alpha=1}^R \sum_{e=1}^M \Omega_e^\alpha \mathcal{E}(\mathbf{F}_e) - \sum_{\alpha=1}^R n_\alpha \bar{\mathbf{f}}_\alpha^{ext} \mathbf{u}_\alpha. \quad (4.20)$$

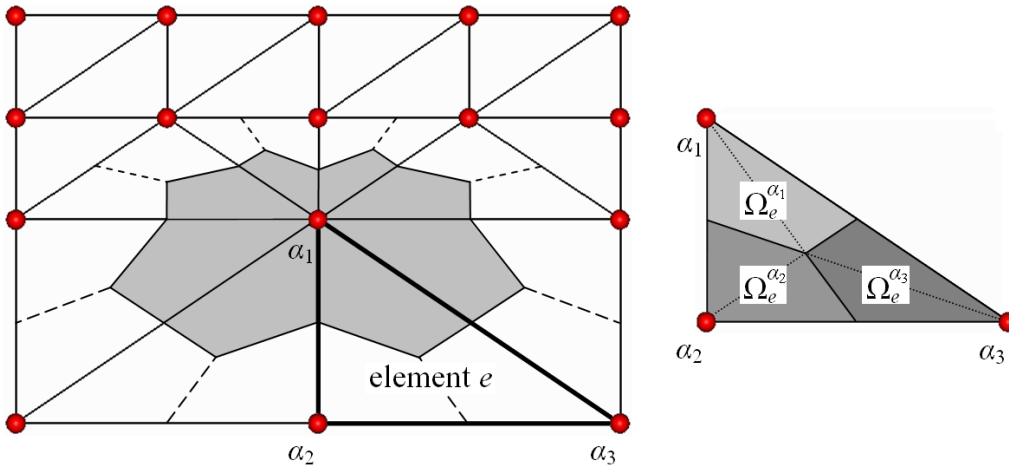


Figure 4.4: Left: The amount of shadowed domains build the cell assigned to representative atom α_1 . Right: Triangular elements are subdivided by medians into equal parts per node. The partitioning can be adopted straightforward to tetrahedral elements.

Due to the introduction of the Cauchy-Born rule the local QC method can be thought as a continuum formulation, but with an atomistic-based constitutive law instead of the usually applied phenomenological one. Since the Cauchy-Born rule assumes uniformly deformed bulk environments, the local QC formulation is suitable only for bulk atoms without defects in their neighborhood. For atoms, which are close to surfaces, interfaces, or other defects, the local QC method can not give an acceptable approximation of the total atomic energies. In such cases the nonlocal QC formulation provides more accurate results.

4.1.3 Nonlocal Quasicontinuum formulation at zero temperature

In contrast to the local QC formulation that calculates the energy of representative atoms depending on the uniform deformation gradient in the associated elements, the nonlocal QC formulation calculates the energy of representative atoms explicitly by the interactions with their atomic neighborhood in the actual displacement state. This means that the energy calculation of the representative atoms is independent on the associated elements as well as on the element size. Accordingly, the nonlocal QC formulation is sensitive to non-uniform deformations and free surfaces, especially in the limit of required full atomistic resolution (Figure 4.5).

In the first version of the QC method, the nonlocal theory was developed as the so called energy-based formulation. The intention of the energy-based formulation is to approximate the atomic energies and to find the equilibrium configuration of the atoms by energy minimization. For this reason, the energies of representative atoms are calculated explicitly and are summarized according to Equation (4.9) to compute the total internal

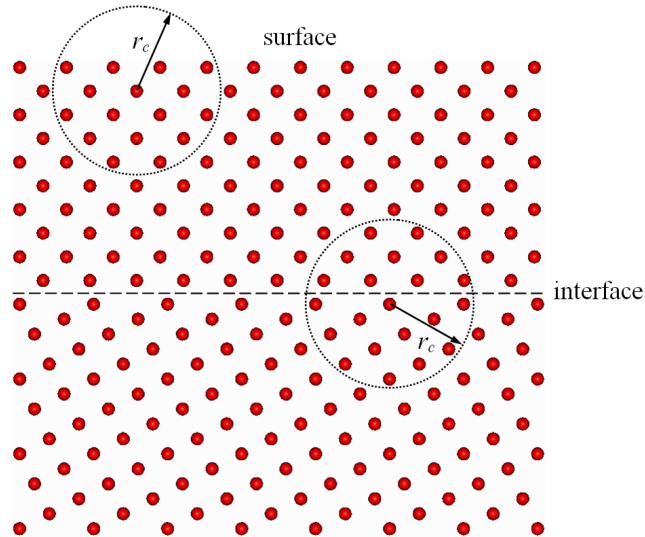


Figure 4.5: Explicit energy calculation of nonlocal representative atoms by interactions within a cutoff distance r_c . Surface and interface effects are directly involved.

energy as

$$E_{tot}^{QC} = \sum_{\alpha=1}^R n_{\alpha} E_{\alpha}(\mathbf{u}^h).$$

Therein, n_{α} can be calculated according to the algorithm in Section 4.1.2. Alternatively, the weighting factor n_{α} of the representative atom α could be obtained by the associated interpolation function N_{α} evaluated at the reference positions of all atoms i in adjacent elements

$$n_{\alpha} = \sum_{i=1}^N N_{\alpha}(\mathbf{X}_i). \quad (4.21)$$

Because the sum of all interpolation functions evaluated at any atomic position in an element equals one, the number of atoms within an element is exactly distributed to the representative atoms at sites of associated element nodes. Therewith, the requirement of Equation (4.10) concerning the weighting factors is fulfilled.

In a revised version of the QC method, Knap and Ortiz [Knap et al. 2001] presented a force-based formulation of the nonlocal QC theory with the intention to approximate the atomic forces directly, rather than from the explicit differentiation of the energy functional. The idea is that the minimum of the energy physically leads to a configuration with vanishing forces at all DOF. Consequently, the aim of the force-based formulation is to search for the equilibrium state by the condition of zero forces at all DOF. Within the framework of the force-based formulation Knap and Ortiz introduced the calculation of equivalent representative atom forces by an averaging procedure from a cluster of atoms around the representative one (Figure 4.6). The cluster size is defined by the cluster radius r_{cl} that is usually chosen to include first and second atomic neighbors. However, an increase of the cluster size accompanies with a higher accuracy of the simulation by

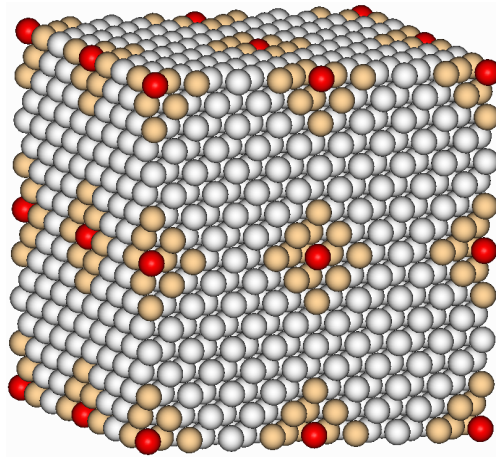


Figure 4.6: Nonlocal QC formulation of [Knap et al. 2001]: Cluster of atoms (dark yellow) are used to calculate forces and energies assigned to representative atoms (red) by an averaging procedure. Remaining atoms (light grey) do not explicitly contribute to calculated forces and energies.

evaluating forces and energies at more atomic sites, but at the same time the computational effort is increasing. That means that the cluster size should be chosen carefully to ensure a sufficient accuracy and an acceptable effort at the same time. This problem is addressed in [Knap et al. 2001] exemplarily by sensitivity studies of QC results with respect to the cluster size.

In regions of high representative atom density the clusters are reduced to avoid overlapping. In zones of virtual overlapping cluster atoms are assigned to the closest representative atom. This ensures, that in the limit of full atomistic resolution all atoms contribute their quantities with a weighting of exactly 1 to the system and the formulation reduces to lattice statics. In any case, the representative atom itself is considered as the first atom of the associated cluster. In the limit of full atomistic resolution, every cluster consists of exactly one atom, which is the representative atom itself. While the cluster summation rule was originally introduced for the approximation of forces, it can also be applied to the energy calculation. For comparison of different formulations by their final expression of the total potential Π , only the energies are treated in this section while a discussion on different approximations of the atomic forces follows in Section 4.2.5. Applying the cluster summation rule from [Knap et al. 2001] also to the energy formulation results in the following averaged energy $\bar{E}_\alpha(\mathbf{u}^h)$ assigned to the representative atom α

$$\bar{E}_\alpha(\mathbf{u}^h) = \frac{1}{n_\alpha^c} \sum_{k=1}^C N_\alpha(\mathbf{X}_k) E_k(\mathbf{u}^h). \quad (4.22)$$

$E_k(\mathbf{u}^h)$ is the energy of cluster atom k and C denotes the number of cluster atoms in the system. The energy $E_k(\mathbf{u}^h)$ is weighted by the interpolation function $N_\alpha(\mathbf{X}_k)$ according to the distance of cluster atom k to the representative atom α . Equation (4.22) also implies that the energy of a cluster atom distributes by the interpolation functions to the representative atoms at nodal sites of the associated element to which the cluster atom is assigned (Figure 4.7). Therewith, the averaged energy calculation for a representative

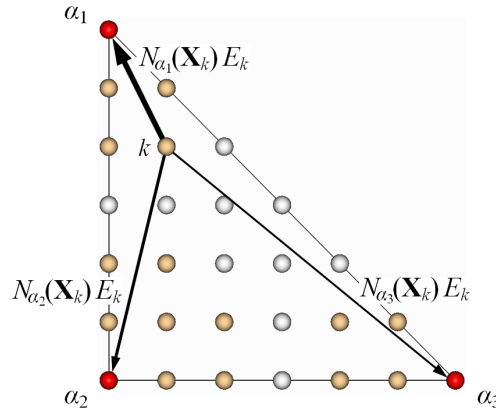


Figure 4.7: Partitioning of energy from cluster atom k to the representative atoms of the associated element.

atom can also participate in atomic values of neighboring clusters and the quantity as well as the quality of information is improved. To relate the cluster energy to an energy per atom, the energy sum has to be multiplied by a cluster weighting factor. For reasons of consistency in the presented thesis the cluster weights are defined as $1/n_\alpha^c$ with

$$n_\alpha^c = \sum_{k=1}^C N_\alpha(\mathbf{X}_k). \quad (4.23)$$

The choice of suitable weighting factors is discussed in detail in Section 4.2.4. Application of the cluster summation rule of Equation (4.22) to the general potential formulation of Equation (4.11) and formulating the external part of the potential according to the cluster summation rule results in the following potential of the nonlocal QC formulation

$$\Pi^{QC}(\mathbf{u}^h) = \sum_{\alpha=1}^R \frac{n_\alpha}{n_\alpha^c} \sum_{k=1}^C N_\alpha(\mathbf{X}_k) E_k(\mathbf{u}^h) - \sum_{\alpha=1}^R \frac{n_\alpha}{n_\alpha^c} \sum_{k=1}^C N_\alpha(\mathbf{X}_k) \mathbf{f}_k^{ext} \mathbf{u}_k^h, \quad (4.24)$$

where the weighting factor n_α is calculated by Equation (4.21). Alternatively to Equation (4.24), a formulation can be applied to calculate the cluster energy simply by a summation over all cluster atoms C_α which are assigned to the same representative atom. The cluster weight can be approximated again by Equation (4.23) and Equation (4.21) or by other suitable approaches. The simplified formulation of the nonlocal QC method with the introduction of general cluster weights w_α reads

$$\Pi^{QC}(\mathbf{u}^h) = \sum_{\alpha=1}^R w_\alpha \sum_{k=1}^{C_\alpha} E_k(\mathbf{u}^h) - \sum_{\alpha=1}^R w_\alpha \sum_{k=1}^{C_\alpha} \mathbf{f}_k^{ext} \mathbf{u}_k^h. \quad (4.25)$$

The above formulations are valid at zero temperature and both, Equation (4.24) and Equation (4.25), exactly reduce to the lattice statics formulation in the limit of full atomistic resolution, in which all atoms are representative atoms and all clusters only consist of their representative atom. Extended formulations of the QC potential for systems at finite temperature or to include the dynamics of atoms are described in Section 4.1.6.

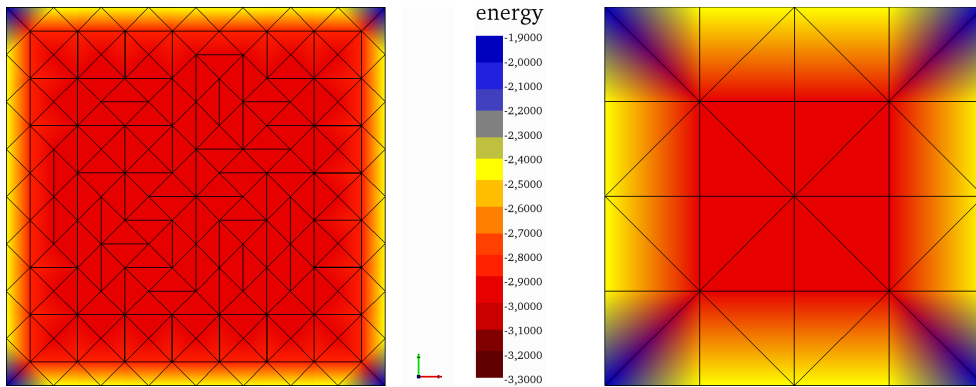


Figure 4.8: Surface energies for samples of the same size. Left: In the limit of full atomistic resolution only the surface region itself is influenced by the surface energy. Right: A coarse mesh at the surface causes unphysical surface energies deep in the solid.

While the local QC formulation is unable to reproduce surface and interface effects, the nonlocal QC formulation overestimates those effects when using a coarse resolution of representative atoms in such regions. This overestimation results from a large weight n_α of the energy of representative atoms in case of coarse resolution. The region that is energetically influenced by a surface or by an interface is numerically enlarged with a coarsen mesh of representative atoms (Figure 4.8). To avoid the overestimation the QC model has to be refined down to the atomistic resolution in regions close to defects including surfaces and interfaces. Then, the nonlocal QC formulation is able to correctly capture interatomic processes, for example at defect cores and grain boundaries.

4.1.4 Coupling of the local and nonlocal Quasicontinuum formulations

The local and nonlocal QC formulations can be coupled to use the computational efficiency of the local formulation in regions of slow variations in the deformation field as well as to exactly capture defect phenomena with atomic scale accuracy by the nonlocal formulation. The coupling of both formulations was already presented in first publications of the QC method [Tadmor 1996] [Tadmor et al. 1996a] by combining the local QC theory and the energy-based nonlocal QC theory in one model.

Since in the nonlocal region the summation of energies is representative-atom-wise, the energies in the local region must also be assigned to representative atoms following Equation (4.17) to combine both formulations. The energy summation over elements (Equation (4.16)) is only possible in totally local QC models. Consequently, for QC models with combined formulations the total internal energy calculation has to be split into the summation over R_{loc} local representative atoms and the summation over R_{nloc} nonlocal ones

$$E_{tot}^{QC} = \sum_{\alpha=1}^{R_{loc}} n_\alpha E_\alpha(\mathbf{u}^h) + \sum_{\alpha=1}^{R_{nloc}} n_\alpha E_\alpha(\mathbf{u}^h). \quad (4.26)$$

By the application of different QC formulations an interface exists between the local and nonlocal region. While the energy of the local representative atoms depends only on the strain energy density in the elements adjacent to them, the energy calculation of nonlocal representative atoms near interfaces is also affected by their local neighbors (Figure 4.9). Due to the different energy approximations of the continuum-based local theory and the atomistic-based nonlocal theory spurious forces arise near the local-to-nonlocal interface [Miller et al. 2002]. These physically unreasonable forces are named “ghost-forces” in the combined QC method. To overcome the force inconsistency near interfaces corrective forces can be added as dead loads to the affected representative atoms [Shenoy et al. 1999b]. The force inconsistency arises in a zone near the local-to-nonlocal interface where the interaction of local and nonlocal atoms contributes variously to the atomic energy calculation. The idea of force correction in these zones is that near the

interface the forces on local atoms should be the same as in a fully nonlocal formulation and vice versa. To ensure this, the missing force terms are added on as dead loads and extraneous force terms are subtracted off for the appropriate atoms as explained in detail in [Miller et al. 2002]. Summarizing, the new QC potential $\Pi^{QC'}(\mathbf{u}^h)$, which incorporates dead loads \mathbf{f}_α^G for the ghost-force correction, can be written

$$\Pi^{QC'}(\mathbf{u}^h) = \sum_{\alpha=1}^{R_{loc}} n_\alpha E_\alpha(\mathbf{u}^h) + \sum_{\alpha=1}^{R_{nloc}} n_\alpha E_\alpha(\mathbf{u}^h) - \sum_{\alpha=1}^R n_\alpha \left(\bar{\mathbf{f}}_\alpha^{ext} + \mathbf{f}_\alpha^G \right) \mathbf{u}_\alpha. \quad (4.27)$$

When using the local and nonlocal QC formulation in one model, a criterion must be defined to decide, whether a representative atom should be treated as local or as nonlocal. Such a nonlocality criterion was introduced by Tadmor [Tadmor 1996] [Tadmor et al. 1996a] and summarized, for example by [Miller et al. 2002]. The criterion analyzes the variation in the deformation gradient around a representative atom. Usually, the deformation gradients in the elements that are located within a certain distance to a given representative atom are investigated. For all of those elements the right stretch tensor \mathbf{U} of Equation (2.7) is calculated by

$$\mathbf{U} = \sqrt{\mathbf{F}^T \mathbf{F}}, \quad (4.28)$$

and the differences in eigenvalues λ_k of these tensors are evaluated. The associated non-locality criterion reads

$$\max_{a,b;k} \|\lambda_k^a - \lambda_k^b\| < \text{tolerance}, \quad (4.29)$$

where k runs over the number of eigenvalues of \mathbf{U} and a and b run over all considered elements near the representative atom. According to [Miller et al. 2002] a value of 0.1 has been found as a reasonable tolerance.

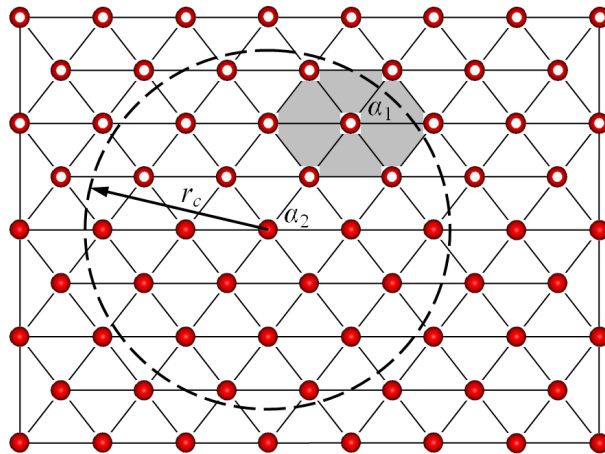


Figure 4.9: “Ghost forces” arise near the interface between local (circles) and nonlocal (dots) representative atoms due to various force calculation rules. The dotted circle includes all atoms within the cutoff distance r_c around atom α_2 . While the interaction between atoms α_1 and α_2 explicitly contributes to the force of nonlocal atom α_2 , local atom α_1 is affected only by the deformation gradient in its associated elements (grey).

The mixed local-nonlocal QC method is suitable to bridge large order of length scales in one concurrent multiscale model by combining continuum and atomistic formulations. Nevertheless, the problem of physically unreasonable spurious forces exist in the interface zone. This problem arises for all mixed atomistic-continuum methods known in the literature as a result of the coupling of various theories of material modeling. However, the corrective force terms in the QC potential again cause new ghost-forces of minor order so that an iterative procedure is needed for the ghost-force correction, and with the increase in numerical complexity the convergence behavior becomes worse. For this reason the application of a pure nonlocal QC model makes sense for problems of a smaller range of length scales. Therein, coarsening of the discretization in defect-free regions is also practicable to reduce the dimension of the numerical problem but the energy and force calculation is completely restricted to atomistic theories and no spurious forces arise. Applications of pure nonlocal QC models are documented in [Knap et al. 2001] and [Eidel et al. 2009].

4.1.5 Adaption of discretization in Quasicontinuum models

In consequence of an evolving deformation process with associated progress of defects an adaption of discretization with representative atoms is provided by the general QC approach. Automatic adaption techniques of the FE method are applicable, since representative atoms are regarded as nodes of finite elements with assumed constant strain.

According to [Shenoy et al. 1999b] the Zienkiewicz-Zhu error estimator, written in terms of the deformation gradient, could be applied to identify elements for mesh refinement. Elements with an error greater than a given tolerance are removed. Constrained atoms closest to the midsides of removed elements become representative atoms. Then, remeshing is performed in the domain of the removed elements considering the new representative atoms as additional nodes. Finally, the new discretization is checked by the error estimator and refinement proceeds until the error of all new elements is lower than the tolerance, or the limit of full atomistic resolution is reached.

Beside mesh refinement, mesh coarsening can also improve the capabilities of concurrent multiscale methods. For QC models the same error estimator as for mesh refinement can be used to identify unnecessary fine discretization. If neighboring elements have errors lower than a given tolerance, a coarsen mesh can be generated based on the outer nodes of the set of these elements. If the estimated error for all new elements again is lower than the tolerance, the old elements are removed. Then, representative atoms associated with former inner nodes of the removed set of elements become constraint atoms. The coarsening algorithm can proceed iteratively until the most coarsen discretization is found for the given error tolerance. Details on the mesh adaption in QC models are published exemplary in [Tadmor 1996], [Shenoy et al. 1999b], and [Miller et al. 2002]. A discussion on the effect of the remeshing-indicator tolerance is done in [Knap et al. 2001].

4.1.6 Approaches of Quasicontinuum formulations with dynamics of atoms and at finite temperature

An approach for the dynamic QC formulation at zero temperature to study the time evolution of QC systems is explained in [Rodney 2003] and [Shenoy 2003]. According to these publications dynamics can be considered by adding the kinetic energy of the atoms to the QC potential of Equation (4.11). This leads to the Hamiltonian H^{QC} of the QC system

$$H^{QC}(\mathbf{u}^h, \mathbf{p}^h) = \sum_{\alpha=1}^R n_{\alpha} E_{\alpha}(\mathbf{u}^h) + \sum_{\alpha=1}^R \frac{(n_{\alpha} \mathbf{p}_{\alpha})^2}{2 n_{\alpha} m} - \sum_{\alpha=1}^R n_{\alpha} \bar{\mathbf{f}}_{\alpha}^{ext} \cdot \mathbf{u}_{\alpha}, \quad (4.30)$$

where the momentum \mathbf{p}_{α} of a representative atom depends on its velocity \mathbf{v}_{α} multiplied with the atomic mass m

$$\mathbf{p}_{\alpha} = m \mathbf{v}_{\alpha}. \quad (4.31)$$

Using the formula

$$E_{tot}^{QC} = \sum_{\alpha=1}^R n_{\alpha} E_{\alpha}(\mathbf{u}^h)$$

from Equation (4.9) for the first part of Equation (4.30) results in the following equations of motion for the representative atom α derived from the Hamiltonian

$$\begin{aligned} \frac{\partial \mathbf{p}_{\alpha}}{\partial t} &= -\frac{1}{n_{\alpha}} \frac{\partial E_{tot}^{QC}}{\partial \mathbf{x}_{\alpha}} + \bar{\mathbf{f}}_{\alpha}^{ext}, \\ \frac{\partial \mathbf{x}_{\alpha}}{\partial t} &= \frac{\mathbf{p}_{\alpha}}{m}. \end{aligned} \quad (4.32)$$

The set of Equations (4.32) has to be integrated to obtain the approximate evolution of atoms in the QC system depending on time t . A comprehensive discussion on the integration of the equations of motion is included in [Shenoy 2003].

As highlighted in [Rodney 2003] the dynamic QC approach has the limitation of an unphysical wave reflection in case of a non-uniform mesh. That is, that the finite elements can transmit only waves of wavelength larger than their size while they reflect waves with smaller wavelength. This effect is investigated in detail in the Ph. D. thesis of Shenoy [Shenoy 1998]. A proposal of [Cai et al. 2000] can be found in the literature to minimize the wave reflections at boundaries between atomistic and surrounding linear regions (e.g. local QC). Therefore, a numerical boundary condition is derived for the simulation in atomistic regions, eliminating the infinite number of DOF of the surrounding linear domain, while preserving the correct dynamics in the atomistic domain. Even though the applicability of this algorithm was demonstrated in [Cai et al. 2000], it is computational expensive and therewith it is not suitable for large 3D simulations.

The above approach of a dynamic QC formulation is only applicable for zero temperature simulations, since in this case the displacement field is smooth enough for an interpolation within elements. By contrast, nonzero temperatures induce thermal fluctuations which cause large variations in the displacements of neighboring atoms.

An approach of Shenoy [Shenoy 1998] for the QC formulation at finite temperature is based on the local harmonic approximation [Lesar et al. 1989]. This theory allows for the consideration of thermal effects in a simplified formulation by an approximation of the energy in terms of average atomic coordinates. In this way, the total energy can be site-wise decomposed. That means that the appropriate energy can be separately calculated for every atom, because the vibrations of the solid are assumed as uncoupled vibrations of individual atoms.

For a body that is affected by forces, Shenoy starts with the thermodynamic function of the Gibbs free energy of an atomistic system, that is

$$G(\mathbf{u}) = \sum_{i=1}^N A_i(\mathbf{u}) - \sum_{i=1}^N \mathbf{f}_i^{ext} \mathbf{u}_i, \quad (4.33)$$

with $A_i(\mathbf{u})$ is the Helmholtz free energy of the i th atom. Application of the local harmonic approximation leads to the following expression for the Helmholtz free energy of atom i

$$A_i(\mathbf{u}) = E_i(\mathbf{u}) + k_B T \ln \left(\left[\frac{h}{2\pi\sqrt{m}k_B T} \right]^3 \sqrt{\det \Phi(i, i)} \right), \quad (4.34)$$

and the Gibbs free energy of the atomic system at finite temperature T can be written

$$G(\mathbf{u}) = E_{tot}(\mathbf{u}) + \sum_{i=1}^N k_B T \ln \left(\left[\frac{h}{2\pi\sqrt{m}k_B T} \right]^3 \sqrt{\det \Phi(i, i)} \right) - \sum_{i=1}^N \mathbf{f}_i^{ext} \mathbf{u}_i. \quad (4.35)$$

Parameter k_B is the Boltzmann constant, h denotes the Planck's constant, m stands for the mass of a single atom, and $\Phi(i, i)$ is the self force constant tensor of the i th atom. The self force constant tensor approximates the forces caused by fluctuations in the atomic position \mathbf{x}_i for each atom i separately, and is calculated from the total energy as follows

$$\Phi(i, i) = \frac{\partial^2 E_{tot}(\mathbf{u})}{\partial \mathbf{x}_i \partial \mathbf{x}_i}. \quad (4.36)$$

In case of the nonlocal QC formulation Equation (4.35) can be directly adopted for the free energy calculation of representative atoms. Thus, the nonlocal QC formulation at finite temperature according to [Shenoy 1998] reads

$$G_{nloc}^{QC}(\mathbf{u}^h, T) = \quad (4.37)$$

$$E_{tot}(\mathbf{u}^h) + \sum_{\alpha=1}^R n_{\alpha} k_B T \ln \left(\left[\frac{h}{2\pi\sqrt{m}k_B T} \right]^3 \sqrt{\det \Phi(\alpha, \alpha)} \right) - \sum_{\alpha=1}^R n_{\alpha} \bar{\mathbf{f}}_{\alpha}^{ext} \mathbf{u}_{\alpha}.$$

For the local formulation the temperature-based energy term can be calculated in a similar way but depending on an adapted calculation of the self force constant tensor. Based on the Cauchy-Born rule, that is assumed for the local QC formulation (Section 4.1.2), the self force constant tensor $\Phi(\mathbf{F}_e)$ is calculated for an atom embedded in an infinite perfect crystal which is subjected to a uniform deformation gradient \mathbf{F}_e . Consequently, the energy summation can be formulated over elements instead of representative atoms and the appropriate local QC formulation at finite temperature is

$$G_{loc}^{QC}(\mathbf{u}^h, T) = \tag{4.38}$$

$$E_{tot}(\mathbf{F}_e) + \sum_{e=1}^{N_{elem}} n_e k_B T \ln \left(\left[\frac{h}{2\pi\sqrt{m}k_B T} \right]^3 \sqrt{\det \Phi(\mathbf{F}_e)} \right) - \sum_{\alpha=1}^R n_\alpha \bar{\mathbf{f}}_\alpha^{ext} \mathbf{u}_\alpha.$$

Other local formulations of the QC Hamiltonian at finite temperature are published by [Shenoy et al. 1999a], [Dupuy et al. 2005], and [Tang et al. 2006]. While all these formulations are founded on the local harmonic approximation, the finally derived Hamiltonians vary in some details. Here, the local formulation of Equation (4.38) is presented to preserve consistency with the appropriate nonlocal formulation of Equation (4.37).

While the above QC formulations allow for qualitatively studies of the finite temperature behavior of solids [Shenoy et al. 1999a], they also adopt the limitations of the local harmonic approximation. That is the applicability of the local harmonic model only at low temperatures and the underestimation of the temperature dependency of defect free energies [Rodney 2003]. Rodney also discusses the problems in combining the proposed dynamic QC formulation with the formulation at finite temperature. As the most important limitation for the combination he points out, that in the dynamic approach the position and momentum of the representative atoms are macroscopic variables (averages) and thus Hamiltonian's equations of finite temperature QC, which apply to microscopic DOF, can not be applied to these variables.

An improvement in the approximation of finite temperature states using the QC method was published by [Kulkarni et al. 2008]. With the aim of applying the QC method for thermodynamic problems including non-equilibrium phenomena, for example heat conductivity, this publication presents a three-dimensional non-equilibrium finite temperature extension of the QC method based on the variational mean-field theory and the maximum-entropy (max-ent) formalism [Giasu et al. 1985] [Weiner 2002] instead of equilibrium statistical mechanics. For details in the numerical expressions of this improved finite temperature QC method the interested reader is referred to the comprehensive summary in [Kulkarni et al. 2008]. Proved by numerical validation tests Kulkarni et al. declared that compared to the quasi-harmonic approximation the max-ent approach leads to improvements in the prediction of thermodynamic quantities, like the thermal expansion coefficient.

4.2 Implementation of a robust and parallelized 3D nonlocal Quasicontinuum method

4.2.1 Motivation and requirements for the implementation

At the beginning of this research a sequential QC code for 2D applications was available on the QC website [Tadmor et al. 2010]. While this code was applicable for the qualitative investigation of special problems, for example nanoindentation in single crystals and analysis of particular GBs, it has shown less robustness in the general analysis of various GB configurations.

The presented multiscale concept includes the numerical simulation of the damage process for arbitrary geometrical GB configurations. Therefore, robust implementations of generalized algorithms were necessary. The realistic simulation of physical damage phenomena leading to intergranular fracture was aimed by taking into account the 3D nature of the atomic lattice. Consequently, the decision was made to implement an own 3D QC code, which is able to simulate GB damage in general, that means for arbitrary GB configurations. It was also possible to follow the intention of a speed-up by parallelized simulations with the new code. Finally, the implementation from scratch supported a deeper understanding of the QC method including starting points for improvements and changes in the numerical algorithms. Problems that showed up during the implementation of the fully 3D nonlocal QC method are discussed in detail in the following sections and the implemented numerical algorithms are presented.

The decision for the **QC method** was made to gradually reduce the number of atomic DOF in zones which are not directly affected by the GB damage. The restriction to the **nonlocal** formulation ensures the overall reproduction of the constitutive behavior based on the physics of atomic interactions. For the numerical investigation of brittle damage phenomena a **quasistatic** method is sufficient, since the time dependency of brittle damage is negligible. Moreover, the extension of the quasistatic formulation to include effects of dynamics and finite temperature was regarded as not useful, since this extension comes along with enormous problems in finding stable energy minima and associated atomic configurations in equilibrium (see Section 4.2.6). As stated before, also the **3D** nature of the atomic lattice was necessarily aimed to be considered, and a **generalized** method was required for damage simulations on arbitrary GB configurations. For this summarized reasons the **generalized quasistatic 3D nonlocal QC formulation** from Section 4.1.3 was implemented with necessary adaptations to apply for the research concerning numerical investigations of brittle intergranular damage phenomena on the microscale.

The computational speed-up of the chosen QC method compared to pure atomistic methods enables the realization of a higher number of simulations with different GB configurations. This is necessarily needed for a derivation of cohesive parameters describing

the GB decohesion on the mesoscale depending on geometrical characteristics of the GBs. For further speed-up the application of state of the art computational technologies was intended, that is the effective use of servers with multi-core processors by a parallelized QC code (Section 4.2.7).

Since the QC method uses shape functions of finite elements for the coupling of atomic DOF to representative ones, a robust meshing procedure has to follow on the geometrical generation of GB configurations. Accordingly, the problem has to be solved to find suitable meshes without highly distorted elements for the usually non-convex hull of GB geometries as well as in the highly disordered zone of adjacent crystallites (Section 4.2.2).

Another important requirement on the implementation relates to the iterative search of equilibrium configurations, that is done by energy minimization in the presented thesis. The large number of variables (atomic DOF) in the energy function and numerous local minima come along with serious convergence problems for standard optimization procedures. A suitable optimization method was needed to ensure stable convergence (Section 4.2.6). As the iterative search for equilibrium configurations requires the computation of atomic energies as well as atomic forces these quantities have to be defined physically reasonable. In the presented dissertation EAM potentials are used for the reproduction of atomic energies in metals. Nevertheless, the derivation of atomic forces from EAM potentials is a non-trivial problem leading to different mathematical expressions in the literature, what is discussed in detail in Section 4.2.5.

The aimed derivation of atomistic-based traction separation laws requires the computation of continuum properties from QC simulations. Exemplary, the computation of averaged stresses is described in Section 4.2.8. Meaningful parameters are useful to detect defects, which nucleate and propagate in the deformed atomistic structure. For this purpose the geometrical centrosymmetry parameter is well suited. Its calculation is explained in Section 4.2.9.

A first validation of the implemented nonlocal QC formulation is documented in Section 4.3.1 for a nanoindentation problem in FCC aluminum. The results of the QC simulation are qualitatively and quantitatively compared to the outcomes of an appropriate lattice statics simulation and to numerical results from literature.

As mentioned before, the applicability of the QC code to arbitrary GB geometries is a strong requirement, since the investigation is aimed on the evaluation of the constitutive behavior of GBs with respect to their geometrical characterizations. This implies, the implementation must show robustness against geometrical variations in the model. In this context, a main problem that is addressed in the simulations is to find configurations with low energy GBs before loading is applied. An appropriate strategy for the generation of suitable geometrical GB representations is explained in Section 4.3.2 and a validation to GB energy calculations of other researchers is done. Additionally, the obtained GB energies are compared to experimental data.

4.2.2 Definition of representative atoms and generation of the FE mesh

The generation of a suitable FE mesh with nodes at sites of representative atoms is a complex problem since the model domain is not explicitly defined by a continuous boundary but by discrete points, namely the atomic sites. First of all, those atomic sites have to be found which are vertices of the smallest hull around all atoms in the system. In the present implementation single crystallites are modeled by the definition of cuboidal solids which contain the atomic lattice. The combination of these cuboidal shaped crystallites yields GB models. As a consequence of the cuboidal shape, the smallest hull around the atoms of a single crystallite is convex, which is convenient for the meshing process. Nevertheless, the smallest hull around a GB model consisting of two different oriented crystallites is frequently non-convex. This problem is illustrated in the example of Figure 4.10 and results from the different orientation of adjacent crystallites and the displacement shift between them. An algorithm is implemented to reasonably define representative atoms and to generate suitable meshes in a non-convex meshing domain of GB models.

The algorithm starts with the determination of the 3D convex hull for each crystallite separately. The free available Qhull library [Barber et al. 1996] is used to find those sites from the set of atomic sites of a crystallite, which define the vertices of the convex hull. The corresponding atoms are declared as representative atoms. Exemplary, Figure 4.10a illustrates a GB configuration of two adjacent crystallites after the first step of representative atom definition. In the second step, further representative atoms are declared within each crystallite domain. This process follows a predefined resolution to reach the full atomistic limit in the GB zone and a coarsen resolution with increasing distance to the GB. The final definition of representative atoms in the model domain is shown in Figure 4.10b.

Following the definition of representative atoms, the corresponding positions are used as generation points for a Delaunay triangulation. The triangulation is realized for the total set of representative atoms, that means for all crystallites of the model. This is necessary to generate a mesh with elements passing the GB and connecting the crystallites for the following numerical simulation. Application of the Delaunay algorithm of the Qhull library leads to a convex mesh of tetrahedron elements in 3D. Figure 4.10c illustrates the 2D counterpart with Delaunay triangles. Therein, the problem of convex meshes for non-convex geometries is clearly visible. Highly distorted elements are generated at the non-convex boundaries because of the convex nature of the Delaunay triangulation. These elements are unnecessary since they do not include any constrained atom. This insight leads to the final step of removing the distorted and unnecessary elements. Therefore, the centroid of each element is calculated. If the element centroid is not located within the convex hull of one of the crystallites, the element can be removed, except that the element is passing the GB. The accurate implementation of the overall meshing algorithm results

in well-proportioned meshes of the frequently non-convex GB geometries as exemplary shown in Figure 4.10d.

The implemented meshing algorithm allows for the generation and application of general QC models consisting of one or more arbitrary oriented cuboidal shaped crystal-

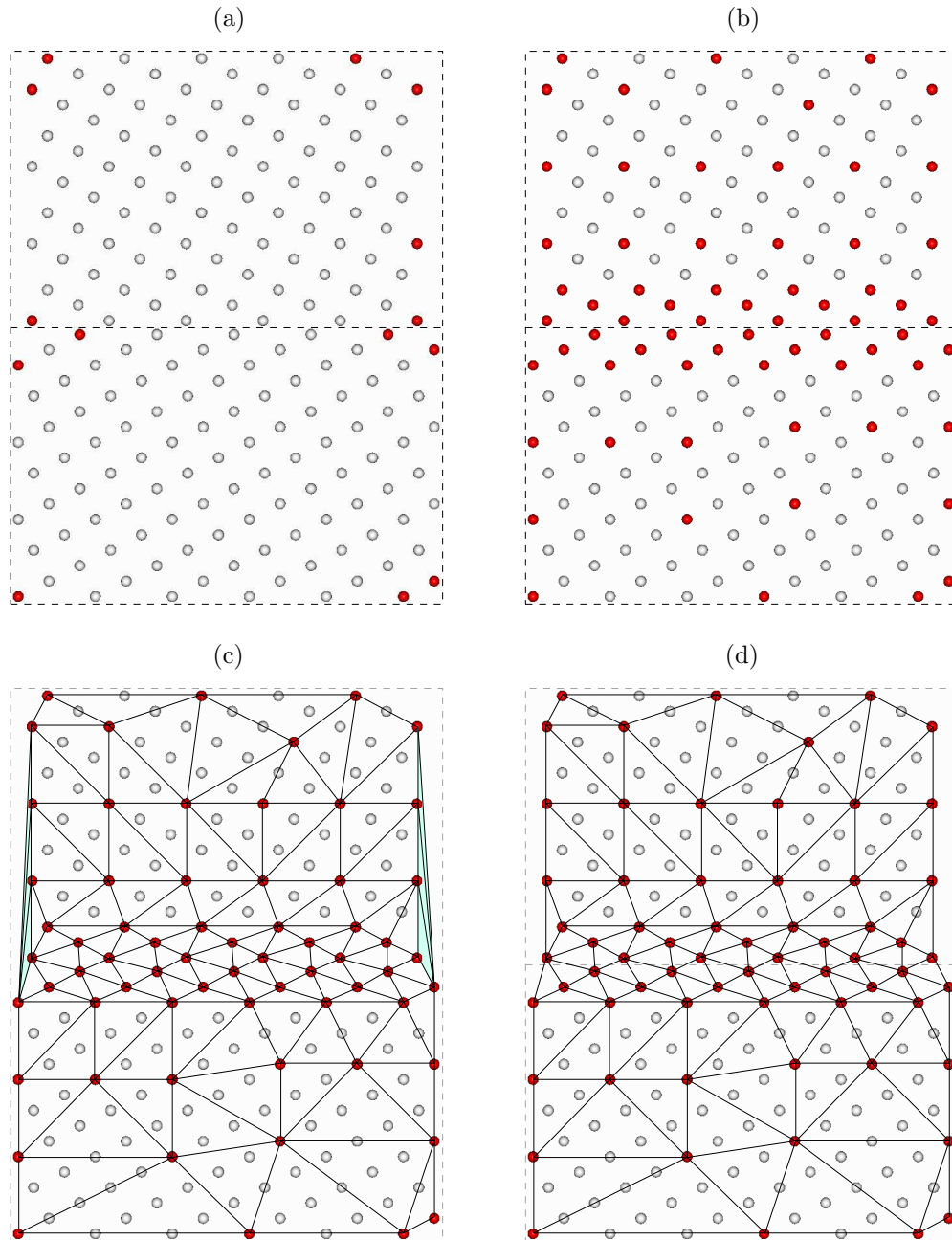


Figure 4.10: Definition of representative atoms (red) from the atomic lattice of a GB model and subsequent mesh generation. Dashed lines surround the adjacent crystallites with different orientation. (a) Vertices of the convex hull of each crystallite define sites of representative atoms. (b) Additional representative atoms are defined by the aimed resolution. (c) Delaunay triangulation with the total set of representative atoms as generation points. Distorted elements (light blue) at non-convex geometrical boundaries can be removed. (d) Final non-convex mesh.

lites. This is advantageously compared to other 3D QC models presented in the literature [Knap et al. 2001] [Eidel et al. 2009], which are restricted to single crystallite representations with special orientation to generate the mesh based on octahedrons. Moreover, meshes of polycrystal models which were applied in the context of the 2D QC formulation, for example in [Tadmor 1996], have a completely convex hull. As explained before and illustrated in Figure 4.10c the limitation to an always convex hull comes along with the problem of unnecessary and highly distorted elements at some boundaries of these polycrystalline QC models resulting in unnecessary numerical errors.

4.2.3 Computation of neighborlists

The QC method requires the computation of atomic energies as well as atomic forces, which both consist of terms that describe the various interactions between atoms in the system. Usually, these terms are functions of the interatomic distance. Section 2.2.1 gives an overview on approximative functions describing interatomic potentials. The potential function values decrease fast with an increasing distance between atoms. Consequently, a cutoff distance r_c is introduced as the upper distance limit for relevant atomic interactions. According to Section 4.1.3 the present formulation of the nonlocal QC method requires the computation of atomic energies and forces for all cluster atoms. This computation takes into account all atoms which are located within the cutoff distance r_c from a cluster atom. Neighborlists are build which store the relevant atomic neighbors of each cluster atom. By reasons of efficiency, a pair of neighboring atoms is stored only once.

The simplest way of finding the relevant neighbors of a cluster atom k is to run through the complete model domain and to compare the distance r_{ki} for each atomic pair k, i with the cutoff distance r_c . This method is less efficient and very time consuming since the number of atomic pairs increases quadratically with the number of atoms in the system. This is valid for the QC method as well as for pure atomistic methods. The efficiency of neighborlist computations is gained by a reasonable partitioning of the geometrical domain to localize possible relevant atomic neighbors. Although complex nearest neighbor calculations are proposed in the literature, for example by [Mattson et al. 1999], a conventional partitioning-based neighbor search was found to be sufficient. Therefore, the geometrical domain of the system is decomposed into a regular grid of sub-domains Ω_n . While a small sub-domain size usually gains higher efficiency in the neighbor search, the grid spacing should be chosen large enough to ensure that relevant atomic neighbors are within neighboring sub-domains. Based on the grid of sub-domains the search of relevant atomic neighbors of a cluster atom is in a first step limited to the atoms of the sub-domain which includes the cluster atom itself. In a second step the search is extended to the atoms of adjacent sub-domains, but only if the closest distance of the cluster atom to the adjacent sub-domain is lower than the relevant neighbor distance $R(r_c)$ of atomic pairs. This procedure, which is illustrated in Figure 4.11, significantly reduces the number

of necessary calculations for the neighborlist computation.

Exemplary, the effort for the neighborlist computation is measured by the number of neighbor checks and by the computational time for the simple algorithm as well as for the sub-domain based method. For this study a nonlocal QC model for the 3D simulation of nanoindentation in an aluminum cube is considered. The investigated configuration of the model consists of about 10^6 atoms, including 10^5 cluster atoms. As explained in the following paragraphs the relevant distance for the neighbor check was chosen as $R = 2r_c$, with $r_c = 5.558 \text{ \AA}$ for aluminum. Hence, a total number of approximately $20 \cdot 10^6$ relevant neighbors have to be stored. Using the simple algorithm comes along with about $98,000 \cdot 10^6$ neighbor checks, that are nearly 4,900 checks per relevant neighbor relation. By contrast, application of the sub-domain based neighbor search leads to only $96 \cdot 10^6$ total neighbor checks, and in average 4.8 checks per relevant atomic pair, respectively. Thus, in the example the total number of neighbor checks is reduced by factor 1,000. Also the reduction in computational time is significantly high. While on a standard workstation (Intel CPU X5472, 3.0 GHz) the simple algorithm runs about 6,800 seconds, the advanced method needs only 2.8 seconds for the neighborlist computation.

Theoretically, the neighborlists have to be updated each time before atomic energies and forces are calculated, that is once per iteration step. By doing so, only the atomic neighbors, which are located in the cutoff distance around the cluster atoms need to be stored. This minimizes the demand for memory, but maximizes the total time spent for neighborlist updates. However, there is a problem if the neighborlists change during an iteration. An atom which is located nearly exact in the cutoff distance from a cluster atom can cause convergence problems, since the system tends to switch between a configuration in which this atom lies within the cutoff distance and a configuration in which this atom is

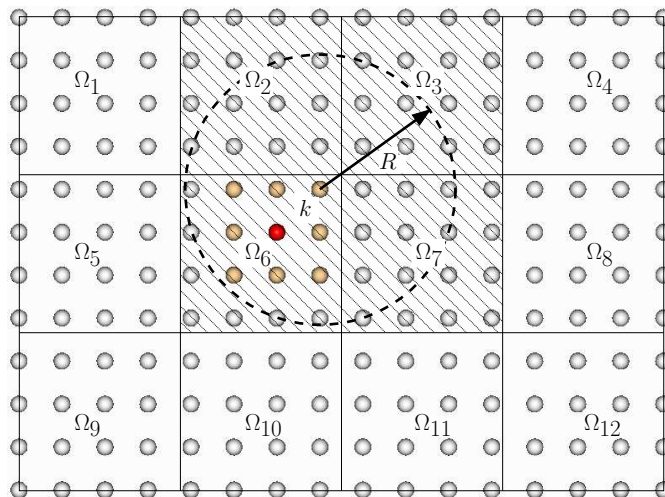


Figure 4.11: Neighbor calculation by domain partitioning: The search of relevant neighbors of cluster atom k is reduced to atoms of its own sub-domain Ω_6 and the adjacent sub-domains $\Omega_2, \Omega_3, \Omega_7$, which partially overlay with the relevant neighbor region (defined by radius R) of atom k .

outside the cutoff distance. The reason is that the contribution to atomic forces rises fast, when the distance between two atoms becomes lower than the cutoff distance. Consequently, jumps higher than the tolerance value can occur in the atomic forces, if an atom moves within the cutoff sphere of a cluster atom. Being aware of this problem, the present implementation keeps the neighborlists constant during the iteration of a load step. The cutoff distance is slightly increased to ensure that finally all interactions between atoms within the initial cutoff sphere are considered. In the present implementation an increase of ten per cent is applied to the user defined cutoff distance.

In principle the neighborlists can be build completely once per load step. However, the most load steps cause small deformations leading to only a few changes in the neighborlists. Based on this experience, a major neighborlist is build at the beginning of the simulation storing all atoms within $R = 2r_c$ around a cluster atom. At the beginning of a load step, a minor neighborlist is build from the data of the major list taking into account all atoms within $1.1r_c$ according to the above motivated increase of the initial cutoff distance by ten per cent. As a result, only a few neighbor checks are necessary per load step. The major neighborlist is only updated if the displacement of a representative atom is greater than $0.45r_c$. This ensures that a pair of atoms with a distance of $2r_c$ at time of the major neighborlist update will be considered for the minor neighborlist if the two atoms shorten their distance both about $0.45r_c$ during the deformation process. The introduction of a major and a minor neighborlist reduces in total the computational time but increases the allocated memory at the same time. Finally, the decision for or against a pre-build greater neighborlist as well as the decision about the frequency of neighborlist updates depends on the available computer capacities and the requirements on the speed of the simulation.

4.2.4 Weighting factor calculation

The Quasicontinuum method implies the calculation of weighting factors n_α applied to energies and forces of representative atoms. These factors n_α can be interpreted as the number of atoms, which are represented by atom α , including itself. Therefrom, the requirement follows, that the sum over all n_α has to equal the total number of atoms in the system (Equation (4.10)). Thinking about the basic idea of the QC method, that is to couple the atomic lattice at sites of representative atoms with an underlying FE mesh, the constraint DOF of atoms within the finite elements are interpolated by the associated FE interpolation functions from the appropriate values of representative atoms. This means that atomic DOF are not only coupled to the displacement field of exactly one representative atom. They are constraint to the displacements of all representative atoms of the associated element. Consequently, in the general case a representative atom α represents a slaved atom i only partially according to the functional value of the interpolation function N_α at the reference position \mathbf{X}_i of atom i . This means that for consistency also

the weighting factors n_α are calculated in the present implementation from the associated interpolation functions N_α evaluated at the positions of slaved atoms i according to Equation (4.21), that is

$$n_\alpha = \sum_{i=1}^N N_\alpha(\mathbf{X}_i).$$

The sum over all n_α equals the number of atoms in the system and the requirement of Equation (4.10) is fulfilled.

Since the present implementation of the nonlocal QC formulation uses the cluster summation rule according to Section 4.1.3, cluster weights have to be found additionally. As pointed out in [Knap et al. 2001] and [Eidel et al. 2009], the calculation of cluster weights requires that the sum over all interpolation function values in the system has to remain exact, also in case of cluster summation. Furthermore, it is required by energy consistency that the total energy of the nonlocal QC system should exactly match the sum over all atomic energies, if the set of all atoms $\{i\}$ equals the set of cluster atoms $\{k\}$ but not necessarily equals the set of representative atoms $\{\alpha\}$

$$E_{tot}^{QC} = \sum_{k=1}^C E_k(\mathbf{u}^h), \quad \text{if } \{i\} = \{k\}. \quad (4.39)$$

This requirement is based on the fact, that the atomic energies of cluster atoms are explicitly calculated, and should be preserved by the summation rule. In the implementation the energy summation follows Equation (4.24), that reduces for the total energy calculation to

$$E_{tot}^{QC} = \sum_{\alpha=1}^R \frac{n_\alpha}{n_\alpha^c} \sum_{k=1}^C N_\alpha(\mathbf{X}_k) E_k(\mathbf{u}^h) \quad (4.40)$$

and the cluster related weighting divisors n_α^c are obtained by Equation (4.23), that is

$$n_\alpha^c = \sum_{k=1}^C N_\alpha(\mathbf{X}_k).$$

The summation rule does not affect the total sum over interpolation function values. Also, it can be shown that the required energy consistency is preserved. Assuming, that all atoms are cluster atoms, for which the atomic energies are explicitly calculated, Equation (4.21) can be rewritten

$$n_\alpha = \sum_{k=1}^C N_\alpha(\mathbf{X}_k), \quad \text{if } \{i\} = \{k\} \quad (4.41)$$

and match exactly the calculation of n_α^c . The weighting factor $\frac{n_\alpha}{n_\alpha^c}$ disappears from Equation (4.40), which simplifies to

$$E_{tot}^{QC} = \sum_{\alpha=1}^R \sum_{k=1}^C N_\alpha(\mathbf{X}_k) E_k(\mathbf{u}^h), \quad \text{if } \{i\} = \{k\}. \quad (4.42)$$

Reordering the summations leads to

$$E_{tot}^{QC} = \sum_{k=1}^C \left(\sum_{\alpha=1}^R N_{\alpha}(\mathbf{X}_k) \right) E_k(\mathbf{u}^h), \quad \text{if } \{i\} = \{k\}. \quad (4.43)$$

Taking into account that the sum over interpolation function values at any position of the model equals 1 results in

$$\sum_{\alpha=1}^R N_{\alpha}(\mathbf{X}_k) = 1 \quad (4.44)$$

and

$$E_{tot}^{QC} = \sum_{k=1}^C E_k(\mathbf{u}^h), \quad \text{if } \{i\} = \{k\}.$$

This exactly describes the requirement of Equation (4.39).

Calculating the total energy of a nonlocal QC system according to Equation (4.25) also preserves the energy of cluster atoms in the special case that all atoms are cluster atoms. Then the general formula of the total energy

$$E_{tot}^{QC} = \sum_{\alpha=1}^R \frac{n_{\alpha}}{n_{\alpha}^c} \sum_{k=1}^{C_{\alpha}} E_k(\mathbf{u}^h) \quad (4.45)$$

reduces by $n_{\alpha} = n_{\alpha}^c$ to

$$E_{tot}^{QC} = \sum_{\alpha=1}^R \sum_{k=1}^{C_{\alpha}} E_k(\mathbf{u}^h), \quad \text{if } \{i\} = \{k\}. \quad (4.46)$$

Since a cluster atom is assigned to exactly one representative atom, the outer and inner summation rules can be summarized to a summation over all cluster atoms in the system, which again leads to Equation (4.39).

From the above formulations the conclusion can be drawn, that energy consistency is only fulfilled, when the calculation of n_{α}^c follows the same approach as the calculation of n_{α} . By contrast, a division of the cluster energy sum by the number of cluster atoms which are assigned to a representative atom does not lead to a consistent representative atom energy E_{α} , as long as n_{α} is calculated from interpolation function values.

Since both, n_{α} and n_{α}^c , depend on the reference position of atoms, the weighting factors

$$w_{\alpha} = \frac{n_{\alpha}}{n_{\alpha}^c} \quad (4.47)$$

for the representative atoms and their associated clusters can be computed once at the beginning of the simulation and remain constant until the mesh changes or the assignment of cluster atoms is updated. This means that the reference positions of all atoms are stored at the time of last meshing to ensure that all reference positions are within the FE mesh and the associated element, respectively.

4.2.5 Energy and force calculation from EAM potentials

The present implementation of the nonlocal QC method makes use of the EAM (Equation (2.69)) to describe atomic energies in metal materials. The application of EAM potentials to the nonlocal QC formulation of Equation (4.24) leads to the following formula for the appropriate energy calculation

$$\Pi^{QC}(\mathbf{u}^h) = \sum_{\alpha=1}^R \frac{n_{\alpha}}{n_{\alpha}^c} \sum_{k=1}^C N_{\alpha}(\mathbf{X}_k) \left[\left(U_k(\rho_k) + \frac{1}{2} \sum_{\substack{i=1 \\ i \neq k}}^N \phi_{ki}(r_{ki}) \right) - \mathbf{f}_k^{ext} \mathbf{u}_k^h \right], \quad (4.48)$$

with the electron density is calculated according to Equation (2.70)

$$\rho_k = \sum_{\substack{i=1 \\ i \neq k}}^N \rho_{ki}(r_{ki}). \quad (4.49)$$

Since, by contrast to i , k is not a counter over all atoms in the system, the expression $i \neq k$ means that atom k is skipped in the set of atoms i .

While Equation (4.24) yields a higher accuracy in the energy calculation, the decision was made to derive the nodal forces from the simpler expression of Equation (4.25), that is for EAM potentials

$$\Pi^{QC}(\mathbf{u}^h) = \sum_{\alpha=1}^R \frac{n_{\alpha}}{n_{\alpha}^c} \sum_{k=1}^{C_{\alpha}} \left[\left(U_k(\rho_k) + \frac{1}{2} \sum_{\substack{i=1 \\ i \neq k}}^N \phi_{ki}(r_{ki}) \right) - \mathbf{f}_k^{ext} \mathbf{u}_k^h \right]. \quad (4.50)$$

Therewith, the high effort of force computation reduces slightly compared to a derivation of forces from Equation (4.48), while no significant worsening was noticed concerning the convergence or the quality of results. The nodal force vector with components acting at sites of representative atoms is obtained from the gradient of the above potential

$$\begin{aligned} -\mathbf{f}_{\mathbf{a}} &= \frac{\partial \Pi^{QC}(\mathbf{u}^h)}{\partial \mathbf{u}_{\mathbf{a}}} \\ &= \sum_{\alpha=1}^R \frac{n_{\alpha}}{n_{\alpha}^c} \sum_{k=1}^{C_{\alpha}} \left[\left(\frac{\partial U_k(\rho_k)}{\partial \rho_k} \frac{\partial \rho_k}{\partial r_{ki}} + \frac{1}{2} \sum_{\substack{i=1 \\ i \neq k}}^N \frac{\partial \phi_{ki}(r_{ki})}{\partial r_{ki}} \right) \frac{\partial r_{ki}}{\partial \mathbf{r}_{ki}} \frac{\partial \mathbf{r}_{ki}}{\partial \mathbf{u}_{\mathbf{a}}} - \mathbf{f}_k^{ext} \frac{\partial \mathbf{u}_k}{\partial \mathbf{u}_{\mathbf{a}}} \right]. \end{aligned} \quad (4.51)$$

With the following abbreviations for the partial derivatives

$$\frac{\partial U_k(\rho_k)}{\partial \rho_k} = U'_k \quad (4.52)$$

$$\frac{\partial \rho_k}{\partial r_{ki}} = \sum_{\substack{i=1 \\ i \neq k}}^N \frac{\partial \rho_{ki}(r_{ki})}{\partial r_{ki}} = \sum_{\substack{i=1 \\ i \neq k}}^N \rho'_{ki} \quad (4.53)$$

$$\frac{\partial \phi_{ki}(r_{ki})}{\partial r_{ki}} = \partial \phi'_{ki} \quad (4.54)$$

$$\frac{\partial r_{ki}}{\partial \mathbf{r}_{ki}} = \frac{\mathbf{r}_{ki}}{r_{ki}} \quad (4.55)$$

$$\frac{\partial \mathbf{r}_{ki}}{\partial \mathbf{u}_a} = N_{\mathbf{a}}(\mathbf{X}_k) - N_{\mathbf{a}}(\mathbf{X}_i), \quad \text{where } \mathbf{r}_{ki} = (\mathbf{X}_k + \mathbf{u}_k) - (\mathbf{X}_i + \mathbf{u}_i) \quad (4.56)$$

$$\frac{\partial \mathbf{u}_k}{\partial \mathbf{u}_a} = N_{\mathbf{a}}(\mathbf{X}_k), \quad \text{where } \mathbf{u}_k = \sum_{\mathbf{a}=1}^R \mathbf{u}_a N_{\mathbf{a}}(\mathbf{X}_k) \quad (4.57)$$

Equation (4.51) reads

$$-\mathbf{f}_{\mathbf{a}} = \sum_{\alpha=1}^R \frac{n_{\alpha}}{n_{\alpha}^c} \sum_{k=1}^{C_{\alpha}} \left[\sum_{\substack{i=1 \\ i \neq k}}^N \left\{ \left[U'_k \rho'_{ki} + \frac{1}{2} \phi'_{ki} \right] \frac{\mathbf{r}_{ki}}{r_{ki}} [N_{\mathbf{a}}(\mathbf{X}_k) - N_{\mathbf{a}}(\mathbf{X}_i)] \right\} - \mathbf{f}_k^{ext} N_{\mathbf{a}}(\mathbf{X}_k) \right]. \quad (4.58)$$

The calculation of nodal forces follows a consistent derivation from cluster energies as proposed by [Eidel et al. 2009] in the framework of a fully-nonlocal QC method with an energy-based cluster scheme (QC-eFNL). It is important to note that this implemented formulation leads to physically consistent interaction forces between cluster atoms, and Newton's third law is full-filled by the condition

$$\mathbf{f}_{ki} = -\mathbf{f}_{ik}, \quad \text{if } \{i\} = \{k\}. \quad (4.59)$$

To show in detail that this condition is preserved for interactions between cluster atoms k and i , the contribution to nodal force $\mathbf{f}_{\mathbf{a}}$ which has origins in the interaction force caused by the energy of cluster atom k according to Equation (4.58) is obtained by

$$\mathbf{f}_{\mathbf{a}}^{k \rightarrow i} = \frac{n_{\alpha}}{n_{\alpha}^c} \left[U'_k \rho'_{ki} + \frac{1}{2} \phi'_{ki} \right] \frac{\mathbf{r}_{ki}}{r_{ki}} [N_{\mathbf{a}}(\mathbf{X}_k) - N_{\mathbf{a}}(\mathbf{X}_i)], \quad (4.60)$$

and the associated contribution to nodal force $\mathbf{f}_{\mathbf{a}}$ that comes from the interaction force caused by the energy of cluster atom i reads

$$\mathbf{f}_{\mathbf{a}}^{i \rightarrow k} = \frac{n_{\alpha}}{n_{\alpha}^c} \left[U'_i \rho'_{ki} + \frac{1}{2} \phi'_{ki} \right] \frac{-\mathbf{r}_{ki}}{r_{ki}} [N_{\mathbf{a}}(\mathbf{X}_i) - N_{\mathbf{a}}(\mathbf{X}_k)]. \quad (4.61)$$

Summarizing, the full contribution of interaction between two cluster atoms to the nodal force vector $\mathbf{f}_{\mathbf{a}}$ is

$$\begin{aligned}\mathbf{f}_a^{ki} &= \mathbf{f}_a^{k \rightarrow i} + \mathbf{f}_a^{i \rightarrow k} \\ &= \frac{n_\alpha}{n_\alpha^c} [(U'_k + U'_i) \rho'_{ki} + \phi'_{ki}] \frac{\mathbf{r}_{ki}}{r_{ki}} [N_{\mathbf{a}}(\mathbf{X}_k) - N_{\mathbf{a}}(\mathbf{X}_i)], \quad \text{if } \{i\} = \{k\}.\end{aligned}\quad (4.62)$$

The interaction force is

$$\mathbf{f}_{ki} = [(U'_k + U'_i) \rho'_{ki} + \phi'_{ki}] \frac{\mathbf{r}_{ki}}{r_{ki}}, \quad (4.63)$$

which obviously fulfills the condition of Equation (4.59). This statement is very important for the implementation, since it clarifies that the interaction force \mathbf{f}_{ki} can be calculated one time according to Equation (4.63) and then has to be distributed by the associated interpolation function values to the nodes of the elements of atom k and atom i . In case of full atomistic resolution Equation (4.62) exactly reduces to the formulation of lattice statics, since

$$\frac{n_\alpha}{n_\alpha^c} = 1, \quad \text{and } N_{\mathbf{a}}(\mathbf{X}_k) = 1, \quad \text{and } N_{\mathbf{a}}(\mathbf{X}_i) = 0, \quad \text{if } \{i\} = \{k\} = \{\alpha\}. \quad (4.64)$$

Attention has to be payed to the case that atom i is not a cluster atom. Then Equation (4.58) yields only the nodal force contribution of Equation (4.60) caused by the interaction between cluster atom k and non-cluster atom i . The contribution of Equation (4.61) is missing. This means that only a reduced part of the interaction force between a cluster atom and a non-cluster atom is considered by the interpolation function values $N_{\mathbf{a}}(\mathbf{X}_k)$ of the cluster atom. The same part is considered also by the interpolation function values $N_{\mathbf{a}}(\mathbf{X}_i)$ of the non-cluster atom, although non-cluster atoms are not explicitly taken into account in the cluster weighting factor $1/n_\alpha^c$. Thus, there is a small mismatch between the weighting factor calculation and the force calculation. While this mismatch is negligible, the calculation of adapted weighting factors would be associated with a significantly higher computational effort. Consequently, the small mismatch is accepted in the implementation.

By contrast to the nonlocal QC formulation with an energy-based cluster scheme, an appropriate formulation with a force-based cluster scheme was proposed by [Knap et al. 2001]. In this proposal, the force equilibrium is build taking into account all forces acting on cluster atoms and distributing these forces to nodes by the associated interpolation function values similar to the energies in Figure 4.7. The appropriate nodal forces derived from EAM potentials are

$$-\mathbf{f}_a = \sum_{\alpha=1}^R \frac{n_\alpha}{n_\alpha^c} \sum_{k=1}^{C_\alpha} \left[\sum_{\substack{i=1 \\ i \neq k}}^N \left\{ [(U'_k + U'_i) \rho'_{ki} + \phi'_{ki}] \frac{\mathbf{r}_{ki}}{r_{ki}} N_{\mathbf{a}}(\mathbf{X}_k) \right\} - \mathbf{f}_k^{ext} N_{\mathbf{a}}(\mathbf{X}_k) \right]. \quad (4.65)$$

This means in case of an interaction between a cluster and a non-cluster atom that the total interaction force is considered at the site of the cluster atom, and no interaction force

is considered at the site of the non-cluster atom. A main disadvantage of the formulation of [Knap et al. 2001] applied to EAM potentials is the additional computation of electron densities at sites of non-cluster atoms, as also pointed out in [Eidel et al. 2009]. This becomes more clear, if by contrast to Equation (4.60) the interaction force contribution of cluster atom k to the nodal forces is written according to the force-based cluster scheme

$$\mathbf{f}_{\mathbf{a}}^{k \rightarrow i} = \frac{n_{\alpha}}{n_{\alpha}^c} [(U'_k + U'_i) \rho'_{ki} + \phi'_{ki}] \frac{\mathbf{r}_{ki}}{r_{ki}} N_{\mathbf{a}}(\mathbf{X}_k) . \quad (4.66)$$

The term U'_i depends on the electron density at site of atom i , also when i is a non-cluster atom. Consequently, the atomic interactions of non-cluster atoms, which are within a cutoff radius r_c around cluster atoms, have to be taken into account for the appropriate electron density calculation. Especially in 3D, this considerably increases the neighbor relations that have to be stored as well as the computational effort of the force calculation, which strongly depends on the evaluated atomic interactions. Figure 4.12 illustrates that in case of force computation not only the atoms within a cutoff radius around the cluster atoms have to be taken into account but also all atoms within a cutoff radius around these first order neighbors.

A further disadvantage of the QC formulation with force-based cluster scheme is the missing symmetry in the system matrix, which can be derived from the nodal forces and reads in the shortened form

$$\mathbf{k}_{\mathbf{ab}} = -\frac{\partial \mathbf{f}_{\mathbf{a}}}{\partial \mathbf{u}_{\mathbf{b}}} = \sum_{\alpha=1}^R \frac{n_{\alpha}}{n_{\alpha}^c} \sum_{k=1}^{C_{\alpha}} \sum_{\substack{i=1 \\ i \neq k}}^N \left\{ 2 \frac{\partial^2 E_k}{(\partial \mathbf{r}_{kl})^2} N_{\mathbf{a}}(\mathbf{X}_k) [N_{\mathbf{b}}(\mathbf{X}_k) - N_{\mathbf{b}}(\mathbf{X}_i)] \right\} . \quad (4.67)$$

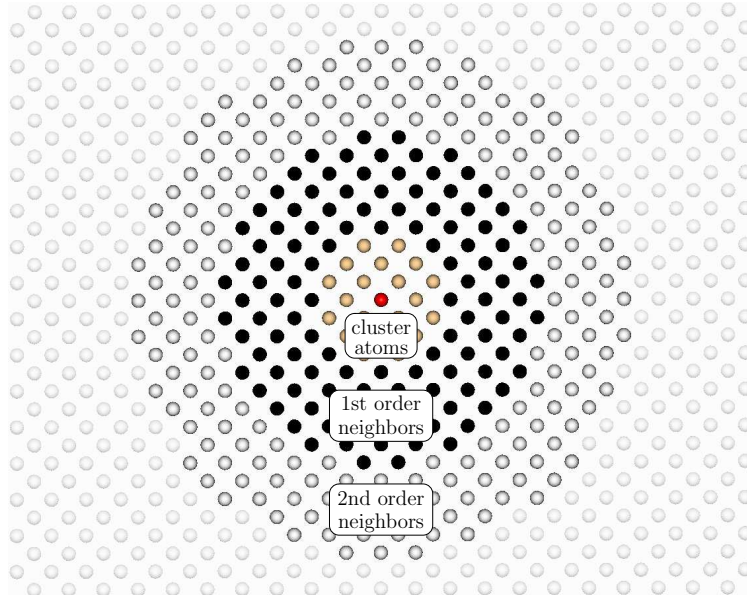


Figure 4.12: The nonlocal QC formulation of [Knap et al. 2001] with force-based cluster scheme implies for cluster atoms (yellow) the calculation of interaction forces also based on the electron density at sites of 1st order neighbors (black). To calculate electron densities at sites of 1st order neighbors, the 2nd order neighbors (grey) have to be considered additionally in the force calculation.

The problem of an unsymmetric system matrix and corresponding nonconservative forces is discussed in [Eidel et al. 2009]. By contrast, the application of the energy-based cluster scheme results in a symmetric system matrix, that is in the shortened form

$$\begin{aligned} \mathbf{k}_{\mathbf{ab}} &= \frac{\partial^2 \Pi^{QC}(\mathbf{u}^h)}{\partial \mathbf{u}_{\mathbf{a}} \partial \mathbf{u}_{\mathbf{b}}} \\ &= \sum_{\alpha=1}^R \frac{n_{\alpha}}{n_{\alpha}^c} \sum_{k=1}^{C_{\alpha}} \sum_{\substack{i=1 \\ i \neq k}}^N \left\{ \frac{\partial^2 E_k}{(\partial \mathbf{r}_{kl})^2} [N_{\mathbf{a}}(\mathbf{X}_k) - N_{\mathbf{a}}(\mathbf{X}_i)] [N_{\mathbf{b}}(\mathbf{X}_k) - N_{\mathbf{b}}(\mathbf{X}_i)] \right\}. \end{aligned} \quad (4.68)$$

The appropriate long formula of the system matrix derived from EAM potentials is given in Appendix A, which contains a summary of the implemented 3D nonlocal QC formulation.

During the implementation of the nonlocal QC method both cluster schemes were tested, the force-based as well as the energy-based. Since the force-based scheme has shown no relevant improvement of the convergency or the quality of results, it comes along with higher computational effort. Additionally, the necessary memory for saving neighbor relations was strongly increased. Also a mixed version, that approximated interaction forces between cluster and non-cluster atoms only based on the electron density at site of the cluster atom, was implemented. In contrast to the energy-based cluster scheme, this version has multiplied the full approximated interaction forces with interpolation function values at the site of the cluster atom, and the site of the non-cluster atom was not taken into account. In this version the high computational costs of the force-based cluster scheme could be reduced again, but finally the implementation of the equally efficient energy-based cluster scheme has shown the best performance. Consequently, the implementation with the force calculation according to Equation (4.58) was applied in the presented simulations.

4.2.6 Optimization method

The search for stable equilibrium states of deformed structures is a main task in computational mechanics. In case of atomic structures the search for an equilibrium configuration means to find the nearest configuration with minimal potential energy, which comes along with an equilibrium in atomic forces. Such equilibrium states are typically found by optimization methods, like steepest descent, conjugate gradient, or Newton's method, for which comprehensive introductions are given in [Kelley 1999].

Early works on the QC method, for example [Tadmor 1996], describe the application of Newton's method with line-search and backtracking according to [Dennis et al. 1983] to find equilibrium configurations of the QC system. These algorithms are also tested in the present 3D QC implementation combined with MKL-DSS, MUMPS, and PARDISO equation solvers, which are available in the software package SLang [SLang 2010]. Finally, Newton's method with line search and backtracking algorithm performs robustly only in

case of a few suitable and small 3D examples with small disturbance in the atomic lattice. However, for the most GB configurations the zone around the interface is characterized by a highly disturbed atomic lattice and the implemented Newton's method did not converge for many generated GB samples. Since the presented thesis is aimed on the general investigation of various kinds of GBs, robustness of the optimization procedure is a significant requirement that could not be fulfilled by Newton's method.

The problems in convergency are caused by the very large number of local minima in the energy function of an atomic system, for which the number of minima strongly increases with the number of unconstrained atoms. Furthermore, the energy function is highly sensitive compared to atomic displacements. For this reasons, it is quit difficult to find minima of the potential energy, which come along with a mechanically stable equilibrium state for systems with a large number of atomic DOF. A promising optimization method for atomic systems is developed and published by [Bitzek et al. 2006]. In this paper the *Fast Inertial Relaxation Engine* (FIRE) is introduced. The FIRE algorithm is implemented in the own nonlocal 3D QC code and has shown a high robustness and efficiency for the investigation of GB samples with arbitrary misorientation. Moreover, this algorithm has a surprising numerical simplicity.

The FIRE algorithm belongs to the group of molecular dynamics (MD) methods and aims for structural relaxation to find a minimum of the potential energy. According to MD, velocities are assigned to the atoms, whereby these velocities have no physical meaning in the implemented quasistatic QC formulation, but they are necessary for the numerical algorithm of FIRE. The idea of FIRE is to define a power P that increases along a sloping path to an energy minima and by contrast the power P decreases along a path with increasing energy values. FIRE is a global optimization method, since the variable P is a system parameter, which depends on all atomic forces and all introduced velocities. On the one hand the power values control the search direction and search velocity, and on the other hand the power allows for the overcoming of local maxima to find deeper local minima.

The efficiency of the minimization procedure is achieved through an adaptive time stepping, that allows for accelerated search in sloping directions and ensures, if needed, a timely correction of the search direction by deceleration. The time step is limited by a maximum, which according to [Bitzek et al. 2006] should be chosen ten times higher than a typical MD time step for the appropriate material. The choice of a reasonable maximum time step is very important, since it mainly influences the efficiency as well as the robustness of the algorithm. If the maximal time step is too low, then too much iteration steps are necessary to find a stable equilibrium configuration. By contrast, if the time steps are allowed to become too large, then the algorithm is not able for corrections in time to run into minima.

Related to the nonlocal QC method the FIRE algorithm of [Bitzek et al. 2006] is implemented to find the positions of representative atoms in a stable equilibrium configuration. These positions correspond with the nodal positions \mathbf{x}_a of the FE mesh, which is linked to the atomic lattice. The iteration scheme of the implemented FIRE algorithm is as follows:

The FIRE parameters are initialized with values, which were found to yield an efficient and robust iteration for the applied QC simulations. These values are equal or similar to those proposed in [Bitzek et al. 2006].

1. Initialize iteration counter k , time step Δt , nodal velocities \mathbf{v}_a and FIRE parameters

$$\begin{aligned}
k &= 0 \\
\mathbf{v}_a^{(-1)} &= \mathbf{0} \\
\mathbf{x}_a^{(0)} &= \mathbf{x}_a^{current} \\
\Delta t^{(0)} &= \frac{1}{2} \Delta t_{max} \\
\alpha^{(0)} &= \alpha_{start} = 0.12 \quad \dots \text{damping factor} \\
f_\alpha &= 0.99 \quad \dots \text{factor to decrease } \alpha \\
f_{inc} &= 1.10 \quad \dots \text{factor to increase } \Delta t \\
f_{dec} &= 0.75 \quad \dots \text{factor to decrease } \Delta t \\
N_{min} &= 3 \quad \dots \text{critical number of time steps} \\
\Delta t_{max} &\approx 10 \Delta t_{MD}
\end{aligned}$$

2. Check the nodal force norm $\|\mathbf{f}_a^{(k)}\|$ and calculate nodal velocities $\mathbf{v}_a^{(k)}$

$$\mathbf{f}_a^{(k)} = - \frac{\partial \Pi^{QC}(\mathbf{u}^{h,(k)})}{\partial \mathbf{u}_a^{(k)}} \tag{4.69}$$

if $\|\mathbf{f}_a^{(k)}\| < tolerance$ then: Exit and accept $\mathbf{u}^{h,(k)}$ and $\mathbf{x}_a^{(k)}$

$$\mathbf{v}_a^{(k)} = \mathbf{v}_a^{(k-1)} + \frac{\mathbf{f}_a^{(k)}}{m_a} \Delta t^{(k)} \tag{4.70}$$

where m_a is the atomic mass

3. Compute modified nodal velocities $\bar{\mathbf{v}}_a^{(k)}$

$$\bar{\mathbf{v}}_a^{(k)} = (1 - \alpha^{(k)}) \mathbf{v}_a^{(k)} + \alpha^{(k)} \|\mathbf{v}_a^{(k)}\| \frac{\mathbf{f}_a^{(k)}}{\|\mathbf{f}_a^{(k)}\|} \tag{4.71}$$

4. Compute and evaluate the global power value P

$$P = \mathbf{f}_a^{(k)} (\bar{\mathbf{v}}_a^{(k)})^T \quad (4.72)$$

if $P < 0$

$$\text{then: } \Delta t^{(k+1)} = f_{dec} \Delta t^{(k)}$$

$$\alpha^{(k+1)} = \alpha_{start}$$

$$\mathbf{v}_a^{(k)} = \mathbf{0}$$

else if $P > 0$ and number of time steps since $P < 0$ is larger than N_{min}

$$\text{then: } \Delta t^{(k+1)} = \min(f_{inc} \Delta t^{(k)}; \Delta t_{max})$$

$$\alpha^{(k+1)} = f_\alpha \alpha^{(k)}$$

else, then: $\Delta t^{(k+1)} = \Delta t^{(k)}$

$$\alpha^{(k+1)} = \alpha^{(k)}$$

5. Compute nodal positions $\mathbf{x}_a^{(k)}$

$$\mathbf{x}_a^{(k+1)} = \mathbf{x}_a^{(k)} + \mathbf{v}_a^{(k)} \Delta t^{(k+1)} + \frac{1}{2} \frac{\mathbf{f}_a^{(k)}}{m_a} (\Delta t^{(k+1)})^2 \quad (4.73)$$

Set $k \leftarrow k + 1$ and continue with 2.

4.2.7 Parallelization

Since simulations on the microscale require suitable model sizes to completely capture the interesting phenomena, the number of DOF in atomistic as well as QC models can be huge. Typical CPU times of such simulations are high, which may lead to long simulation runs in case of sequential computation. Using state of the art computational technologies including multi-core CPUs and multi-processor systems, a significant speed-up in simulation times can be gained by the parallelized implementation of uncoupled computations. For simplicity, in the following the term *processor* refers to a single-core processor or one core of a multi-core processor.

In the present QC implementation the computational most intensive subroutines are parallelized by uncoupling the numerical processes before, and communication of resulting data after parallelized computation. The set of parallelized QC subroutines is listed in Table 4.1. Therein the average distribution of CPU time to the parallelized subroutines is measured for the nanoindentation problem of Section 4.3.1. The last column refers to a FIRE iteration step according to Section 4.2.6. The most CPU time is needed for the computation of electron densities and atomic forces, since these computations require the evaluation of all atomic interactions considered in the QC model. The middle column of Table 4.1 refers to a Newton iteration step, since Newton's method with line-search and backtracking was implemented before the more robust FIRE algorithm was used.

parallelized QC subroutines	CPU time in Newton’s method	CPU time in FIRE algorithm
interpolation of atomic positions	2.2 %	6.3 %
computation of electron densities	14.5 %	27.5 %
computation of atomic energies	1.3 %	3.6 %
computation of atomic forces (and system matrix)	57.0 %	59.1 %
equation solver (PARDISO)	24.1 %	-
total	99.1 %	96.5 %

Table 4.1: Distribution of CPU time to several parallelized QC subroutines for the application of Newton’s method, and for the application of the gradient-based FIRE algorithm. The CPU time is measured for the nanoindentation problem of Section 4.3.1.

Newton’s method additionally requires the time consuming computation of the system matrix (Equation (A.1)) and the solution of the resulting equation system, which is here realized by the parallelized PARDISO solver [Schenk et al. 2004]. For both optimization methods the control outputs, the update of the elements Jacobian matrix, and the general managing of the optimization remain sequentially.

There are three main approaches of the parallelization of numerical methods for computing atomic DOF. According to [Plimpton 1995] these approaches are named the atom-decomposition, the force-decomposition, and the spatial-decomposition. The atom-decomposition assigns each processor a fixed subset of atoms, the force-decomposition assigns each processor a fixed subset of interatomic forces, and the spatial-decomposition assigns each processor a fixed spatial region. The spatial-decomposition is well suited for full atomistic models, for which a regular decomposition of the model domain comes along with an equal distribution of atomic DOF because of their uniform distribution in the model domain. Furthermore, a regular spatial-decomposition minimizes necessary communications between involved processors. Since the uniform distribution of DOF is not given in a QC model, the spatial-decomposition becomes unattractive due to the necessary non-regular domain partitioning, appropriate pre-calculations, and more communications. Consequently, either the atom-decomposition or the force-decomposition are applied to parallelize the QC subroutines. The parallelization is done using OpenMP [OpenMP 2008].

In the original definition of [Plimpton 1995] the force-decomposition is characterized by the assignment of a fixed subset of interatomic forces to each processor. This definition is changed in the present implementation to the assignment of a fixed subset of atomic interactions to each processor. The redefinition does not change the idea of the force-decomposition, since the interatomic forces are in direct relation to the atomic in-

teractions. The redefinition is necessary due to the application of the concept also to the computation of electron densities at atomic sites. For EAM potentials the electron densities have to be precalculated before the computation of atomic forces and, if necessary, of the system matrix can start. The computation of electron densities, atomic forces, and the system matrix is parallelized by a decomposition according to atomic interactions, since computational loops run over these interactions. The subroutines for the interpolation of atomic positions of non-representative atoms as well as for the computation of atomic energies are parallelized according to the atom-decomposition, since the internal loops run only over atoms. The PARDISO solver is a parallelized external library independent on the above mentioned decomposition schemes for systems of atomic DOF.

According to Amdahl' law [Sutmann 2002] perfectly parallelized computations result in a linear speed-up of the computational time with respect to the number of applied processors. This theoretical law considers neither the necessary communications nor the adaption of the numerical algorithm to the number of applied processors. Practical measurements of the speed-up due to parallelization are based on the relation between sequentially performed operations and parallelized performed operations in the parallelized

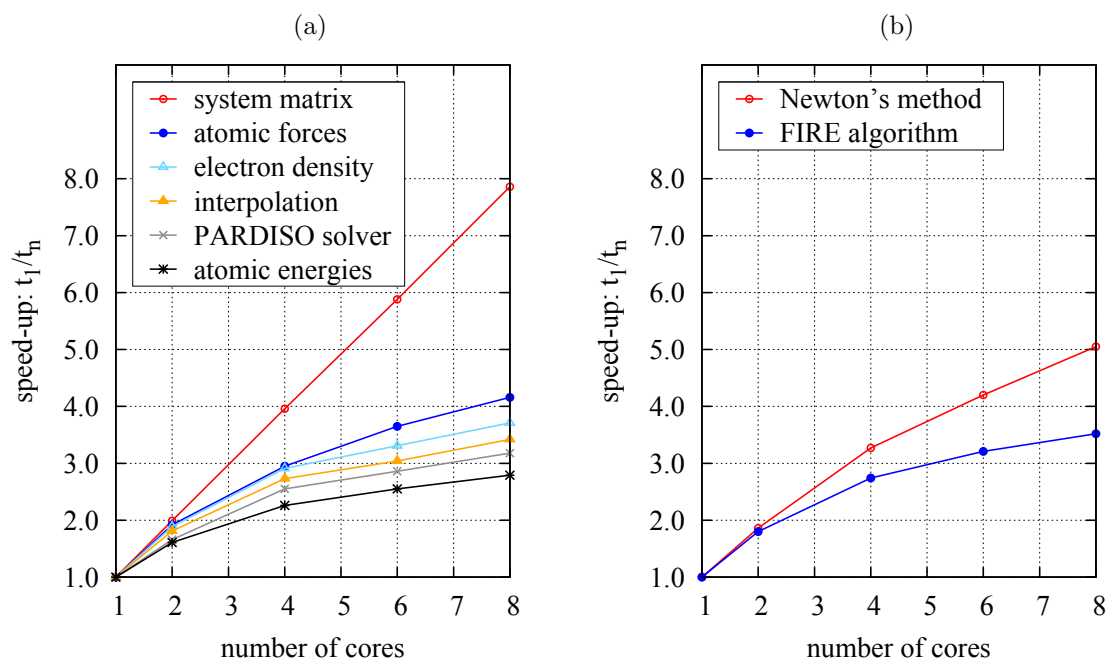


Figure 4.13: (a) Speed-up of parallelized subroutines in the present QC implementation. The computations of the system matrix, atomic forces, electron densities, and atomic energies as well as the interpolation of atomic positions in the deformed configuration and the PARDISO equation solver are evaluated. (b) Speed-up of one complete iteration step using Newton's method with line-search and backtracking, and the FIRE algorithm. The speed-up is measured for the nanoindentation problem of Section 4.3.1.

system [Gustafson 1988]. Accordingly, the speed-up is given by

$$\frac{1}{s + \frac{p}{N}}, \quad (4.74)$$

with N is the number of processors, s is the CPU time spent on serial parts, and p is the CPU time spent on parallelized parts of the implementation. The expression *CPU time* refers to the time, which is spent on the computation by a serial processor. The practical measurement of the speed-up asymptotically converges to the value

$$\frac{1}{s}. \quad (4.75)$$

The speed-up of parallelized subroutines in the present QC implementation is illustrated in Figure 4.13a again for the nanoindentation problem of Section 4.3.1. Disregarding the external PARDISO library, the diagram clarifies that the speed-up decreases, when a subroutine is less computational intensive (Table 4.1). The reason is that in computational intensive subroutines, especially in the one for the computation of the system matrix, more parallelized internal operations are possible, while the sequential part of communication is approximately equal for all subroutines. Thus, the numerical complexity of a subroutine rules the speed-up of parallelized computations. Figure 4.13b shows the speed-up of a total iteration step for both, Newton's method and the FIRE algorithm. The evaluation of computational speed-up was done using a workstation with two Intel Quad-Core X5472 processors.

4.2.8 Calculation of stress at the atomic level

In the course of the QC implementation an atomic-level stress calculation was considered. A discussion of different theories for the stress calculation at the atomic level can be found in [Shen et al. 2004]. As pointed out in [Buehler 2008] the concepts of virial stress and strain are introduced to couple the deformation behavior of atomistic systems with continuum theories. A convergence to the continuum Cauchy stress tensor can be reached if the virial stress is averaged over space and time. The concept of virial stress assumes homogeneous deformation of the atomic system.

Since the atomic-level stress calculation has to be applied for inhomogeneous deformed systems, the BDT stress calculation introduced by Basinski, Duesberry and Taylor [Basinski et al. 1971] was applied, which is valid for homogeneous systems. In contrast to the virial stress which assumes an average over the total volume, the BDT stress is related to the volume Ω_i of a single atom and calculates for atom i

$$\boldsymbol{\sigma}_i^{BDT} = \frac{1}{2\Omega_i} \sum_{\substack{j=1 \\ j \neq i}}^N \mathbf{r}_{ij} \otimes \mathbf{f}_{ij}. \quad (4.76)$$

Therein, \mathbf{r}_{ij} and \mathbf{f}_{ij} are the distance vector and the force vector between atoms i and j . In the present QC implementation the BDT stress is available for the representative atoms and additionally for the cluster atoms.

4.2.9 Determination of the geometry of defects

A special problem that accompanies with 3D simulations is the determination and also the visualization of defects in the solid. Atoms which are part of the defect are filtered according to properties, which distinguish them from the unaffected atoms. Such a property is the potential atomic energy which is used in the energy method to determine defects by filtering the associated high energy atoms, as explained in [Buehler 2008]. The energy method is well suited to accurately determine the geometry of cracks since atoms at the fracture surface have a distinctly higher potential energy. An example for the application of the energy method to visualize a crack in a 3D aluminum sample is shown in Figure 4.14. In this example the atomic region around a crack at the surface is observed. However, it is difficult to determine dislocations and stacking faults by the energy method. The reason is that these types of defects only cause small variations in the potential energy of affected atoms and therewith the filter algorithm must be highly sensitive. An example for the energy-based filtering of atoms, which are associated with dislocation loops caused by nanoindentation in aluminum, is given in the left part of Figure 4.15. It is visible that the accurate determination of the dislocation loops is difficult since the appropriate energy values of the corresponding upper part of the legend (red) only differ slightly from each other. In comparison, the energy values of the lower part of the legend (blue), which belongs to surface atoms, differ significantly from the energy values of bulk atoms.

A second way for the determination of the geometry of defects is given by the cen-

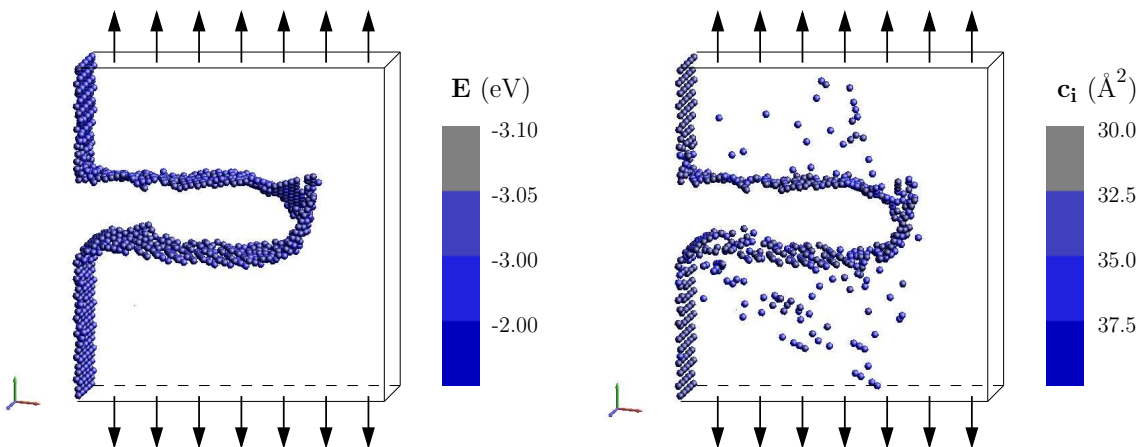


Figure 4.14: Determination of fracture surfaces by the energy method (left) and the centrosymmetry technique (right). Observed is a cracked surface part of an aluminum sample under tension. Atoms on the left sample boundary indicate the free surface.

trosymmetry technique, which was introduced by [Kelchner et al. 1998]. By contrast to the energy method the centrosymmetry technique is only based on geometrical characteristics. The basic principle is that a homogeneous deformation preserves the centrosymmetry of centrosymmetric crystals. Against this, defects like surfaces, dislocations, and stacking faults lead to measurable deviations from the centrosymmetry. A centrosymmetry parameter c_i is defined to measure and distinguish these deviations according to different defects. This geometrical parameter observes changes in the symmetry of the nearest atomic neighbors of an atom. In case of FCC crystals, like aluminum, twelve atoms are considered as nearest neighbors which are in undeformed perfect crystals in a distance of $a_0/\sqrt{2}$ around the evaluated atom, with a_0 is the lattice parameter. The centrosymmetry parameter c_i of an atom i is calculated by

$$c_i = \sum_{j, \bar{j}=1}^6 \|\mathbf{r}_{ij} + \mathbf{r}_{i\bar{j}}\|^2, \quad (4.77)$$

where atom \bar{j} defines the symmetric counterpart of atom j , and \mathbf{r}_{ij} as well as $\mathbf{r}_{i\bar{j}}$ are distance vectors from the evaluated atom i to its nearest neighbors j and \bar{j} , respectively. The centrosymmetry parameter is very sensitive to defects in the bulk material. Moreover, it is affected by free and fracture surfaces. The right part of Figure 4.15 shows the visualization of dislocation loops according to the centrosymmetry parameter, which determines the geometry of this type of defect much better than the energy method. An example for the visualization of fracture surfaces by the centrosymmetry technique is given in the right part of Figure 4.14. Although the centrosymmetry parameter is suited for the determination of fracture surfaces, the energy method works better for such defects. Table 4.2 contains normalized centrosymmetry parameters for various types of defects. The table is taken from [Buehler 2008] and includes the therein proposed ranges of the parameter for a distinction of defect variants.

The present QC implementation allows for the application of the energy method as well as the centrosymmetry technique since for cluster atoms both, the potential energy and the centrosymmetry parameter, are calculated.

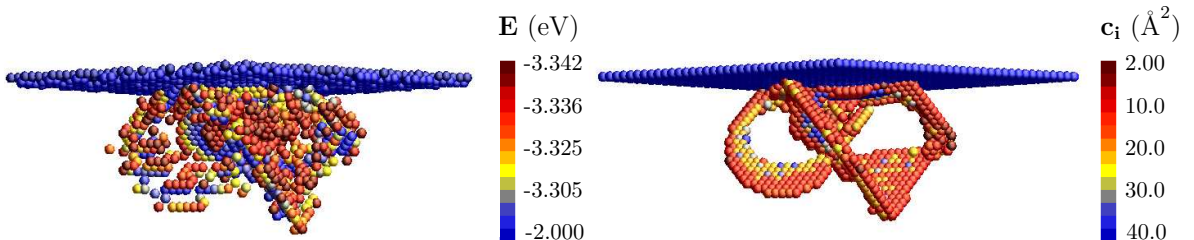


Figure 4.15: Determination of dislocation loops by the energy method (left), and the centrosymmetry technique (right). Observed is a part of an aluminum sample in a nanoindentation simulation. Blue atoms on the top indicate the free surface.

type of defect	c_i/a_0^2	range
perfect lattice	0.0000	$c_i/a_0^2 < 0.1$
partial dislocation	0.1423	$0.01 < c_i/a_0^2 < 2.0$
stacking fault	0.4966	$0.2 < c_i/a_0^2 < 1.0$
surface atom	1.6881	$c_i/a_0^2 > 1.0$

Table 4.2: Normalized centrosymmetry parameters for various types of defects. Therein, a_0 is the lattice parameter. The last column contains ranges for the distinction of defects. The table is taken from [Buehler 2008].

4.3 Examples

4.3.1 Nanoindentation in FCC aluminum

In the first example the present QC implementation is validated with results from lattice statics and external tests. A nanoindentation is simulated, since this test is well documented in literature. Referring to [Eidel et al. 2009], who also simulated nanoindentation using a QC model, an aluminum cube with edge size $64 a_0$ is modeled, where the lattice parameter a_0 of aluminum is set to 4.032 \AA . The crystal orientation is chosen with unit cell axes parallel to the global coordinate system and the spherical indenter is driven into

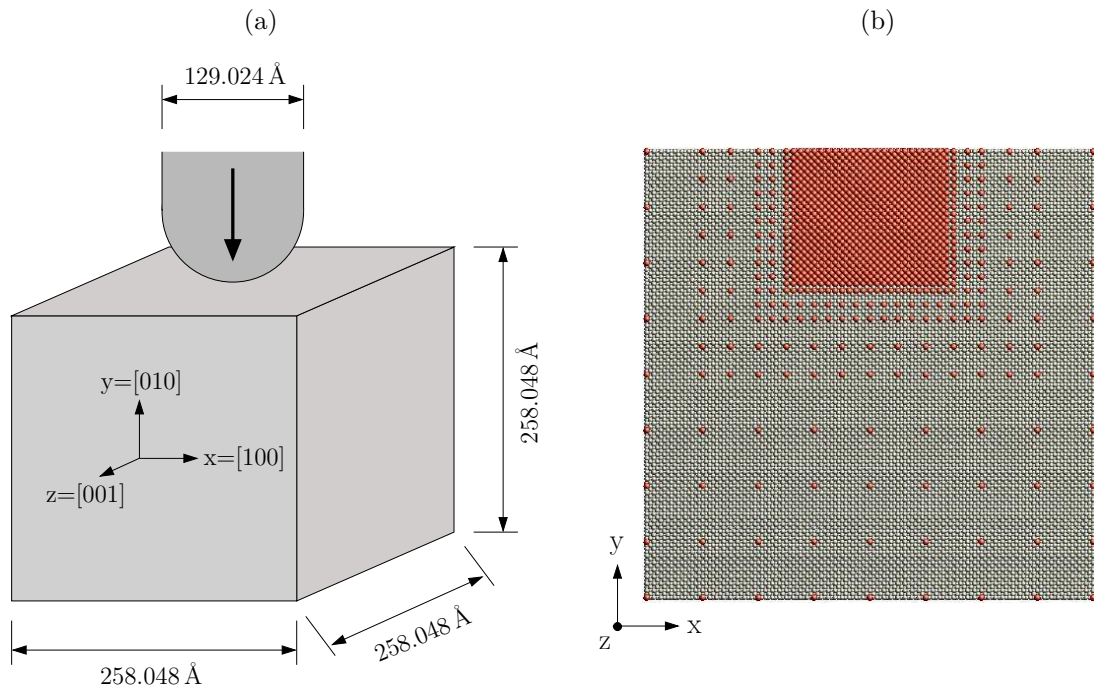


Figure 4.16: (a) Model dimensions and crystal orientation for the simulation of nanoindentation in a FCC aluminum cube of approximately one million atoms. (b) Cut at middle z -dimension through the atomic lattice of the QC model with representative atoms (red).

the (010) plane. The geometrical properties of the model as well as the crystal orientation are illustrated in Figure 4.16a. For reasons of comparability the same boundary conditions as in [Eidel et al. 2009] are applied. Atoms at the lateral surfaces and at the bottom are fixed in normal direction, while atoms at the top are free. The spherical indenter is modeled as an external potential, which is defined according to [Kelchner et al. 1998] as

$$\Pi^{ext}(\mathbf{x}) = A \cdot \theta(R^{ind} - r) \cdot (R^{ind} - r)^3, \quad (4.78)$$

with the step function $\theta(R^{ind} - r)$ and

$$r = |\mathbf{x} - \mathbf{c}^{ind}|. \quad (4.79)$$

The vector \mathbf{x} denotes atomic positions, \mathbf{c}^{ind} is the position vector of the indenter center, R^{ind} is the indenter radius, and A defines the strength of the repulsive force. The appropriate values in the simulation are $R^{ind} = 16 a_0$ and $A = 2,000 \text{ eV}/\text{\AA}^3$. The atomic bonds are described by EAM potentials according to [Ercolessi et al. 1994], which are freely available for aluminum from the website of F. Ercolessi [Ercolessi 2009]. The cutoff radius r_c is set to 5.558 \AA .

The nanoindentation was simulated once by lattice statics with the full number of 3,178,430 DOF. Then, the model was coarse grained away from the zone which is directly affected by the indentation. This led to a model with 45,369 representative atoms and 135,702 DOF, which was used for the QC simulations. The arrangement of representative atoms is shown in Figure 4.16b for the x-y-plane at middle z-dimension, which equals the z-y-plane at middle x-dimension due to symmetry. For the QC simulations the cluster

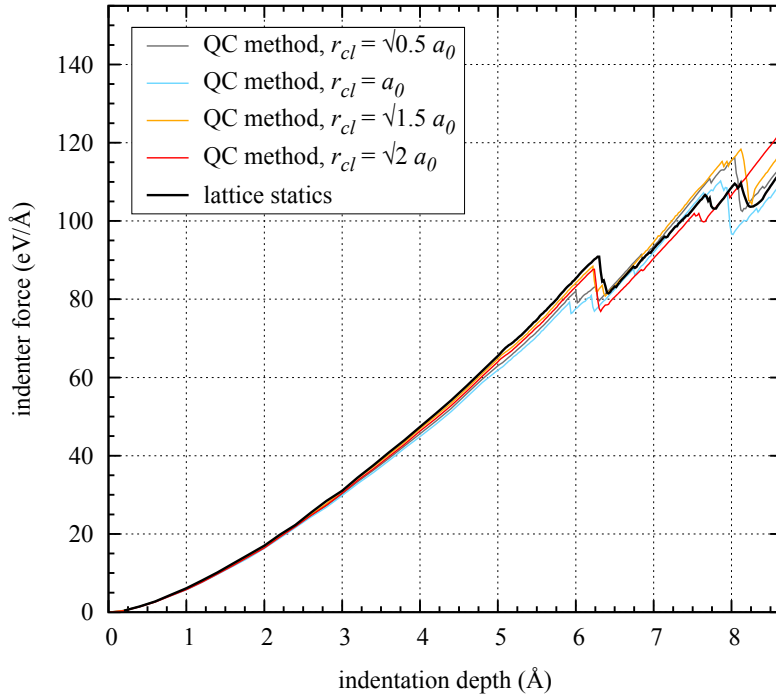


Figure 4.17: Force-depth curves of nanoindentation simulation with lattice statics and the QC implementation.

cluster radius	number of cluster atoms	dislocation nucleation starts at depth (Å)	force (eV/Å)	speed-up relating to lattice statics
$\sqrt{\frac{1}{2}}a_0$	95,517	6.00	82.1	11.7
a_0	112,195	5.92	79.2	10.3
$\sqrt{\frac{3}{2}}a_0$	166,795	6.22	88.4	7.8
$\sqrt{2}a_0$	188,251	6.24	87.6	7.0
lattice statics	1,073,345	6.30	90.9	1

Table 4.3: Summary of simulating nanoindentation into the (010) plane of aluminum.

radius was varied from $r_{cl} = a_0/\sqrt{2}$ to include only the first neighbors of representative atoms, up to $r_{cl} = \sqrt{2}a_0$. Table 4.3 gives an overview of the investigated cluster radii and the associated number of cluster atoms, which includes the representative ones. In case of lattice statics all atoms are similar to cluster atoms, since at all these atoms forces and energies are explicitly computed.

The diagram of Figure 4.17 shows the indenter force over the indentation depth for the lattice statics simulation and the QC simulations with various cluster radii. A strong match of the force-depth curves is observed until dislocation nucleation starts coming along with downward jumps of the force at about 6 Å indentation depth. In this first range only an inessential weaker behavior of the QC models is observed. Furthermore, the force-depth curves differ only slightly after the beginning of dislocation nucleation. The diagram, and also Table 4.3, prove that compared to the full atomistic reference model the QC models with $r_{cl} \geq \sqrt{3/2}a_0$ well predict the depth at which dislocation nucleation starts, and also the corresponding forces have less than five per cent deviation from the reference value of lattice statics. However, the QC models with small cluster size $r_{cl} \leq a_0$ predict earlier dislocation nucleation at about ten per cent lower initiation forces. Summarizing, the results of the present QC simulations agree well with the results of [Eidel et al. 2009] for simulated nanoindentation with equal conditions.

The formation of first dislocation loops in the lattice statics simulation is visualized in Figure 4.18. Comparison with the appropriate dislocation microstructure of the QC model with $r_{cl} = \sqrt{2}a_0$ in Figure 4.19 shows an excellent agreement considering the model symmetry. By contrast, Figure 4.20 shows a different formation of dislocations for the QC model with $r_{cl} = \sqrt{1/2}a_0$. As stated before, this dislocation microstructure is initiated by an approximately ten per cent lower indenter force in relation to lattice statics. Consequently, a moderate cluster radius of at least $r_{cl} \geq \sqrt{3/2}a_0$ should be chosen to ensure the quality of results.

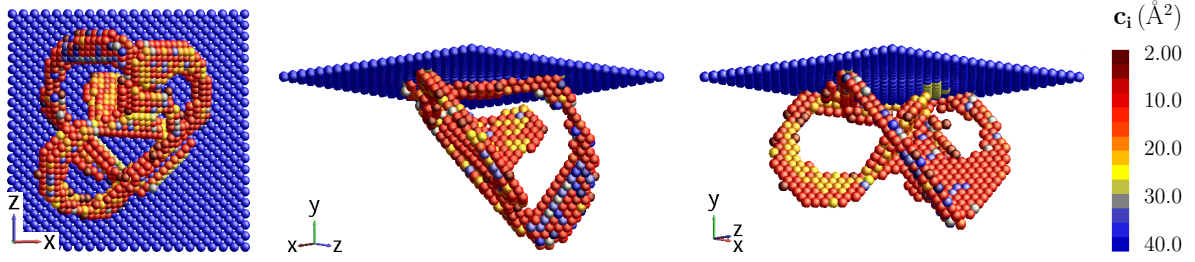


Figure 4.18: Three different views on dislocation loops under the indenter visualized by the centrosymmetry technique. The graphics refer to the lattice statics simulation at indenter depth 7.5 Å.

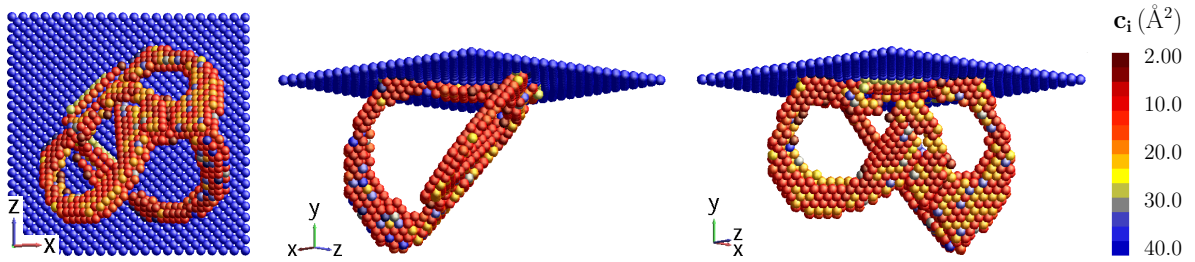


Figure 4.19: Three different views on dislocation loops in the QC simulation with $r_{cl} = \sqrt{2} a_0$ at indenter depth 7.5 Å.

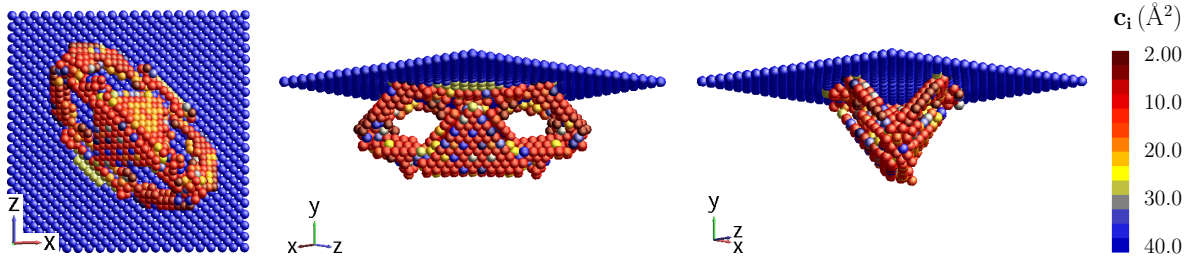


Figure 4.20: Three different views on dislocation loops in the QC simulation with $r_{cl} = \sqrt{\frac{1}{2}} a_0$ at indenter depth 7.5 Å.

For the nanoindentation problem, Table 4.3 also shows that the benefit by the application of the QC method with reduced number of DOF is evident from significantly faster simulations compared to the application of the full atomistic model, while a similar quality of results is verified. The speed-up was measured for each parallelized computation with six threads.

4.3.2 Generation of samples with low energy grain boundaries

The investigation of intergranular fracture on the microscale requires the generation of suitable GB samples consisting of atomic positions in equilibrium. Since structural materials tend to minimize their potential energy, polycrystals naturally consist of low energy GBs between adjacent crystallites. Thus, reasonable simulations of the intergranular fracture process require the generation of samples with low energy GBs.

Various strategies are proposed in literature to obtain the relative shift between adjacent crystallites which leads to a minimum of the GB energy. For instance, [Wolf et al. 1992] suggest a procedure to minimize the GB energy of an atomistic modeled bicrystal with periodic boundary conditions in directions parallel to the GB. During the relaxation of the atomic configuration a translation of the crystallites parallel to the GB is allowed according to the computed mutual forces. Moreover, the model can expand or contract in the direction perpendicular to the GB. Since the allowed translation only optimizes the GB configuration for a limited range, various initial rigid-body translations of the two adjacent crystallites are tested incrementally to find the configuration with the lowest GB energy. Applications of the corresponding GB energy calculation to tilt grain boundaries are explicitly documented in [Coffman et al. 2008a], as well as in [Rittner et al. 1996] in combination with Monte Carlo simulations to test the stability of zero temperature GB structures.

In principle the described proceeding was applied also by [Sansoz et al. 2005] to obtain low energy configurations for bicrystal models with tilt GBs. In these models the atoms at the bottom of the lower crystallite are totally fixed, while all other boundaries of the x-y-plane are free during the relaxation process. Since periodic boundary conditions are applied in the z-direction, these models with small z-dimension behave quasi-planar. Again the upper crystallite is able for small translations parallel to the GB plane and changes in perpendicular direction are enabled. The search for the relevant low energy GB is also done by relaxation of a set of various configurations with incrementally changed

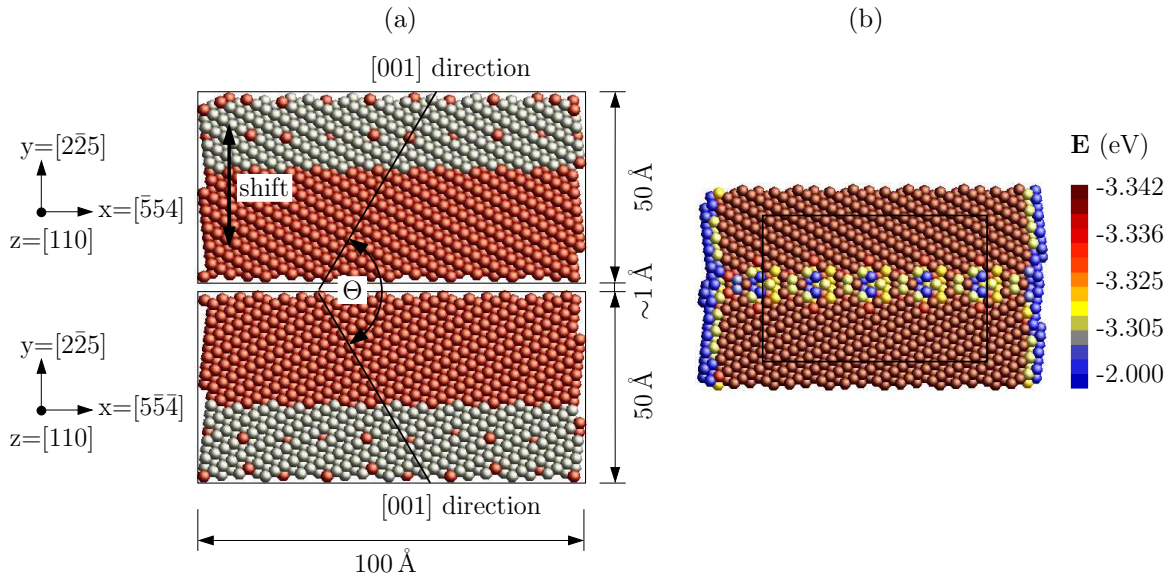


Figure 4.21: Search for the low energy configuration of a $\Sigma_{33} \langle 110 \rangle (2\bar{2}5)$ STGB. (a) Initial configuration of two separate crystallites with a distance of about 1 Å between them. The z-dimension is also 100 Å. Red atoms are representative atoms of the QC model with free surfaces. (b) Cut through the final configuration with atomic energies in the GB region. The GB energy is calculated from an analysis of the atoms within the centered box of size 60 Å x 40 Å x 60 Å (black lines).

shifts in the GB plane between the two crystallites. Thereby, the analysis of the GB energy is restricted to the bulk material, whose atoms are not directly affected by surface effects. According to [Sansoz et al. 2005] the GB energy is computed by subtracting the energy of an appropriate bulk single crystal from the bicrystal energy and dividing by the GB area.

In the presented dissertation the concept of [Sansoz et al. 2005] is adopted partially, but by contrast the actual model is fully three dimensional without any periodicity, since the reasonable formulation of periodic boundary conditions is only possible for a limited set of GBs, especially tilt GBs. Figure 4.21a illustrates the strategy, which is applied in this thesis to find the GB configuration with minimized energy. Two oriented three dimensional crystallites are generated one above the other by its atomic positions, each within a domain of size $100 \text{ \AA} \times 50 \text{ \AA} \times 100 \text{ \AA}$. The distance in y-direction between the two domains is about 1 \AA . Using the nonlocal QC method a full atomistic resolution within a distance of 30 \AA from the GB is applied to both crystallites. Out of this distance the resolution of representative atoms is coarsened as visualized in Figure 4.21a and Figure 4.24a. The models consist of approximately 61,000 atoms and about 37,000 representative ones. Similar to the model of [Sansoz et al. 2005] the atoms at the bottom of the lower crystallite are fixed in all directions. The remaining boundaries of the two crystallites are free. While the relaxation of the model is simulated, the upper crystallite is able to move in a stable bond configuration to build a bicrystal with the lower one. Also, various initial states are investigated to find the GB configuration with the lowest energy. The bond between atoms is described by EAM potentials for aluminum provided by F. Ercolessi on his website [Ercolessi 2009].

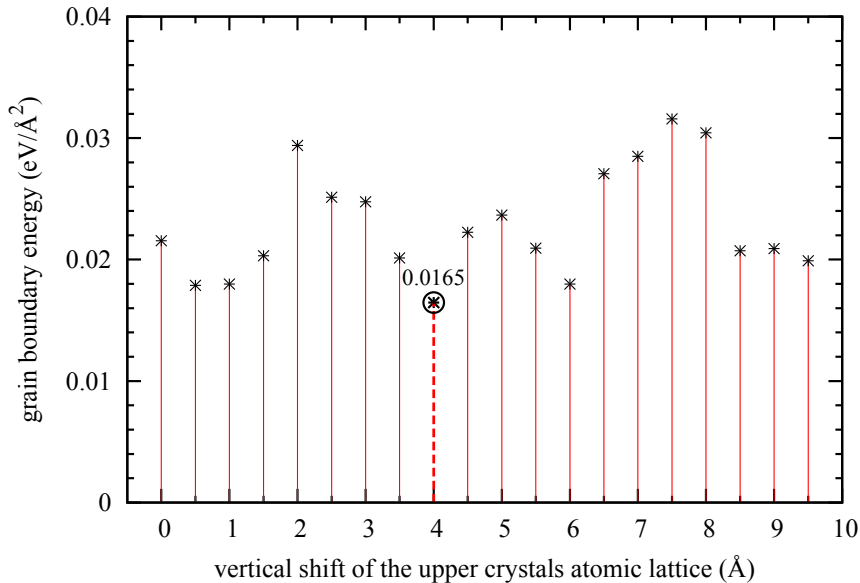


Figure 4.22: Calculated GB energies of $\Sigma 33 \langle 110 \rangle (2\bar{2}5)$ STGB configurations with various vertical shifts of the atomic lattice of the upper crystallite. The minimum GB energy is calculated with a shift of 4 \AA .

Following [Sansoz et al. 2005] the initial states were varied by shifts of the upper crystallite parallel to the GB plane. This strategy was not very effective in searching for low energy configurations. For this reason the proceeding was changed to fasten the search for a convenient combination of net planes of the lower and upper crystallites along the GB. Taking into account, that multiple energy minima may exist for different GB structures [Wang et al. 1984] the configuration with lowest energy can be found by adding or removing atomic layers at the GB plane before relaxation is simulated. Therefore, a shift of the upper crystallite perpendicular to the GB plane was introduced. This shift does not act between the two crystallites directly, but it moves the atomic lattice of the upper crystallite within its domain bounds which remain constant. Layers of atoms move out of, or into the upper model domain and the initial GB configuration changes. This procedure was applied to find the minimized energy GB states for several misorientations by investigating only a few initial configurations. For example, Figure 4.22 illustrates the calculated GB energies of the $\Sigma 33 \langle 110 \rangle (2\bar{2}5)$ symmetric tilt GB (STGB) depending on the applied shift. The GB configuration with the lowest GB energy is found for a

STGB plane	misorientation Θ ($^\circ$)	GB energy ($\text{eV}/\text{\AA}^2$)		
		present study	[Sansoz et al. 2005]	[Chandra et al. 1999]
$\Sigma 73(6\bar{6}1)$	13.44	0.0227	0.0235	-
$\Sigma 33(4\bar{4}1)$	20.05	0.0266	0.0267	-
$\Sigma 27(5\bar{5}2)$	31.59	0.0285	0.0306	-
$\Sigma 9(2\bar{2}1)$	38.94	0.0265	0.0301	0.0269
$\Sigma 11(3\bar{3}2)$	50.48	0.0222	0.0254	0.0259
$\Sigma 33(5\bar{5}4)$	58.99	0.0184	0.0181	-
$\Sigma 3(1\bar{1}1)$	70.53	0.0036	0.0037	0.00024
$\Sigma 43(3\bar{3}5)$	99.37	0.0224	-	0.0262
$\Sigma 3(1\bar{1}2)$	109.47	0.0203	-	0.0203
$\Sigma 33(2\bar{2}5)$	121.01	0.0165	-	0.0234
$\Sigma 11(1\bar{1}3)$	129.52	0.0080	0.0082	0.0091
$\Sigma 9(1\bar{1}4)$	141.06	0.0218	-	0.0218
$\Sigma 27(1\bar{1}5)$	148.41	0.0237	0.0243	-

ATGB plane	misorientation Θ ($^\circ$)	GB energy ($\text{eV}/\text{\AA}^2$)	
		present study	[Sansoz et al. 2005]
$\Sigma 11(2\bar{2}5)/(4\bar{4}1)$	129.52	0.0221	

Table 4.4: Calculated GB energies of thirteen $\langle 110 \rangle$ symmetric tilt GBs (STGB) and one $\langle 110 \rangle$ asymmetric tilt GB (ATGB). Comparison with computational results of [Sansoz et al. 2005] and [Chandra et al. 1999].

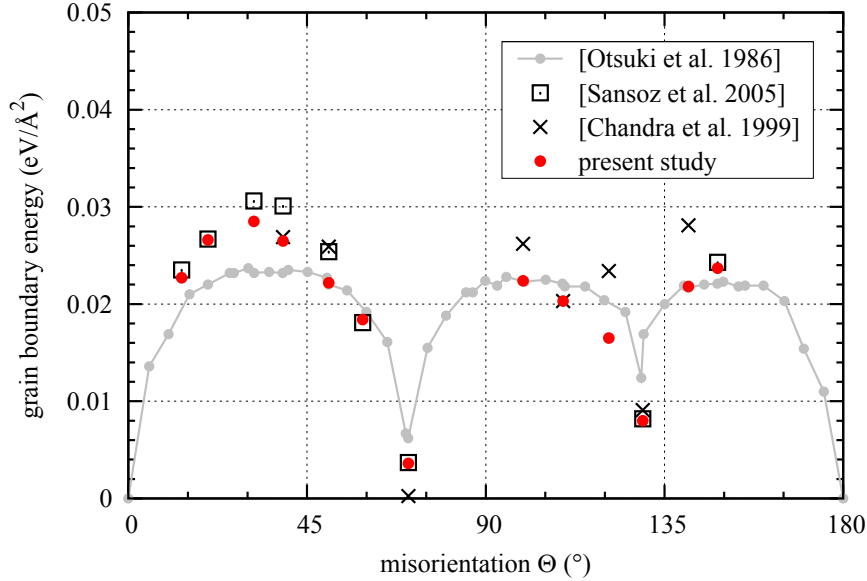


Figure 4.23: GB energies of $\langle 110 \rangle$ STGBs calculated by [Sansoz et al. 2005], [Chandra et al. 1999], and in the present study, in comparison with experimental values of [Otsuki et al. 1986].

shift value of 4 \AA . Figure 4.21b shows the atomic energies in the fully atomistic region of the finally obtained $\Sigma 33 \langle 110 \rangle (2\bar{2}5)$ STGB configuration. The GB energy is calculated by an analysis of all atoms within a box, which excludes the free surfaces and coarse grained QC regions. Figure 4.21b illustrates this box of size $60 \text{ \AA} \times 40 \text{ \AA} \times 60 \text{ \AA}$ which is centered within the model. Since the bulk atomic energy shows only small fluctuation while it clearly differs from the energy of surface atoms, a nonuniform legend scaling is used. Therewith, the change in energy of the GB atoms compared to the bulk atoms is clearly visible as well as for the surface atoms at the boundaries. As stated before the GB energy is calculated by the energetic difference to an ideal crystal with the same number of atoms and divided by the GB area.

For validation of the GB model, the low energy configurations of thirteen $\langle 110 \rangle$ STGBs were computed and in Table 4.4 the corresponding GB energies are compared to calculations of [Sansoz et al. 2005] and [Chandra et al. 1999]. While [Sansoz et al. 2005] applied the above described quasi-planar Quasicontinuum model in their simulations, [Chandra et al. 1999] used a molecular statics code to calculate the GB energy of 3D bicrystal models with periodic boundary conditions in the GB plane. The GB energies of the present study were found to be in good agreement with the reference values and in some cases configurations with lower GB energy could be found. The calculated STGB energies are also compared in Figure 4.23 to the experimental results of [Otsuki et al. 1986], which are taken from [Nishitani et al. 2001]. From the diagram, which shows the GB energy depending on the misorientation, the conclusion can be drawn, that in comparison to the other references, the calculated GB energies of the present study are very close to the experimental values. A detailed study of the dependency of GB energies on the misorien-

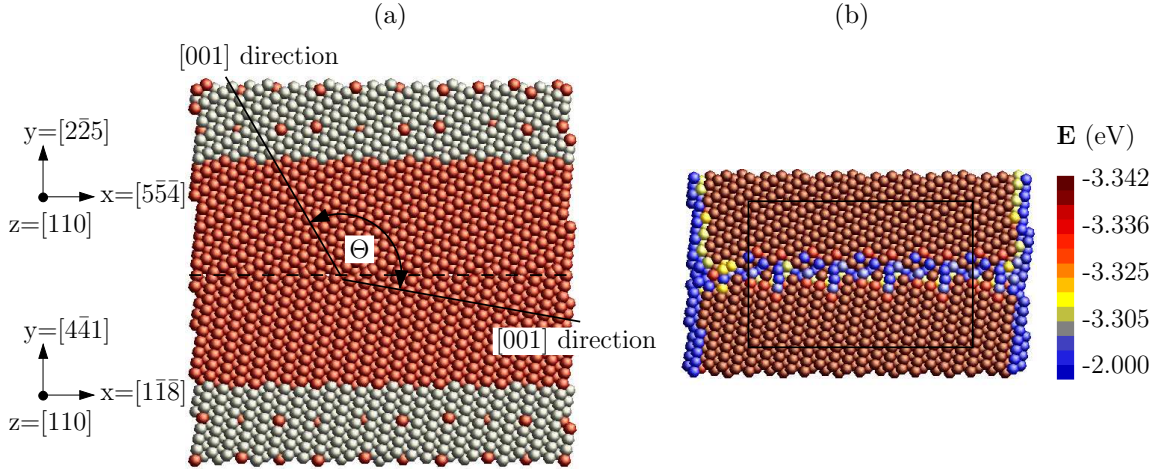


Figure 4.24: $\Sigma 11 \langle 110 \rangle (2\bar{2}5)/(4\bar{4}1)$ ATGB. (a) Initial atomic configuration of the QC model with free surfaces. Representative atoms are red colored. The z-dimension is 100 Å. (b) Cut through the final configuration with atomic energies in the GB region and with the energy evaluation box (black lines).

tation angle in aluminum and copper $\langle 110 \rangle$ STGBs is also documented in the Ph. D. thesis of [Spearot 2005], who used a molecular statics code for atomistic simulations. The corresponding results are qualitatively comparable with the present study for aluminum interfaces, but show partially higher GB energies especially for the upper range of the misorientation angle.

The presently proposed strategy is well suited to obtain GB states with minimized energy using 3D models since in 3D, equally to 2D, only a few initial configurations have to be investigated, which results in a high numerical efficiency. This strategy is not limited to STGBs only, but can be applied to arbitrary GB configurations. For instance, the procedure was applied to a $\Sigma 11 \langle 110 \rangle (2\bar{2}5)/(4\bar{4}1)$ asymmetric tilt GB (ATGB), which is illustrated in Figure 4.24a with its orientation data and in Figure 4.24b with its relaxed configuration showing the corresponding atomic energies. Table 4.4 contains the associated values of misorientation and GB energy.

A collection of GB structures with minimized energy can also be found in the Interface Structure Data Bank of N. Erwin and D. Warner [Erwin et al. 2010], which likewise provides the GB configurations of [Sansoz et al. 2005].

Chapter 5

Scale transition by atomistic-based cohesive zone representations

5.1 A review on cohesive zone representations

5.1.1 On the history of cohesive zone models

The idea of cohesive zone models (CZM) is based on models of [Dugdale 1960] and [Barenblatt 1962], who divided a crack in a stress free part and the plastic process zone, which is loaded by a cohesive stress. These models describe the damage in the plastic zone by a traction-displacement relation. Later cohesive models considered the cohesive stress depending on material separation [Hillerborg et al. 1976] [Needleman 1987] [Tvergaard 1990]. A coupled CZM was introduced by [Tvergaard et al. 1992], who coupled the relative normal and tangential displacements of the cohesive zone. A comprehensive discussion on the developments of CZMs can be found in [Anvari et al. 2006]. In finite element applications of CZMs interface elements are introduced between continuum elements and a traction separation law (TSL) describes the constitutive behavior of these interfaces, for example in [Bouvard et al. 2009]. Alternatively, additional shape functions are introduced to finite elements (XFEM) or meshfree approaches to reproduce cracks as discontinuities in the displacement field. In case of cohesive cracks a CZM is applied to consider cohesive forces through the crack in the energy balance [Moës et al. 2002] [Rabczuk et al. 2007]. [de Borst 2003] exemplarily discusses the various ways to apply CZMs in computational methods of fracture mechanics.

5.1.2 Atomistic-based cohesive zone representations

As stated, for example, in [Yamakov et al. 2006] the above introduced CZMs use values of strength and fracture toughness which are derived from macroscale representations of materials. These parameters of the CZMs are average values which are derived from specimens with large numbers of grains and GBs including a variety of defects. Therewith, local fracture phenomena, which depend on the geometrical and mechanical characteristics

of a particular GB, can not be simulated. In the last decade, approaches for atomistic-based cohesive zone representations were followed by different researchers to overcome the problem of homogenized representations of the mechanical response of GBs. The new strategy of parameterization of decohesion laws based on atomistic simulations aims at a more realistic description of the interface decohesion process.

Several publications document investigations of the mechanical response of a small number of symmetric tilt grain boundaries (STGB) [Shenderova et al. 2000] [Spearot et al. 2004] [Spearot 2005] [Sansoz et al. 2004] [Sansoz et al. 2005] [Warner et al. 2006] [Warner et al. 2008] [Yamakov et al. 2006]. Although these investigations are performed for one special GB or a strongly limited set of GBs in 2D respectively, they demonstrate generic approaches of deriving cohesive zone representations from atomistic methods. A comprehensive study on the energy and fracture strength of a wide range of GBs is documented in [Coffman et al. 2008a]. This theoretical 2D study refers to a virtual material with triangular atomic lattice, but investigates all GB configurations which can be reasonably generated with acceptable repeat distances to apply periodic boundary conditions in directions of the GB plane. Furthermore, [Coffman et al. 2008b] give suggestions for the analysis of GBs without finite repeat distances, which are taken into account for the present paper. Also, the procedure of deriving cohesive laws from atomistic GB fracture simulations is described in detail in their publication.

While the above referenced studies mainly simulate the interfacial adhesion process, an approach for extracting decohesion laws from simulations of crack propagation is proposed by Yamakov et al. [Yamakov et al. 2006] [Yamakov et al. 2007] [Yamakov et al. 2008]. They define an atomistic analog to a continuum CZM element to recast the atomistic results for representing the cohesive behavior of a GB along a characteristic length. The approach is applied to the atomistic-based analysis of crack propagation along a high-energy GB in aluminum under hydrostatic loading conditions. Therefrom, also the dependency of the fracture toughness from the direction of crack propagation is observed and explained.

Most simulations of intergranular fracture are documented for perfect GBs. Beyond that, discussions on the influence of atomic level defects at material interfaces can be found in [Spearot et al. 2004], [Spearot 2005], and [Gall et al. 2000]. Especially [Gall et al. 2000] investigate the dependency of fracture strength from point vacancies near the interface and from crack-like vacancy defects in the bulk material. This investigation analyzes the fracture behavior of a hetero-phase boundary between aluminum and silicon, while the before named studies refer to GBs between identical materials. Since the atomistic-based simulation of hetero-phase damage phenomena comes along with problems in defining reasonable potentials for the atomic interaction of different chemical materials, the present dissertation focuses on GB damage by restriction to one chemical material. Nevertheless, studies on GBs with atomic level defects are performed and described in Section 5.3.

5.2 Calculation of cohesive parameters from atomistics

The intended multiscale concept involves the formulation of atomistic-based cohesive zone representations for arbitrary 3D GBs. Since a finite repeat distance is not given for interface configurations in general, a computational model without periodic boundary conditions is aimed on the atomistic scale. Consequently, a proposal of [Coffman et al. 2008b] is followed by applying rolled boundary conditions to the atomistic models.

At first, the methodology of extracting relevant constitutive parameters for a coupled CZM from atomistic simulations is explained by examples. Therefore, perfect GBs without additional defects are modeled. As discussed in [Coffman et al. 2008a] and explained in Chapter 3 the 3D interface geometry is described by eight parameters. Five macroscopic parameters describe the orientation of adjacent crystallites as well as the orientation of the interface between them. Additionally, three microscopic parameters describe the three possible relative translations between the crystallites. These translational DOF are obtained by the determination of the minimized energy GB configuration according to Section 4.3.2. Consequently, the five macroscopic DOF remain for the geometrical description of a perfect interface.

Since the five macroscopic DOF result in a huge number of possible combinations, it is less reasonable to derive cohesive laws as a function of the interface geometry by systematically performed studies. Such studies are documented in [Coffman et al. 2008a] for the 2D case, where the interface geometry is described by only two macroscopic DOF. This publication points out that already in 2D the cohesive law is not a smooth function of the geometrical parameters and for the 3D case the meaningful suggestion of on-the-fly simulations of cohesive GB characteristics is given. According to this suggestion and based on the previous argumentation the following sections describe a method for the calculation of cohesive parameters of individual GB configurations from atomistics. This method can be applied for on-the-fly-simulations of cohesive interface parameters describing the GB decohesion process in continuum polycrystal models.

After demonstrating the micro-meso scale transition for perfect GBs, improvements on the microscale model are realized by introducing additional defects. In this way more realistic studies of the intergranular damage are aimed. In the presented dissertation investigations of imperfect GBs with point vacancies are done and the influence of those defects, especially on the GB fracture strength, is documented.

5.2.1 Modeling of general grain boundaries without periodicity

The calculation of cohesive parameters from atomistics is realized by the simulation of tensile and shear states using a 3D QC model of size $100 \text{ \AA} \times 100 \text{ \AA}$ parallel to the interface plane and with a height of 130 \AA perpendicular to the interface. The model dimensions are illustrated in Figure 5.1 for a $\Sigma 33 \langle 110 \rangle (2\bar{2}5)$ STGB. In each crystallite a full atomistic

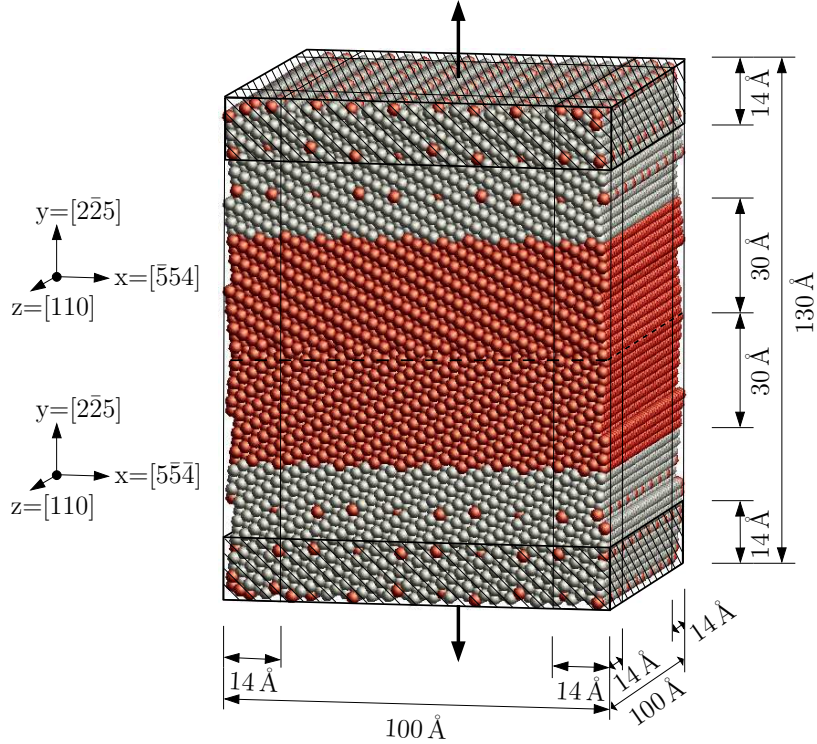


Figure 5.1: 3D QC model with boundary layers of 14 Å thickness at all six boundary faces of the model. Constraints are applied to the atoms in the boundary layers to realize rolled boundary conditions. Additionally, displacements are applied to some of these atoms to force tensile (illustrated) or shear stress.

zone of approximately 30 Å around the GB ensures the necessary accuracy just as in the models of Section 4.3.2, while only a limited number of representative atoms is chosen in the remaining model domain. Finally, the model consists of approximately 80,000 atoms including about 38,000 representative ones. Representative atoms are emphasized by red color in the sketch of the model.

Following [Coffman et al. 2008b] rolled boundary conditions are applied to the QC model to study the intergranular fracture of arbitrary GBs. Rolled boundary conditions are realized by constraint layers of atoms at all six boundary faces of the model. The thickness of these layers is chosen to fulfill two criteria. First, surface effects in the full atomistic domain shall be restricted to the constrained atoms, what requires a layer thickness of twice the cutoff radius, which is 5.558 Å in the simulations. Second, also in the coarsen domain the influence of free surfaces shall be limited by constraining two layers of representative atoms at the boundary. For this reasons a layer thickness of 14 Å was chosen as illustrated in Figure 5.1. The atomic DOF of the boundary layers are constrained not to move perpendicular to the boundary face or to displace according to the displacement controlled loading conditions, respectively.

material	C_{11}	C_{12}	C_{44}
FCC aluminum	118.1 GPa	62.3 GPa	36.7 GPa

Table 5.1: Elastic constants of FCC aluminum, from [Ercolessi et al. 1994].

5.2.2 Cohesive parameters from tensile simulations

At first, tensile loading on GBs is simulated to extract cohesive parameters, which characterize the process of interface decohesion normal to the interface. Uniform displacements in normal direction of the boundary face are applied step-wise to atoms of the upper and lower boundary layers to force tensile stress at the interface. According to the definitions in Figure 5.1 the displacements are applied in global y-direction. As explained in Section 5.2.1, rolled boundary conditions are assigned to the four remaining boundary layers.

The determination of the interface separation law requires the consideration of a relative interface displacement u at the GB. Therefore, the elastic part u^e has to be subtracted from the applied boundary displacements u^b

$$u = u^b - u^e . \quad (5.1)$$

In case of normal loading the displacement $u_y^{e,gl}$ in global y-direction, which is caused by elastic deformation can be written

$$u_y^{e,gl} = \epsilon_{yy}^{gl} h^e , \quad (5.2)$$

with ϵ_{yy}^{gl} is the effective strain in the global (model) y-direction, and h^e is the height of the elastic model region. As stated in [Coffman et al. 2008b] the use of rolled boundary conditions ensures that no Poisson-effect contraction is caused. Then, according to [Coffman et al. 2008b] the strain ϵ_{yy}^{gl} and the effective tensile stress σ_{yy}^{gl} are linked by the elastic constant C_{22}^{gl} which refers to the global y-direction

$$\sigma_{yy}^{gl} = C_{22}^{gl} \epsilon_{yy}^{gl} . \quad (5.3)$$

Combining Equations (5.1) to (5.3) results in the final formulation to estimate the normal interface opening u_n as follows

$$u_n = u_y^b - \frac{\sigma_{yy}^{gl}}{C_{22}^{gl}} h^e . \quad (5.4)$$

The elastic parameters for the applied EAM potentials from the website of F. Ercolessi [Ercolessi 2009] are specified for FCC aluminum in [Ercolessi et al. 1994]. Table 5.1 lists the three independent elastic parameters, which refer to the main directions of the FCC unit cell. Taking into account the symmetry of FCC crystals by the following dependencies

$$C_{11} = C_{22} = C_{33} , \quad (5.5)$$

$$C_{44} = C_{55} = C_{66} , \quad (5.6)$$

$$C_{12} = C_{21} = C_{13} = C_{31} = C_{23} = C_{32}, \quad (5.7)$$

the transformation of elastic parameters from the crystal unit cell directions into the global model directions can be written for C_{22}^{gl} according to [Wortman et al. 1965]

$$C_{22}^{gl} = C_{22} + (C_{11} - C_{12} - 2C_{44}) (l_2^4 + m_2^4 + n_2^4 - 1), \quad (5.8)$$

with direction cosines l_i , m_i , and n_i defined by

$$x_i^{gl} = l_i x_1 + m_i x_2 + n_i x_3, \quad i = 1, 2, 3. \quad (5.9)$$

The height h^e of the elastic model region is calculated in [Coffman et al. 2008b] by subtracting from the model height the thickness of the upper and lower boundary layer as well as an interface layer thickness, for which a significant higher stiffness is assumed. Since a high accuracy of the determination of interface opening is not possible due to many assumptions and due to the fact that a general size definition for the stiffer interface zone can not be made, these zone is neglected in the present estimate of interface opening. Consequently, the elastic height h^e of the model in Figure 5.1 calculates

$$h^e = 130 \text{ \AA} - 2 \cdot 14 \text{ \AA} = 102 \text{ \AA}.$$

First simulations of the interface decohesion by tensile stress were exemplary performed for a $\Sigma 33 \langle 110 \rangle (2\bar{2}5)$ STGB and for a $\Sigma 11 \langle 110 \rangle (2\bar{2}5)/(4\bar{4}1)$ ATGB using model dimensions according to Figure 5.1. The measured stress-strain curves are illustrated in the left diagram of Figure 5.2 and the derived stress-opening curves related to the normal interface opening are illustrated in the right diagram of the figure. The stress is measured as an average stress from the constrained atoms of the upper and lower boundary layers and the effective strain of the model is calculated by the ratio of the applied boundary displacement to the unconstrained model height, which equals h^e . Additionally, the

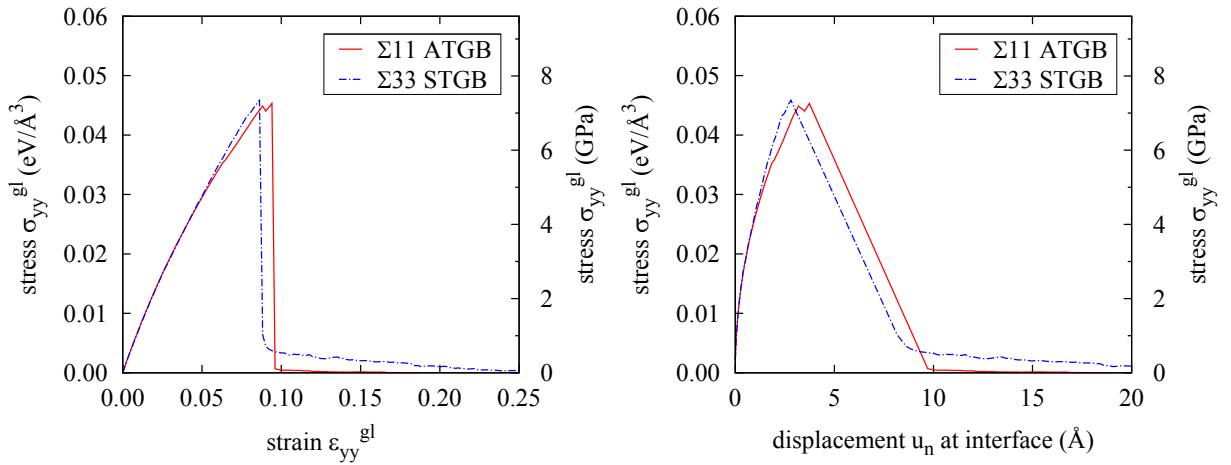


Figure 5.2: Interface separation curves from tensile simulations on aluminum models with $\Sigma 33 \langle 110 \rangle (2\bar{2}5)$ STGB and $\Sigma 11 \langle 110 \rangle (2\bar{2}5)/(4\bar{4}1)$ ATGB, respectively.

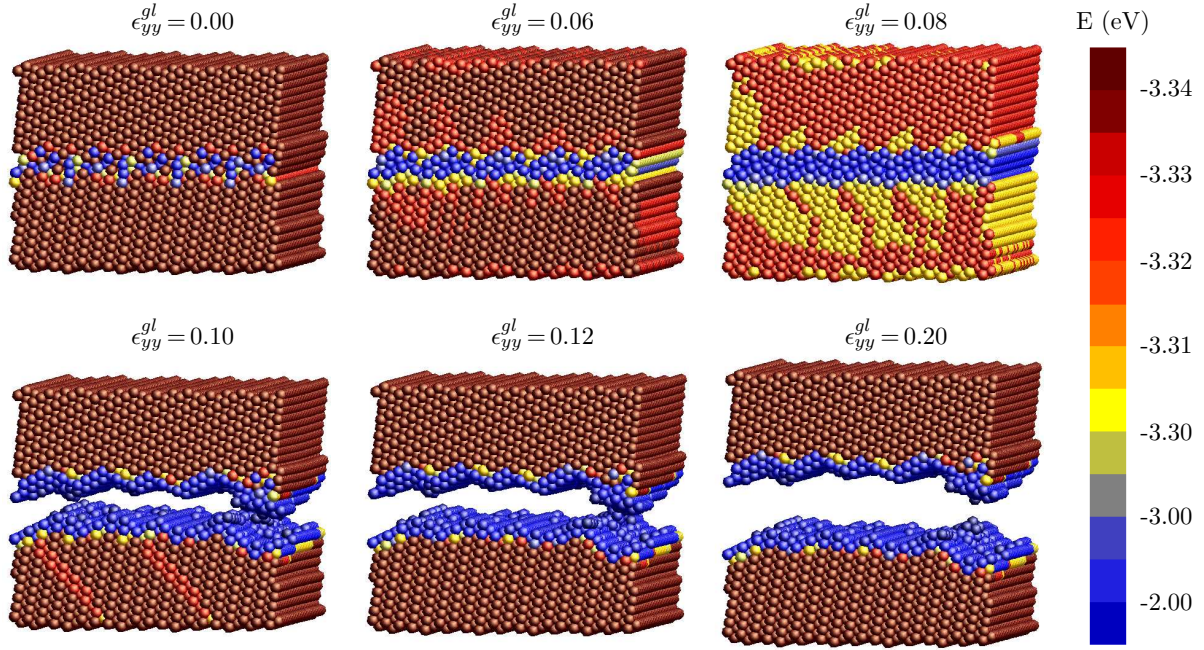


Figure 5.3: Simulated fracture process of $\Sigma 11 \langle 110 \rangle (2\bar{2}\bar{5})/(4\bar{4}\bar{1})$ ATGB under tension. Atoms within a central part of the model are visualized by the energy method. Strain ϵ_{yy}^{gl} means the effective sample strain perpendicular to the interface.

simulated process of intergranular fracture in tension is visualized in Figure 5.3 for the $\Sigma 11 \langle 110 \rangle (2\bar{2}\bar{5})/(4\bar{4}\bar{1})$ ATGB by a sequence of different strain states.

In the following, the influence of sample size on characteristic parameters of the interface separation curve is investigated by tensile simulations on the $\Sigma 33 \langle 110 \rangle (2\bar{2}\bar{5})$ STGB. In a first study only the sample height is varied. Since the thickness of boundary layers remains constant, the variations directly affect the elastic height. The resulting stress-opening curves for three different model heights are illustrated in Figure 5.4. In these curves, variations in the interface peak strength and in the corresponding interface opening are very small. Slightly different slopes in the decohesion path of the stress-opening curves are caused by the error-prone estimate of interface opening from boundary displacements. Concluding, the influence of the sample height to the simulated interface separation curves is negligible.

In a second study, additional to the model height, the size of the interface plane was changed for three tensile tests on the same STGB. The stress-strain curves and stress-opening curves were extracted and are visualized in Figure 5.5. Therefrom, slightly higher variations in the peak strength and the corresponding interface opening are obtained. A small trend of increasing strength with decreasing model size is recognized. This trend is caused by the use of models with free surfaces instead of periodic boundary conditions. Since the measured influence of the model size on the interface separation curves is in a small range, the decision was made to further apply the small model. The decision was also influenced by the high computational costs of the simulations. For example, the

tensile simulations ran about three hours in average doing parallelized computations with six threads on an AMD Opteron server (2.8 GHz) to completely run into the decohesion path.

A summary of all parameters, which are extracted from tensile simulations on the $\Sigma_{11} \langle 110 \rangle (2\bar{2}5)/(4\bar{4}1)$ ATGB and $\Sigma_{33} \langle 110 \rangle (2\bar{2}5)$ STGB using different model sizes, is given in Table 5.2. Therein, $\max \sigma_{yy}^{gl}$ denotes the peak strength and $u_n (\max \sigma_{yy}^{gl})$ indicates the corresponding normal interface opening. The initial stiffness k_n is calculated by

$$k_n = \max \sigma_{yy}^{gl} / u_n (\max \sigma_{yy}^{gl}) . \quad (5.10)$$

The localized fracture energy G_f is obtained from the difference between the GB energy of the relaxed unloaded model (Section 4.3.2) and the specific energy of the fracture surfaces of the broken interface model. The values of G_f vary strongly associated with different crack patterns in the models.

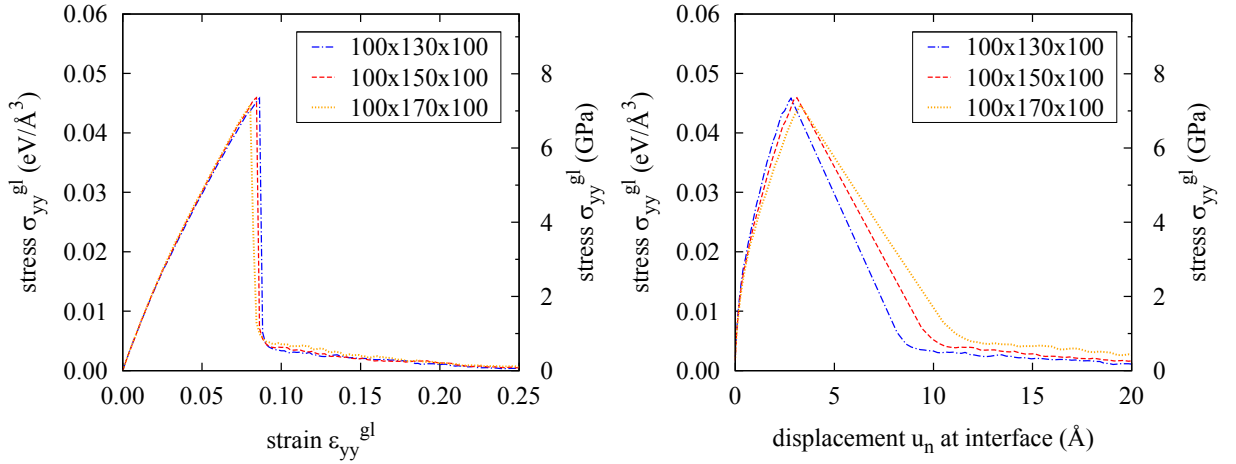


Figure 5.4: Interface separation curves from tensile simulations on aluminum $\Sigma_{33} \langle 110 \rangle (2\bar{2}5)$ STGB models of different sample height.

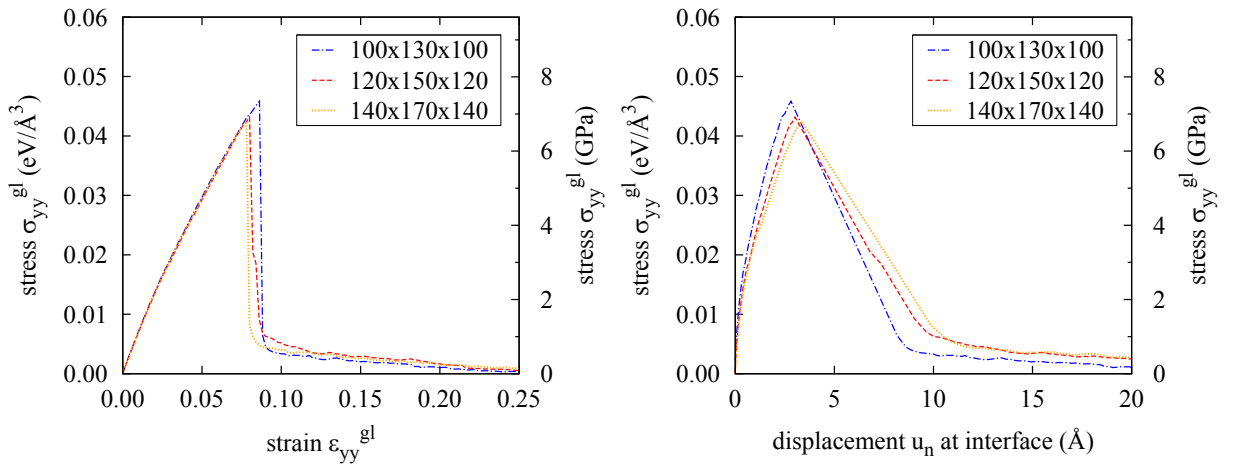


Figure 5.5: Interface separation curves from tensile simulations on aluminum $\Sigma_{33} \langle 110 \rangle (2\bar{2}5)$ STGB models of different sample size.

size of STGB model (ÅxÅxÅ)	$\max \sigma_{yy}^{gl}$ (eV/Å ³)	u_n ($\max \sigma_{yy}^{gl}$) (Å)	k_n (eV/Å ⁴)	G_f (eV/Å ²)
100x170x100	0.0447	3.28	0.0136	0.191
100x150x100	0.0459	3.11	0.0148	0.132
100x130x100	0.0458	2.81	0.0163	0.162
120x150x120	0.0432	3.01	0.0143	0.168
140x170x140	0.0425	3.35	0.0127	0.279

size of ATGB model (ÅxÅxÅ)	$\max \sigma_{yy}^{gl}$ (eV/Å ³)	u_n ($\max \sigma_{yy}^{gl}$) (Å)	k_n (eV/Å ⁴)	G_f (eV/Å ²)
100x130x100	0.0453	3.74	0.0121	0.120

Table 5.2: Cohesive parameters of five aluminum $\Sigma 33 \langle 110 \rangle (2\bar{2}5)$ STGB models and one aluminum $\Sigma 11 \langle 110 \rangle (2\bar{2}5)/(4\bar{4}1)$ ATGB model, extracted from tensile simulations.

5.2.3 Cohesive parameters from shear simulations

In a next step shear loading is simulated to extract cohesive parameters which characterize the process of GB decohesion tangential to the interface. Uniform displacements in tangential direction of the boundary face are applied step-wise to atoms of the upper and lower boundary layers to force shear stress at the interface. While in 3D tangential displacements are possible in various directions in planes parallel to the GB, the study is restricted to displacements applied parallel to global x-axis and parallel to global z-axis according to the definition in Figure 5.1.

The atomic DOF in direction of shear loading have to remain unconstrained in the interface region to enable shear fracture by relative displacements of the adjacent crystallites against each other. Consequently, roller boundary conditions are applied only to the appropriate boundary layers in x-direction when shear loading is applied in z-direction, and vice versa. Additionally, atomic DOF of the upper and lower boundary layers are fixed not to move perpendicular to the boundary face. Therewith, the process of intergranular fracture by shear loading is not reproduced exactly, but as best as possible in the framework of discrete atomistic models. The problem of simulating intergranular fracture by shear loading is discussed in detail in [Spearot et al. 2004].

Following the remarks in Section 5.2.2 the elastic displacement parts $u_x^{e,gl}$ and $u_z^{e,gl}$ have to be subtracted from tangential boundary displacements u_x^b and u_z^b respectively to obtain the relative tangential displacements of two crystallites at the interface. The elastic displacement parts approximately calculate from the shear distortion γ_{xy}^{gl} and γ_{yz}^{gl}

respectively as follows

$$u_x^{e,gl} = \tan(\gamma_{xy}^{gl}) h^e, \quad u_z^{e,gl} = \tan(\gamma_{yz}^{gl}) h^e. \quad (5.11)$$

The shear distortions and the shear stresses are linked by the appropriate elastic constants C_{66}^{gl} and C_{44}^{gl} in the global CS

$$\sigma_{xy}^{gl} = C_{66}^{gl} \gamma_{xy}^{gl}, \quad \sigma_{yz}^{gl} = C_{44}^{gl} \gamma_{yz}^{gl}. \quad (5.12)$$

The relative tangential displacements $u_{t,x}$ and $u_{t,z}$ of the two crystallites at the interface can be obtained from

$$u_{t,x} = u_x^b - \tan\left(\frac{\sigma_{xy}^{gl}}{C_{66}^{gl}}\right) h^e, \quad u_{t,z} = u_z^b - \tan\left(\frac{\sigma_{yz}^{gl}}{C_{44}^{gl}}\right) h^e. \quad (5.13)$$

Considering the direction cosines l_i , m_i , and n_i of Equation (5.9) the global elastic constants calculate from the local one again by transformation according to [Wortman et al. 1965]

$$\begin{aligned} C_{66}^{gl} &= C_{66} + (C_{11} - C_{12} - 2C_{44}) (l_1^2 l_2^2 + m_1^2 m_2^2 + n_1^2 n_2^2), \\ C_{44}^{gl} &= C_{44} + (C_{11} - C_{12} - 2C_{44}) (l_2^2 l_3^2 + m_2^2 m_3^2 + n_2^2 n_3^2). \end{aligned} \quad (5.14)$$

As stated previously, in case of shear fracture the shear direction plays an important role due to the influence of crystallography. Accordingly, different fracture behavior is expected for shear simulations with displacements in one direction and in the opposite direction. A similar experience is documented, for example, in [Yamakov et al. 2006] for simulating intergranular crack propagation in different directions. Thus, a first investigation of intergranular shear fracture by boundary displacements parallel to global x-axis

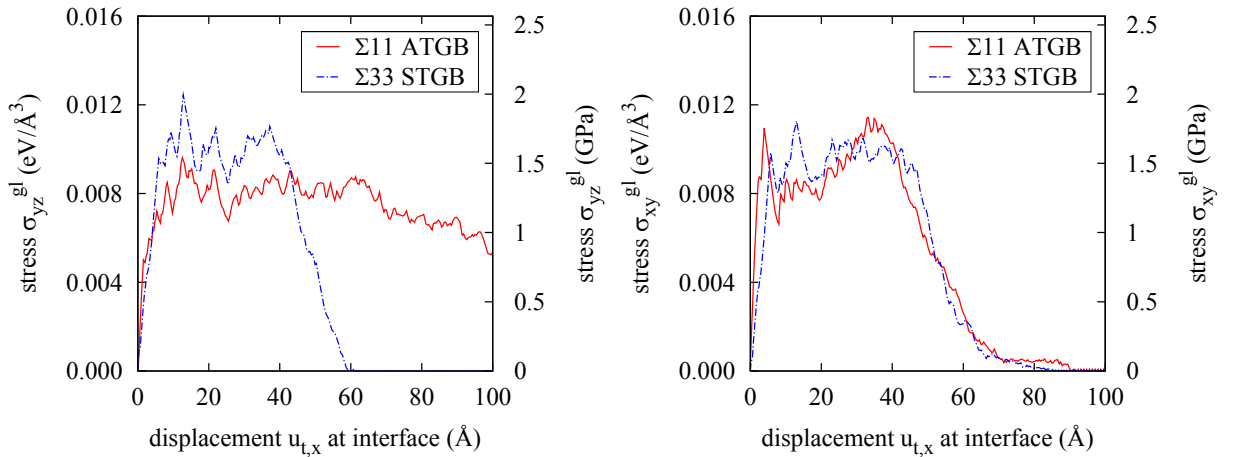


Figure 5.6: Interface separation curves from shear simulations on aluminum models with $\Sigma 33 \langle 110 \rangle (2\bar{2}5)$ STGB and $\Sigma 11 \langle 110 \rangle (2\bar{2}5)/(4\bar{4}1)$ ATGB, respectively. Boundary displacements are applied parallel to the global x-axis in positive (left diagram) and negative (right diagram) direction.

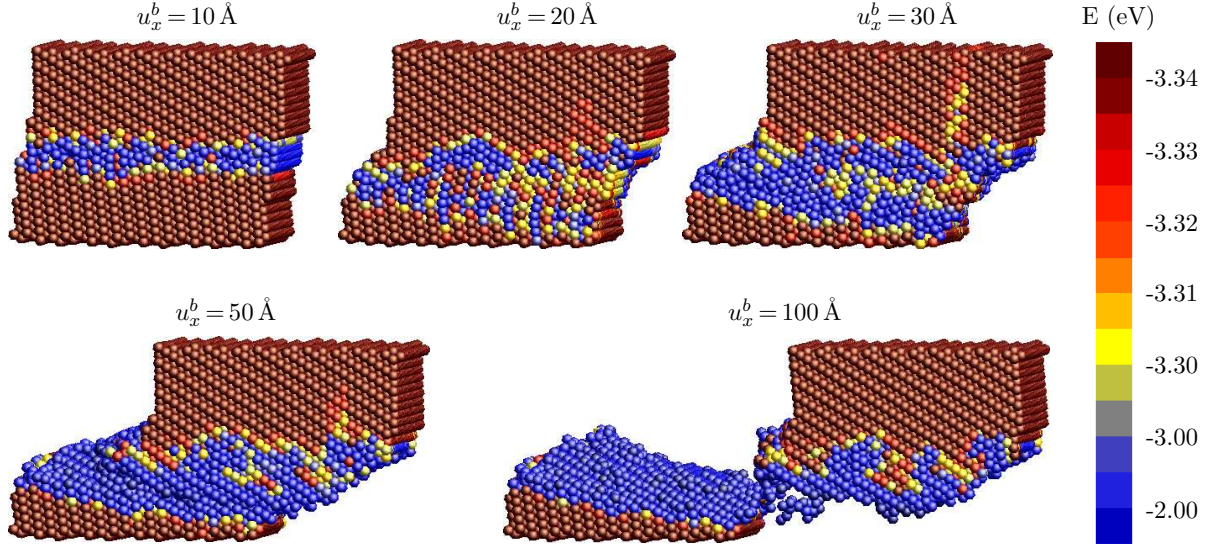


Figure 5.7: Simulated fracture process of $\Sigma_{11} \langle 110 \rangle (2\bar{2}5)/(4\bar{4}1)$ ATGB under shear in negative x-direction. Atoms within a central part of the model are visualized by their potential energy values. Displacement u_x^b refers to the relative x-displacement of the upper boundary layer compared to the lower boundary layer.

is performed twice, applying boundary displacements in positive x-direction and in negative x-direction. Again, the model dimensions are $100 \text{ \AA} \times 130 \text{ \AA} \times 100 \text{ \AA}$ corresponding to Figure 5.1. The resulting stress-opening curves of the investigated $\Sigma_{11} \langle 110 \rangle (2\bar{2}5)/(4\bar{4}1)$ ATGB and $\Sigma_{33} \langle 110 \rangle (2\bar{2}5)$ STGB are drawn in Figure 5.6. While the STGB has shown similar fracture behavior for both shear directions, the ATGB behaves highly different depending on the direction of shear. This proves that several shear directions should be investigated to obtain reasonable information on the shear fracture characteristics of a GB. Figure 5.7 visualizes the fracture process of shear parallel to the global x-axis by a

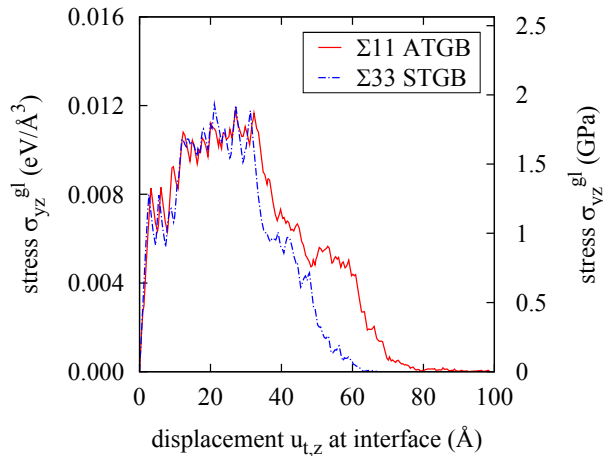


Figure 5.8: Interface separation curves from shear simulations on aluminum models with $\Sigma_{33} \langle 110 \rangle (2\bar{2}5)$ STGB and $\Sigma_{11} \langle 110 \rangle (2\bar{2}5)/(4\bar{4}1)$ ATGB, respectively. Boundary displacements are applied parallel to the global z-axis.

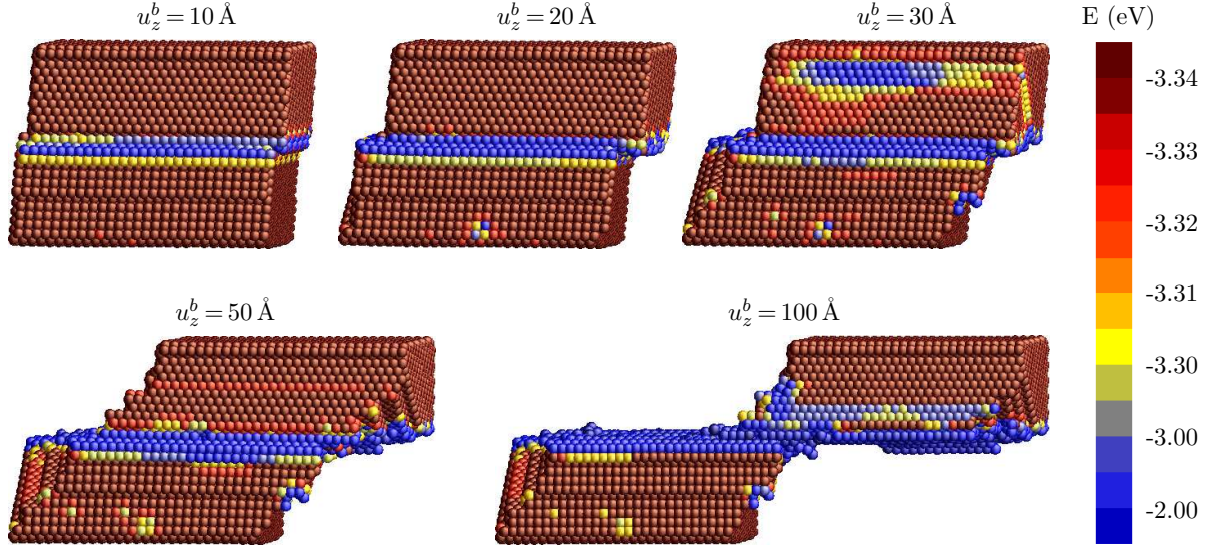


Figure 5.9: Simulated fracture process of $\Sigma_{11} \langle 110 \rangle (2\bar{2}5)/(4\bar{4}1)$ ATGB under shear in z-direction. Atoms within a central part of the model are visualized by their potential energy values. Displacement u_z^b refers to the relative z-displacement of the upper boundary layer compared to the lower boundary layer.

sequence of subsequent deformation states of the $\Sigma_{11} \langle 110 \rangle (2\bar{2}5)/(4\bar{4}1)$ ATGB. Therein, the atomic representations are restricted to a central part of the full atomistic model domain around the interface. The pictures show that compared to the appropriate tensile simulation (Figure 5.3) the simulated shear fracture process is not restricted to the GB only, but spreads into the lower crystallite.

Investigations of the same STGB and ATGB are done concerning their fracture behavior caused by shear parallel to global z-axis. Since for each of these GBs the global z-axis is parallel to the $[110]$ direction of both modeled crystallites, the crystallographic influence is the same for relative boundary displacements in positive z-directions as well as in negative z-directions. For this reason, only one simulation of shear in z-direction is documented for a particular GB configuration. The resulting stress-opening curves of investigated $\Sigma_{11} \langle 110 \rangle (2\bar{2}5)/(4\bar{4}1)$ ATGB and $\Sigma_{33} \langle 110 \rangle (2\bar{2}5)$ STGB are drawn in Figure 5.8. Additionally, Figure 5.9 visualizes the fracture process of shear parallel to the global z-axis by a sequence of subsequent deformation states of the $\Sigma_{11} \langle 110 \rangle (2\bar{2}5)/(4\bar{4}1)$ ATGB. Again, the fracture process is bounded to a small zone around the interface similar to the tensile simulation.

A summary of all parameters which are extracted from shear simulations on the $\Sigma_{11} \langle 110 \rangle (2\bar{2}5)/(4\bar{4}1)$ ATGB and on the $\Sigma_{33} \langle 110 \rangle (2\bar{2}5)$ STGB is given in Table 5.3. The table also documents the investigated influence of model size on the shear strength $\max \sigma_{xy(+x)}^{gl}$ for boundary displacements in positive x-direction. The same model sizes are studied as in tensile simulations, but no significant trend was identified. Nevertheless, a general variation in shear strength values of about fifteen per cent is observed from these simulations.

size of STGB model ($\text{\AA}\times\text{\AA}\times\text{\AA}$)	$\max \sigma_{xy(+x)}^{gl}$ ($\text{eV}/\text{\AA}^3$)	$\max \sigma_{xy(-x)}^{gl}$ ($\text{eV}/\text{\AA}^3$)	$\max \sigma_{yz}^{gl}$ ($\text{eV}/\text{\AA}^3$)	$\max \sigma_{shear}^{gl}$ ($\text{eV}/\text{\AA}^3$)	G_f ($\text{eV}/\text{\AA}^2$)
100x170x100	0.0128	-	-	-	-
100x150x100	0.0114	-	-	-	-
100x130x100	0.0124	0.0113	0.0121	0.0120	0.156
120x150x120	0.0109	-	-	-	-
140x170x140	0.0120	-	-	-	-

size of ATGB model ($\text{\AA}\times\text{\AA}\times\text{\AA}$)	$\max \sigma_{xy(+x)}^{gl}$ ($\text{eV}/\text{\AA}^3$)	$\max \sigma_{xy(-x)}^{gl}$ ($\text{eV}/\text{\AA}^3$)	$\max \sigma_{yz}^{gl}$ ($\text{eV}/\text{\AA}^3$)	$\max \sigma_{shear}^{gl}$ ($\text{eV}/\text{\AA}^3$)	G_f ($\text{eV}/\text{\AA}^2$)
100x130x100	0.0096	0.0114	0.0118	0.0112	0.193

Table 5.3: Cohesive parameters extracted from shear simulations on five aluminum $\Sigma 33 \langle 110 \rangle (2\bar{2}5)$ STGB models and one aluminum $\Sigma 11 \langle 110 \rangle (2\bar{2}5)/(4\bar{4}1)$ ATGB model.

In order to integrate the cohesive parameters of intergranular shear fracture into a coupled CZM, the parameters of different shear directions are summarized to only one parameter. According to the definitions of the presently chosen coupled CZM (Section 5.2.4) an average shear strength and an average fracture energy have to be transmitted from the shear simulations to the coupled CZM formulation of the appropriate interface. Exemplary, in Table 5.3 the average shear strength $\max \sigma_{shear}^{gl}$ is calculated from the three performed simulations of shear in positive x-direction, in negative x-direction and in z-direction, by

$$\max \sigma_{shear}^{gl} = \frac{1}{4} \left(\max \sigma_{xy(+x)}^{gl} + \max \sigma_{xy(-x)}^{gl} + 2 \cdot \max \sigma_{yz}^{gl} \right). \quad (5.15)$$

The calculation of averaged localized fracture energy G_f is done equivalently.

Although the presented thesis restricts to the methodology of extracting cohesive parameters from 3D microscale simulations of intergranular fracture, the observed variations in the cohesive parameters motivate a stochastic study in subsequent research. As well, the influence of shear directions on shear fracture characteristics taking into account the crystallography around interfaces opens a novel field of research.

5.2.4 Combining properties from normal and shear loading in a coupled CZM

A reversible coupled CZM is assigned to the interface elements on the mesoscale to simulate crack propagation along GBs. The coupled CZM was available in the software package SLang, which is developed and used at the Institute. Since the main intention is to extract constitutive parameters of the coupled CZM from atomistic scale simulations,

the coupled CZM and the applied TSL are described in the following and the necessary constitutive parameters are specified.

A TSL with sharp peak and exponential decohesion path was used in the previous studies. In principle, the TSL has to be chosen carefully according to the aimed application since the shape of the TSL as well as the strength and the cohesive energy can considerably influence the mechanical response of the system [Chandra et al. 2002]. The generic TSL of the coupled CZM which was applied in [Luther et al. 2009] is shown in Figure 5.10 and was formulated by [Unger et al. 2007] as follows

$$t(\lambda) = \begin{cases} k_n \cdot \lambda & \text{for } \lambda < \lambda_0 \\ t_p \cdot e^{\frac{-t_p \cdot (\lambda - \lambda_0)}{G_f}} & \text{for } \lambda \geq \lambda_0 \end{cases}, \quad (5.16)$$

with the relative displacement

$$\lambda = \sqrt{u_n^2 + (\alpha u_t)^2} \quad \text{if } u_n > 0, \quad \text{otherwise } \lambda = |\alpha u_t| \quad (5.17)$$

and

$$\lambda_0 = \frac{t_p}{k_n}, \quad (5.18)$$

where λ_0 is the maximal relative crack opening of the linear elastic path. The model is sufficiently defined by the initial normal stiffness k_n , the peak strength t_p , the localized fracture energy G_f , and the material constant α that controls the ratio between normal and tangential interface opening. The coupling of the interface opening in normal direction u_n and the relative tangential slip of the two interface surfaces u_t is realized by introducing a relative displacement λ according to [Tvergaard 2003]. The relation for λ is given in Equation (5.17). As outlined in [Unger et al. 2007] the coupling of normal and tangential interface opening by the introduction of λ and the description of the total potential as a function of the mixed displacements lead to a symmetric stiffness matrix, which

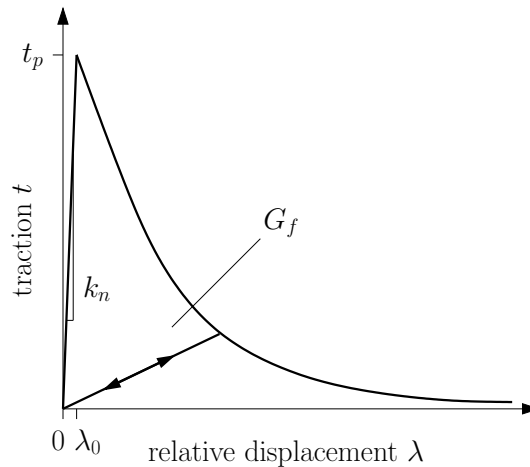


Figure 5.10: TSL of the coupled CZM which is assigned to interfaces in continuum polycrystal models.

benefits the numerical simulation. The localized fracture energy G_f rules the ductility or brittleness respectively of the cohesive interfaces. However, the identification of the interface parameters of engineering materials is non-trivial and establishes an own field of research. Consequently, this was one reason for the detailed investigation of the interface damage behavior on the atomistic scale taking into account the physical sources of damage.

The normal and tangential traction of the applied TSL are computed by the assumption of an existing potential $\Phi(u_n, u_t)$ as follows

$$T_n = \frac{\partial \Phi(u_n, u_t)}{\partial u_n} = t(\lambda) \frac{u_n}{\lambda} \quad (5.19)$$

and

$$T_t = \frac{\partial \Phi(u_n, u_t)}{\partial u_t} = t(\lambda) \frac{\alpha^2 u_t}{\lambda}. \quad (5.20)$$

In case of unloading the cohesive model assumes a linear path back to the origin

$$T_n = t(\lambda_{max}) \frac{u_n}{\lambda_{max}} \quad (5.21)$$

and

$$T_t = t(\lambda_{max}) \frac{\alpha^2 u_t}{\lambda_{max}}, \quad (5.22)$$

and the interface stiffness is adequately reduced if the decohesion path was reached in the loading process ($\lambda_{max} > \lambda_0$). Restricting to normal traction at the interface simplifies Equation (5.19) to

$$T_n = t(\lambda = u_n), \quad (5.23)$$

from which the definition of maximal interface strength t_p , also named peak strength, is

$$t_p = T_{n,p}. \quad (5.24)$$

$T_{n,p}$ is the maximal tensile strength of the interface

$$T_{n,p} = \max \sigma_{yy}^{gl},$$

as it is exemplary extracted in Section 5.2.2 from atomistic simulations. Restricting to tangential traction at the interface simplifies Equation (5.20) to

$$T_t = \text{sgn}(u_t) \cdot \alpha \cdot t(\lambda = |\alpha u_t|), \quad (5.25)$$

which results in the following relation of maximal strength values

$$|T_{t,p}| = \alpha \cdot t_p. \quad (5.26)$$

$|T_{t,p}|$ is the maximal absolute shear strength of the interface

$$|T_{t,p}| = \max \sigma_{yz}^{gl},$$

GB type	$T_{t,p}$ (GPa)	$T_{n,p} = t_p$ (GPa)	α (-)	k_n (GPa/mm)	G_f (N/mm)
$\Sigma 33 \langle 110 \rangle (2\bar{2}5)$ STGB	1.92	7.34	0.262	$2.61 \cdot 10^7$	0.00255
$\Sigma 11 \langle 110 \rangle (2\bar{2}5)/(4\bar{4}1)$ ATGB	1.79	7.26	0.247	$1.94 \cdot 10^7$	0.00251

Table 5.4: Atomistic-based constitutive parameters of a coupled CZM, exemplary derived for two different aluminum GBs.

as it is exemplary determined in Section 5.2.3 from atomistic simulations. Substituting Equation (5.24) into Equation (5.26) yields the definition of parameter α

$$\alpha = \frac{|T_{t,p}|}{T_{n,p}}. \quad (5.27)$$

Finally, the constitutive parameters which are exemplary derived for the $\Sigma 33 \langle 110 \rangle (2\bar{2}5)$ STGB and for the $\Sigma 11 \langle 110 \rangle (2\bar{2}5)/(4\bar{4}1)$ ATGB from atomistic-based microscale simulations are summarized in Table 5.4. While these parameters were given in atomistic units before, they are now converted in usual engineering units for applications on the mesoscale. The conversion from units which are used on the atomistic informed microscale into units of the continuum mesoscale is as follows

$$G_f : 1 \left(\frac{\text{eV}}{\text{\AA}^2} \right) = 1.602 \cdot 10^{-2} \left(\frac{\text{N}}{\text{mm}} \right), \quad (5.28)$$

$$T_{t,p}, T_{n,p}, t_p : 1 \left(\frac{\text{eV}}{\text{\AA}^3} \right) = 1.602 \cdot 10^2 \text{ (GPa)}, \quad (5.29)$$

$$k_n : 1 \left(\frac{\text{eV}}{\text{\AA}^4} \right) = 1.602 \cdot 10^9 \left(\frac{\text{GPa}}{\text{mm}} \right). \quad (5.30)$$

The resulting TSLs of the coupled CZM are illustrated in Figure 5.11 for the two investigated GB configurations.

Cohesive parameters which are extracted from microscale simulations show significant deviations compared to their macroscopic counterparts which are used in engineering models. Macroscopic values of cohesive zone representations are listed in Table 6.1 of the following chapter. For instance, the extracted values of cohesive peak strength are about ten times higher than the range of natural GB strength values. There are several reasons for this mismatch. One reason is the simulated fracture process on perfect GBs, while natural GBs consist of more defects than only the misorientation. Being aware of the importance of defects in crystalline materials, the next step of modeling and analyzing imperfect GBs starts with Section 5.3.

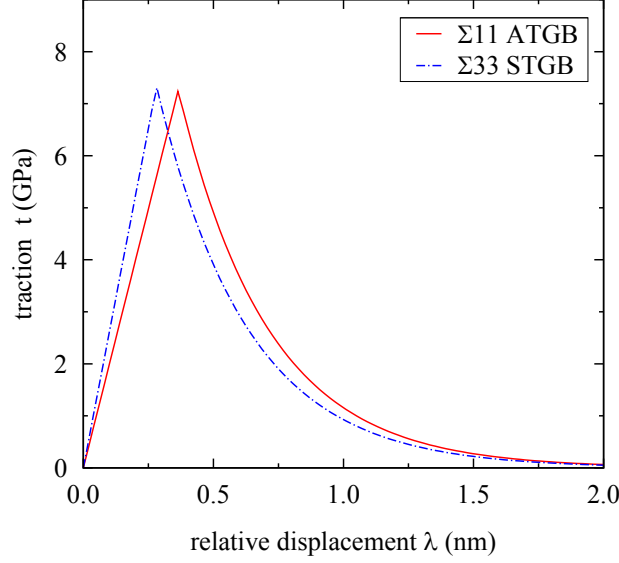


Figure 5.11: Atomistic-based traction separation laws of the coupled CZM for an aluminum $\Sigma 33 \langle 110 \rangle (2\bar{2}5)$ STGB and an aluminum $\Sigma 11 \langle 110 \rangle (2\bar{2}5)/(4\bar{4}1)$ ATGB, respectively.

5.3 Influence of atomic level defects on grain boundary characteristics

5.3.1 Measurement of nanoporosity near interfaces

On the atomic level a measure of nanoporosity corresponding to the number of broken bonds was introduced in [Spearot et al. 2004] and [Spearot 2005] by investigating bonds to atomic neighbors of first order. In the following, this measure is used to define damage in the region of interfaces. The measurement of nanoporosity examines the bonds of an atom to its first-nearest neighbors, whose number is expressed by the reference first-order coordination number Z_{ref} , which is 12 in case of FCC crystals, like aluminum. If the number of first-nearest neighbors remains 12 in the deformed configuration, the damage parameter D_i of an atom i is 0 and no damage is detected. By contrast, a damage parameter $D_i = 1$ corresponds to the threshold first-order coordination number Z_{th} , which is 8 for FCC crystals. The value $Z_{th} = 8$ indicates surface atoms, which are characterized by the complete lost of atomic bonds in one direction. With the determined first-order coordination number Z_i of an atom i the associated damage parameter D_i for point-wise damage measure is defined according to [Spearot et al. 2004] by

$$D_i = 1 - \left\langle \frac{Z_i - Z_{th}}{Z_{ref} - Z_{th}} \right\rangle. \quad (5.31)$$

The expression within angle brackets is set 0 if it is lower 0 and is set 1 if it is greater 1. This convention is necessary, since the numerical calculation of Z_i can lead to values lower Z_{th} or greater Z_{ref} .

GB type	D_c of initial GB	D_c of broken GB
$\Sigma 33 \langle 110 \rangle (2\bar{2}5)$ STGB	0.035	0.204
$\Sigma 11 \langle 110 \rangle (2\bar{2}5)/(4\bar{4}1)$ ATGB	0.042	0.221

Table 5.5: Measured values of nanoporosity for initial and broken configurations of two different GBs.

The point-wise damage measure can be averaged over a set of atoms within a statistical volume, which leads to the cumulative measure of damage by the parameter D_c

$$D_c = \frac{1}{\hat{N}} \sum_{i=1}^{\hat{N}} D_i = \frac{1}{\hat{N}} \sum_{i=1}^{\hat{N}} \left(1 - \left\langle \frac{Z_i - Z_{th}}{Z_{ref} - Z_{th}} \right\rangle \right), \quad (5.32)$$

with \hat{N} is the number of atoms within the statistical volume minus the number of *naturally damaged* atoms at free boundary surfaces in the initial state.

In atomistic simulations of GB decohesion the nanoporosity expressed by D_c was measured within a statistical volume defined by a zone of ± 10 Å around the interface. The resulting nanoporosities of two different GBs are given in Table 5.5 for the initial and for the completely broken state. Since GBs are natural defects in polycrystalline structures they always come along with an initial damage $D_c > 0$ depending on the complexity of the interface. The values of D_c of broken GBs depend on the size of the statistical volume and are lower 1. Assuming a constant statistical volume, higher D_c values of broken configurations correspond to higher roughness of fracture surfaces.

Figure 5.12 illustrates for tensile and shear simulations on the $\Sigma 11 \langle 110 \rangle (2\bar{2}5)/(4\bar{4}1)$ ATGB that the evolution of nanoporosity measured by D_c directly corresponds to the formation of fracture surfaces measured by the interface energy. The dependency of nanoporosity on the stress at interfaces is illustrated in Figure 5.13. The diagrams of the two figures show that the measured nanoporosity correlates with corresponding energy

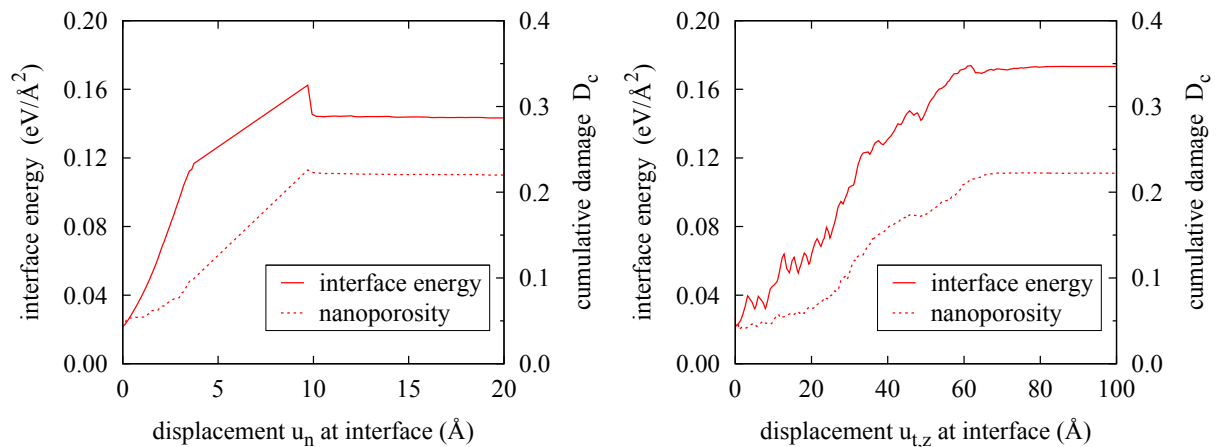


Figure 5.12: Evolution of interface energy and nanoporosity in tensile (left) and shear (right) simulations on the $\Sigma 11 \langle 110 \rangle (2\bar{2}5)/(4\bar{4}1)$ ATGB.

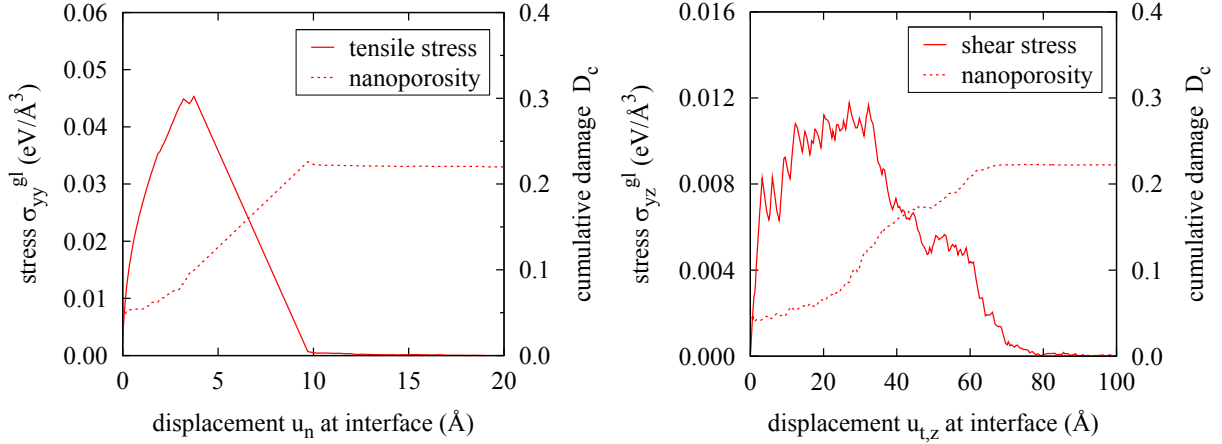


Figure 5.13: Evolution of nanoporosity compared to the stress state of the $\Sigma 11 \langle 110 \rangle (2\bar{2}5)/(4\bar{4}1)$ ATGB in tensile (left) and shear (right) simulations.

and stress states at the GB. Therefrom, the conclusion is drawn that this damage measure is well suited to capture the interfacial damage evolution.

5.3.2 Effect of introduced point vacancies near interfaces

The influence of artificially introduced atomic level defects on mechanical GB characteristics shall be investigated. A first step in the realization of this intention is done by the introduction of point vacancies near interfaces. This ensures the applicability of the same potential functions as before to describe the interaction forces between atoms. By contrast, the introduction of chemical impurities at GBs would mean the assembling of atoms of different chemical materials, which needs the application of special potential functions. Since only a few potential functions for the interaction of different chemical materials exist in the literature [Mishin 2009] [Ercolessi 2009] and their derivation is a non-trivial physical problem of ongoing research, the presented investigation of atomic level defects is restricted to randomly introduced point vacancies.

A former study of the influence of vacancies at interfaces was published by [Gall et al. 2000]. This paper documents the effects of randomly dispersed point vacancies at an aluminum-silicon interface on the average stress-strain response of atomistic models in tension. Although up to 25% vacancies were introduced in the first two atomic planes near the interface, only a slight reduction in the tensile strength was obtained from defected interfaces. However, it was stated that according to [Meyers et al. 1984] the overall concentration of vacancies traditionally found in metals is less than 1%. From that, [Gall et al. 2000] concluded that the reduction in tensile strength due to randomly dispersed vacancies is negligible. In this paper further investigations were done for the influence of crack-like vacancies in the bulk material, but it was found by the authors that very large vacancies are necessary to cause failure in the bulk material instead along the interface.

In the study of the presented dissertation, point vacancies are randomly dispersed

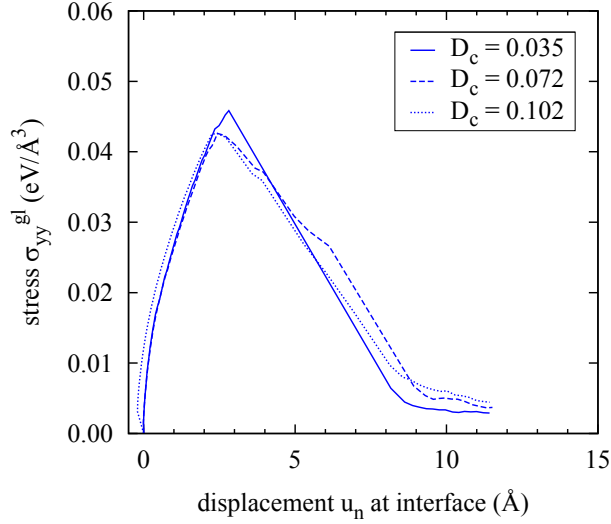


Figure 5.14: Average stress-opening response curves of an aluminum $\Sigma 33 \langle 110 \rangle (2\bar{2}5)$ STGB with different levels of initial damage D_c .

in a zone of $\pm 5 \text{ \AA}$ around relaxed aluminum GBs and tensile and shear simulations are analyzed by their resulting average stress-opening response. In order to start the simulations from an equilibrium configuration of the atomic system the defected GB models are relaxed without loading. As a result the introduced point vacancies are not preserved, but the measured initial nanoporosity in the relaxed pre-defected interface structures is increased compared to perfect GBs. Consequently, the nanoporosity parameter D_c , calculated according to Section 5.3.1 in the relaxed pre-defected interface structure, is used as a measure of the pre-existing defects along the interface.

The average stress-opening response curves of an aluminum $\Sigma 33 \langle 110 \rangle (2\bar{2}5)$ STGB with different levels of initial damage D_c , from 3.5% of the perfect GB up to 10%, are illustrated in Figure 5.14. These curves show less dependency on additionally introduced

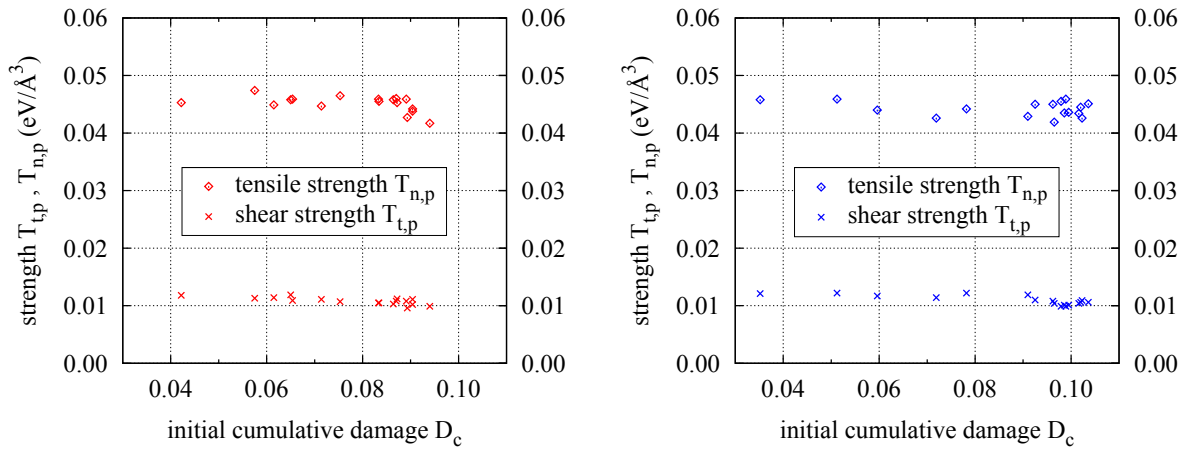


Figure 5.15: Tensile and shear strength vs initial cumulative damage of an aluminum $\Sigma 11 \langle 110 \rangle (2\bar{2}5)/(4\bar{1}1)$ ATGB (left) and an aluminum $\Sigma 33 \langle 110 \rangle (2\bar{2}5)$ STGB (right).

vacancies. The extracted tensile and shear strength of investigated GB configurations with various initial damage are visualized in the diagrams of Figure 5.15. These diagrams show that the slight trend to reduced strengths in case of increasing initial nanoporosity near the interface is negligible for the presently studied aluminum GBs. Therewith, the investigation confirms the outcomes of [Gall et al. 2000].

Suggestions of further advancements in atomistic GB models, which in future are necessary to capture the mechanical behavior of imperfect GBs, follow in the outlook (Chapter 8).

Chapter 6

Polycrystal modeling on the mesoscale

6.1 A review on polycrystal modeling and damage mechanics

Typically, random micro structures are generated to reflect the geometry of polycrystals, for example ceramics or metals, on the mesoscale. Exemplary, [Raabe 1998] and [Torquato 2002] give comprehensive overviews on random microstructures. These microstructures are frequently generated using a Voronoi tessellation or grain growth algorithms. Grain growth can be simulated based on initially defined Voronoi diagrams as well [Raabe 1998] or completely on nucleation and growth as done by [Thompson 2000] and [Fayad et al. 1999]. In the context of fracture and damage mechanics the application of Voronoi diagrams has been accepted to generate polycrystal models, especially for the analysis of brittle material behavior of ceramics [D'Addetta et al. 2001] [Ibrahimbegovic et al. 2003] and metals [Toi et al. 1995] [Ingraffea et al. 2002] [Iesulauro et al. 2002]. The present chapter refers to the analysis of the intergranular fracture process in metallic polycrystals similar to the papers published by [Ingraffea et al. 2002] and [Iesulauro et al. 2002]. Their model is characterized by the introduction of cohesive interfaces along GBs to allow for the natural initiation of intergranular cracks in numerical 2D samples of aluminum. In [Ingraffea et al. 2002] the Voronoi-based polycrystal model was extended for highly parallelized computations in 3D using a simple coupled cohesive zone approach. Because of the advance in computational capacities in the last years, there is the ability to perform computations using more complex models as well in 3D on standard PC's, now.

In engineering science damage phenomena are often simulated by material models of continuum damage mechanics. Based on representative volume elements (RVE), the relation between stress and strain rates is defined by material tensors. The process of damage is considered in the constitutive equations by additional internal variables, which describe the quantity of damage within the RVE. In dependency of the relevant internal variables, damage evolution laws are able to predict changes in the state of damage.

Overviews on continuum damage mechanics are given, for example, in [Kachanov 1986], [Krajcinovic 1998], and [Lemaitre 1992]. The continuum damage models can be distinguished in phenomenological models, which design idealized mathematical models to cover the mechanical and thermodynamical material behavior [McClintock 1968] [Gurson 1977] [Chaboche 1988a] [Chaboche 1988b] [Tvergaard 1990] and multiscale models, which homogenize meso- or microscopic material descriptions [Bazant 1987] [Maugnin 1992]. The second way is followed by the hierarchical multiscale concept proposed in the presented thesis. Within this concept, a cohesive zone model (CZM) is used on the mesoscale to simulate the intergranular fracture process. An introduction to cohesive zone models was given in Section 5.1.

6.2 Geometrical features

6.2.1 Classical 2D and 3D Voronoi diagrams

The application of classical Voronoi algorithms [Aurenhammer 1991] [Okabe et al. 1992] to generate polycrystalline material structures has become state of the art in polycrystal modeling on the mesoscale. The advantage of a classical Voronoi diagram (Figure 6.1), as applied in [Ingraffea et al. 2002] and [Iesulauro et al. 2002], is given by the simplicity of its algorithm and its random characteristics. However, classical Voronoi diagrams are not well adapted to flexibly reproduce a realistic grain size distribution in polycrystalline materials (Figure 6.2). Experimental measurements have proven that in steady state the grain size distribution is better fit by a lognormal distribution function [Kirchner 2001] [Thompson 1990] or a Weibull distribution function [Fayad et al. 1999]. Figure 6.3 shows a cumulative grain size distribution function in heat treated thin layer aluminum measured by [Kirchner 2001] and compared to a Voronoi grain size distribution function and a lognormal distribution function. In grain size distribution functions the size of a single grain is defined by the diameter d of a circle with equivalent area. The plotted cumulative

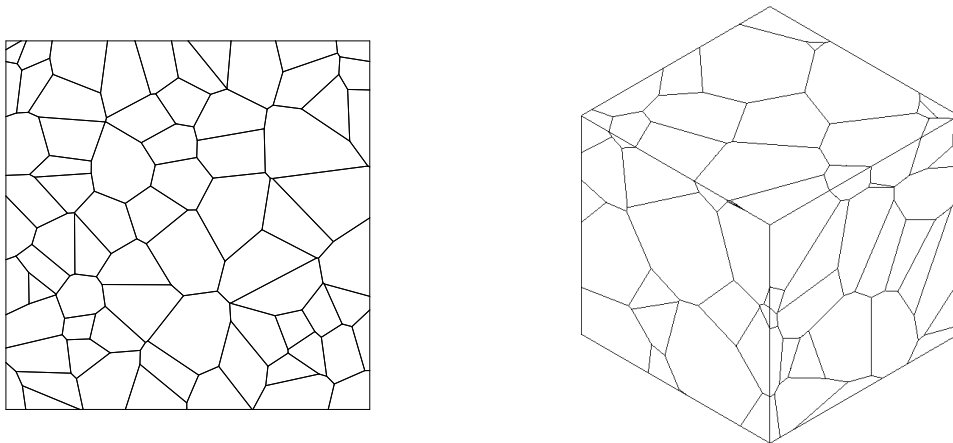


Figure 6.1: Classical 2D and 3D Voronoi diagrams.

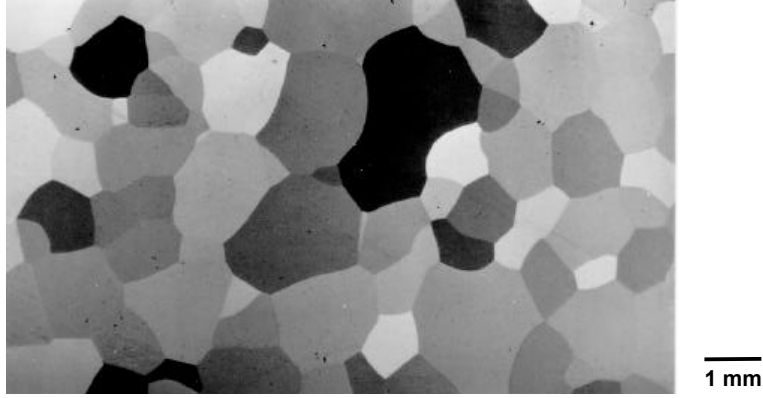


Figure 6.2: Light microscopy photograph of an Al-Si-Ge grain structure (from [Kirchner 2001]).

lognormal distribution function is computed with the median value $d_{50} = 0.94 \mu\text{m}$ and the standard deviation $\sigma_d = 0.78$ that was measured in [Kirchner 2001]. The Voronoi grain size distribution was calculated by means of generated classical Voronoi diagrams with the same median value.

6.2.2 Modified 2D Voronoi diagram

Based on the drawn conclusion the classical Voronoi algorithm was modified to generate more realistic 2D grain structures of polycrystals [Luther et al. 2009]. The concept follows the approach to predefine the size of single grains according to a specified grain size distribution and to construct a modified Voronoi diagram considering this a priori information. In the following the lognormal distribution function $f_{LN}(d)$ is applied as starting point for the grain structure generation

$$f_{LN}(d) = \frac{1}{\sigma_d d \sqrt{2\pi}} e^{-\left(\frac{1}{\sqrt{2}\sigma_d} \ln(d/d_{50})\right)^2}, \quad (6.1)$$

where the median grain size d_{50} and the standard deviation σ_d are the two variable distribution parameters. Alternatively, a Weibull distribution function $f_W(d)$ is defined by the two variable distribution parameters a and b Nevertheless

$$f_W(d) = \frac{b}{a^b} d^{b-1} e^{-(d/a)^b}. \quad (6.2)$$

The main advantage of the lognormal distribution function is the straightforward interpretation of the associated distribution parameters, which is not given in case of Weibull distribution.

In a first step the grain structure generation starts with a random generation of diameters d according to the specified distribution function. In case of Weibull distribution it is possible to transform the cumulative distribution function $F_W(d)$

$$F_W(d) = 1 - e^{-(d/a)^b} \quad (6.3)$$

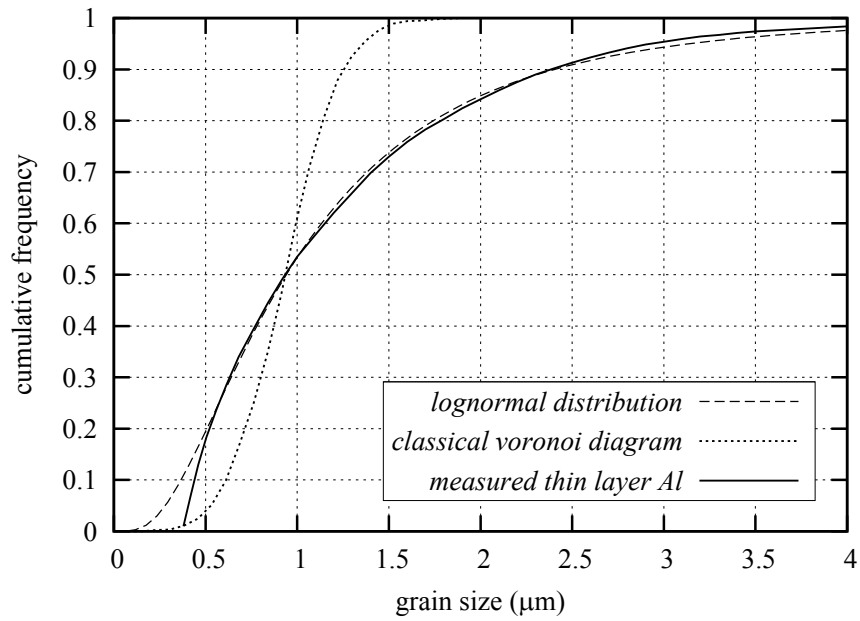


Figure 6.3: Cumulative grain size distribution.

into the form

$$d = a \{-\ln(1 - F_W(d))\}^{1/b}. \quad (6.4)$$

Therewith, one can find a suitable set of diameters d based on random values $0 < F_W(d) < 1$. For distribution functions, that can not be transformed into a dependency $d = d(F(d))$, for example the lognormal distribution function, it is proposed to discretize the argument domain $0 < d \leq d_{max}$ of the distribution function $f(d)$. The discretization yields a finite number of discrete intervals $\Delta d_i = d_{i+1} - d_i$. Probability limits $F(d_i) < F(\Delta d_i) \leq F(d_{i+1})$

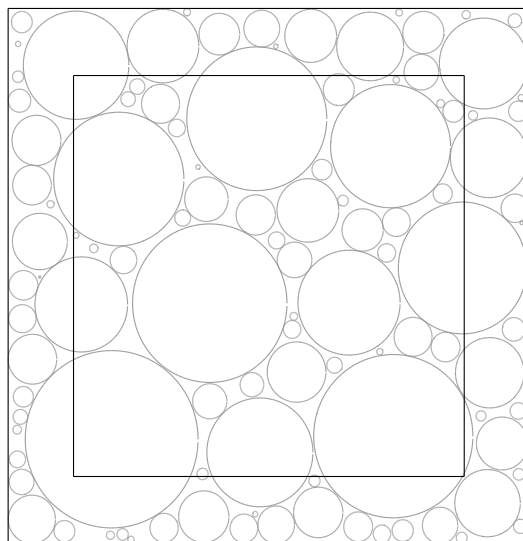


Figure 6.4: Circles are placed into a box (outer boundary) larger than the aimed sample (inner boundary).

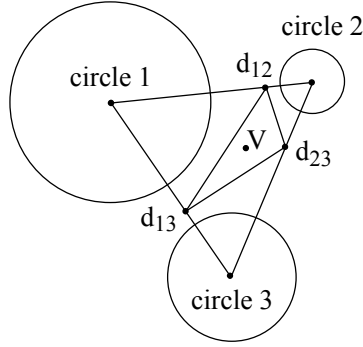


Figure 6.5: Construction of modified Voronoi points after Delaunay triangulation.

are assigned to each step Δd_i according to the cumulative distribution function $F(d)$. In this way a suitable set of diameters d , based on random values $0 < F(d) \leq F(d_{max})$, can be generated.

In a second step, circles with the generated diameters are defined. The circles are placed, starting with the largest one, into a box (Figure 6.4). The box (outer boundary) must be larger than the aimed polycrystal samples (inner boundary) on the mesoscale to take into account that grains at the sample boundaries can be positioned partially outside the sample. The area, that can be filled by circles, is smaller than the box area A , because the density of circles in the box is limited. Hence, the diameter generation stops when the sum of circle areas, belonging to diameters d_j , is larger than a specified limit $f \cdot A$:

$$\sum \frac{\pi}{4} d_j^2 \geq f \cdot A. \quad (6.5)$$

The limit of Equation (6.5) should be reasonably defined to guaranty, that all circles can be placed into the box. Suitable values for the factor f are between 0.7 and 0.9. However,

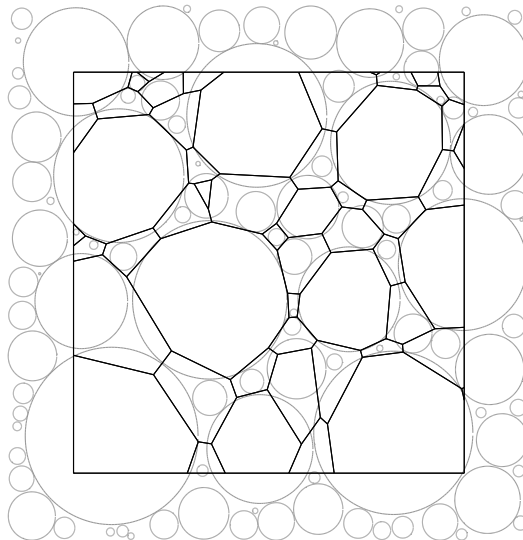


Figure 6.6: Cell structure around the circles within the sample.

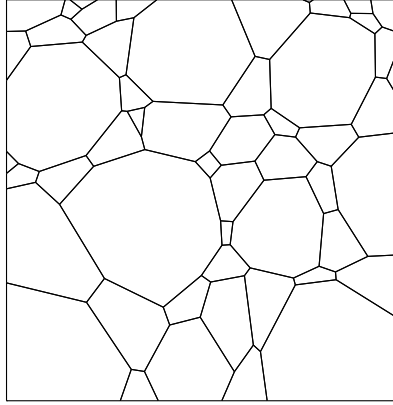


Figure 6.7: Sample with modified Voronoi diagram.

it strongly depends on the standard deviation of grain size distribution.

In a third step a Delaunay triangulation for the circle center points is computed. Based on this triangulation the positions of 'modified' Voronoi points are calculated for each triangle following Figure 6.5. Assuming a triangle (123), that is constructed by the center points of circles 1 to 3. First, each triangle edge is divided into two parts proportional to the relation of radii belonging to the circles of edge vertices. For example, the edge connecting the center points of circles 1 and 2 is divided by the division point d_{12} at a distance of l_1 ,

$$l_1 = \frac{r_1 l}{r_1 + r_2} \quad (6.6)$$

from circle center 1 to circle center 2. l is the distance between center points of circles 1 and 2. r_1 and r_2 are the radii of circles 1 and 2. Second the edge division points d_{12} , d_{23} , and d_{13} of triangle (123) define a new triangle for which the centroid V can be computed. Point V is the modified Voronoi point of triangle (123).

In a fourth step all modified Voronoi points inside the sample bounds are connected according to a classical Voronoi procedure. Finally, the modified Voronoi structure is cut along the sample bounds. The resulting geometrical grain structure inside the sample is illustrated in Figures 6.6 and 6.7. A comparison with the classical Voronoi cell diagram in Figure 6.1 shows significant differences especially with respect to the grain size distribution.

The circles in the box do not fill the complete area of the cell structure. This results in a modified grain size distribution of the final cell structure compared to the initial size distribution of circles. Consequently, an adaptation is necessary for the free parameters of the distribution function, which has been used to generate the circle diameters d_j to obtain a cell structure corresponding to a predefined grain size distribution. Exemplary, a cell structure with median value $d_{50} = 0.94 \mu\text{m}$ and standard deviation $\sigma_d = 0.78$ as measured in thin layer aluminum by [Kirchner 2001] shall be generated. In order to obtain this cell structure the circle diameters are generated according to a cumulative lognormal

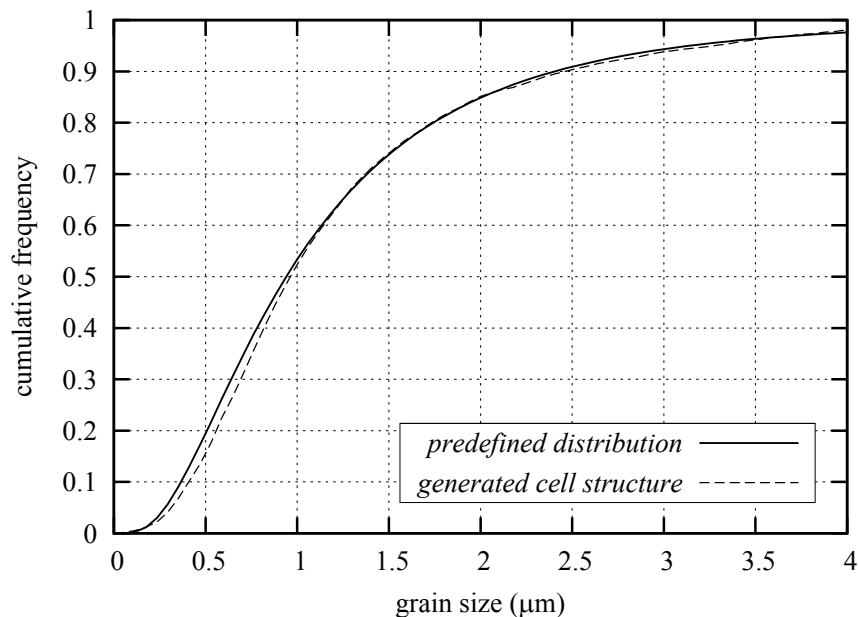


Figure 6.8: Comparison of predefined cumulative lognormal distribution function and resulting grain size distribution of generated cell structure.

distribution function with adapted values $\bar{d}_{50} = 0.66 \mu\text{m}$ and $\bar{\sigma}_d = 1.40$. The parameters are adapted by an iterative fitting procedure. The resulting grain size distribution shows good agreement with the predefined cumulative lognormal distribution function (Figure 6.8). An example of the generated cell structure is illustrated in Figure 6.7. It is possible to reproduce any arbitrary grain size distribution in 2D with high accuracy by the proposed algorithm.

6.2.3 Modified 3D Voronoi diagram

A transfer of the proposed modification algorithm from 2D to 3D is not possible. In contrast to the case of plane Voronoi cells the modification of spatial Voronoi cells would lead to inter-penetrating entities. The Cornell Fracture Group [CFG 2010] presented different alternative strategies [Veilleux et al. 2009] for the generation of realistic 3D polycrystal geometries that were developed and tested in collaboration with the Materials Research and Engineering Center [MRSEC 2010] of the Carnegie Mellon University.

One of these strategies, which is also based on Voronoi tessellation, was developed by Rollett and Sintay and implemented within a former version of the *mBuilder* software package [Rollett et al. 2010]. Therein, a Voronoi diagram with sufficient number of cells is overlaid with ellipsoids representing the aimed grains. Then, all Voronoi cells are assigned each to the nearest ellipsoidal. Following this approach, one obtains a polycrystal structure consisting of connected volumes of Voronoi cells. In the software, information of shapes and size distribution of grains is considered to generate geometries representing technical materials after forming processes. Figure 6.9 shows a polycrystal geometry that

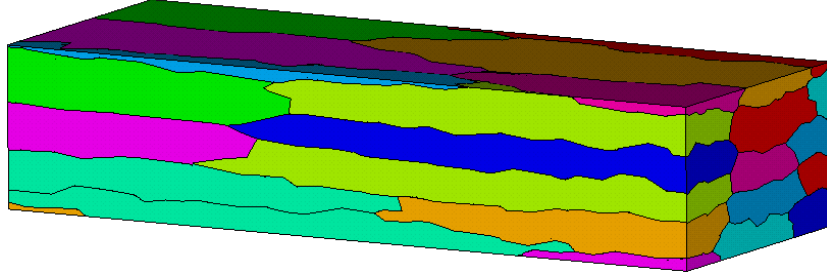


Figure 6.9: Geometrical 3D polycrystal structure generated by a former *mBuilder* version provided by [Rollett et al. 2010]. The grains are build by clusters of Voronoi cells.

was generated by the former *mBuilder* version provided by Rollett and Sintay. However, the generated geometries show significant problems concerning meshing because of the complex grain shapes with numerous sharp corners. Consequently, this strategy is not satisfactory for the robust development of discretized polycrystal models.

For this reason another concept of voxel-based geometries was followed also in the *mBuilder* project [Rollett et al. 2010]. The idea of voxel-based geometry generation is to overlay a voxel mesh with ellipsoids. Similar to the former strategy, each voxel is assigned to the nearest ellipsoidal and the amount of voxel associated with the same ellipsoidal defines the basis of the appropriate grain. Subsequently, the voxel-based shapes of the grains are improved, for example, by a marching cube algorithm to obtain smooth surfaces. For reasonable succeeding FE simulations the shape improvement is necessary to avoid artificial stress concentrations in corners of voxeled surfaces. While the implementation of a well working smoothening procedure is an important but difficult task, the resulting smoothed grain shapes offer a suitable basis for meshing and further application to numerical damage analysis.

In the presented dissertation, classical Voronoi diagrams are applied in 3D for numerical simulation on the mesoscale, while improved models based on voxellation and marching cubes are in development.

6.3 Constitutive Models

The discretization of grains in the various geometrical models is done by triangular finite elements with quadratic shape functions in 2D and tetrahedral finite elements with linear shape functions in 3D, respectively. Appropriate interface elements are assigned to the GBs to cover crack initiation and propagation in these zones. Following [Ingraffea et al. 2002] and [Iesulauro et al. 2002] an orthotropic material model is applied to the grain elements and a coupled cohesive zone model is assigned to the interface elements.

6.3.1 Orthotropic grains

Taking into account the dependency of material properties on crystal orientation, orthotropic material models with and without plasticity are assigned to the crystallites (grains). As a part of this thesis these material models were implemented into the software package SLang [SLang 2010] that is developed and used at the Institute of Structural Mechanics in Weimar.

Transformation of stresses, strains, and constitutive matrix

The orthotropic material parameters are related to the normal directions of the three orthogonal planes. In the polycrystal model the material directions of crystallites are defined by a sequence of rotations from the global CS (XYZ) into the materials CS (X'Y'Z') using Eulerian angles, similar to the description in Section 3.1.2. While the implemented definition of orthotropic material orientation allows for any sequence of three rotations by Eulerian angles, the following paragraphs exemplary refer to the most usual Z'X'Z'-rotation as previously explained by Figure 3.3.

During the simulation process the global stresses have to be computed from the global strains using the constitutive matrix, which is initially defined in the local materials CS. Thus, a transformation procedure is necessary. The basic transformation matrices are derived for transformation of the stress matrix from one Cartesian CS into another one as shown, for example, in [Möller 2007]. The relation between the global stress matrix $\boldsymbol{\sigma}^{gl}$ and the local stress matrix $\boldsymbol{\sigma}^l$ is defined by

$$\boldsymbol{\sigma}^l = \mathbf{T} \boldsymbol{\sigma}^{gl}, \quad (6.7)$$

with

$$\boldsymbol{\sigma}^l = \begin{bmatrix} \sigma_{x'x'} \\ \sigma_{y'y'} \\ \sigma_{z'z'} \\ \tau_{x'y'} \\ \tau_{x'z'} \\ \tau_{y'z'} \end{bmatrix} \quad \text{and} \quad \boldsymbol{\sigma}^{gl} = \begin{bmatrix} \sigma_{xx} \\ \sigma_{yy} \\ \sigma_{zz} \\ \tau_{xy} \\ \tau_{xz} \\ \tau_{yz} \end{bmatrix}, \quad (6.8)$$

where the transformation matrix \mathbf{T} describes the sequence of rotations by Eulerian angles. The three possible rotations about local axes are expressed in matrix notation as follows

$$\mathbf{T}_\phi^{X'} = \begin{bmatrix} 1 & 0 & 0 & 0 & 0 & 0 \\ 0 & \cos^2 \phi & \sin^2 \phi & 0 & 0 & 2 \sin \phi \cos \phi \\ 0 & \sin^2 \phi & \cos^2 \phi & 0 & 0 & -2 \sin \phi \cos \phi \\ 0 & 0 & 0 & \cos \phi & \sin \phi & 0 \\ 0 & 0 & 0 & -\sin \phi & \cos \phi & 0 \\ 0 & -\sin \phi \cos \phi & \sin \phi \cos \phi & 0 & 0 & \cos^2 \phi - \sin^2 \phi \end{bmatrix}, \quad (6.9)$$

$$\mathbf{T}_{\psi}^{Y'} = \begin{bmatrix} \cos^2 \psi & 0 & \sin^2 \psi & 0 & 2 \sin \psi \cos \psi & 0 \\ 0 & 1 & 0 & 0 & 0 & 0 \\ \sin^2 \psi & 0 & \cos^2 \psi & 0 & -2 \sin \psi \cos \psi & 0 \\ 0 & 0 & 0 & \cos \psi & 0 & \sin \psi \\ -\sin \psi \cos \psi & 0 & \sin \psi \cos \psi & 0 & \cos^2 \psi - \sin^2 \psi & 0 \\ 0 & 0 & 0 & -\sin \psi & 0 & \cos \psi \end{bmatrix}, \quad (6.10)$$

$$\mathbf{T}_{\varphi}^{Z'} = \begin{bmatrix} \cos^2 \varphi & \sin^2 \varphi & 0 & 2 \sin \varphi \cos \varphi & 0 & 0 \\ \sin^2 \varphi & \cos^2 \varphi & 0 & -2 \sin \varphi \cos \varphi & 0 & 0 \\ 0 & 0 & 1 & 0 & 0 & 0 \\ -\sin \varphi \cos \varphi & \sin \varphi \cos \varphi & 0 & \cos^2 \varphi - \sin^2 \varphi & 0 & 0 \\ 0 & 0 & 0 & 0 & \cos \varphi & -\sin \varphi \\ 0 & 0 & 0 & 0 & \sin \varphi & \cos \varphi \end{bmatrix}, \quad (6.11)$$

where ϕ is the rotation angle about local X' axis, ψ is the rotation angle about local Y' axis, and φ is the rotation angle about local Z' axis. Therewith, the Z'X'Z'-rotation by three Eulerian angles $\varphi_1\phi\varphi_2$ can be summarized to

$$\mathbf{T} = \mathbf{T}_{\varphi_2}^{Z'} \cdot \mathbf{T}_{\phi}^{X'} \cdot \mathbf{T}_{\varphi_1}^{Z'}. \quad (6.12)$$

The transformation of strains follows almost the same relation. Considering the tensorial shear strain the transformation is exactly the same as for stresses

$$\begin{bmatrix} \epsilon_{x'x'} \\ \epsilon_{y'y'} \\ \epsilon_{z'z'} \\ \frac{1}{2}\gamma_{x'y'} \\ \frac{1}{2}\gamma_{x'z'} \\ \frac{1}{2}\gamma_{y'z'} \end{bmatrix} = \mathbf{T} \begin{bmatrix} \epsilon_{xx} \\ \epsilon_{yy} \\ \epsilon_{zz} \\ \frac{1}{2}\gamma_{xy} \\ \frac{1}{2}\gamma_{xz} \\ \frac{1}{2}\gamma_{yz} \end{bmatrix}. \quad (6.13)$$

Since the classical definition of shear strain is twice the tensorial shear strain, the transformation of the classical strain matrix is extended by the application of the Reuter's matrix \mathbf{R}

$$\mathbf{R} = \begin{bmatrix} 1 & 0 & 0 & 0 & 0 & 0 \\ 0 & 1 & 0 & 0 & 0 & 0 \\ 0 & 0 & 1 & 0 & 0 & 0 \\ 0 & 0 & 0 & 2 & 0 & 0 \\ 0 & 0 & 0 & 0 & 2 & 0 \\ 0 & 0 & 0 & 0 & 0 & 2 \end{bmatrix} \quad \text{and} \quad \mathbf{R}^{-1} = \begin{bmatrix} 1 & 0 & 0 & 0 & 0 & 0 \\ 0 & 1 & 0 & 0 & 0 & 0 \\ 0 & 0 & 1 & 0 & 0 & 0 \\ 0 & 0 & 0 & \frac{1}{2} & 0 & 0 \\ 0 & 0 & 0 & 0 & \frac{1}{2} & 0 \\ 0 & 0 & 0 & 0 & 0 & \frac{1}{2} \end{bmatrix}. \quad (6.14)$$

Based on the Reuter's matrix the transformation of the classical strain matrix reads

$$\epsilon^l = \mathbf{RTR}^{-1} \epsilon^{gl}, \quad (6.15)$$

with

$$\boldsymbol{\epsilon}^l = \begin{bmatrix} \epsilon_{x'x'} \\ \epsilon_{y'y'} \\ \epsilon_{z'z'} \\ \gamma_{x'y'} \\ \gamma_{x'z'} \\ \gamma_{y'z'} \end{bmatrix} \quad \text{and} \quad \boldsymbol{\epsilon}^{gl} = \begin{bmatrix} \epsilon_{xx} \\ \epsilon_{yy} \\ \epsilon_{zz} \\ \gamma_{xy} \\ \gamma_{xz} \\ \gamma_{yz} \end{bmatrix}. \quad (6.16)$$

The orthotropic constitutive matrix $\mathbf{E}^{ort,l}$ is defined in the local (material) CS and is equal to the inverse orthotropic compliance matrix \mathbf{N}^{ort} of Equation (2.28)

$$\mathbf{E}^{ort,l} = (\mathbf{N}^{ort})^{-1}. \quad (6.17)$$

Now, the constitutive equation in the local CS reads

$$\boldsymbol{\sigma}^l = \mathbf{E}^{ort,l} \boldsymbol{\epsilon}^l. \quad (6.18)$$

Substituting Equations (6.7) and (6.15) into (Equation 6.18) and isolating $\boldsymbol{\sigma}^{gl}$ leads to the constitutive equation in the global CS

$$\boldsymbol{\sigma}^{gl} = \mathbf{T}^{-1} \mathbf{E}^{ort,l} \mathbf{RTR}^{-1} \boldsymbol{\epsilon}^{gl}. \quad (6.19)$$

Making use of the characteristics of \mathbf{R} and \mathbf{T} , that is

$$\mathbf{RTR}^{-1} = (\mathbf{T}^{-1})^T \quad (6.20)$$

simplifies Equation (6.19) and yields

$$\boldsymbol{\sigma}^{gl} = \mathbf{T}^{-1} \mathbf{E}^{ort,l} (\mathbf{T}^{-1})^T \boldsymbol{\epsilon}^{gl}. \quad (6.21)$$

For further simplicity the transformation matrix

$$\mathbf{A} = \mathbf{T}^{-1} \quad (6.22)$$

is introduced, which leads to the following formulation of the global orthotropic constitutive matrix

$$\mathbf{E}^{ort,gl} = \mathbf{A} \mathbf{E}^{ort,l} \mathbf{A}^T. \quad (6.23)$$

Assuming a constant orthotropic constitutive matrix during the simulation process results in the computation of $\mathbf{E}^{ort,gl}$ only one times. This means that the transformation of the constitutive matrix is only made at the beginning of the simulation and for orthotropic linear elastic material behavior the computation of global stresses during the simulation process reduces to

$$\boldsymbol{\sigma}^{gl} = \mathbf{E}^{ort,gl} \boldsymbol{\epsilon}^{gl}. \quad (6.24)$$

The transformation matrix \mathbf{A} , which is applied to the constitutive matrix, can be calculated from the separate transformation matrices as follows

$$\mathbf{A} = \mathbf{T}^{-1} = \left(\mathbf{T}_{\varphi_2}^{Z'} \cdot \mathbf{T}_{\phi}^{X'} \cdot \mathbf{T}_{\varphi_1}^{Z'} \right)^{-1} = \left(\mathbf{T}_{\varphi_1}^{Z'} \right)^{-1} \cdot \left(\mathbf{T}_{\phi}^{X'} \right)^{-1} \cdot \left(\mathbf{T}_{\varphi_2}^{Z'} \right)^{-1} \quad (6.25)$$

assuming a $Z'X'Z'$ -rotation, again. Introducing

$$\mathbf{A}_{\phi}^{X'} = \begin{bmatrix} 1 & 0 & 0 & 0 & 0 & 0 \\ 0 & \cos^2 \phi & \sin^2 \phi & 0 & 0 & -2 \sin \phi \cos \phi \\ 0 & \sin^2 \phi & \cos^2 \phi & 0 & 0 & 2 \sin \phi \cos \phi \\ 0 & 0 & 0 & \cos \phi & -\sin \phi & 0 \\ 0 & 0 & 0 & \sin \phi & \cos \phi & 0 \\ 0 & \sin \phi \cos \phi & -\sin \phi \cos \phi & 0 & 0 & \cos^2 \phi - \sin^2 \phi \end{bmatrix}, \quad (6.26)$$

$$\mathbf{A}_{\psi}^{Y'} = \begin{bmatrix} \cos^2 \psi & 0 & \sin^2 \psi & 0 & -2 \sin \psi \cos \psi & 0 \\ 0 & 1 & 0 & 0 & 0 & 0 \\ \sin^2 \psi & 0 & \cos^2 \psi & 0 & 2 \sin \psi \cos \psi & 0 \\ 0 & 0 & 0 & \cos \psi & 0 & -\sin \psi \\ \sin \psi \cos \psi & 0 & -\sin \psi \cos \psi & 0 & \cos^2 \psi - \sin^2 \psi & 0 \\ 0 & 0 & 0 & \sin \psi & 0 & \cos \psi \end{bmatrix}, \quad (6.27)$$

$$\mathbf{A}_{\varphi}^{Z'} = \begin{bmatrix} \cos^2 \varphi & \sin^2 \varphi & 0 & -2 \sin \varphi \cos \varphi & 0 & 0 \\ \sin^2 \varphi & \cos^2 \varphi & 0 & 2 \sin \varphi \cos \varphi & 0 & 0 \\ 0 & 0 & 1 & 0 & 0 & 0 \\ \sin \varphi \cos \varphi & -\sin \varphi \cos \varphi & 0 & \cos^2 \varphi - \sin^2 \varphi & 0 & 0 \\ 0 & 0 & 0 & 0 & \cos \varphi & \sin \varphi \\ 0 & 0 & 0 & 0 & -\sin \varphi & \cos \varphi \end{bmatrix}, \quad (6.28)$$

results in the short formulation of Equation (6.25)

$$\mathbf{A} = \mathbf{A}_{\varphi_1}^{Z'} \cdot \mathbf{A}_{\phi}^{X'} \cdot \mathbf{A}_{\varphi_2}^{Z'}. \quad (6.29)$$

In the plane stress case with

$$\boldsymbol{\sigma}^{gl} = \begin{bmatrix} \sigma_{xx} \\ \sigma_{yy} \\ \tau_{xy} \end{bmatrix} \quad \text{and} \quad \boldsymbol{\epsilon}^{gl} = \begin{bmatrix} \epsilon_{xx} \\ \epsilon_{yy} \\ \gamma_{xy} \end{bmatrix} \quad (6.30)$$

the orthotropic compliance matrix and the appropriate constitutive matrix are

$$\mathbf{N}^{ort,l} = \frac{1}{h} \begin{bmatrix} \frac{1}{E_1} & \frac{-\nu_{21}}{E_2} & 0 \\ \frac{-\nu_{12}}{E_1} & \frac{1}{E_2} & 0 \\ 0 & 0 & \frac{1}{G_{12}} \end{bmatrix} \quad (6.31)$$

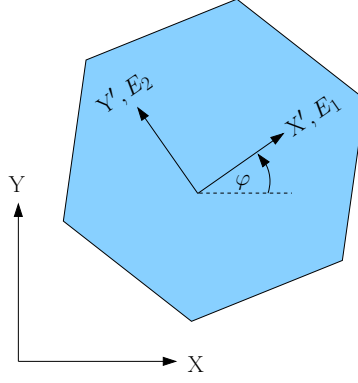


Figure 6.10: 2D crystallite with local CS ($X'Y'$) defined by the orthotropic material axes. The crystal orientation is obtained by a counterclockwise rotation from global CS (XY) by angle φ .

and

$$\mathbf{E}^{ort,l} = h \begin{bmatrix} \frac{E_1}{1 - \nu_{12}\nu_{21}} & \frac{\nu_{21}E_1}{1 - \nu_{12}\nu_{21}} & 0 \\ \frac{\nu_{12}E_2}{1 - \nu_{12}\nu_{21}} & \frac{E_2}{1 - \nu_{12}\nu_{21}} & 0 \\ 0 & 0 & G_{12} \end{bmatrix}, \quad (6.32)$$

respectively, where h is the plane thickness and

$$\nu_{21} = \frac{E_2}{E_1}\nu_{12} \quad (6.33)$$

$$G_{12} = \frac{E_1}{2(1 + \nu_{12})}. \quad (6.34)$$

The transformation matrices for counterclockwise rotation from global CS to local CS about angle φ (Figure 6.10) read

$$\mathbf{T} = \begin{bmatrix} \cos^2 \varphi & \sin^2 \varphi & 2 \sin \varphi \cos \varphi \\ \sin^2 \varphi & \cos^2 \varphi & -2 \sin \varphi \cos \varphi \\ -\sin \varphi \cos \varphi & \sin \varphi \cos \varphi & \cos^2 \varphi - \sin^2 \varphi \end{bmatrix} \quad (6.35)$$

and

$$\mathbf{A} = \begin{bmatrix} \cos^2 \varphi & \sin^2 \varphi & -2 \sin \varphi \cos \varphi \\ \sin^2 \varphi & \cos^2 \varphi & 2 \sin \varphi \cos \varphi \\ \sin \varphi \cos \varphi & -\sin \varphi \cos \varphi & \cos^2 \varphi - \sin^2 \varphi \end{bmatrix}. \quad (6.36)$$

The Reuter's matrix reduces to

$$\mathbf{R} = \begin{bmatrix} 1 & 0 & 0 \\ 0 & 1 & 0 \\ 0 & 0 & 2 \end{bmatrix} \quad \text{and} \quad \mathbf{R}^{-1} = \begin{bmatrix} 1 & 0 & 0 \\ 0 & 1 & 0 \\ 0 & 0 & \frac{1}{2} \end{bmatrix}. \quad (6.37)$$

Orthotropic Hill plasticity criterion

Additionally to the orthotropic linear elastic material model an orthotropic linear elastic ideal plastic material model with Hill plasticity criterion was implemented. According to [Ottosen et al. 2005] the Hill plasticity criterion can be formulated depending on the components of the stress deviator tensor \mathbf{s} and the orthotropic yield stresses σ_{yld} . Starting with the Cauchy stress tensor in the local (material) CS of a crystallite

$$\boldsymbol{\sigma}^l = \begin{bmatrix} \sigma_{x'x'} & \tau_{x'y'} & \tau_{x'z'} \\ \tau_{y'x'} & \sigma_{y'y'} & \tau_{y'z'} \\ \tau_{z'x'} & \tau_{z'y'} & \sigma_{z'z'} \end{bmatrix} \quad (6.38)$$

the corresponding stress deviator tensor is defined as

$$\mathbf{s} = \begin{bmatrix} s_{11} & s_{12} & s_{13} \\ s_{21} & s_{22} & s_{23} \\ s_{31} & s_{32} & s_{33} \end{bmatrix} = \begin{bmatrix} \sigma_{x'x'} - p & \tau_{x'y'} & \tau_{x'z'} \\ \tau_{y'x'} & \sigma_{y'y'} - p & \tau_{y'z'} \\ \tau_{z'x'} & \tau_{z'y'} & \sigma_{z'z'} - p \end{bmatrix}, \quad (6.39)$$

where

$$p = \frac{1}{3}I_1 = \frac{\sigma_{x'x'} + \sigma_{y'y'} + \sigma_{z'z'}}{3} \quad (6.40)$$

is the hydrostatic stress that correlates to the first invariant I_1 of the Cauchy stress tensor.

Based on the deviatoric stresses the general Equation (2.38) reads for Hill's orthotropic yield criterion [Hill 1950]

$$f(\boldsymbol{\sigma}^l, \mathbf{K}_\alpha = \mathbf{0})^{Hill} = \quad (6.41)$$

$$F(s_{11} - s_{22})^2 + G(s_{11} - s_{33})^2 + H(s_{22} - s_{33})^2 + 2L s_{12}^2 + 2M s_{13}^2 + 2N s_{23}^2 - 1 = 0.$$

The parameters F , G , and H depend on the initial yield stresses $\sigma_{yldx'}$, $\sigma_{yldy'}$, and $\sigma_{yldz'}$ in directions of the orthotropic material axes (X'Y'Z')

$$F = \frac{1}{2} \left(\frac{1}{\sigma_{yldx'}^2} + \frac{1}{\sigma_{yldy'}^2} - \frac{1}{\sigma_{yldz'}^2} \right), \quad (6.42)$$

$$G = \frac{1}{2} \left(\frac{1}{\sigma_{yldx'}^2} - \frac{1}{\sigma_{yldy'}^2} + \frac{1}{\sigma_{yldz'}^2} \right), \quad (6.43)$$

$$H = \frac{1}{2} \left(-\frac{1}{\sigma_{yldx'}^2} + \frac{1}{\sigma_{yldy'}^2} + \frac{1}{\sigma_{yldz'}^2} \right), \quad (6.44)$$

and the parameters L , M , and N depend on the initial yield shear stresses $\tau_{yldx'y'}$, $\tau_{yldx'z'}$, and $\tau_{yldy'z'}$ as follows

$$L = \frac{1}{2\tau_{yldx'y'}^2}, \quad (6.45)$$

$$M = \frac{1}{2\tau_{yldx'z'}^2}, \quad (6.46)$$

$$N = \frac{1}{2\tau_{yldy'z'}^2}. \quad (6.47)$$

Substituting these parameters in Equation (6.41), which describes the initial yield surface, and using the Cauchy stresses instead of deviatoric stresses, the flow rule of Equation (2.40) reads

$$\begin{aligned} f(\boldsymbol{\sigma}^l)^{Hill} = & \left[\sigma_{x'x'}^2 + \frac{\sigma_{yldx'}^2}{\sigma_{yldy'}^2} \sigma_{y'y'}^2 + \frac{\sigma_{yldx'}^2}{\sigma_{yldz'}^2} \sigma_{z'z'}^2 - \left(1 + \frac{\sigma_{yldx'}^2}{\sigma_{yldy'}^2} - \frac{\sigma_{yldx'}^2}{\sigma_{yldz'}^2} \right) \sigma_{x'x'} \sigma_{y'y'} \right. \\ & - \left(1 - \frac{\sigma_{yldx'}^2}{\sigma_{yldy'}^2} + \frac{\sigma_{yldx'}^2}{\sigma_{yldz'}^2} \right) \sigma_{x'x'} \sigma_{z'z'} - \left(-1 + \frac{\sigma_{yldx'}^2}{\sigma_{yldy'}^2} + \frac{\sigma_{yldx'}^2}{\sigma_{yldz'}^2} \right) \sigma_{y'y'} \sigma_{z'z'} \\ & \left. + \frac{\sigma_{yldx'}^2}{\tau_{yldx'y'}^2} \tau_{x'y'}^2 + \frac{\sigma_{yldx'}^2}{\tau_{yldx'z'}^2} \tau_{x'z'}^2 + \frac{\sigma_{yldx'}^2}{\tau_{yldy'z'}^2} \tau_{y'z'}^2 \right]^{\frac{1}{2}} - \sigma_{yldx'} \leq 0, \end{aligned} \quad (6.48)$$

wherein the square root is taken by convention. For isotropic materials with

$$\sigma_{yldx'} = \sigma_{yldy'} = \sigma_{yldz'} = \sigma_{yld} \quad (6.49)$$

and

$$\tau_{yldx'y'} = \tau_{yldx'z'} = \tau_{yldy'z'} = \tau_{yld} = \frac{\sigma_{yld}}{\sqrt{3}} \quad (6.50)$$

the above flow rule reduces to the flow rule of the von Mises criterion [Ottosen et al. 2005], which is due to isotropy independent on the CS

$$f(\boldsymbol{\sigma})^{Mises} = \quad (6.51)$$

$$\left[\sigma_{xx}^2 + \sigma_{yy}^2 + \sigma_{zz}^2 - \sigma_{xx}\sigma_{yy} - \sigma_{xx}\sigma_{zz} - \sigma_{yy}\sigma_{zz} + 3(\tau_{xy}^2 + \tau_{xz}^2 + \tau_{yz}^2) \right]^{\frac{1}{2}} - \sigma_{yld} \leq 0.$$

In the plane stress case the Hill flow rule reads

$$f(\boldsymbol{\sigma}^l)^{Hill} = \left[\sigma_{x'x'}^2 + \frac{\sigma_{yldx'}^2}{\sigma_{yldy'}^2} \sigma_{y'y'}^2 - \sigma_{x'x'} \sigma_{y'y'} + \frac{\sigma_{yldx'}^2}{\tau_{yldx'y'}^2} \tau_{x'y'}^2 \right]^{\frac{1}{2}} - \sigma_{yldx'} \leq 0, \quad (6.52)$$

assuming that

$$\sigma_{yldz'} = \sigma_{yldx'} \quad \text{OR} \quad \sigma_{yldz'} = \sigma_{yldy'}. \quad (6.53)$$

Implementation of the plasticity model by an implicit solution algorithm

The orthotropic linear elastic ideal plastic material model with Hill plasticity criterion was implemented in SLang for the plane stress case using an implicit solution algorithm. While explicit algorithms solve a set of independent differential equations for an incremental time step, a set of interdependent differential equations is formulated and solved by implicit algorithms. That is in case of implicit solution strategies, that the equilibrium is formulated for the total system and a set of dependent algebraic equations is solved by an incremental iterative method. Such methods allow trial stress states that are clearly out of the range of the yield function. Nevertheless, the algorithm should ensure that the stress states return back to the yield surface [Will 1996].

In the framework of the presented dissertation an implicit return-mapping algorithm, the so called closest point projection, was implemented to solve the plastic corrector problem for the plane stress orthotropic Hill plasticity model. The implementation follows the iteration algorithm of the general closest point projection summarized in [Simo et al. 1998]. For the implemented orthotropic plasticity model without hardening the general iteration algorithm to compute the local stresses $\boldsymbol{\sigma}_{n+1}^l$ from local strains $\boldsymbol{\epsilon}_{n+1}^l$ for load step $n + 1$ is as follows:

1. Initialize iteration counter k , plastic strains $\boldsymbol{\epsilon}_{n+1}^{p,l}$, and consistency parameter $\Delta\gamma_{n+1}$

$$\begin{aligned} k &= 0 \\ \boldsymbol{\epsilon}_{n+1}^{p,l(0)} &= \boldsymbol{\epsilon}_n^{p,l} \\ \Delta\gamma_{n+1}^{(0)} &= 0 \end{aligned}$$

2. Check the yield criterion $f_{n+1}^{Hill(k)}$ and evaluate the flow rule and its residuals $\mathbf{R}_{n+1}^{(k)}$

$$\boldsymbol{\sigma}_{n+1}^{l(k)} = \mathbf{E}^{ort,l} \left(\boldsymbol{\epsilon}_{n+1}^l - \boldsymbol{\epsilon}_{n+1}^{p,l(k)} \right) \quad (6.54)$$

$$f_{n+1}^{Hill(k)} = f(\boldsymbol{\sigma}_{n+1}^{l(k)})^{Hill}$$

if $k = 0$ and $f_{n+1}^{Hill(k)} < 0$ then: Exit because of elastic behavior

$$\mathbf{R}_{n+1}^{(k)} = -\boldsymbol{\epsilon}_{n+1}^{p,l(k)} + \boldsymbol{\epsilon}_n^{p,l} + \Delta\gamma_{n+1}^{(k)} \frac{\partial f_{n+1}^{Hill(k)}}{\partial \boldsymbol{\sigma}^l} \quad (6.55)$$

if $\|f_{n+1}^{Hill(k)}\| < tolerance_f$ and $\|\mathbf{R}_{n+1}^{(k)}\| < tolerance_R$ then: Exit

3. Compute the algorithmic moduli $\boldsymbol{\Xi}_{n+1}^{(k)}$

$$\boldsymbol{\Xi}_{n+1}^{(k)} = \left(\mathbf{N}^{ort,l} + \Delta\gamma_{n+1}^{(k)} \frac{\partial^2 f_{n+1}^{Hill(k)}}{(\partial \boldsymbol{\sigma}^l)^2} \right)^{-1} \quad (6.56)$$

4. Compute increment to consistency parameter

$$\Delta^2 \gamma_{n+1}^{(k)} = \frac{f_{n+1}^{Hill^{(k)}} - \left(\mathbf{R}_{n+1}^{(k)} \right)^T \Xi_{n+1}^{(k)} \frac{\partial f_{n+1}^{Hill^{(k)}}}{\partial \boldsymbol{\sigma}^l}}{\left(\frac{\partial f_{n+1}^{Hill^{(k)}}}{\partial \boldsymbol{\sigma}^l} \right)^T \Xi_{n+1}^{(k)} \frac{\partial f_{n+1}^{Hill^{(k)}}}{\partial \boldsymbol{\sigma}^l}} \quad (6.57)$$

5. Compute increment to stresses and plastic strains

$$\Delta \boldsymbol{\sigma}_{n+1}^{l(k)} = \Xi_{n+1}^{(k)} \left(-\mathbf{R}_{n+1}^{(k)} - \Delta^2 \gamma_{n+1}^{(k)} \frac{\partial f_{n+1}^{Hill^{(k)}}}{\partial \boldsymbol{\sigma}^l} \right) \quad (6.58)$$

$$\Delta \boldsymbol{\epsilon}_{n+1}^{p,l(k)} = \mathbf{N}^{ort,l} \Delta \boldsymbol{\sigma}_{n+1}^{l(k)} \quad (6.59)$$

6. Update consistency parameter and plastic strains

$$\begin{aligned} \Delta \gamma_{n+1}^{(k+1)} &= \Delta \gamma_{n+1}^{(k)} + \Delta^2 \gamma_{n+1}^{(k)} \\ \boldsymbol{\epsilon}_{n+1}^{p,l(k+1)} &= \boldsymbol{\epsilon}_{n+1}^{p,l(k)} + \Delta \boldsymbol{\epsilon}_{n+1}^{p,l(k)} \end{aligned}$$

Set $k \leftarrow k + 1$ and continue with 2.

7. If needed, compute the elastoplastic tangent moduli $\mathbf{D}^{ort,l}$ according to [Simo et al. 1998]

$$\mathbf{D}^{ort,l} = \left. \frac{d\boldsymbol{\sigma}^l}{d\boldsymbol{\epsilon}^l} \right| = \Xi_{n+1} - \mathbf{M}_{n+1} \otimes \mathbf{M}_{n+1}, \quad (6.60)$$

with

$$\mathbf{M}_{n+1} = \frac{\Xi_{n+1} \frac{\partial f_{n+1}^{Hill}}{\partial \boldsymbol{\sigma}^l}}{\sqrt{\frac{\partial f_{n+1}^{Hill}}{\partial \boldsymbol{\sigma}^l} \Xi_{n+1} \frac{\partial f_{n+1}^{Hill}}{\partial \boldsymbol{\sigma}^l}}}. \quad (6.61)$$

In the plane stress case with stresses and strains according to Equation (6.30) and the compliance matrix of Equation (6.31) the derivatives of the flow rule (Equation (6.52)) are

$$\frac{\partial f^{Hill}}{\partial \boldsymbol{\sigma}^l} = \frac{1}{\sigma_e} \begin{bmatrix} \sigma_{x'x'} - \frac{1}{2} \sigma_{y'y'} \\ A_1 \sigma_{y'y'} - \frac{1}{2} \sigma_{x'x'} \\ A_3 \tau_{x'y'} \end{bmatrix} \quad (6.62)$$

and

$$\frac{\partial^2 f^{Hill}}{(\partial \boldsymbol{\sigma}^l)^2} = \quad (6.63)$$

$$\frac{1}{\sigma_e^3} \begin{bmatrix} \left(A_1 - \frac{1}{4} \right) \sigma_{y'y'}^2 + A_3 \tau_{x'y'}^2 & \left(\frac{1}{4} - A_1 \right) \sigma_{x'x'} \sigma_{y'y'} - \frac{1}{2} A_3 \tau_{x'y'}^2 & \left(\frac{1}{2} \sigma_{y'y'} - \sigma_{x'x'} \right) A_3 \tau_{x'y'} \\ & \left(A_1 - \frac{1}{4} \right) \sigma_{x'x'}^2 + A_1 A_3 \tau_{x'y'}^2 & \left(\frac{1}{2} \sigma_{x'x'} - A_1 \sigma_{y'y'} \right) A_3 \tau_{x'y'} \\ \text{symmetry} & & A_3 \left(\sigma_{x'x'}^2 + A_1 \sigma_{y'y'}^2 - \sigma_{x'x'} \sigma_{y'y'} \right) \end{bmatrix},$$

with the equivalent stress

$$\sigma_e = \left(\sigma_{x'x'}^2 + A_1 \sigma_{y'y'}^2 - \sigma_{x'x'} \sigma_{y'y'} + A_3 \tau_{x'y'}^2 \right)^{\frac{1}{2}} \quad (6.64)$$

and the yield stress ratios

$$A_1 = \frac{\sigma_{yldx'}^2}{\sigma_{yldy'}^2} \quad \text{and} \quad A_3 = \frac{\sigma_{yldx'}^2}{\tau_{yldx'y'}^2}. \quad (6.65)$$

6.3.2 Cohesive grain boundaries

A reversible coupled CZM is assigned to the interface elements to simulate crack propagation along GBs. Details of the applied TSL and the coupled CZM, which was available in the software package SLang, are summarized in Section 5.2.4.

Coupled cohesive zone model with exponential traction separation law

A TSL with sharp peak and exponential decohesion path was chosen to simulate brittle intergranular fracture in the mesoscale model. The TSL was qualitatively drawn previously in Figure 5.10 of Section 5.2.4.

In first studies on the mesoscale (Sections 6.4.1 and 6.4.2) the peak strength t_p of the TSL depends directly on the misorientation β between adjacent crystallites. For the plane stress case the peak strength can be approximated as follows [Iesulauro et al. 2002]

$$t_p(\beta) = t_p^{avg} + \Delta t_p \cos(4\beta), \quad (6.66)$$

and in 3D the presently applied computation is

$$t_p(\beta_i) = t_p^{avg} + \frac{1}{3} \Delta t_p \sum_{i=1}^3 \cos(4\beta_i), \quad (6.67)$$

where t_p^{avg} is the average value of peak strength and Δt_p is the maximal peak strength deviation.

In the improved study of Section 6.5 cohesive parameters from atomistic-based on-the-fly simulations are used to substitute the phenomenological character of the TSL.

Calculation of grain boundary misorientation

In the 2D plane stress case the misorientation β between adjacent crystallites calculates as the absolute difference between the orientation angles of the appropriate material CS (Figure 6.10) in reference to the global CS

$$\beta = |\varphi_1 - \varphi_2|, \quad (6.68)$$

as illustrated also in the right part of Figure 6.11. The left part of this Figure shows that three angles ($\beta_1, \beta_2, \beta_3$) are used to characterize the misorientation in 3D. Each β_i describes the angle between one pair of the different material axes of adjacent crystallites. The calculation of these angles is based on a definition of the local material axes in global coordinates. Starting with a vectorial description of the global axes

$$\mathbf{X} = \begin{bmatrix} 1 \\ 0 \\ 0 \end{bmatrix}, \quad \mathbf{Y} = \begin{bmatrix} 0 \\ 1 \\ 0 \end{bmatrix}, \quad \mathbf{Z} = \begin{bmatrix} 0 \\ 0 \\ 1 \end{bmatrix} \quad (6.69)$$

the material axes of the adjacent crystallites can be expressed in global coordinates by a coordinate transformation of \mathbf{X} , \mathbf{Y} , and \mathbf{Z} based on Eulerian angles, which define the material orientation. The coordinate transformation has to be done by a passive rotation as described in Section 3.1.2. Consequently, the transformation matrices for the three basic passive rotations are $(\mathbf{g}_\phi^{X'})^T$, $(\mathbf{g}_\psi^{Y'})^T$, and $(\mathbf{g}_\varphi^{Z'})^T$ and the complete 3D coordinate transformation can be expressed by a matrix \mathbf{g}^{pas} that follows from the product of the basic transformation matrices as explained in Section 3.1.2. This section describes the passive rotation exemplary for the frequently used $Z'X'Z'$ -rotation.

With the transformation matrices \mathbf{g}_1^{pas} and \mathbf{g}_2^{pas} for two adjacent crystallites the appropriate normalized material axes in global coordinates are obtained by

$$\mathbf{X}'_1 = (\mathbf{g}_1^{pas})^T \mathbf{X}, \quad \mathbf{Y}'_1 = (\mathbf{g}_1^{pas})^T \mathbf{Y}, \quad \mathbf{Z}'_1 = (\mathbf{g}_1^{pas})^T \mathbf{Z}, \quad (6.70)$$

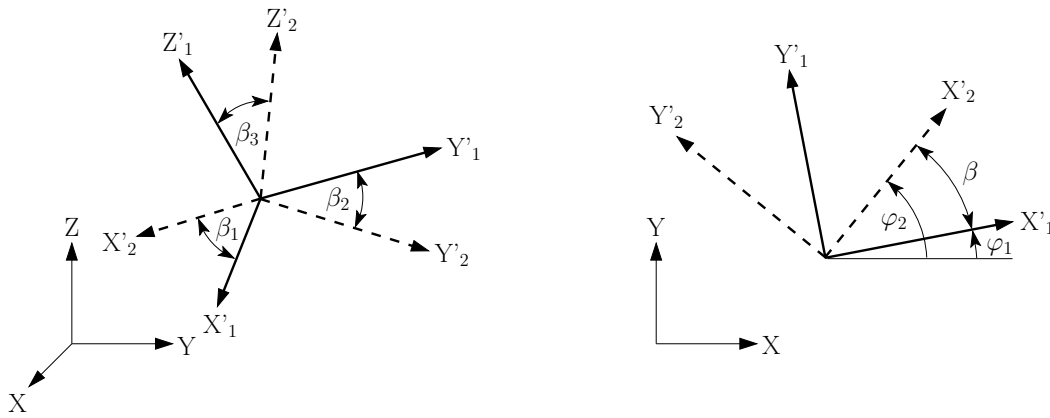


Figure 6.11: Description of misorientation in 3D by angles β_i (left), and in 2D by angle β (right).

and

$$\mathbf{X}'_2 = (\mathbf{g}_2^{pas})^T \mathbf{X}, \quad \mathbf{Y}'_2 = (\mathbf{g}_2^{pas})^T \mathbf{Y}, \quad \mathbf{Z}'_2 = (\mathbf{g}_2^{pas})^T \mathbf{Z}, \quad (6.71)$$

Therewith, the misorientation angles in 3D can be calculated as

$$\beta_1 = \arccos \left(\frac{\mathbf{X}'_1 \cdot \mathbf{X}'_2}{\|\mathbf{X}'_1\| \|\mathbf{X}'_2\|} \right), \quad (6.72)$$

$$\beta_2 = \arccos \left(\frac{\mathbf{Y}'_1 \cdot \mathbf{Y}'_2}{\|\mathbf{Y}'_1\| \|\mathbf{Y}'_2\|} \right), \quad (6.73)$$

$$\beta_3 = \arccos \left(\frac{\mathbf{Z}'_1 \cdot \mathbf{Z}'_2}{\|\mathbf{Z}'_1\| \|\mathbf{Z}'_2\|} \right). \quad (6.74)$$

6.4 Examples

6.4.1 Polycrystal models with orthotropic linear elastic grains

The applicability of the generated polycrystal models on the mesoscale is proved by finite element (FE) computations of stochastic tensile tests on numerical aluminum samples of different underlying kinds of geometry and different sample size. The tensile tests are chosen to be similar to the FE simulations of [Ingraffea et al. 2002] and [Iesulauro et al. 2002], who analyzed the damage in numerical aluminum samples with an underlying classical Voronoi geometry in 2D and 3D. Therewith, the present polycrystal models can be validated qualitatively with the results of [Ingraffea et al. 2002] and [Iesulauro et al. 2002].

Taking into account the dependency of material properties on crystal orientation, an orthotropic linear elastic material model is assigned to the crystallites. The material parameters required to describe the orthotropic linear elastic material behavior in the plane stress case are the Young's moduli E_1 and E_2 , the Poisson's ratio ν_{12} , and the shear modulus G_{12} . The crystal orientation in plane is defined by a random angle $0 \leq \varphi \leq \pi$ that indicates the orientation of the material coordinates related to the global coordinates as illustrated in Figure 6.10. In the 3D case the set of material parameters additionally includes the Young's modulus E_3 in the out of plane direction, the appropriate Poisson's ratios ν_{13} and ν_{23} , and the corresponding shear moduli G_{13} and G_{23} . The crystal orientation in 3D is defined by Eulerian angles $0 \leq \varphi_1, \phi, \varphi_2 \leq \pi$ corresponding to a $Z'X'Z'$ rotation to obtain the material CS in reference to the global CS.

Tension tests on 2D models

At first, 2D samples are generated based on classical Voronoi structures as well as on modified Voronoi structures. In case of modified Voronoi structures the grains are generated following the lognormal grain size distribution function of Equation (6.1) with a median

2D crystallites	interfaces
mean $E_1 = 72,000$ MPa	$t_p^{avg} = 500$ MPa
mean $E_2 = 42,000$ MPa	$\Delta t_p = 0.05 t_p^{avg}$
mean $G_{12} = 26,900$ MPa	$k_n = 10^9$ MPa/mm
$\sigma_d = 0.05$	$G_f = 0.15$ N/mm
$\nu_{12} = 0.33$	$\alpha = 1$
$0 \leq \varphi \leq \pi$	

Table 6.1: Material parameters of the 2D polycrystal model with linear elastic grains.

value $d_{50} = 0.94 \mu\text{m}$ and a standard deviation $\sigma_d = 0.78$. The small grain size was chosen according to measurements in heat treated thin layer aluminum by reference [Kirchner 2001]. With it, the amount of samples match the lognormal grain size distribution of Figure 6.8. In principle, the comparison between classical and modified Voronoi geometries is not affected by the quantity of median grain size, but depends strongly on the corresponding grain size distribution. The classical Voronoi structures are generated with a grain number that was equal to the average grain number of modified Voronoi structures of the same sample size. The same material properties of aluminum as in [Iesulauro et al. 2002] are assigned to the crystallites (grains) using the orthotropic linear elastic model. In the numerical analysis both, crystal orientation φ and material properties of each crystallite, are defined as normally distributed independent variables. The applied coupled CZM differs from the one that was used in [Iesulauro et al. 2002] only by the exponential decohesion path. However, the material properties are chosen similar. All material parameters as well as the stochastic parameters that are applied for the tensile test are summarized in Table 6.1. For grain material the standard deviation σ_d is applied to the

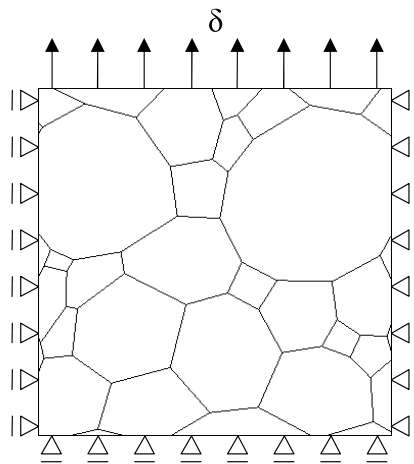


Figure 6.12: Boundary and loading conditions of tensile test.

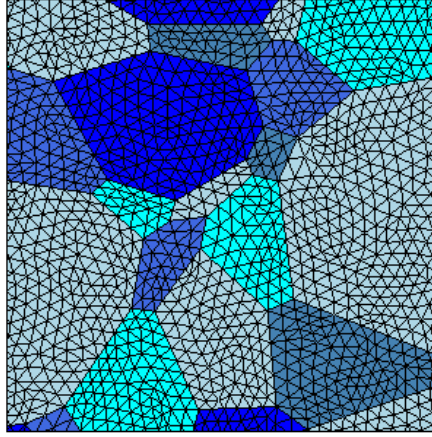


Figure 6.13: Example of a 2D FE mesh (sample size/median grain size = 5.3).

Young's moduli E_1 and E_2 , as well as to the shear modulus G_{12} . The Poisson's ratio ν_{12} is kept constant. The Dirichlet boundary conditions of the initially undamaged samples are illustrated in Figure 6.12. During the simulation the tension state is controlled by the applied continuous displacement δ .

The effective tensile strength of the mesoscale samples is analyzed for both kinds of Voronoi structures and for different sample sizes. For each sample size 200 FE computations are done with underlying classical and with modified Voronoi structure. Exemplary, Figure 6.13 shows a 2D FE mesh of the smallest sample size with underlying modified Voronoi geometry. On average 2,400 DOF and approximately 500 triangular elements in grains as well as 90 interface element, each with quadratic shape functions, are used to simulate crack initiation and propagation in the smallest 2D samples with about 20

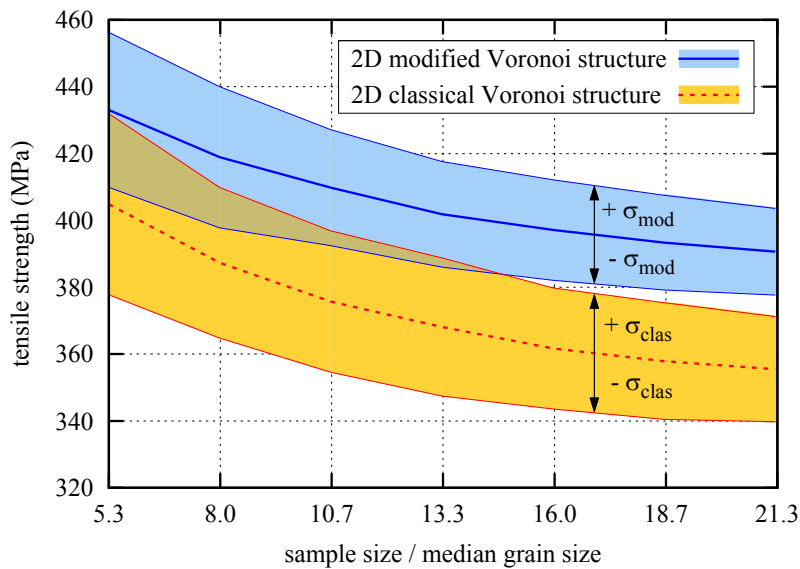


Figure 6.14: Mean values and standard deviation σ of tensile strength calculated on numerical samples of aluminum on the mesoscale.

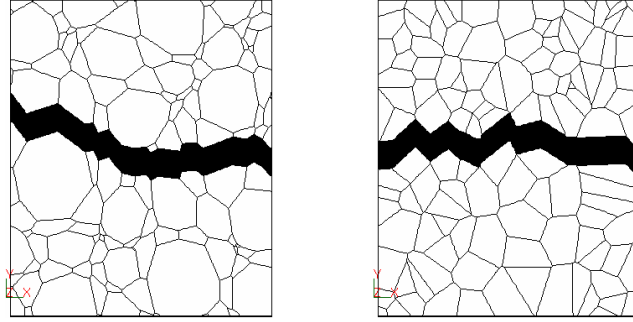


Figure 6.15: Representative 2D examples of simulated crack propagation showing the deformed state at 1.0% global strain. Deformation is enlarged by factor 10. Left: Modified Voronoi structure, Right: Classical Voronoi structure.

grains. On average 21 CPU-seconds are needed on an Intel Xeon X5472 processor (3.0 GHz) for one computation of the deformed state at 1.0% global strain that was calculated in 280 load steps using a full Newton-Raphson method with line search. The results of the stochastic simulations are summarized in the diagram of Figure 6.14. The diagram shows the effective tensile strength with its mean value and standard deviation depending on the ratio between sample size and median grain size. Therefrom, the importance of the size effect of damaged meso-structures that is caused by the localization of damage is clearly visible. For the subsequent numerical homogenization on these mesostructural samples the information of sample size has to be strictly considered, especially for the derivation of a macroscopic fracture energy.

Beside the known size effect, the main interest of the investigations is aimed at the

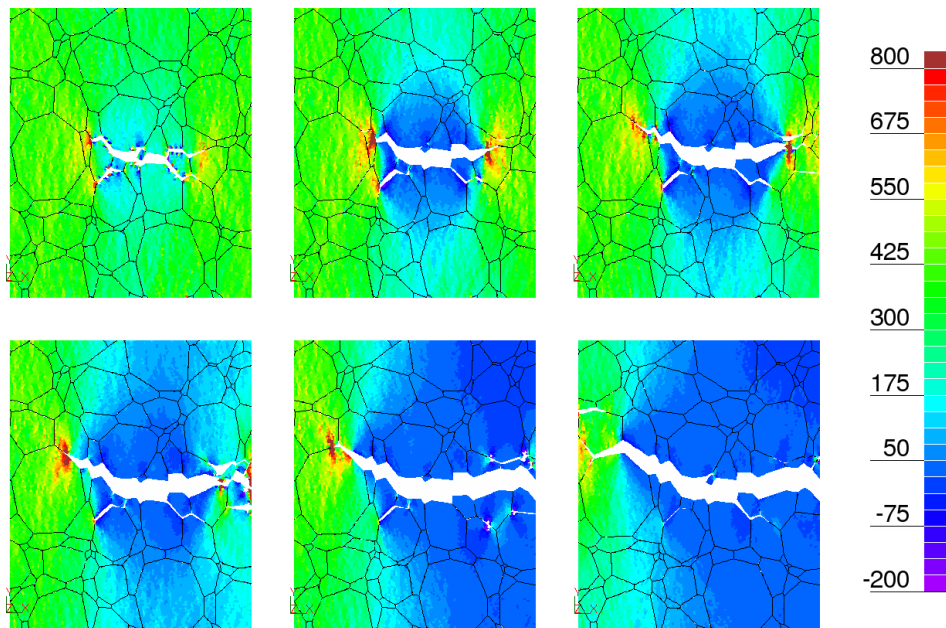


Figure 6.16: Von Mises stress states with values in (MPa) in a 2D modified Voronoi structure while the crack propagates at about 0.875% global strain. Deformation is enlarged by factor 10.

dependency of the effective parameters on the underlying geometry. Figure 6.14 shows that this dependency is significant for the analyzed effective tensile strength. In the stochastic investigations the mean value of the effective tensile strength of samples with underlying modified Voronoi structure is up to ten per cent higher than the one of samples with underlying classical Voronoi structure. Thus, the more realistic wide range of grain sizes of the modified geometries leads to higher tensile strength in case of brittle GB damage in ideal polycrystals that is analyzed by the applied models.

Representative examples of 2D polycrystalline mesostructures after damage simulation are illustrated in Figure 6.15 for a modified Voronoi structure and for a classical Voronoi structure. The distribution of the von Mises stress while crack propagation is shown exemplary for one sample with modified Voronoi structure in Figure 6.16. Crack initiation and propagation during the tensile test is reproduced by an opening of the interfaces assigned to GBs. In the simulations the complexity of crack formation depends on both, the geometry of grain structure as well as the distribution of material parameters and crystal orientation. Altogether, the simulated tensile tests on the mesoscale qualitatively match the results of [Ingraffea et al. 2002] and [Iesulauro et al. 2002].

Tension tests on 3D models

Combined with an underlying classical Voronoi structure the polycrystal model is extended additionally to 3D to prove the approaches of the mesoscale model in this case. The same material models and boundary conditions are applied as before and displacement controlled tensile tests are performed. The parameters of the coupled CZM assigned to GB interfaces remain unchanged. The set of material parameters for the orthotropic grains is extended by Table 6.2 and again the crystal orientations are randomly defined.

Having regard to the considerable increase in the computational time the 3D model is only proved for a small sample size (sample size/median grain size = 5.3) with about 125 grains with the same median value of grain size as in the 2D models. These 3D models consist of approximately 100,000 tetrahedron elements and 19,000 triangular shaped interface elements, each with linear shape functions, leading to about 90,000 DOF. The fine

3D crystallites (additional parameters)
mean $E_3 = 42,000$ MPa
mean $G_{13} = 20,000$ MPa
mean $G_{23} = 20,000$ MPa
$\nu_{13} = 0.25$
$\nu_{23} = 0.25$

Table 6.2: Additional material parameters of the 3D polycrystal model with linear elastic grains.

3D classical Voronoi	2D classical Voronoi	2D modified Voronoi
381.9 MPa	404.9 MPa	433.1 MPa

Table 6.3: Mean values of tensile strength for the smallest sample size.

discretization is necessary to avoid numerical errors by highly distorted elements in sharp corners of the grains. On average the 3D computation of a deformed state at 1.0% global strain, that was reached in approximately 500 load steps, needs about 80,000 CPU-seconds on an Intel Xeon X5472 processor (3.0 GHz). As well a full Newton-Raphson method with line search was used. Again 200 simulations are analyzed and the mean value of the tensile strength is calculated. Table 6.3 shows the result in comparison to the appropriate 2D cases depending on the underlying geometries.

Related to the appropriate smallest analyzed 2D model with classical Voronoi structure, that has the same ratio between sample size and median grain size, the calculated effective tensile strengths of the 3D simulations are decreased about five per cent. Therefore, the conclusion is drawn that the reduction to 2D leads to a higher strength of the computational model compared to the real 3D material. Exemplary, Figure 6.17 illustrates the von Mises stress states in a 3D sample during the process of damage.

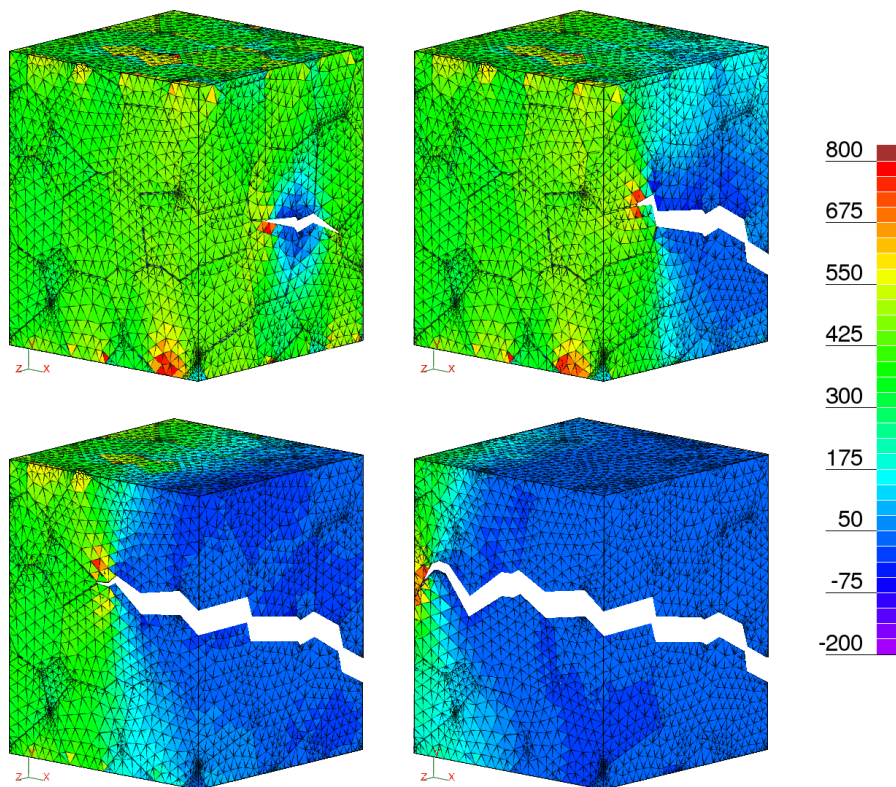


Figure 6.17: Von Mises stress states with values in (MPa) in a 3D classical Voronoi structure while the crack propagates at about 0.9% global strain. Deformation is enlarged by factor 10.

set 1	set 2
mean $\sigma_{yldx'} = 500$ MPa	mean $\sigma_{yldx'} = 550$ MPa
mean $\sigma_{yldy'} = 400$ MPa	mean $\sigma_{yldy'} = 440$ MPa
mean $\sigma_{yldx'y'} = 330$ MPa	mean $\sigma_{yldx'y'} = 363$ MPa
$\sigma_d = 0.05$	$\sigma_d = 0.05$

Table 6.4: Mean values of yield stress and standard deviation σ_d .

6.4.2 2D Polycrystal models with orthotropic elastoplastic grains

After analyses with elastic grains, the influence of plasticity was investigated. Therefore, the constitutive model of grains was extended to an orthotropic linear elastic ideal plastic material model with Hill plasticity criterion according to Section 6.3.1. Again, tensile tests on 2D aluminum samples were performed with boundary and loading conditions taken from Section 6.4.1. The underlying geometry of the investigated models was generated by the classical Voronoi tessellation. The resulting sample contains 100 grains and the ratio of sample size to median grain size is 8.8. The yield stress values and stiffness moduli of the grain plasticity model are normally distributed independent variables. A standard deviation of 5% is chosen similar to previous analyses. The elasticity parameters can be found in Table 6.1 again and additional plasticity parameters are written in Table 6.4. For the investigation of the influence of plasticity, combined with the interface decohesion, two different parameter sets are defined in Table 6.4. The yield stress values of set 1 are taken from [Iesulauro 2006] and set 2 includes 10% higher values.

As first, the elastic model was compared to two plastic models with yield stress values

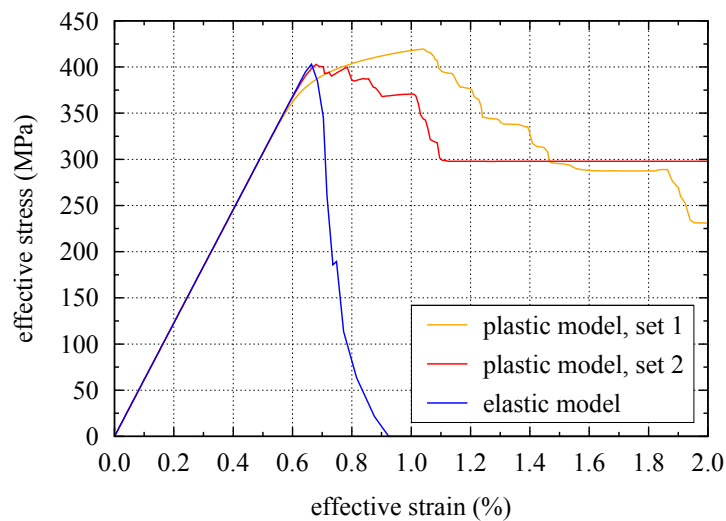


Figure 6.18: Response curves of tensile test simulations using samples with the same underlying geometry and the same elastic material parameters.

of set 1 and set 2, respectively. For all investigations the same geometrical polycrystal structure was applied. The normally distributed stiffness moduli and orientation of grains are defined once for the elastic model and the same values are transferred and assigned to the appropriate grains of the plastic models. Also yield stresses are defined only once and the original values are assigned to grains of the first plastic model and the 10% higher values are assigned to the appropriate grains of the second plastic model.

During the displacement controlled tensile test simulations the effective stress of a sample is calculated from the reaction force divided by the sample width. The effective stress of a sample is related to its effective strain, which is calculated from the applied uniform displacement of the top boundary divided by the sample height. The resulting effective stress-strain curves of the three models are visualized in Figure 6.18. While brittle interface characteristics are directly reflected in the response of the elastic model, the ductile response of the two elastoplastic models shows the influence of the applied Hill plasticity criterion. The assigned ideal plasticity of grains is reflected by the associated effective stress-strain curves, which asymptotically run to a residual value if yielding is activated. Figure 6.19 illustrates resulting crack patterns of the three models. Grey colored zones can be interpreted as damaged grains due to the corresponding high values of equivalent plastic strain.

The lower yield stress values of the plastic model with parameter set 1 are reflected in a well-marked yielding process before reaching the tensile strength, which is about 5% higher compared to the other two models. This yielding process comes along with a later initiation of interface decohesion compared to the plastic model with increased yield stresses (parameter set 2) as shown by the evolution of plastic zones and interface openings in Figures 6.20 and 6.21.

The diagram of Figure 6.22 shows a comparison of three effective stress-strain curves

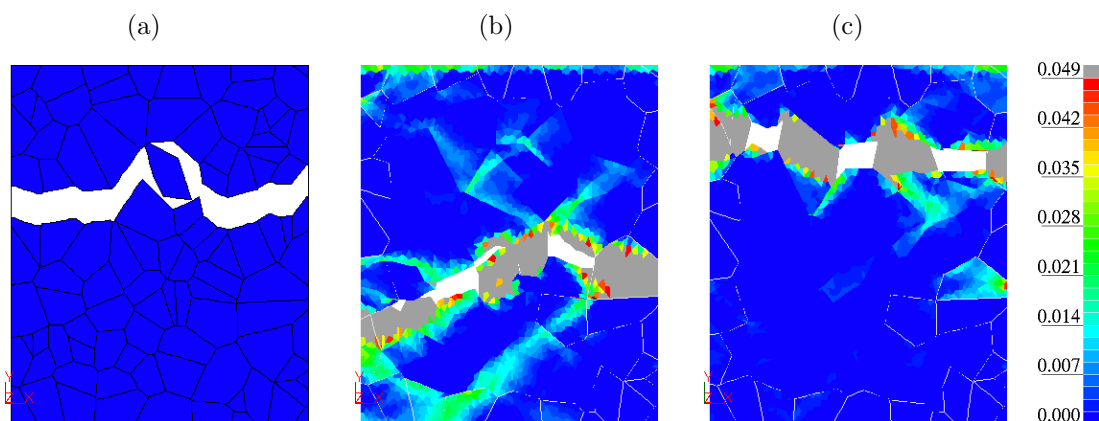


Figure 6.19: Simulated crack propagation in the elastic model (a), the plastic model with yield stress values of set 1 (b), and set 2 (c), respectively. Equivalent plastic strain in grains is visualized, where grey color indicates the highest value. White color indicates interface opening. Deformation is enlarged by factor 10.

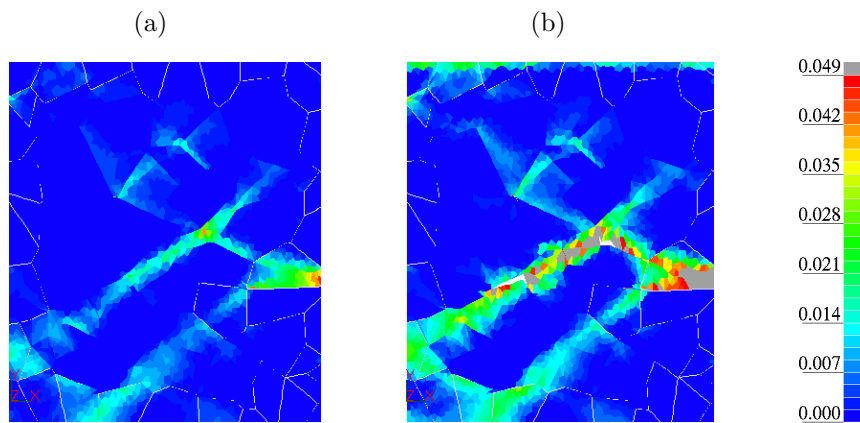


Figure 6.20: Equivalent plastic strain states at (a) 0.9% global strain, and (b) 1.2% global strain, simulated with yield stress values of set 1. Deformation is enlarged by factor 10.

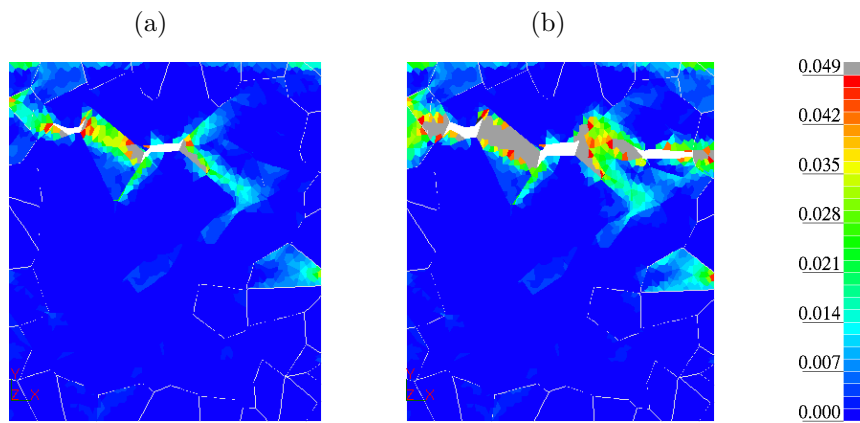


Figure 6.21: Equivalent plastic strain states at (a) 0.9% global strain, and (b) 1.2% global strain, simulated with yield stress values of set 2. Deformation is enlarged by factor 10.

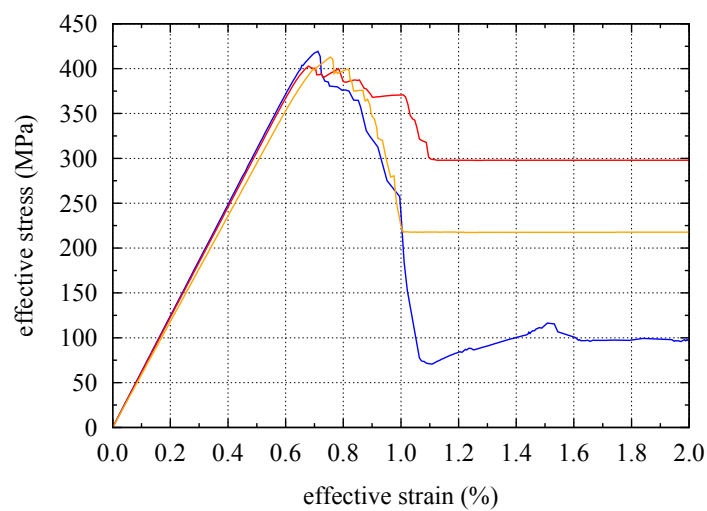


Figure 6.22: Response curves of tensile test simulations using samples with the same underlying geometry. Mean values of elastic and plastic material properties (set 2) are the same, but individual values vary due to different stochastic realizations.

belonging to samples with the same polycrystalline geometry and the same mean values of material parameters, but with different stochastic realizations of grain orientations, stiffness moduli, and yield stresses. While the response curves are close together until reaching the tensile strength of the sample, the softening path strongly differs depending on the ratio between interface opening with zero force transmission and yielding in grains with constant force transmission.

Although the linear elastic ideal plastic material model allows for the simulation of plasticity driven damage in grains, a plasticity model with hardening is suggested for further developments on the mesoscale. A reasonably defined hardening modulus could improve the combination of interface decohesion and evolution of plasticity in grains.

6.5 Application of atomistic-based cohesive zone representations in continuum polycrystal models

A final example documents the methodology of applying atomistic-based cohesive zone representations to interface elements of the continuum polycrystal model on mesoscale. Since the focus is on the methodology, the damage characteristics of perfect GBs are analyzed on microscale. These qualitative analyses could be quantitatively improved by the consideration of natural material defects as discussed in Chapters 5 and 8.

The starting point of the final example is a 2D polycrystal model of size $7.5 \mu\text{m} \times 7.5 \mu\text{m}$ with grain structure generated by the modified Voronoi algorithm with median value $d_{50} = 0.94 \mu\text{m}$ and standard deviation $\sigma_d = 0.78$. This mesoscale model consists of 12 grains and 24 GBs. The grains are discretized with 575 triangular elements, and 60 interface elements are assigned to the GBs. All finite elements use quadratic shape functions. Again, the polycrystal model is exemplary applied in a tensile simulation with boundary conditions according to Figure 6.12, which results in 2,551 unconstrained DOF.

The grain orientations are randomly generated by a normal distribution and linear elastic orthotropic material behavior with stochastically distributed parameters accord-

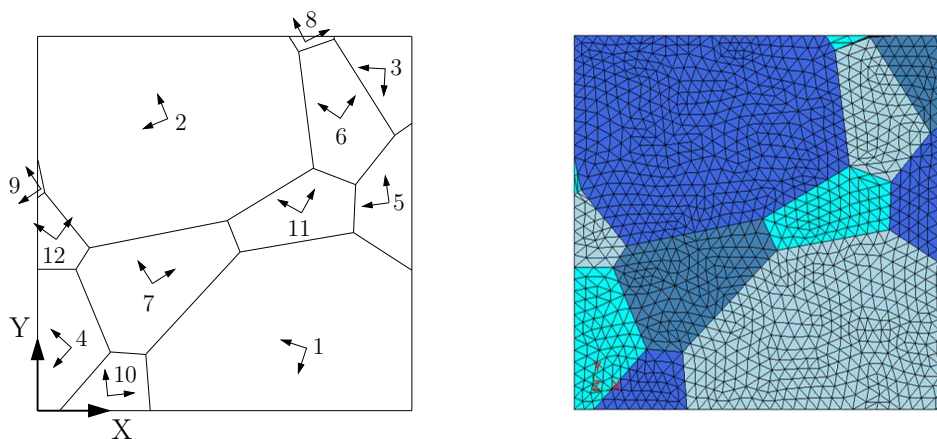


Figure 6.23: Left: Grain structure with orientation of material axes. Right: FE mesh.

ing to Table 6.1 is assigned to grain elements. The cohesive parameters of the coupled CZM with exponential decohesion path, which is assigned to the interface elements, are extracted from atomistic-based on-the-fly simulations. On the left-hand side of Figure 6.23 the applied grain structure with associated orientations of grain material axes is illustrated. The numbers are used as grain identifiers in the following tables. The discretized FE-model is visualized on the right-hand side of Figure 6.23. For the grains, a summary of orientation angles φ and the assigned orthotropic material parameters is listed in Table 6.5.

In preparation for the GB damage simulations on microscale the GB orientations $\delta_{i,j}$ have to be obtained with respect to the global (X,Y)-CS. From that and from the grain orientations φ_i , the approximative determination of Miller indices is possible which describe in the microscale model the GB orientation in the local (x,y,z)-coordinates of adjacent grains. The definition of Miller indices and the determination from Eulerian angles is explained in detail in Chapter 3. On the microscale, 3D QC simulations are performed to preserve the 3D nature of the crystallographic lattice including the corresponding mechanical characteristics. Since for presentiveness of the example a 2D mesoscale model is chosen, the assumption is made to consider the crystallographic $\langle 110 \rangle$ plane for all grains in the model. Therewith, the z-orientation of all crystallites (grains) in the 3D microscale models is $z = [110]$.

grain	φ (°)	ν_{12}	E_1 (GPa)	E_2 (GPa)	G_{12} (GPa)
1	162.4	0.33	69.2	43.3	27.6
2	112.2	0.33	71.8	43.6	25.0
3	177.4	0.33	75.2	39.9	26.6
4	138.2	0.33	70.8	38.9	25.1
5	98.2	0.33	70.3	42.4	25.9
6	56.1	0.33	72.0	45.9	24.1
7	32.4	0.33	77.2	45.1	30.2
8	27.2	0.33	71.4	37.6	26.4
9	124.3	0.33	73.0	44.3	25.8
10	5.6	0.33	71.2	40.1	26.8
11	60.7	0.33	76.3	38.6	28.5
12	54.1	0.33	73.3	46.2	27.2

Table 6.5: Orientation of orthotropic grain material axes by angle φ and stochastically distributed orthotropic material parameters of grains.

Figure 6.24 demonstrates the definition of GB orientations $\delta_{i,j}$ and grain orientations φ_i for grains 1, 5, and 11 with associated GBs. The determined Miller indices for microscale modeling are written in dashed rectangles each corresponding to one GB. With these geometrical characteristics, microscale models are generated as described in Chapter 5 and cohesive parameters are extracted for each GB by atomistic-based tensile and shear simulations using the nonlocal QC method.

A list of geometrical data of all 24 GBs in the polycrystal model is given in Table 6.6. Therein, the GBs are identified by the combination of adjacent grains written in the second column. In the third column the orientation of a GB between grains i and j is defined by the angle $\delta_{i,j}$ from the GB line to a line parallel to the global X-axis. The GB misorientation in the mesoscale model is given in the fourth column by the difference in orientation of grains i and j . The Miller indices, which approximately describe the orientation of crystallites in the atomistic GB model on the microscale, are calculated according to the definitions in Chapter 3. Column five specifies the local x-axis of crystallite i , which is parallel to the GB, as well as the local y-axis of crystallite i , which is perpendicular to the GB. The sixth column gives the appropriate axis-definitions of crystallite j in Miller indices. The term *crystallite* mainly used on the microscale corresponds to the term *grain* which is mainly applied on the mesoscale. Finally, the last column shows the GB misorientations of the microscale models which are calculated from the approximated Miller indices and which differ slightly from the original misorientations on the mesoscale.

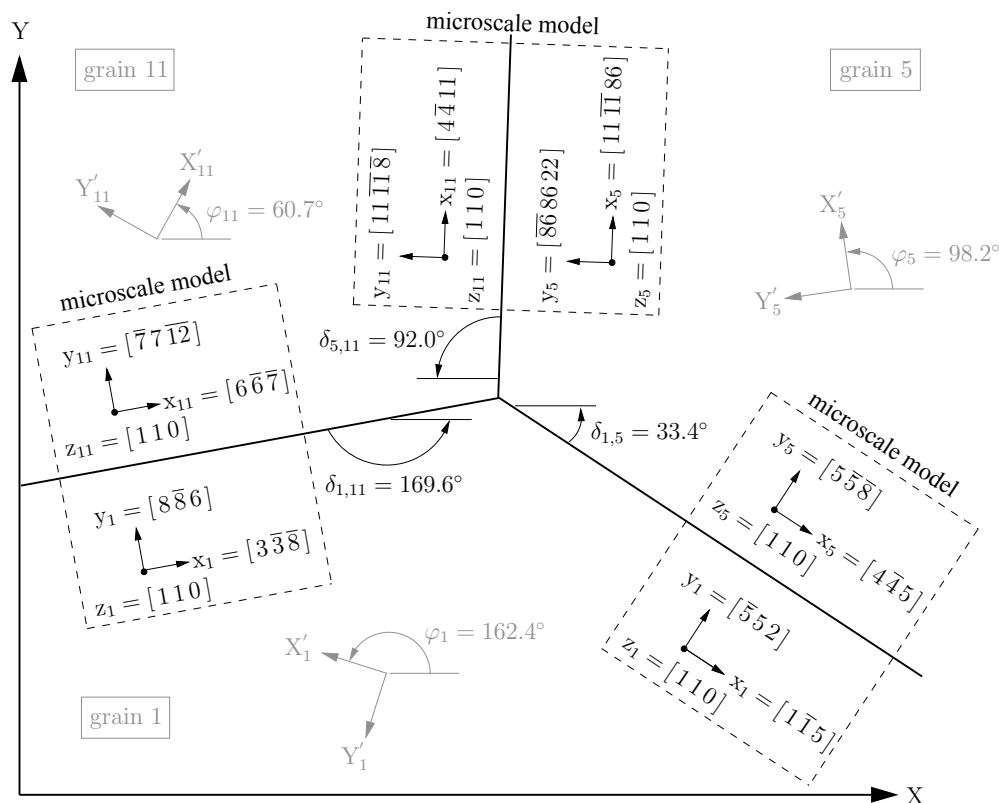


Figure 6.24: Definition of GB orientations $\delta_{i,j}$ and grain orientations φ_i . Thick continuous lines indicate GBs. Dashed rectangles contain orientation data of crystallites for the GB models on microscale.

GB	adjacent grains i, j	GB orientation δ in global CS ($^{\circ}$)	GB misorientation from angles φ_i ($^{\circ}$)	Miller Indices of GB description		GB misorientation from Miller Indices ($^{\circ}$)
				grain i	grain j	
1	1, 5	33.4	64.1	$x_i = [1\bar{1}5]$ $y_i = [5\bar{5}2]$	$x_j = [4\bar{4}5]$ $y_j = [5\bar{5}8]$	64.3
2	1, 7	132.8	130.0	$x_i = [3\bar{3}2]$ $y_i = [2\bar{2}6]$	$x_j = [14\bar{14}75]$ $y_j = [75\bar{75}28]$	130.0
3	1, 10	85.6	156.8	$x_i = [7\bar{7}4]$ $y_i = [44\bar{14}]$	$x_j = [32\bar{32}1]$ $y_j = [1\bar{1}64]$	156.7
4	1, 11	169.6	78.3	$x_i = [3\bar{3}8]$ $y_i = [8\bar{8}6]$	$x_j = [6\bar{6}7]$ $y_j = [7\bar{7}12]$	78.2
5	2, 6	82.8	56.2	$x_i = [44\bar{21}]$ $y_i = [21\bar{21}8]$	$x_j = [8\bar{8}13]$ $y_j = [13\bar{13}16]$	56.1
6	2, 7	168.7	100.2	$x_i = [11\bar{11}3]$ $y_i = [3\bar{3}22]$	$x_j = [3\bar{3}11]$ $y_j = [11\bar{11}6]$	100.2
7	2, 8	56.8	95.0	$x_i = [7\bar{7}51]$ $y_i = [51\bar{51}14]$	$x_j = [7\bar{7}1]$ $y_j = [1\bar{1}14]$	95.2
8	2, 9	78.4	168.0	$x_i = [99\bar{68}]$ $y_i = [68\bar{68}18]$	$x_j = [13\bar{13}44]$ $y_j = [44\bar{44}26]$	167.9
9	2, 11	148.9	128.5	$x_i = [99\bar{2}]$ $y_i = [22\bar{2}18]$	$x_j = [2\bar{2}5]$ $y_j = [5\bar{5}4]$	128.4
10	2, 12	50.8	121.9	$x_i = [11\bar{11}51]$ $y_i = [51\bar{51}22]$	$x_j = [8\bar{8}3]$ $y_j = [3\bar{3}16]$	121.8
11	3, 5	145.5	100.9	$x_i = [15\bar{15}28]$ $y_i = [28\bar{28}30]$	$x_j = [10\bar{10}7]$ $y_j = [7\bar{7}20]$	100.8
12	3, 6	57.6	121.3	$x_i = [1\bar{1}1]$ $y_i = [1\bar{1}2]$	$x_j = [8\bar{8}5]$ $y_j = [5\bar{5}16]$	120.9
13	3, 8	84.8	150.2	$x_i = [5\bar{5}1]$ $y_i = [1\bar{1}10]$	$x_j = [7\bar{7}4]$ $y_j = [44\bar{14}]$	149.9
14	4, 7	67.5	105.9	$x_i = [14\bar{14}41]$ $y_i = [41\bar{41}28]$	$x_j = [44\bar{1}]$ $y_j = [1\bar{1}8]$	105.8
15	4, 10	131.1	132.6	$x_i = [1\bar{1}0]$ $y_i = [002]$	$x_j = [2\bar{2}3]$ $y_j = [3\bar{3}4]$	133.3
16	4, 12	0.6	95.9	$x_i = [8\bar{8}13]$ $y_i = [13\bar{13}16]$	$x_j = [1\bar{1}1]$ $y_j = [1\bar{1}2]$	95.8
17	5, 6	128.7	137.8	$x_i = [3\bar{3}4]$ $y_i = [446]$	$x_j = [1\bar{1}17]$ $y_j = [17\bar{17}2]$	138.1

Continued on next page

Continued from previous page

GB	adjacent grains i, j	GB orientation δ in global CS ($^\circ$)	GB misorientation from angles φ ($^\circ$)	Miller Indices of GB description		GB misorientation from Miller Indices ($^\circ$)
				grain i	grain j	
18	5, 11	92.0	37.6	$x_i = [11 \bar{1} 1 86]$ $y_i = [\bar{8} 6 86 22]$	$x_j = [4 \bar{4} 11]$ $y_j = [11 \bar{1} 1 \bar{8}]$	37.5
19	6, 8	159.5	151.2	$x_i = [1 \bar{1} 2]$ $y_i = [2 2 2]$	$x_j = [15 \bar{1} 5 179]$ $y_j = [179 179 \bar{3} 0]$	151.5
20	6, 11	20.9	175.4	$x_i = [3 \bar{3} 1]$ $y_i = [\bar{1} 1 6]$	$x_j = [5 \bar{5} \bar{1}]$ $y_j = [\bar{1} 1 \bar{1} 0]$	174.8
21	7, 10	5.0	153.2	$x_i = [7 \bar{7} 13]$ $y_i = [\bar{1} 3 13 14]$	$x_j = [11 \bar{1} 1 \bar{8} 3]$ $y_j = [\bar{8} 3 83 22]$	153.3
22	7, 11	65.8	151.7	$x_i = [5 \bar{5} \bar{1}]$ $y_i = [1 \bar{1} 10]$	$x_j = [22 \bar{2} 2 23]$ $y_j = [23 \bar{2} 3 44]$	151.6
23	7, 12	122.1	158.2	$x_i = [1 \bar{1} \bar{3}]$ $y_i = [3 \bar{3} 2]$	$x_j = [1 \bar{1} 22]$ $y_j = [11 \bar{1} 1 \bar{1}]$	158.4
24	9, 12	142.4	109.9	$x_i = [12 \bar{1} 2 1]$ $y_i = [\bar{1} 1 24]$	$x_j = [13 \bar{1} 3 \bar{6} 2]$ $y_j = [\bar{6} 2 62 \bar{2} 6]$	109.9

Table 6.6: Geometrical data of grain boundaries.

On the microscale one tensile simulation and two shear simulations are realized on the atomistic interface models to extract the necessary cohesive parameters. The two shear simulations correspond to the two opposing shear directions in the 2D model on the mesoscale. The microscale simulations are realized as described in Section 4.3.2 and in Chapter 5 for perfect GBs. Table 6.7 lists the results of these simulations. The second column contains the minimized GB energy of the obtained stable GB configurations, which are all $\langle 110 \rangle$ ATGBs. The dependency of GB energies on the misorientation is visualized in Figure 6.25 on the basis of simulated $\langle 110 \rangle$ ATGBs. Therein, three regions of maximum GB energy values are around 35° , 95° , and 150° misorientation similar to the investigated $\langle 110 \rangle$ STGBs, whose energy values are visualized in Figure 4.23.

The third column of Table 6.7 lists the shear peak strength, which is the mean value of the two realized shear simulations. The fourth column contains the tensile peak strength, that equals the peak strength of the TSL in the coupled CZM applied on the mesoscale. The ratio between shear and tensile strength yields the coupling factor α in column five. The initial normal stiffness k_n in column six is calculated from the tensile strength and the corresponding normal interface opening. Finally, the last column gives values of the localized fracture energy G_f , which is extracted only from tensile simulations, since shear simulations are broken after reaching the peak strength, but before completely free fracture surfaces are formed.

The distribution of GB tensile and shear strength depending on the GB misorientation is illustrated in Figure 6.26. Therefrom, a dependency of the GB strength on the GB geometry can not be recognized. This insight agrees with statements in [Warner et al. 2006] and [Coffman et al. 2008a] concerning the tensile response of GBs. However, the present study shows high variations especially in the calculated tensile strength of GB configurations with similar misorientation. One reason could be the residual influence of

GB	GB energy (eV/Å ²)	$T_{t,p}$ (GPa)	$T_{n,p} = t_p$ (GPa)	α (-)	k_n (GPa/mm)	G_f (N/mm)
1	0.0221	1.70	7.60	0.223	$1.92 \cdot 10^7$	0.00267
2	0.0249	1.57	7.29	0.215	$2.22 \cdot 10^7$	0.00211
3	0.0304	1.90	7.99	0.238	$3.04 \cdot 10^7$	0.00191
4	0.0207	1.74	6.64	0.261	$2.61 \cdot 10^7$	0.00278
5	0.0247	1.80	6.62	0.272	$2.40 \cdot 10^7$	0.00275
6	0.0292	1.85	7.39	0.250	$2.23 \cdot 10^7$	0.00234
7	0.0267	1.76	7.69	0.229	$2.40 \cdot 10^7$	0.00239
8	0.0231	1.63	6.99	0.232	$2.16 \cdot 10^7$	0.00201
9	0.0244	1.94	7.83	0.248	$2.65 \cdot 10^7$	0.00257
10	0.0218	1.69	7.39	0.228	$2.10 \cdot 10^7$	0.00244
11	0.0275	1.67	6.80	0.245	$2.49 \cdot 10^7$	0.00227
12	0.0244	1.71	7.55	0.226	$2.49 \cdot 10^7$	0.00247
13	0.0294	1.78	7.68	0.232	$2.83 \cdot 10^7$	0.00190
14	0.0275	1.81	7.05	0.256	$2.07 \cdot 10^7$	0.00202
15	0.0213	1.86	7.29	0.254	$3.07 \cdot 10^7$	0.00243
16	0.0296	1.61	6.80	0.236	$2.13 \cdot 10^7$	0.00263
17	0.0303	1.55	7.28	0.213	$1.92 \cdot 10^7$	0.00244
18	0.0304	1.77	7.53	0.234	$1.97 \cdot 10^7$	0.00241
19	0.0300	1.72	7.45	0.231	$1.82 \cdot 10^7$	0.00221
20	0.0247	2.00	7.85	0.255	$3.43 \cdot 10^7$	0.00180
21	0.0299	1.59	6.97	0.227	$1.90 \cdot 10^7$	0.00253
22	0.0274	1.72	6.75	0.255	$2.82 \cdot 10^7$	0.00234
23	0.0296	1.62	7.01	0.231	$1.83 \cdot 10^7$	0.00263
24	0.0233	1.71	7.32	0.233	$2.50 \cdot 10^7$	0.00222

Table 6.7: Atomistic-based constitutive parameters of the coupled CZMs.

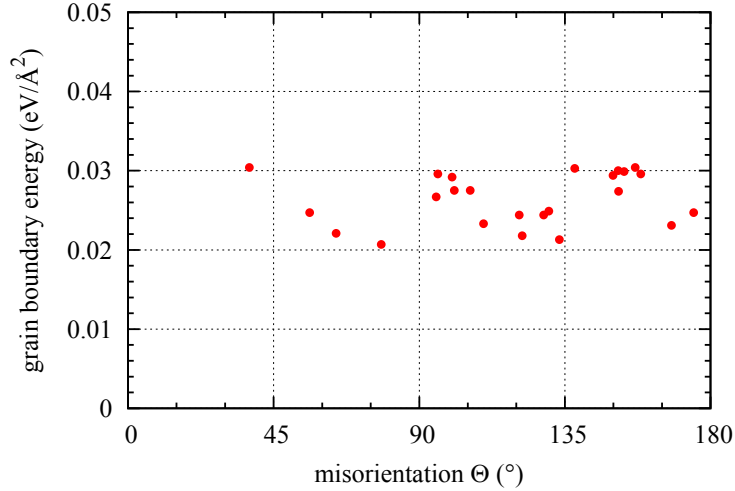


Figure 6.25: GB energies of $\langle 110 \rangle$ ATGBs with various misorientation.

unnatural free surfaces at model boundaries, which slightly disturbs the damage analysis and increases the simulation error.

The material parameters in Table 6.7 are assigned to the appropriate interface elements on the mesoscale and a displacement driven tensile simulation is performed on this continuum scale. The obtained response curve with the effective stress in global tensile direction versus the corresponding effective strain is drawn in Figure 6.27. The brittle response is clearly visible by the abrupt drop down of tensile stress accompanied with brittle interface decohesion. The failure process at about 3.8% global strain is visualized by a sequence of different states of interface opening in Figure 6.28. Additionally, a final state of complete failure at 6.7% global strain is illustrated.

A tensile strength of 3.42 GPa was obtained from the tensile simulation on the mesoscale. As discussed previously at the end of Section 5.2.4, the interface strength values extracted from atomistic simulations are about ten times higher than their macroscopic

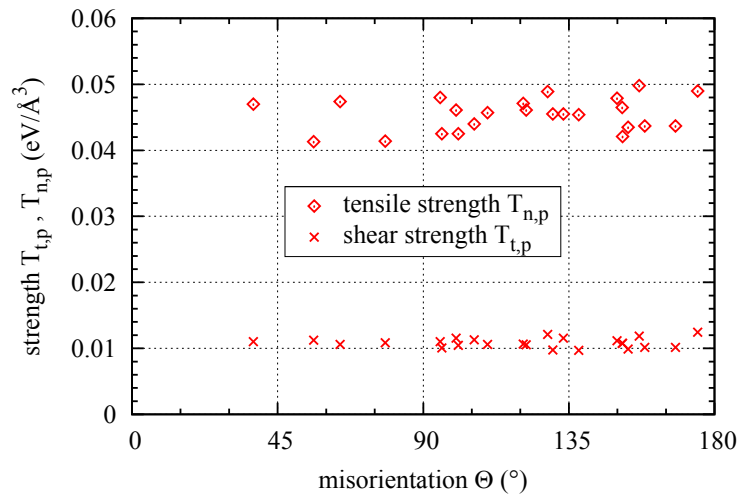


Figure 6.26: GB strength of $\langle 110 \rangle$ ATGBs with various misorientation.

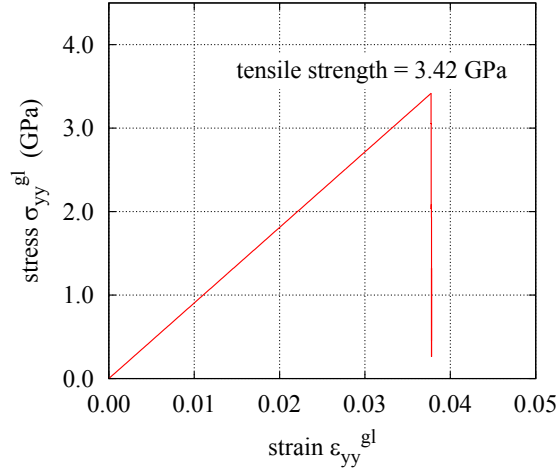


Figure 6.27: Response curve of the tensile simulation on mesoscale.

counterparts. Since interface decohesion is the only considered failure mechanism in the polycrystal model, the effective tensile strength on the mesoscale correlates to the interface strength. Consequently, also the tensile strength of the polycrystal model with atomistic-based interface parameters is about ten times higher than the tensile strength of polycrystal models with macroscopically measured interface parameters (Section 6.4.1). However, the example shows that the methodology of applying atomistic-based cohesive zone representation works in general. Improvements in the microscale models, especially

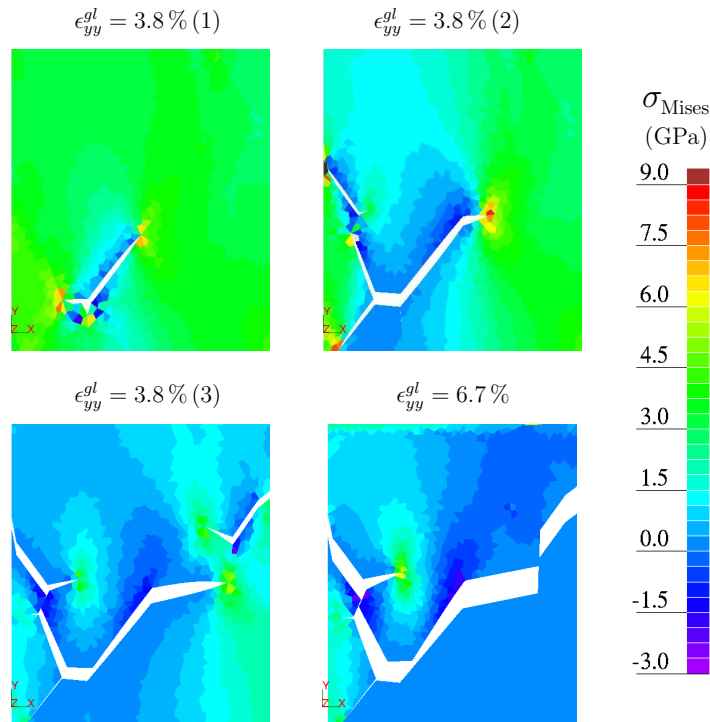


Figure 6.28: Progress of interface decohesion during tensile simulation on mesoscale. The contour plots visualize the von Mises stress in grains.

the consideration of impurities along GBs, will provide numerical results which are closer to the macroscopic ones derived from experiments.

The documented 2D example is kept small for reasons of presentiveness, but also to lower the computational time. Overall, the necessary computations for this example ran about 12 days using in average 12 cores of an AMD Opteron Server with processor type 8439 SE (2.8 GHz). The computational costs for the final mesoscale simulation is negligible but the high number of atomistic simulations with many atomic DOF increases the numerical effort significantly. At first, 24 simulations are necessary to obtain the minimized energy configurations of the 24 GBs. Starting from the obtained low energy configurations, 24 tensile simulations and 48 shear simulations are performed to parameterize the TSLs of the coupled CZM applied on the mesoscale. Referring to the presented example, one energy minimization simulation needs about 8 CPU hours, one tensile simulation needs about 21 CPU hours, and one shear simulation needs about 54 CPU hours. Nevertheless, atomistic-based cohesive zone representations are a promising numerical tool to partially substitute expensive failure experiments in future, when the progress in related research accompanies with the progress in computational technologies.

Chapter 7

Conclusions

7.1 Application of the 3D nonlocal Quasicontinuum method on the microscale

- An overview on various QC formulations was given in Chapter 4. From that, the quasistatic nonlocal QC formulation of Section 4.1.3 was chosen to investigate the problem of brittle intergranular damage using an atomistic material description. A quasistatic method is sufficient for the numerical investigation of brittle damage phenomena, since the time dependency of brittle damage is negligible. Moreover, the numerical effort is reduced by the QC concept to capture the essence of the phenomena of interest.
- The extension of the quasistatic **nonlocal** QC formulation to include effects of dynamics and finite temperature in case of ductile damage is not suggested. Just as in lattice statics, the energy minimization procedure of the nonlocal QC method comes along with low convergency due to the fact that the associated energy function has numerous local minima corresponding to various atomic configurations. Even robust and fast optimization methods, like the applied FIRE algorithm, require a large number of iteration steps to ensure an acceptable quality of results. The implementation of the nonlocal QC formulation at finite temperature and/or with the dynamics of atoms (Section 4.1.6) further increases the numerical complexity as well as the difficulties in finding energy minima of stable atomic configurations. If for an extended QC formulation the optimization procedure could be adjusted to run robustly, the number of necessary iteration steps is expected to further increase compared to the quasistatic implementation. Since the number of numerical operations per iteration step also increases, the total computational costs will reach or exceed the costs that have to be spent for pure atomistic simulation methods. Therewith, the intended efficiency of the QC method due to the reduced number of DOF gets lost by the increasing effort in computing equilibrium states. Consequently, molecular dynamics (Section 2.2.3) are suggested to investigate damage phenomena depending on dy-

namics and finite temperature on the atomistic scale, since this method naturally includes the dynamics of atoms. For the 3D investigation of dynamically driven processes (e.g. dislocation motion) in reasonably large models, couplings of MD regions to continuum domains are necessary, which allow for the transition of plastic deformations. Therefore, an own field of research has been established and promising approaches are followed, for example by the CADD method [Shilkrot et al. 2004].

As proved by several publications (e.g. [Rodney 2003], [Shenoy 1998]) the efficiency of the **local** QC formulation with dynamics and/or finite temperature survives due to the basic continuum approach of local QC. However, by the introduction of the Cauchy-Born rule from continuum mechanics, the local QC method loses the atomistic character. For this reason the local QC formulation is not suitable for the aimed investigation of intergranular damage based on physical phenomena of atomistics.

- A 3D nonlocal QC method was implemented, that robustly works for quasistatic simulations on GB samples of various misorientation. The implementation provides the efficient computation of atomistic processes due to parallelization of the computationally most intensive subroutines. The calculation of forces according to the QC-eFNL formulation (Section 4.2.5) and the application of the FIRE algorithm for energy minimization (Section 4.2.6) raise the efficiency and robustness of the implementation.

The implementation strictly ensures consistency in the formulations of weighting factor calculation, energy calculation, and force calculation. At the same time the implemented method fulfills the requirement of reducing to lattice statics in the limit of full atomistic resolution. By the simplicity but consistency of its formulation, the weighting factor calculation (Section 4.2.4) contributes to the robustness of the implementation, while at once its calculation is faster than in other implementations. Moreover, the present weighting factor calculation prevents numerical errors since by the way of implementation the factors are always greater or equal 1, which corresponds to the weight of the associated representative atom, itself.

The automatic generation of suitable FE meshes for arbitrary GB samples involves the intelligent predefinition of representative atoms due to the requirement of nodal positions at sites of representative atoms. Therewith, the nodes can not be generally placed on ideal positions of a grid, combined with an octree-based mesh generation as done, for example, in [Eidel et al. 2009] for the simulation of nanoindentation in a sample with convenient crystal orientation. Consequently, Section 4.2.2 suggests a qualified meshing algorithm which was introduced to prevent warped finite elements, especially in case of GB samples with arbitrary misorientation. As a result, the numerical error due to finite elements with high aspect ratio is kept small.

- The successful validation of the implemented 3D nonlocal QC method with lattice statics was done by a nanoindentation simulation (Section 4.3.1). This example was also used to investigate the quality of the method depending on the chosen cluster size. The QC results were found to be in good agreement to the results of lattice statics in case of cluster radii $r_{cl} \geq \sqrt{3/2} a_0$. Applying those cluster radii, the present QC implementation was validated to provide high quality results related to lattice statics. Both, the force-depth curves and the dislocation microstructures, have shown satisfying accordance. Moreover, the presented nanoindentation results are in good agreement with results of [Eidel et al. 2009]. At last, compared to lattice statics, a relevant speed-up of the simulation process was possible by the application of the quasistatic nonlocal QC method.
- The investigation of intergranular damage involves the generation of suitable GB samples. In Section 4.3.2 a procedure for 3D problems was proposed to reliably find the lowest energy GB configuration for a given misorientation. The procedure was validated to published numerically and experimentally observed values by calculated GB energies of $\langle 110 \rangle$ symmetric tilt GBs in aluminum. Own calculations are partially closer to the experimental curve than numerical results from literature. By additional investigations of asymmetric GBs the conclusion was drawn, that the procedure generally works for interfaces with arbitrary misorientation.

7.2 Derivation of traction separation laws from atomistic simulations

- Following a proposal of [Coffman et al. 2008b] a modeling strategy was demonstrated in Section 5.2.1 to create 3D QC models of unperiodic GB configurations for the simulation of the intergranular damage process on microscale. The QC models are applied to extract cohesive parameters from atomistical tensile and shear simulations.
- The tensile strength and the associated normal interface opening can be determined from atomistical tensile simulations and the initial elastic stiffness of the GB is derived from these parameters. The shear strength can be extracted from atomistical shear simulations and values of the localized fracture energy are obtained from both simulation types. These atomistical determined parameters are sufficient to reproduce the interface decohesion process by a coupled CZM on the mesoscale.
- The cohesive parameters which are obtained from shear simulations depend on the shear direction within the interface plane because of the anisotropic crystallography. Consequently, the fracture characteristics in different shear directions have to be taken into account. In the presented dissertation shear in positive and negative directions of the global GB coordinate system was analyzed and resulting strength

values are averaged to define a general shear strength for the coupled CZM on the mesoscale.

- The influence of sample size on extracted cohesive parameters was investigated for tensile and shear simulations on models without periodic boundary conditions. The size effect was found to be small in tensile simulations. In shear simulations no size effect was recognized but general variations of about fifteen per cent in the shear strength motivate a stochastic study in subsequent research.
- Associated with the coupled CZM a TSL with exponential decohesion path was introduced to describe the interface decohesion process on the mesoscale. The TSL can be parameterized with atomistical determined values. According to [Tvergaard 2003] the normal and tangential interface openings are coupled by an introduced relative interface opening. The ratio between normal and tangential interface opening is controlled by a factor α depending on the GB tensile strength and the GB shear strength.
- Cohesive parameters which are extracted from microscale simulations show significant deviations compared to their macroscopic counterparts, for example, the atomistical derived cohesive peak strength values are about ten times higher than natural GB strength values. One reason is that natural GBs consists of more defects than only the misorientation, while perfect GBs were applied in the simulations. Consequently, atomic level defects have to be considered in more realistic studies of intergranular damage.
- According to a definition from [Spearot et al. 2004] a measure of nanoporosity, that describes the damage at the atomic level by broken bonds, was applied for the determination of the initial damage at GBs. The evolution of damage in tensile and shear simulations was also followed by the measure of nanoporosity. The correlation of measured nanoporosity with corresponding energy and stress states at the GB has shown that this damage measure is well suited to capture the interfacial damage evolution.
- A first investigation of GBs with additional defects was realized by increasing the initial nanoporosity near the interface due to a random dispersion of point vacancies followed by a relaxation of the model. Simulations on two different GB types have shown that the influence of the increased initial nanoporosity on the extracted tensile and shear strength values is negligible. Further improvements in modeling interfaces on the atomistic microscale are necessary to simulate the intergranular damage evolution on imperfect GBs.

7.3 Damage simulations by continuum polycrystal models on the mesoscale

- The proposed continuum model for polycrystalline materials on the mesoscale enables the simulation of brittle intergranular damage in statically loaded 2D and 3D samples without the necessity of initial damage definition as it is necessary in classical approaches of linear elastic fracture mechanics. Additionally, the application of an orthotropic material model with Hill plasticity criterion to grains generally allows for the combined investigation of intergranular damage and plasticity driven intra-granular damage.
- A main advantage of the 2D mesoscale model is the underlying realistic polycrystalline geometry that is generated by a modified Voronoi algorithm. The modified Voronoi diagram shows a better fit to measured grain size distribution in polycrystalline materials compared to the frequently used classical Voronoi diagram. In principle, the presented modified Voronoi algorithm is able to generate 2D polycrystalline structures with an arbitrary predefined grain size distribution.
- The simulated 2D tensile tests on the mesoscale proved that the grain size distribution in the applied numerical samples has a considerable influence on the effective tensile strength of these samples. The mean value of the effective tensile strength increases with a wider range of grain sizes. Furthermore, the polycrystal model with classical Voronoi geometry was successfully applied to simulations of intergranular damage in 3D samples resulting in a decrease of tensile strength compared to the appropriate 2D simulations.
- The assignment of the linear elastic ideal plastic material model to grains improves the capabilities of the mesoscale model by taking into account inelastic intra-granular processes. Due to the ideal plastic character of the applied constitutive law the mechanical behavior of the related mesoscale model switches between brittle and ductile response within a small range, depending on the magnitude of yield stresses. A plasticity model with hardening is suggested to improve the combination of interface decohesion and intra-granular evolution of plasticity.
- The integration of atomistic-based cohesive zone representations on the mesoscale is demonstrated using atomistic on-the-fly simulations of the intergranular fracture process on the microscale to parameterize the separation laws assigned to GBs in a 2D continuum polycrystal model. The documented example is a first proof of the general applicability of the proceeding. However, the computational costs are high and future developments are necessary to increase the quality of results, especially by an improved consideration of material defects and triple junctions.

Chapter 8

Outlook

8.1 Atomistic-based cohesive zone representations

Atomistic-based cohesive zone representations are derived to substitute phenomenologically defined traction separation laws of coupled cohesive zone models. However, the documented damage simulations on aluminum models have shown that, for example, cohesive strength values in tension which were extracted from atomistic simulations (~ 7 GPa) are significantly higher than natural strength values (~ 500 MPa). There are several reasons for this mismatch which motivate further research in atomistic interface modeling.

The almost defect and impurity free interfaces of applied perfect GB models allow for high stress levels. Only misorientation of adjacent grains has caused defects which were measured by the nanoporosity parameter. A small but negligible reduction in GB strength was observed for additionally introduced point vacancies. The consideration of natural defects such as crack-like vacancies, dislocations, and impurities will further lower the simulated strength of interfaces. A problem which has to be solved on this way is the derivation of suitable potential functions, especially to reproduce the atomic interaction forces between atoms of different chemical materials, as it is necessary to model impurities. A small number of such functions is provided by the groups of Mishin [Mishin 2009] and Ercolessi [Ercolessi 2009] for particular compounds of metals. Ongoing research is necessary in this field of physics to deliver a wide range of potential functions for atomistic simulations.

Another reason for the high stress levels in atomistic interface simulations is pointed out by [Gall et al. 2000], who note “that under some stress states other than pure tension, a size scale effect, which is the basis of strain gradient plasticity, will also cause the local stresses to be much higher than experimental observations on large scale samples.” This means that exemplary dislocation movement, as a source of plasticity and damage, is suppressed due to small model sizes and constraints at the boundaries.

The documented investigations were restricted to interfaces between two grains to derive cohesive laws for the quantitative description of the GB decohesion process. Nevertheless, [Coffman et al. 2008b] found that crack nucleation mainly occurs at triple

junctions, edges, and corners which are not described by cohesive laws. The stress level, for example at triple junctions, is higher than in the middle of GBs. In future, models could be developed which consider the stress concentration in such regions. A proposal is made in [Coffman et al. 2010] to combine full-atomistic simulations of triple junctions with continuum simulations. The combination is imaginable by atomistic on-the-fly simulations and subsequent information transfer to the continuum model as well as by concurrent multiscale models consisting of continuum domains and adaptively introduced atomistic domains in regions of high stress levels.

8.2 Polycrystal modeling on the mesoscale and transition to the macroscale

On the mesoscale a heterogeneous polycrystal model is introduced to simulate the intergranular fracture process without initially defined damage. Concerning the geometry of polycrystal models the focus was on an improved algorithm for the reproduction of measured grain size distribution. The change in shape and orientation of grains due to forming processes was not yet treated. Changes in the shape of grains can be considered by individual length scaling in different directions, which exemplary means for the modified Voronoi algorithm the substitution of circles by ellipses in the process of grain generation (Section 6.2.2). Alternatively, the geometry of formed polycrystals can be analyzed by images and realistic grain structures could be created by image processing.

The orientation of grains is expressed by orientation distribution functions (ODF), which can be extracted, for example, from microscopic image analyses. Usually, polycrystalline materials have a preferred orientation, the so called texture, which is characterized by the normal direction (ND), the rolling direction (RD), and the transverse direction (TD) [Randle et al. 2000]. Pole figures are well suited to visualize the texture or distribution of grain orientations respectively in polycrystalline materials. For example, a $\{100\}$ pole figure is illustrated in Figure 8.1. This pole figure from [DolTPoMS 2010] shows that the $\{100\}$ poles of the crystallites have preferred orientation aligned with the rolling, transverse and normal directions. The extension of the presented polycrystal models to reproduce elongated grains with preferred orientations is one of the next intended steps of model improvement on the mesoscale.

Another advancement of the mesoscale model is aimed by the introduction of an anisotropic plasticity model to capture crystal plasticity effects in grains. Therewith, an analysis of combined brittle and ductile damage would be improved in extension to the investigations of the presented dissertation which focuses on brittle GB damage. A first step in the direction of plasticity models for grains has shown, that the applied ideal plastic orthotropic material law with Hill criterion is not sufficient to satisfactory model crystal plasticity (Section 6.4.2).

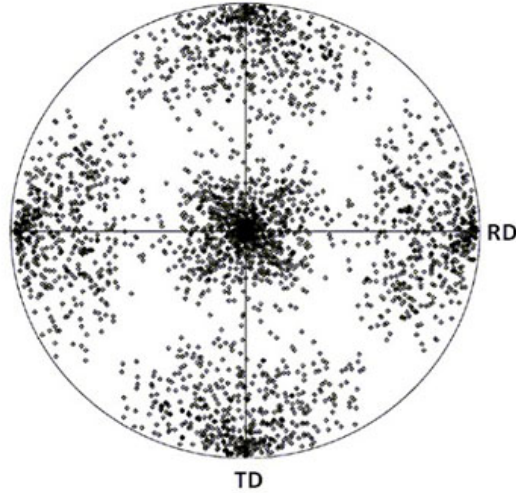


Figure 8.1: $\{100\}$ pole figure from [DoITPoMS 2010]. Black dots indicate $\{100\}$ poles of the crystallites. RD and TD denote the rolling and transverse directions, respectively.

Additionally, the application of improved algorithms in 3D is a future work, since until now the 3D polycrystal model is restricted to classical Voronoi geometries and linear elastic orthotropic grains.

Referring to the overall multiscale concept, which was presented in the introduction (Chapter 1), the transition to the macroscale is a final part of the proposed research which should follow this dissertation. The integration of micro- and mesoscale results into an engineering damage model on the macroscale is aimed for the applicability of the multiscale approach. For the transition to the macroscale the problem of unperiodic damage situations in mesoscale samples has to be considered again. That means that classical homogenization techniques can not be applied and numerical homogenization with scale transition of damage information in stochastic parameters is suggested. These stochastic parameters can describe the damage in the macroscale model as inputs of an anisotropic damage tensor.

Appendices

Appendix A

Summary of the implemented 3D nonlocal QC formulation

The implementation of the 3D nonlocal QC formulation with EAM potentials is based on the following formulas:

- Total potential

$$\Pi^{QC}(\mathbf{u}^h) = E_{tot}^{QC}(\mathbf{u}^h) + E_{tot}^{QC,ext}(\mathbf{u}^h)$$

- Total internal energy

$$E_{tot}^{QC}(\mathbf{u}^h) = \sum_{\alpha=1}^R \frac{n_{\alpha}}{n_{\alpha}^c} \sum_{k=1}^{C_{\alpha}} \left(U_k(\rho_k) + \frac{1}{2} \sum_{\substack{i=1 \\ i \neq k}}^N \phi_{ki}(r_{ki}) \right)$$

$$\text{with } \rho_k = \sum_{\substack{i=1 \\ i \neq k}}^N \rho_{ki}(r_{ki})$$

- Total external energy

$$E_{tot}^{QC,ext}(\mathbf{u}^h) = - \sum_{\alpha=1}^R \frac{n_{\alpha}}{n_{\alpha}^c} \sum_{k=1}^{C_{\alpha}} \mathbf{f}_k^{ext} \mathbf{u}_k^h$$

$$\text{or } E_{tot}^{QC,ext}(\mathbf{u}^h) = \sum_{\alpha=1}^R \frac{n_{\alpha}}{n_{\alpha}^c} \sum_{k=1}^{C_{\alpha}} \Pi_k^{ext}$$

- Nodal force vector

$$-\mathbf{f}_{\mathbf{a}} = \sum_{\alpha=1}^R \frac{n_{\alpha}}{n_{\alpha}^c} \sum_{k=1}^{C_{\alpha}} \left[\sum_{\substack{i=1 \\ i \neq k}}^N \left\{ \left[U'_k \rho'_{ki} + \frac{1}{2} \phi'_{ki} \right] \frac{\mathbf{r}_{ki}}{r_{ki}} [N_{\mathbf{a}}(\mathbf{X}_k) - N_{\mathbf{a}}(\mathbf{X}_i)] \right\} - \mathbf{f}_k^{ext} N_{\mathbf{a}}(\mathbf{X}_k) \right]$$

- System matrix (in case of Newton-Raphson iteration)

$$\mathbf{k}_{\mathbf{ab}} = \sum_{\alpha=1}^R \frac{n_{\alpha}}{n_{\alpha}^c} \sum_{k=1}^{C_{\alpha}} \sum_{\substack{i=1 \\ i \neq k}}^N \left\{ \left[\left(U_k'' \rho'_{ki} \sum_{\substack{i=1 \\ i \neq k}}^N \rho'_{ki} + U_k' \rho''_{kl} + \frac{1}{2} \phi''_{ki} \right) \frac{\mathbf{r}_{ki} \otimes \mathbf{r}_{ki}}{r_{ki}^2} \right. \right. \\ \left. \left. + \left(U_k' \rho'_{ki} + \frac{1}{2} \phi'_{ki} \right) \left(\frac{\mathbf{I}}{r_{ki}} - \frac{\mathbf{r}_{ki} \otimes \mathbf{r}_{ki}}{r_{ki}^3} \right) \right] [N_{\mathbf{a}}(\mathbf{X}_k) - N_{\mathbf{a}}(\mathbf{X}_i)] [N_{\mathbf{b}}(\mathbf{X}_k) - N_{\mathbf{b}}(\mathbf{X}_i)] \right\}$$

- Weighting factors

$$n_{\alpha} = \sum_{i=1}^N N_{\alpha}(\mathbf{X}_i)$$

$$n_{\alpha}^c = \sum_{k=1}^C N_{\alpha}(\mathbf{X}_k)$$

Appendix B

SLang commands for atomistic-based microscale simulations

The command description follows the structure of the public SLang documentation [SLang 2010]. A command line in SLang consists of:

- the **command_group** and the **command** finished by comma
- the optional **attributes** finished by comma
- the **inputs** finished by comma
- the **outputs** finished by slash

For example, a SLang command line can be written as follows:

command_group command , attribute , input , output /

The SLang commands and material laws, which are implemented for the damage analysis on mesoscale, can be found in the public SLang documentation [SLang 2010].

The following pages document SLang commands, which are implemented for atomistic-based microscale simulations. These commands are not part of the public SLang documentation. The commands are not in alphabetic order, but in chronological order according to their application in a reasonable modeling and simulation process. Attribute groups are taken together in one line in which the default attribute is underlined.

Command: crystal create

Attributes: noreplace/replace/append
two_d/three_d
nonperiodic/periodic
noobject/object

Inputs: *crystal identification number* (integer)
lattice type (ident): fcc/bcc/hdp
lattice parameter (real)
if **two_d**: not available yet
if **three_d**: *min. coordinates x, y, z* and *max. coordinates x, y, z* (real)
if **three_d**: *reference atom coordinates x, y, z* (real)
3 *Miller indices of crystal orientation parallel to global x-axis* (integer)
3 *Miller indices of crystal orientation parallel to global y-axis* (integer)
if **periodic**: *number of periodic directions* (integer)
if **periodic**: *sequence of periodic directions* (ident): x/y/z
if **periodic**: *cutoff radius* (real)

Outputs: if **object**: *generated atomic positions by coordinates x, y, z* (real, matrix)

Example: crystal create , replace three_d nonperiodic object ,
2 fcc 4.032
0.0 0.0 0.0 100.0 100.0 100.0
1.0 1.0 1.0
-5 5 4
2 -2 5 ,
crystal_2 /
* *Generates the atomic positions of a three dimensional nonperiodic fcc-lattice with lattice parameter 4.032. The crystal identifier is 2 and former crystals with this identifier will be replaced. The atomic positions are generated in a cuboid with minimum coordinates x=0.0, y=0.0, z=0.0 and maximum coordinates x=100.0, y=100.0, z=100.0. Coordinates of the reference atomic position are x=1.0, y=1.0, z=1.0. The crystal orientation is defined by Miller indices x=[554] in global x-direction and y=[225] in global y-direction. The generated atomic positions are stored in the object crystal_2. /*

Description: Generates atomic positions of an ideal crystal lattice of cuboidal shape and stores the generated coordinates in an internal table. If the user defined Miller indices of global x-axis and global y-axis do not span an orthogonal right-hand-system, the Miller indices of the global y-axis are changed to define the y-axis according to an orthogonal right-hand-system perpendicular to the user defined x-axis and within the user defined x-y-plane. The orientation of the z-axis is defined by the cross product of x and y indices to build an orthogonal right-hand-system.

Command: crystal dataread

Attributes: -

Inputs: *filename* (string)

Outputs: -

Example: crystal dataread , , crystal_data.txt , /
** Reads crystal data from the file crystal_data.txt and stores the data in internal tables. /*

Description: Reads data of one or more crystals from a text file, which is usually written by the command **crystal datawrite**. The text file contains geometrical data of crystals as well as data of the corresponding QC model, for example, representative atoms and elements.

Command: crystal datawrite

Attributes: -

Inputs: *filename* (string)

Outputs: -

Example: crystal datawrite , , crystal_data.txt , /
* *Writes crystal data from internal tables to the file crystal_data.txt. /*

Description: Writes data of one or more crystals from internal tables to a text file which can be read by the command **crystal dataread**. The text file contains geometrical data of crystals as well as data of the corresponding QC model, for example, representative atoms and elements.

Command: crystal prepare

Attributes: single/group/total
domains/qc_domains/rep_atoms
uniform/gb/atomistic
noobject/object

Inputs: if **single:** *crystal identification number* (integer)
if **group:** *number of crystals* (integer)
if **group:** *list of crystal identification numbers* (integer)
if **domains/qc_domains:** *minimal domain size* (real)
if **domains/qc_domains:** *number of parallel tables* (integer)
if **rep_atoms:**
 if **uniform:** *number of represent. atoms in x, y, z-direction* (integer)
 if **gb:** *list of grain boundary identifications - one per crystal* (ident):
 x_min/x_max/y_min/y_max/z_min/z_max
 if **gb:** *thickness of full atomistic zone on grain boundary* (real):

Outputs: if **object:** *coordinates x, y, z of representative atoms* (real, matrix)

Examples: crystal prepare , single domains , 2 10 4 , /
* *Applies domain decomposition to the crystal with identification number 2 by dividing this crystal in cuboidal sub-domains of edge sizes ≥ 10 . Sub-domains are prepared for MD simulation using 4 atomic data tables to accelerate a parallelized MD simulation with 4 threads. /*

crystal prepare , total qc_domains , 10 1 , /
* *Applies domain decomposition to all defined crystals by dividing the crystals in cuboidal sub-domains of edge sizes ≥ 10 . Sub-domains are prepared for QC simulation. The number of parallel tables (1) is ignored for attribute qc_domains. /*

crystal prepare , total rep_atoms atomistic , , /
* *Assigns the status of represent. atoms to all atoms of all crystals. /*

crystal prepare , total rep_atoms uniform , 8 10 8 , rep_atoms /
* *Assigns the status of represent. atoms to those atoms of all crystals, which are closest to a regular raster of 8x10x8 positions within this crystal. The coordinates of defined representative atoms are stored in the object rep_atoms. /*

crystal prepare , group rep_atoms gb object , 2 1 2 y_max y_min 30 , /
* *Assigns the status of represent. atoms to all atoms of crystal 1 in a zone of 30 length units from the associated maximum y-coordinate, and to all atoms of crystal 2 in a zone of 30 length units from the associated minimum y-coordinate. The resolution of representative atoms in the remaining model domains is reasonable coarsen by a program defined coarsening factor. /*

Description: Prepares crystal geometries by domain decomposition for molecular dynamics (MD: attribute **domains**) or quasicontinuum (QC: attribute **qc_domains**) simulations. The partitioning in sub-domains accelerates neighbor search and is the basis for parallelization of MD simulations. By contrast, the parallelization of QC simulations follows atom-decomposition and force-decomposition, respectively.

Application of the attribute **rep_atoms** offers different possibilities for the assignment of representative atoms in QC models. The combination with attribute **atomistic** creates full atomistic QC models, in which all atoms are representative. Therewith, lattice statics simulations can be realized, since the QC formulation reduces to lattice statics in the limit of full atomistic resolution. The combination with attribute **uniform** assigns uniformly distributed representative atoms in the model domain. The combination with attribute **gb** assigns full atomistic resolution in a zone of user defined thickness along user defined crystal boundaries. A program defined reasonable coarsening of the resolution of representative atoms is applied in the remaining model domains to ensure a high quality of the corresponding FE-mesh.

Domain data and representative atom data are stored in internal tables.

Command: crystal restraints

Attributes: single/group/total
x_range/y_range/z_range
alltime/relaxation/loading

Inputs: if **single**: *crystal identification number* (integer)
if **group**: *number of crystals* (integer)
if **group**: *list of crystal identification numbers* (integer)
lower coordinate limit of restraint range (real)
upper coordinate limit of restraint range (real)
direction of restraint (ident): x/y/z
displacement applied to restraint atoms (real):
flag for reaction force output (char): 0 ... no output/1 ... output

Outputs: if {*flag for reaction force output*} = 1: corresponding reaction force per relaxation and load step (real, vector)

Examples: crystal restraints , single y_range relaxation ,
1 -1.0 1.0 x 0.0 1 , reaction_y1 /
* *Defines restraints to selected atoms of crystal 1. Restraints are applied only for the relaxation step. Restraints are applied in x-direction by a displacement of 0.0 (fixed) to all atoms with coordinates $-1.0 \leq y \leq 1.0$ (y_range). The reaction force is stored in the object reaction_y1. /*

crystal restraints , total y_range loading , 99.0 101.0 y 5.0 0 , /
* *Defines restraints to selected atoms of all crystals. Restraints are applied only for load steps. Restraints are applied in y-direction by increments of the final displacement 5.0 to all atoms with coordinates $99.0 \leq y \leq 101.0$ (y_range). The reaction force is not stored. /*

Description: Defines restraints to selected atoms with coordinates in a user defined range. Restraints are applied only for the preceding relaxation step (attribute **relaxation**), or only for load steps (attribute **loading**), or for both (attribute **alltime**).

Command: crystal triangulate

Attributes: single/group/total

Inputs: if **single:** *crystal identification number* (integer)
if **group:** *number of crystals* (integer)
if **group:** *list of crystal identification numbers* (integer)

Outputs: -

Example: crystal triangulate, total , , /
* *Applies 3D Delaunay triangulation to all defined crystals, if they are prepared with representative atoms. /*

Description: Applies 3D Delaunay triangulation to crystals in case of intended QC simulation. Preparation with representative atoms is required before, since these atoms are the generation points of the Delaunay triangulation. The triangulation yields the FE mesh of the QC model consisting of tetrahedrons with nodes at sites of representative atoms.

Command: potential create

Attributes: noreplace/replace/append
internal/external
noobject/object

Inputs: *potential identification number* (integer)
if **internal:** *filename* (string)
if **external:** *indenter radius* (real)
if **external:** *indenter force constant* (real)
if **external:** *indenter center coordinates x, y, z* (real)
if **external:** *indenter displacement u_x, u_y, u_z* (real)
if **external:** *state at which indentation increment is reduced* (real)
if **external:** *reduction factor for indentation increment* (integer)

Outputs: if **internal** and **object:** *arguments and values of potential functions and their derivatives in discrete steps* (real, matrix)

Examples: potential create , internal object , 1 aluminum.fcn , potential_1 /
* *Discrete values of potential functions and their derivatives are generated from the parameters of input file aluminum.fcn. The values are assigned to a potential with identification number 1. Arguments and functional values are written in discrete steps to the object potential_1. /*

```
potential create , external , 2
  64.5 2000.0
  49.0 164.5 49.0
  0.0 -5.0 0.0
  0.5 10 , /
```

* *Creates a spherical external potential with potential identification number 2. The indenter radius is 64.5 and the indenter force constant is 2000.0. The indenter center is placed at coordinates $(x,y,z) = (49.0,164.5,49.0)$ and the final displacements applied to the indenter center during the simulation are $(u_x,u_y,u_z) = (0.0,-5.0,0.0)$. When 0.5 times the final indentation is reached, the indentation increment per simulation step is reduced by factor 10 and the number of remaining simulation steps is adapted to reach the user defined final indentation. /*

Description: If attribute **internal** is used, the command generates and stores discrete values of potential functions and their derivatives, which are calculated from parameters taken from an input file. Exemplary, the input file for EAM potential functions of aluminum is partially given in Appendix C.

If attribute **external** is used, the command creates a spherical external potential, which can be applied for simulations of nanoindentation to model a spherical indenter.

Command: potential assign

Attributes: single/group/total

Inputs: if **single:** *crystal identification number* (integer)
if **group:** *number of crystals* (integer)
if **group:** *list of crystal identification numbers* (integer)
potential identification number (integer)

Outputs: -

Example: potential assign , single , 2 1 , /
* *Assigns potential 1 to crystal 2.* /

Description: Assigns an internal potential by its identification number to one or more crystals which are also selected by their identification number.

Command: atom_continuum initialize

Attributes: single/group/total
position/velocity
noobject/object

Inputs: if **single:** *crystal identification number* (integer)
if **group:** *number of crystals* (integer)
if **group:** *list of crystal identification numbers* (integer)
lower limit of initial value (real)
upper limit of initial value (real)

Outputs: if **object:** *initial atomic positions or velocities, respectively* (real, matrix)

Examples: atom_continuum initialize , position object , 1 -0.05 0.05 , atomic_pos /
* *Initializes atomic positions of crystal 1 for MD simulation by application of initial displacements. These displacements are randomly generated by normal distribution within a range from -0.05 to 0.05. The new atomic positions are written to the object atomic_pos. /*

atom_continuum initialize , velocity object , 1 -0.1 0.1 , atomic_velo /
* *Initializes atomic velocities of crystal 1 for MD simulation by application of initial values. These values are randomly generated by normal distribution within a range from -0.1 to 0.1. The initial velocities are written to the object atomic_velo. /*

Description: Initializes atomic positions by application of initial displacements, and atomic velocities by initial values. The initialization is usually necessary for MD simulations.

Command: atom_continuum simulate

Attributes: single/group/total
md/qc
nonperiodic/periodic
noindenter/indenter
mkl_dss/mumps/pardiso/fire
noenergy/energy
nomeasuredamage/measuredamage
nodamage/pointdamage
noobject/object

Inputs:

- if **single:** *crystal identification number* (integer)
- if **group:** *number of crystals* (integer)
- if **group:** *list of crystal identification numbers* (integer)
- if **md:** *time step* (real)
- if **md:** *number of time steps* (integer)
- if **md:** *cutoff radius* (real)
- if **md:** *temperature in °C* (real)
- if **md:**
 - if **periodic:** *number of periodic directions* (integer)
sequence of periodic directions (ident): x/y/z
 - if **indenter:** *identification number of external potential* (integer)
- if **qc:** *number of load steps* (integer)
- if **qc:** *cluster radius* (real)
- if **qc:** *cutoff radius* (real)
- if **qc:**
 - if **indenter:** *identification number of external potential* (integer)
 - if **fire:** α_{start} (real)
 f_{α} (real)
 $f_{decrease}$ (real)
 $f_{increase}$ (real)
 N_{min} (integer)
 Δt (real)
 Δt_{max} (real)
- if **qc:** *maximum value of initial atomic displacement* (real)
- if **qc:**
 - if **energy:** *bounding coordinates $x_{min}, x_{max}, y_{min}, y_{max}, z_{min}, z_{max}$ of energy evaluation zone* (real)
 - if **measuredamage:** *direction* (ident): x/y/z
coordinate (real)
coordinate \pm deviation (real)
 - if **pointdamage:** *direction* (ident): x/y/z
coordinate (real)
density of point vacancies (real)
- if **qc:** *name of result directory* (string)

Outputs: if **object:** *resulting atomic positions by coordinates x, y, z (real, matrix)*

Examples: atom_continuum simulate , single md periodic indenter object ,

```
1
0.0032 100000 5.5 20.0
2 x z
3 ,
md_result /
```

** Starts a molecular dynamics simulation applied to atoms of crystal 1. One time step is 0.0032 and 100000 time steps will be simulated with a cutoff radius of 5.5 and at temperature 20.0°C. Periodic boundary conditions are applied in x- and z-direction and the crystal is loaded by an external potential with identification number 3. The resulting atomic positions are written to the object md_result. /*

```
atom_continuum simulate , total qc fire energy measuredamage object ,
60
4.5 5.558
0.12 0.99 0.75 1.10 3 0.05 0.10
0.00
20.0 80.0 45.0 85.0 20.0 80.0
y 65.0 10.0
qc_simulation ,
qc_result /
```

** Starts a quasicontinuum simulation applied to atoms of all defined crystals. 60 load steps will be simulated with a cluster radius of 4.5 and a cutoff radius of 5.558. The parameters of the FIRE optimization algorithm are: $\alpha_{start} = 0.12$, $f_{\alpha} = 0.99$, $f_{decrease} = 0.75$, $f_{increase} = 1.10$, $N_{min} = 3$, $\Delta t = 0.05$, $\Delta t_{max} = 0.10$. The maximum value of normally distributed initial atomic displacements is 0.00. The atomic energies are evaluated within a subregion defined by coordinates $20.0 \leq x \leq 80.0$, $45.0 \leq y \leq 85.0$, $20.0 \leq z \leq 80.0$. The cumulative damage D_c is measured within a subregion defined by coordinates $65.0-10.0 \leq y \leq 65.0+10.0$. Result files are created in the directory ./qc_simulation/. The resulting atomic positions are written to the object qc_result. /*

```

atom_continuum simulate , total qc fire energy pointdamage object ,
60
4.5 5.558
0.12 0.99 0.75 1.10 3 0.05 0.10
0.00
20.0 80.0 45.0 85.0 20.0 80.0
y 65.0 0.025
qc_simulation ,
qc_result /

```

* *The example equals the example before with one exception: attribute **measuredamage** is exchanged by attribute **pointdamage**. Consequently, point vacancies are introduced within a subregion defined by coordinates $65.0-5.0 \leq y \leq 65.0+5.0$, where 5.0 is an internal constant defined in the code. The applied point vacancy density in this subregion is 0.025, that means 2.5%. /*

Description: Starts a molecular dynamics (MD) or quasicontinuum (QC) simulation, respectively. An initial relaxation step is followed by user defined load steps. A logfile (*logfile.txt*), which will be written to the working directory, contains information on the simulation progress. In case of QC simulations several result files are written depending on applied attributes and stored in the result directory.

Appendix C

Input file with EAM potential functions

The parametric input files for the definition of EAM potential functions contain data which are provided by F. Ercolessi on his website [Ercolessi 2009]. On this website the meaning of the parameters is explained in detail. The input file for aluminum, which is used in the documented QC simulations, is partially listed below to show the file format. The file starts with a heading including the atomic coordination number and the atomic mass. Then, parameters are listed to describe the pair potential $\phi_{ij}(r_{ij})$ (!v2) and its first and second derivatives. The file continues with parameters describing the electron density $\rho_{ij}(r_{ij})$ (!rh) and its first and second derivatives. Finally, parameters are listed to describe the embedding energy $U_i(\rho_i)$ (!uu) and its first and second derivatives.

```
!Aluminum (fcc): pair potential and its first two derivatives.
13 26.981539
!v2
17 5.55805441821810
2.02111069753385
2.27374953472558
...
.362829766922787
!rh
17 5.55805441821810
2.02111069753385
2.27374953472558
...
-.0912720300911022
!uu
13 .00000000000000
.000000000000000
.100000000000000
...
.160139339245701
```

Bibliography

- Abraham F. F., Broughton J. Q., Bernstein N., and Kaxiras E. (1998). Spanning the length scales in dynamic simulation. *Computers in Physics* 12, 538–546.
- Anderson T. L. (2005). *Fracture Mechanics: Fundamentals and Applications* (3rd ed.). CRC Press, Boca Raton.
- Anvari M., Scheider I., and Thaulow C. (2006). Simulation of dynamic ductile crack growth using strain-rate and triaxiality-dependent cohesive elements. *Engineering Fracture Mechanics* 73, 2210–2228.
- Aurenhammer F. (1991). Voronoi diagrams - a survey of a fundamental geometric data structure. *ACM Computing Surveys* 23(3), 345–405.
- Barber C. B., Dobkin D. P., and Huhdanpaa H. T. (Dec 1996). The Quickhull algorithm for convex hulls. *ACM Trans. on Mathematical Software* 22(4), 469–483, <http://www.qhull.org>.
- Barenblatt G. I. (1962). The mathematical theory of equilibrium cracks in brittle fracture. *Advances in Applied Mechanics* 7, 55–129.
- Basinski Z. S., Duesberry M. S., and Taylor R. (1971). Influence of shear stress on screw dislocations in a model sodium lattice. *Canadian Journal of Physics* 49, 2160.
- Bathe K.-J. (1996). *Finite Element Procedures*. Englewood Cliffs: Prentice Hall.
- Bazant Z. P. (1987). Why continuum damage is nonlocal: justification by quasiperiodic microcrack array. *Mechanics Research Communications* 14, 407–419.
- Binder K. and Heermann D. W. (1992). *Monte Carlo Simulation in Statistical Physics* (2nd ed.). Springer Verlag.
- Bishop G. H. and Chalmers B. (1968). A coincidence - ledge - dislocation description of grain boundaries. *Scripta Metallurgica* 2, 133–140.
- Bitzek E., Koskinen P., Gähler F., Moseler M., and Gumbsch P. (2006). Structural relaxation made simple. *Physical Review Letters* 97(17), Art. No. 170201.
- Bouvard J. L., Chaboche J. L., and Gallerneau F. (2009). A cohesive zone model for fatigue and creep-fatigue crack growth in single crystal superalloys. *International Journal of Fatigue* 31, 868–879.

- Boyer L. L. and Hardy J. R. (1971). Lattice statics applied to screw dislocations in cubic metals. *Philosophical Magazine* 24, 647–671.
- Broughton J. Q., Abraham F. F., Bernstein N., and Kaxiras E. (1999). Concurrent coupling of length scales: Methodology and application. *Physical Review B* 60, 2391–2403.
- Buehler M. J. (2008). *Atomistic Modeling of Materials Failure* (1st ed.). Springer Verlag.
- Buehler M. J. and Gao H. (2005). Ultra-large scale simulations of dynamic materials failure. In Rieth M. and Schommers W. (Eds.), *Handbook of Theoretical and Computational Nanotechnology*, pp. Volume X: 1 – 41. American Scientific Publishers.
- Bunge H.-J. (1993). *Texture Analysis in Material Science - Mathematical Methods* (1st ed.). Cuvillier Verlag.
- Cai W., de Koning M., Bulatov V. V., and Yip S. (2000). Minimizing boundary reflections in coupled-domain simulations. *Physical Review Letters* 85, 3213–3216.
- Car R. and Parrinello (1985). Unified approach for molecular dynamics and density-functional theory. *Physical Review Letters* 55, 2471–2474.
- CFG (2010, January). Cornell Fracture Group. <http://www.cfg.cornell.edu/>.
- Chaboche J. L. (1988a). Continuum damage mechanics: Part I - general concepts. *Journal of Applied Mechanics* 55, 59–64.
- Chaboche J. L. (1988b). Continuum damage mechanics: Part II - damage growth, crack initiation, and crack growth. *Journal of Applied Mechanics* 55, 65–72.
- Chandra N. and Dang P. (1999). Atomistic simulation of grain boundary sliding and migration. *Journal of Materials Science* 34, 655–666.
- Chandra N., Li H., Shet C., and Ghonem H. (2002). Some issues in the application of cohesive zone models for metal-ceramic interfaces. *International Journal of Solids and Structures* 39, 2827–2855.
- Coffman V. R. and Sethna J. P. (2008a). Grain boundary energies and cohesive strength as a function of geometry. *Physical Review B* 77(14), Art. No. 144111.
- Coffman V. R., Sethna J. P., Bozek J., Ingraffea A., Bailey N. P., and Barker E. I. (2010). Challenges in continuum modeling of intergranular fracture. *Accepted*.
- Coffman V. R., Sethna J. P., Heber G., Liu M., Ingraffea A., Bailey N. P., and Barker E. I. (2008b). A comparison of finite element and atomistic modelling of fracture. *Modelling and Simulation in Materials Science and Engineering* 16, Art. No. 065008.
- D’Addetta G. A., Kun F., Ramm E., and Herrmann H. J. (2001). From solids to granulates - discrete element simulations of fracture and fragmentation processes in geomaterials. In Vermeer P. A., Diebels S., Ehlers W., Herrmann H. J., Luding S., and Ramm E. (Eds.), *Continuous and Discontinuous Modelling of Cohesive-Frictional Materials*, Berlin, pp. 231–258. Springer.

- Dash P. C. and Murti Y. V. G. S. (1983). Lattice statics reformulation of defect volumes - vacancies in ionic solids. *Physica B* 123, 27–34.
- Daw M. S. and Baskes M. I. (1983). Semiempirical, quantum mechanical calculation of hydrogen embrittlement in metals. *Physical Review Letters* 50(17), 1285–1288.
- Daw M. S. and Baskes M. I. (1984). Embedded-atom method: Derivation and application to impurities and other defects in metals. *Physical Review B* 29(12), 6443–6453.
- de Borst R. (2003). Numerical aspects of cohesive-zone models. *Engineering Fracture Mechanics* 70, 1743–1757.
- Dennis J. E. and Schnabel R. B. (1983). *Numerical Methods for Unconstrained Optimization and Nonlinear Equations*. Prentice-Hall, Inc.
- DolTPoMS (2010, June). University of Cambridge: Teaching and Learning Packages. http://www.msm.cam.ac.uk/doitpoms//tlplib/crystallographic_texture/texture_representation.php.
- Dugdale D. S. (1960). Yielding of steel shields containing slits. *Journal of the Mechanics and Physics of Solids* 8, 100–104.
- Dupuy L. M., Tadmor E. B., Miller R. E., and Phillips R. (2005). Finite temperature quasicontinuum: Molecular dynamics without all the atoms. *Physical Review Letters* 95, Art. No. 060202.
- Eidel B. and Stukowski A. (2009). A variational formulation of the quasicontinuum method based on energy sampling in clusters. *Journal of the Mechanics and Physics of Solids* 57, 87–108.
- Ercolessi F. (2009, November). The Ercolessi-Adams glue potential for aluminum. <http://www.ud.infn.it/~ercolessi/potentials/Al/>.
- Ercolessi F. and Adams J. B. (1994). Interatomic potentials from first-principles calculations: The force-matching method. *Europhysics Letters* 26, 583–588.
- Erwin N. and Warner D. (2010, February). Interface Structure Data Bank. <http://www.isdb.cee.cornell.edu/>.
- Fayad W., Thompson C. V., and Frost H. J. (1999). Steady-state grain-size distributions resulting from grain growth in two dimensions. *Scripta Materialia* 40(10), 1199–1204.
- Fish J., Nuggehally M. A., Shephard M. S., Picu C. R., Badia S., Parks M. L., and Gunzburger M. (2007). Concurrent AtC coupling based on a blend of the continuum stress and the atomistic force. *Computer Methods in Applied Mechanics and Engineering* 196, 4548–4560.
- Flocken J. W. and Hardy J. R. (1968). Application of the method of lattice statics to interstitial Cu atoms in Cu*. *Physical Review* 175, 919–927.

- Foiles S. M., Baskes M. I., and Daw M. S. (1986). Embedded-atom-method functions for the fcc metals Cu, Ag, Au, Ni, Pd, Pt, and their alloys. *Physical Review B* *33*, 7983–7991.
- Frenkel D. and Smit B. (2002). *Understanding Molecular Simulation: From Algorithms to Applications* (2nd ed.). Academic Press.
- Gall K., Horstemeyer M. F., Van Schilfhaarde M., and Baskes M. I. (2000). Atomistic simulations on the tensile debonding of an aluminum-silicon interface. *Journal of the Mechanics and Physics of Solids* *48*, 2183–2212.
- Guiasu S. and Shenitzer A. (1985). The principle of maximum entropy. *The Mathematical Intelligencer* *7*(1), 42–48.
- Gumbsch P. (1995). An atomistic study of brittle fracture: Toward explicit failure criteria from atomistic modeling. *Journal of Materials Research* *10*, 2897–2907.
- Gurson A. L. (1977). Continuum theory of ductile rupture by void nucleation and growth: Part I - yield criteria and flow rules for porous ductile media. *Journal of Engineering Materials and Technology* *99*, 2–15.
- Gustafson J. L. (1988). Reevaluating Amdahl’s law. *Communications of the ACM* *31*, 532–533.
- Hardy J. R. (1968). The elastic strength of point defects. *Journal of Physics and Chemistry of Solids* *29*, 2009–2014.
- Hill R. (1950). *The Mathematical Theory of Plasticity*. Oxford University Press.
- Hillerborg A., Mod er M., and Petersson P. E. (1976). Analysis of crack formation and crack growth in concrete by means of fracture mechanics and finite elements. *Cement and Concrete Research* *6*, 773–782.
- Hu W., Molodov D. A., Sch onfelder B., Shvindlerman L. S., and Gottstein G. (2000). HRTEM study on $\Sigma 7$ grain boundary in aluminium bicrystals with and without Ga doping. *Interface Science* *8*, 335–349.
- Hughes T. J. R. (2000). *The Finite Element Method: Linear Static and Dynamic Finite Element Analysis*. Dover Publications, Inc.
- Ibrahimbegovic A. and Delaplace A. (2003). Microscale and mesoscale discrete models for dynamic fracture of structures built of brittle material. *Computers & Structures* *81*, 1255–1265.
- Iesulauro E. (2006). *Decohesion of grain boundaries in statistical representations of aluminum polycrystals*. Ph. D. thesis, Cornell University, Ithaca, NY.
- Iesulauro E., Ingraffea A. R., Arwade S. R., and Wawrzynek P. A. (2002). Simulation of grain boundary decohesion and crack propagation in aluminum microstructure models. In Reuter W. G. and Piascik R. S. (Eds.), *Fatigue and Fracture Mechanics:*

- 33rd Volume, *ASTM STP 1417*, American Society for Testing and Materials, West Conshohocken, PA.
- Ingraffea A. R., Iesulauro E., Heber G., Dodhia K., and Wawrzynek P. A. (2002). A multiscale modeling approach to crack initiation in aluminum polycrystals. In Mang H. A., Rammerstorfer F. G., and Eberhardsteiner J. (Eds.), *Proceedings of the Fifth World Congress on Computational Mechanics, WCCM V*, Vienna, Austria.
- Jog C. S. (2007). *Foundations and Applications of Mechanics: Volume I: Continuum Mechanics* (2nd ed.). CRC Press.
- Kachanov L. M. (1986). *Introduction to Continuum Damage Mechanics*. Kluwer Academic Publishers, Dordrecht.
- Kanzaki H. (1957). Point defects in face-centred cubic lattice-I distortion around defects. *Journal of Physics and Chemistry of Solids* 2, 24–36.
- Kelchner C. L., Plimpton S. J., and Hamilton J. C. (1998). Dislocation nucleation and defect structure during surface indentation. *Physical Review B* 58(17), 11085–11088.
- Kelley C. T. (1999). *Iterative Methods for Optimization*. Society for Industrial and Applied Mathematics, Philadelphia.
- Kirchner S. (2001). *Ausscheidungshärtung dünner Al-0,6Si-0,6Ge-Schichten: Studie zur Übertragbarkeit eines Massivmaterial-Legierungskonzeptes*. Ph. D. thesis, Universität Stuttgart.
- Knap J. and Ortiz M. (2001). An analysis of the quasicontinuum method. *Journal of the Mechanics and Physics of Solids* 49, 1899–1923.
- Kobayashi H. (2009, November). Failure Knowledge Database: Brittle fracture of Liberty Ships. <http://shippai.jst.go.jp/en/Detail?fn=0&id=CB1011020&>.
- Kohlhoff S., Gumbsch P., and Fischmeister H. F. (1991). Crack propagation in b.c.c. crystals studied with a combined finite-element and atomistic model. *Philosophical Magazine* 64, 851–878.
- Krajcinovic D. (1998). *Damache Mechanics*. Elsevier, Amsterdam.
- Kröner E. (1963). On the physical reality of torque stresses in continuum mechanics. *International Journal of Engineering Science* 1, 261–262.
- Kulkarni Y., Knap J., and Ortiz M. (2008). A variational approach to coarse graining of equilibrium and non-equilibrium atomistic description at finite temperature. *Journal of the Mechanics and Physics of Solids* 56, 1417–1449.
- Lemaitre J. (1992). *Course on Damache Mechanics*. Springer, Berlin.
- Lesar R., Najafabadi R., and Srolovitz D. J. (1989). Finite-temperature defect properties from free-energy minimisation. *Physical Review Letters* 63, 624–627.
- Li J. (2005). Basic molecular dynamics. In Yip S. (Ed.), *Handbook of Materials Modeling*. Kluwer Academic Publishers.

- Luther T. and Könke C. (2009). Polycrystal models for the analysis of intergranular crack growth in metallic materials. *Engineering Fracture Mechanics* 76, 2332–2343.
- Matsubara T. (1952). Theory of diffuse scattering of X-rays by local lattice distortions. *Journal of the Physical Society of Japan* 7, 270–274.
- Mattson W. and Betsy M. R. (1999). Near-neighbor calculations using a modified cell-linked method. *Computer Physics Communications* 119, 135–148.
- Maugnin G. A. (1992). *The Thermomechanics of Plasticity and Fracture*. Cambridge University Press, Cambridge.
- McClintock F. A. (1968). A criterion for ductile fracture by the growth of holes. *Journal of Applied Mechanics* 35, 363–371.
- Meyers M. A. and Chawla K. K. (1984). *Mechanical Metallurgy*. Prentice-Hall Inc, Englewood Cliffs, NJ.
- Miller R. E. (1997). *On the Generalization of Continuum Models to Include Atomistic Features*. Ph. D. thesis, Brown University.
- Miller R. E. and Tadmor E. B. (2002). The quasicontinuum method: Overview, application and current directions. *Journal of Computer-Aided Materials Design* 9, 203–239.
- Mishin Y. (2009, November). CCM6 Embedded Atom Potentials. <http://cst-www.nrl.navy.mil/ccm6/ap/eam/index.html>.
- Mishin Y., Farkas D., Mehl M. J., and Papaconstantopoulos D. A. (1999). Interatomic potentials for monoatomic metals from experimental data and ab initio calculations. *Physical Review B* 59(5), 3393–3407.
- Moës N. and Belytschko T. (2002). Extended finite element method for cohesive crack growth. *Engineering Fracture Mechanics* 69, 813–833.
- Möller G. (2007). *Geotechnik* (1st ed.). Ernst und Sohn, Berlin.
- MRSEC (2010, January). Carnegie Mellon University: Materials Research and Engineering Center. <http://mimp.materials.cmu.edu/>.
- Mullins M. and Dokainish M. A. (1982). Simulation of the (001) plane crack in α -iron employing a new boundary scheme. *Philosophical Magazine A* 46, 771–787.
- Needleman A. (1987). A continuum model for void nucleation by inclusion debonding. *Journal of Applied Mechanics* 54, 525–531.
- Nishitani S. R., Ohgushi S., Inoue Y., and Adachi H. (2001). Grain boundary energies of Al simulated by environment-dependent embedded atom method. *Materials Science and Engineering A309-310*, 490–494.
- Okabe A., Boots B., and Sugihara K. (1992). *Spatial Tessellations: Concepts and Applications of Voronoi Diagrams*. Wiley.

- OpenMP (2008). *OpenMP Application Program Interface: Version 3.0*. OpenMP Architecture Review Board.
- Otsuki A. and Mizuno M. (1986). Grain boundary structure and related phenomena. *Suppl. Trans. JIM 27*, Japan Institute of Metals, 789.
- Ottosen N. S. and Ristinmaa M. (2005). *The Mechanics of Constitutive Modeling* (1st ed.). Elsevier.
- Park H. S., Karpov E. G., and Liu W. K. (2004). A temperature equation for coupled atomistic/continuum simulations. *Computer Methods in Applied Mechanics and Engineering 193*, 1713–1732.
- Pfeiler W. (2007). *Alloy Physics: A Comprehensive Reference*. Wiley-VCH.
- Plimpton S. (1995). Fast parallel algorithms for short-range molecular dynamics. *Journal of Computational Physics 117*, 1–19.
- Raabe D. (1998). *Computational Material Science*. Wiley-VCH.
- Rabczuk T. and Belytschko T. (2007). A three-dimensional large deformation meshfree method for arbitrary evolving cracks. *Computer Methods in Applied Mechanics and Engineering 196*, 2777–2799.
- Randle V. and Engler O. (2000). *Introduction to Texture Analysis: Macrotexture, Microtexture and Orientation Mapping*. CRC Press.
- Rittner J. D. and Seidman D. N. (1996). $\langle 110 \rangle$ symmetric tilt grain-boundary structures in fcc metals with low stacking-fault energies. *Physical Review B 54*(10), 6999–7015.
- Rodney D. (2003). Mixed atomistic/continuum methods: static and dynamic quasicontinuum methods. In Finel A., Maziere D., and Veron M. (Eds.), *NATO Science Series II, Vol. 108*, Dordrecht, pp. 265–274. Kluwer Academic Publishers.
- Rollett A. D. and Sintay S. (2010, January). CMU Microstructure Builder (mBuilder). <http://code.google.com/p/mbuilder/>.
- Rudd R. E. and Broughton J. Q. (2000). Concurrent coupling of length scales in solid state systems. *Physica Status Solidi B 217*, 251–291.
- Saether E., Yamakov V., and Glaessgen E. H. (2009). An embedded statistical method for coupling molecular dynamics and finite element analyses. *International Journal for Numerical Methods in Engineering 78*, 1292–1319.
- Sansoz F. and Molinari J. F. (2004). Incidence of atom shuffling on the shear and decohesion behavior of a symmetric tilt grain boundary in copper. *Scripta Materialia 50*(10), 1283–1288.
- Sansoz F. and Molinari J. F. (2005). Mechanical behavior of Σ tilt grain boundaries in nanoscale Cu and Al: A quasicontinuum study. *Acta Materialia 53*, 1931–1944.
- Schenk O. and Gärtner K. (2004). Solving unsymmetric sparse systems of linear equations with PARDISO. *Future Generation Computer Systems 20*, 475–487.

- Schmidt S. (2003). *Elektronenmikroskopische Untersuchungen zur Segregation von Ga an Al-Korngrenzen*. Ph. D. thesis, Universität Stuttgart.
- Shen S. and Atluri S. N. (2004). Atomic-level stress calculation and continuum-molecular system equivalence. *Computer Modeling in Engineering and Sciences* 6(1), 91–104.
- Shenderova O. A., Brenner D. W., Omeltchenko A., Su X., and Yang L. H. (2000). Atomistic modeling of the fracture of polycrystalline diamond. *Physical Review B* 61(6), 3877–3888.
- Shenoy V., Shenoy V., and Phillips R. (1999a). Finite temperature quasicontinuum methods. *Materials Research Society Symposium Proceedings* 538, 465–471.
- Shenoy V. B. (1998). *Quasicontinuum Models of Atomic-Scale Mechanics*. Ph. D. thesis, Brown University.
- Shenoy V. B. (2003). Multi-scale modeling strategies in material science - the quasicontinuum method. *Bull. Mater. Sci.* 26(1), 53–62.
- Shenoy V. B., Miller R., Tadmor E. B., Rodney D., Phillips R., and Ortiz M. (1999b). An adaptive finite element approach to atomic-scale mechanics - the quasicontinuum method. *Journal of the Mechanics and Physics of Solids* 47, 611–642.
- Shilkrot L. E., Curtin W. A., and Miller R. E. (2002a). A coupled atomistic/continuum model of defects in solids. *Journal of the Mechanics and Physics of Solids* 50, 2085–2106.
- Shilkrot L. E., Miller R. E., and Curtin W. A. (2002b). Coupled atomistic and discrete dislocation plasticity. *Physical Review Letters* 89, Art. No. 025501.
- Shilkrot L. E., Miller R. E., and Curtin W. A. (2004). Multiscale plasticity modeling: coupled atomistics and discrete dislocation mechanics. *Journal of the Mechanics and Physics of Solids* 52, 755–787.
- Sholl D. S. and Steckel J. A. (2009). *Density Functional Theory: A Practical Introduction* (1st ed.). Wiley.
- Simo J. C. and Hughes T. J. R. (1998). *Computational Inelasticity* (1st ed.). Springer.
- SLang (2010). *SLang: the Structural Language*. Institute of Structural Mechanics, Bauhaus University Weimar.
- Spearot D. E. (2005). *Atomistic Calculations of Nanoscale Interface Behavior in FCC Metals*. Ph. D. thesis, Georgia Institute of Technology.
- Spearot D. E., Jacob K. I., and McDowell D. L. (2004). Non-local separation constitutive laws for interfaces and their relation to nanoscale simulations. *Mechanics of Materials* 36, 825–847.
- Stukowski A. (2006). Atomistische Multiskalenmethoden zur Simulation kristalliner Festkörper. Diplomarbeit, Technische Universität Darmstadt.

- Sunyk R. and Steinmann P. (2006). Transition to plasticity in continuum-atomistic modelling. *Multidiscipline Modeling in Materials and Structures* 2(3), 249–286.
- Sutmann G. (2002). Classical molecular dynamics and parallel computing. In Groten-dorst J. (Ed.), *Quantum simulations of many-body systems: from theory to algorithm*, pp. 211–254. NIC-series 10.
- Sutton A. P. and Balluffi R. W. (1996). *Interfaces in Crystalline Materials*. Oxford University Press/Clarendon Press.
- Tadmor E. B. (1996). *The Quasicontinuum Method - Modeling Microstructure on Multiple Length Scales: A Mixed Continuum and Atomistic Approach*. Ph. D. thesis, Brown University.
- Tadmor E. B. and Miller R. (2010, January). Quasicontinuum. <http://www.qcmethod.com/>.
- Tadmor E. B. and Miller R. E. (2005). The theory and implementation of the quasicontinuum method. In Yip S. (Ed.), *Handbook of Materials Modeling*. Kluwer Academic Publishers.
- Tadmor E. B., Ortiz M., and Phillips R. (1996a). Quasicontinuum analysis of defects in solids. *Philosophical Magazine A* 73, 1529–1563.
- Tadmor E. B., Phillips R., and Ortiz M. (1996b). Mixed atomistic and continuum models of deformation in solids. *Langmuir* 12, 4529–4534.
- Tang Z., Zhao H., Li G., and Aluru N. R. (2006). Finite-temperature quasicontinuum method for multiscale analysis of silicon nanostructures. *Physical Review B* 74, Art. No. 064110.
- Thompson C. V. (1990). Grain growth in thin films. *Annual Review of Materials Science* 20, 245–268.
- Thompson C. V. (2000). Grain growth and evolution of other cellular structures. *Solid State Physics* 55, 269–314.
- Toi Y. and Kiyosue T. (1995). Damage mechanics models for brittle microcracking solids based on three-dimensional mesoscopic simulations. *Engineering Fracture Mechanics* 50(1), 11–27.
- Torquato S. (2002). *Random Heterogeneous Materials: Microstructure and Macroscopic Properties*. Springer.
- Tvergaard V. (1990). Material failure by void growth to coalescence. *Advances in Applied Mechanics* 27, 83–151.
- Tvergaard V. (2003). Cohesive zone representations of failure between elastic or rigid solids and ductile solids. *Engineering Fracture Mechanics* 70, 1859–1868.

- Tvergaard V. and Hutchinson J. W. (1992). The relation between crack growth resistance and fracture process parameters in elastic-plastic solids. *Mechanics and Physics in Solids* 40, 1377–1397.
- Uberuaga B. P. (2005). Accelerated molecular dynamics method. In Yip S. (Ed.), *Handbook of Materials Modeling*. Kluwer Academic Publishers.
- Unger J. F., Eckardt S., and Könke C. (2007). Modelling of cohesive crack growth in concrete structures with the extended finite element method. *Computer Methods in Applied Mechanics and Engineering* 196, 4087–4100.
- van der Giessen E. and Tvergaard V. (1996). Micromechanics of intergranular creep failure under cyclic loading. *Acta Metallurgica* 44, 2697–2710.
- Veilleux M. G., Hochhalter J. D., Bozek J. E., Wawrzynek P. A., and Ingraffea A. R. (2009). A geometric approach to stochastically modeling fatigue crack propagation at the microstructural length scale. In 12th *International Conference on Fracture*, Ottawa, Ontario, Canada.
- Voter A. F. (1996). Interatomic potentials for atomistic simulations. *MRS Bulletin* 21, 17–19.
- Wagner G. J. and Liu W. K. (2003). Coupling of atomistic and continuum simulations using a bridging scale decomposition. *Journal of Computational Physics* 190, 249–274.
- Wang G. J., Sutton A. P., and Vitek V. (1984). A computer simulation study of $\langle 001 \rangle$ and $\langle 111 \rangle$ tilt grain boundaries: the multiplicity of structures. *Acta Metallurgica* 32(7), 1093–1104.
- Warner D. H. and Molinari J. F. (2008). Deformation by grain boundary hinge-like behavior. *Materials Letters* 62, 57–60.
- Warner D. H., Sansoz F., and Molinari J. F. (2006). Atomistic based continuum investigation of plastic deformation in nanocrystalline copper. *International Journal of Plasticity* 22, 754–774.
- Weinan E. and Zhongyi H. (2002). A dynamic atomistic-continuum method for the simulation of crystalline materials. *Journal of Computational Physics* 182, 234–261.
- Weiner J. H. (2002). *Statistical Mechanics of Elasticity*. Dover Publications.
- Will J. (1996). Vergleich expliziter und impliziter Lösungsverfahren zur Verarbeitung von nichtlinearen, zusammengesetzten (multi surface) Fließbedingungen am Beispiel der Berechnung des geklüfteten Felsgesteines. In *Mitteilungen des ISM 96-2*, Weimar, Germany.
- Wolf D. (1992). Atomic-level geometry of crystalline interfaces. In Wolf D. and Yip S. (Eds.), *Materials Interfaces* (1st ed.), pp. 1–57. Chapman & Hall.

- Wolf D. and Lutsko J. F. (1989). On the geometrical relationship between tilt and twist grain boundaries. *Zeitschrift für Kristallographie* 189, 239–262.
- Wolf D. and Merkle K. L. (1992). Correlation between the structure and energy of grain boundaries in metals. In Wolf D. and Yip S. (Eds.), *Materials Interfaces* (1st ed.), pp. 87–150. Chapman & Hall.
- Wortman J. J. and Evans R. A. (1965). Young’s modulus, shear modulus, and Poisson’s ratio in silicon and germanium. *Journal of Applied Physics* 36(1), 153–156.
- Xiao S. P. and Belytschko T. (2004). A bridging domain method for coupling continua with molecular dynamics. *Computer Methods in Applied Mechanics and Engineering* 193, 1645–1669.
- Yamakov V., Saether E., and Glaessgen E. H. (2008). Multiscale modeling of intergranular fracture in aluminum: constitutive relation for interface debonding. *Journal of Materials Science* 43, 7488–7494.
- Yamakov V., Saether E., Phillips D. R., and Glaessgen E. H. (2006). Molecular-dynamics simulation-based cohesive zone representation of intergranular fracture processes in aluminum. *Journal of the Mechanics and Physics of Solids* 54, 1899–1928.
- Yamakov V., Saether E., Phillips D. R., and Glaessgen E. H. (2007). Dynamics of nanoscale grain-boundary decohesion in aluminum by molecular-dynamics simulation. *Journal of Materials Science* 42, 1466–1476.